Effect of Lean-Burn Combustor Outlet Flows on Nozzle Guide Vane Aerothermal Performance: an Experimental and Computational Study

A thesis submitted for the degree of
Doctor of Philosophy



Jonas Elias Amend
Supervisor: Prof. Thomas Povey

Department of Engineering Science
University of Oxford

Christ Church January 2024

This page is intentionally blank

Abstract

Regulatory pressures aimed at reducing NO_x and particulate emissions from civil aviation have seen engine manufacturers gravitate towards *lean-burn* combustor architectures. Compared to their conventional *rich-burn* counterparts, lean-burn combustors generate significant swirl and alter the temperature distribution at the interface with the high-pressure turbine. We examine the impact of lean-burn on the aerothermal performance of high-pressure nozzle guide vanes (NGV), leveraging engine-scale experiments and simulations.

Experiments were conducted in the Engine Component AeroThermal facility—an annular NGV test facility designed to operate at engine-matched conditions of Mach number, Reynolds number, and coolant flow. Two test cases were considered: a reference case with uniform inflow, and a lean-burn case, which used a combustor simulator to generate representative inlet profiles of swirl and temperature distortion. Mean-flow and turbulence conditions *upstream* of the NGV were characterized in detail using a purpose-built traverse system. These served as reference conditions for measurements of flow angle, kinetic energy loss, and total temperature taken *downstream* of the NGV, and were used as inlet boundary conditions in complementary simulations.

In a first instance, turbulence model sensitivities were explored, using the experimental dataset with uniform inflow as a benchmark. Simulations based on the k–ω shear stress transport model captured radial distributions of whirl angle, loss, and non-dimensional temperature reasonably well, but failed to accurately predict mixing rates of the aerodynamic and thermal wakes. Undermixing is a common problem in simulations of flows where significant unsteady vortex shedding *occurs* in reality, but is not *modeled* due to steady-state assumptions. For the current geometry and inlet conditions, the baseline k–ω algebraic Reynolds stress model had enhanced free shear mixing, resulting in a slightly better overall collapse with experimental data.

In a second instance, the effect of lean-burn was studied. Compared to the uniform inflow reference case, lean-burn caused significant residual swirl in the downstream flow, and amplified integral loss slightly. Changes in the downstream thermal field were primarily driven by the upstream temperature profile, with a secondary influence from swirl-induced redistribution of vane coolant. Coolant redistribution was especially pronounced on the vane pressure side, where uneven film coverage led to significant deterioration of cooling performance.

This thesis represents a comprehensive analysis of the impact of lean-burn on NGV performance, gives insight into the robustness of commonly-used simulation tools, and highlights areas for redesign to optimize for lean-burn profiles.

This page is intentionally blank

Acknowledgments

First and foremost, I would like to thank my supervisor and mentor, Thomas Povey, for offering me the incredible opportunity to work under his supervision, and for always providing insightful input. I am also indebted to Nafiz Chowdhury, who tirelessly worked many late nights to support my experimental work, and Andrew Messenger, whose expert knowledge of engineering design I was always keen to consult. By the same token, I extend my gratitude to outgoing post-doctoral researchers Francesco Ornano, and Roderick Lubbock, whose projects I inherited at the beginning of my DPhil—their guidance was vital to getting me off to a quick start. My thanks also goes out to my peers Daniel Burdett, and Mathias Michaud for their patience in responding to my countless questions about the ECAT facility, and to Zelimhan Akhmiev as well as Matthew Stokes for the stimulating discussions we held throughout our many spontaneous conference calls. Special thanks goes to Masha Folk for generously sharing her experimental flat plate data, which I used to benchmark turbulence models.

Of course, none of the experimental or computational work would have been possible without the many dedicated support staff, machinists, and electrical workshop staff at both the Southwell and Thom buildings. In particular, I would like to thank Bill Godfrey, Hal Surtell, and Dominic Harris for supporting test facility operations throughout my experimental campaign, Jiaju Du for her extremely precise soldering work, Duncan Constable for quickly turning around machined parts, and Gregory King for advising me on electrical safety and wiring. Likewise, I would like to express my heartfelt appreciation to Craig Parsons, Josh Baker, and Roger Robinson for their commitment to maintaining and improving the IT infrastructure at the Southwell building—be it the setup of new equipment, the installation of software, or the rapid resolution of unexpected hardware failures.

This project was jointly funded by Rolls-Royce plc and the Engineering and Physical Sciences Research Council, covering University fees, college fees, and maintenance payments. At Rolls-Royce, I had the privilege of working with Frédéric Goenaga and Sulfi Noor Mohamed who both helped shape my project, and offered me an industry perspective on turbomachinery research.

Last but not least, my deepest gratitude goes out to my family for supporting me throughout this exciting journey. I could not have done it without your unrelenting encouragement and love!

This page is intentionally blank

Contents

Abstract i

Acknowledgments iii

Contents v

Nomenclature xi

1 Introduction 1
- 1.1 Research outcomes . . . 2
- 1.2 Thesis outline . . . 3

2 Literature Review 5
- 2.1 Brayton cycle with component losses . . . 6
- 2.2 Historic trends in turbine entry temperature . . . 7
- 2.3 Brayton cycle: component efficiency, cooling flow, and real gas effects . . . 8
- 2.4 Emissions, air quality, and climate . . . 9
  - Combustion process . . . 9
  - Effect on air quality and health . . . 9
  - Effect on climate warming . . . 10
  - Climate policy and emission standards . . . 12
- 2.5 Combustors . . . 13
  - Conventional combustor . . . 13
  - Factors affecting pollutant emissions . . . 14
  - Low emission strategy . . . 16
  - Overview of low emissions combustors . . . 16
  - Comparison of combustor architectures . . . 20
- 2.6 Conditions at lean-burn combustor outlet . . . 21
  - Residual swirl . . . 21
  - Temperature distribution . . . 23
  - Unsteadiness and turbulence . . . 24
- 2.7 Combustor simulators . . . 25
- 2.8 Lean-burn combustor–turbine interactions . . . 26
  - Definition of clocking and swirl direction . . . 26
  - Effect of inlet swirl on NGV and turbine performance . . . 27
  - Effect of inlet swirl combined with temperature non-uniformity (hot streak) . . . 29
  - Geometry and clocking optimization . . . 31

3 Lean-burn combustor simulator for an engine component test facility 33
- 3.1 Introduction . . . 34
- 3.2 Review of combustor simulators with combined swirl and temperature distortion . . . 36
- 3.3 The ECAT facility . . . 38
- 3.4 Design of the combustor simulator . . . 38
  - Combustor simulator design optimization . . . 39
  - Swirler count and geometry . . . 41
- 3.5 Combustor simulator commissioning . . . 41
  - Geometry and hardware . . . 41
  - Instrumentation . . . 42
  - Experimental conditions for commissioning experiments . . . 44
  - Transient effectiveness correction . . . 46

3.6 Numerical methods . . . 48
CFD domains . . . 48
Numerical test matrix . . . 49
Mesh and boundary conditions . . . 50
Models and solver settings . . . 50
3.7 Experimental and numerical results . . . 51
Distributions of loss, temperature, pitch and yaw . . . 52
Radial profiles of pitch and yaw . . . 53
3.8 Effect of Mach number mismatch and vane potential field . . . 55
Reynolds and Mach number scaling . . . 56
Effects of back-pressure (on M) and the vane potential field . . . 57
3.9 Circumferential flow migration . . . 59
3.10 Numerical study on circumferential flow migration . . . 59
3.11 Conclusions and recommendations . . . 62
3.A Grid sensitivity study . . . 65
3.B Effect of net-circulation on flow migration . . . 67

4 Ultra-compact traverse system for transonic annular cascade 70
4.1 Introduction . . . 71
4.2 Literature review . . . 72
4.3 Traverse plane location . . . 74
4.4 Traverse system overview . . . 74
4.5 Subsystems and interfaces . . . 75
Cassette housing assembly . . . 75
Carriage frame assembly . . . 76
Radial traverse gear assembly . . . 76
Circumferential traverse gear assembly . . . 76
Entire traverse assembly . . . 76
4.6 Traverse electronics and control . . . 77
Traverse system electronics box . . . 77
Communication and control . . . 77
4.7 Experimental methods . . . 78
Overview of probes . . . 78
Build configuration for reported data . . . 78
Constant temperature anemometer setup and calibration . . . 79
Hotwire data reduction . . . 80
Decomposition & turbulence statistics . . . 81
Pressure and temperature data processing . . . 82
Traverse patterns . . . 82
4.8 Sample data . . . 82
4.9 Uncertainty and repeatability . . . 84
Bias uncertainty . . . 84
Precision uncertainty . . . 84
Repeatability in practice . . . 85
4.10 Conclusions . . . 86

5 Facility flow conditioning system redesign 87
5.1 Original design . . . 87
Working section mechanical design . . . 87
Flow conditioning system aerodynamic design . . . 88
5.2 Experimental methods . . . 90
5.3 Numerical methods . . . 90

Domain and mesh . . . 91
Boundary conditions . . . 91
Model and solver settings . . . 91
5.4 Non-uniformity at inlet plane . . . 91
Experimental results . . . 93
Numerical results . . . 93
5.5 Cause of non-uniformity . . . 94
Circumferential distortion . . . 94
Radial distortion . . . 95
5.6 Redesign process . . . 96
5.7 Revised design . . . 96
5.8 Flow field comparison of original and revised design . . . 97
Circumferential distortion . . . 97
Radial distortion . . . 99
5.9 Conclusions . . . 100
5.10 Recommendations . . . 101

6 Aerodynamic and thermal field development of cooled transonic HP NGV 103
6.1 Introduction . . . 104
6.2 Experimental methods . . . 106
Test section layout and instrumentation . . . 106
Experimental operating conditions . . . 108
Experimental inlet profiles . . . 108
6.3 Numerical methods . . . 111
Computational domain . . . 111
Computational grid . . . 112
Boundary conditions . . . 113
Solver settings . . . 113
6.4 Performance metrics . . . 113
Whirl angle definition . . . 113
Kinetic energy loss coefficients . . . 113
Flow effectiveness: the non-dimensional flow temperature . . . 116
6.5 Experimental and numerical results . . . 116
NGV exit circumferential static pressure profiles . . . 116
Whirl angle profiles . . . 118
Local kinetic energy loss . . . 121
Circumferential kinetic energy loss distributions at midspan: wake width, peak loss, and integrated loss . . . 123
Mixed-out and plane-averaged kinetic energy loss coefficients . . . 129
Downstream thermal field . . . 133
Mixing rates of thermal field . . . 136
6.6 Conclusions . . . 140
6.A Measurement uncertainty . . . 143
6.B Grid sensitivity study . . . 143

7 Comparison of eddy viscosity models for high turbulence NGV flows 149
7.1 Introduction . . . 150
7.2 Shear stress transport model . . . 151
Eddy viscosity and turbulence scales . . . 151
SST transport equations . . . 153
Model/closure coefficient blending . . . 155
Shear stress limiter . . . 156

Standard k–ω and baseline model . . . 157
Production limiters . . . 158
7.3 High turbulence flat plate test . . . 158
7.4 High turbulence NGV flows . . . 160
7.5 Modified blending and stress limiter . . . 162
Modified closure coefficient blending . . . 162
Modified shear stress/realizability limiter . . . 163
7.6 Additional models . . . 165
Explicit algebraic Reynolds stress model . . . 165
Spalart–Allmaras model . . . 166
7.7 Experimental data and setup . . . 166
Test section layout . . . 166
Instrumentation . . . 167
Cascade inlet conditions . . . 167
7.8 Numerical methods . . . 169
Domain and grid . . . 169
Model settings and discretization . . . 169
Boundary conditions . . . 170
7.9 Performance metrics . . . 170
7.10 Results and analysis . . . 172
Kinetic energy loss and cold gas mass fraction at downstream measurement plane 172
Plane-averaged, profile-region, and endwall-region loss . . . 177
Aerodynamic and thermal wake shapes . . . 180
Aerodynamic wake spreading and decay . . . 183
Thermal wake spreading and decay . . . 186
7.11 Conclusion . . . 189
7.A Flat plate test data . . . 194
7.B Modified blending function . . . 195
7.C Inlet turbulence intensity . . . 197
7.D Length scale definition . . . 199

8 Impact of lean-burn combustor flow on NGV performance 201
8.1 Introduction . . . 203
8.2 Experimental methods . . . 206
Test section overview . . . 206
Instrumentation and measurements . . . 208
Experimental operating conditions . . . 209
8.3 Performance metrics . . . 209
Flow angle definitions . . . 209
Upstream normalized total pressure . . . 209
Upstream non-dimensional total temperature . . . 210
Upstream turbulence intensity and integral length scale . . . 210
Kinetic energy loss coefficients . . . 211
Non-dimensional downstream/surface total temperature . . . 211
8.4 Combustor simulator outlet profiles . . . 211
8.5 Numerical methods . . . 215
Computational domain and grid . . . 215
Boundary conditions . . . 216
Model and solver settings . . . 216
8.6 NGV loading and streamline pattern . . . 217
NGV loading distribution . . . 217
Surface streamlines . . . 218

8.7 Effect on cooling system . . . 220
Description of internal cooling configuration . . . 220
Internal flow redistribution . . . 220
Adiabatic wall temperature . . . 222
8.8 Effect on downstream flow . . . 225
Whirl angle and residual combustor swirl . . . 225
Kinetic energy loss coefficient . . . 229
Axial development of integral kinetic energy loss . . . 233
Separating mean-flow and turbulence effects . . . 235
Downstream thermal field . . . 236
Separating effects on downstream thermal field due to inlet temperature profile migration and coolant migration . . . 239
8.9 Conclusions . . . 241

9 Conclusion **245**
9.1 Facility and equipment design . . . 245
9.2 Impact of lean-burn on NGV performance . . . 246
9.3 Numerical modeling observations and recommendations . . . 247

References **248**

Statement of authorship **262**
Chapter 3 . . . 262
Chapter 4 . . . 263
Chapter 6 . . . 264
Chapter 7 . . . 265
Chapter 8 . . . 266

This page is intentionally blank

Nomenclature

Symbols and subscripts

Several chapters in this thesis have previously been published in the form of peer-reviewed papers. To maintain consistency with published work, and to avoid multiple definitions or conflicts, a separate list of symbols is included at the end of each chapter. References and acronyms have been consolidated throughout.

Acronyms

ALECSys	Advanced Low Emissions Combustor System
ARSM	Algebraic Reynolds Stress Model
ASC	Axially Staged Combustor
BPR	Bypass Ratio
BSL	Baseline zonal k–ω model
BSL-ARSM	Baseline zonal k–ω model combined with non-linear stress–strain relation.
CCW	Counter-Clockwise
CFD	Computational Fluid Dynamics
CMC	Ceramic Matrix Composite
CS	Combustor Simulator
CCW	Counter Clockwise
CW	Clockwise
CTA	Constant Temperature Anemometry
DAC	Double Annular Combustor
ECAT	Engine Component AeroThermal (facility)
FACTOR	Full Aerothermal Combustor–Turbine interactiOn Research
FAR	Fuel-to-Air Ratio
FWHM	Full Width at Half Maximum
GE	General Electric Aerospace
HP	High-Pressure
HPT	High-Pressure Turbine
HTC	Heat Transfer Coefficient
IATA	International Air Transport Association
ICAO	International Civil Aviation Organization
KE	Kinetic Energy
LE	Leading Edge
LSTR	Large Scale Turbine Rig
LTO	Landing and TakeOff (cycle)
LV	Leading Vane
LES	Large Eddy Simulation
NGV	Nozzle Guide Vane
NO_x	Nitrogen Oxides
nvPM	non-volatile Particulate Matter
OLCS	Oxford Lean-burn Combustor Simulator
OPR	Operating Pressure Ratio
OTDF	Overall Temperature Distribution Factor
OTRF	Oxford Turbine Research Facility

PR	Pressure Ratio
PS	Pressure Side
PVC	Precessing Vortex Core
RANS	Reynolds-Averaged Navier–Stokes
RF	Radiative Forcing
RISE	Revolutionary Innovation for Sustainable Engines
RQL	Rich-burn Quick-quench Lean-burn
RR	Rolls-Royce plc
RSM	Reynolds Stress Model
RTDF	Radial Temperature Distribution Factor
SA	Spalart–Allmaras (model)
SAF	Sustainable Aviation Fuel
SKE	Secondary Kinetic Energy (coefficient) **or** Standard k–ϵ (model)
SKO	Standard k–ω (model)
SO_x	Sulfur Oxides
SS	Suction Side
SST	Shear Stress Transport k–ω (model)
TALON X	Technology for Advanced LOw NO_x
TAPS	Twin Annular Premixing Swirler
TDC	Top Dead Center
TE	Trailing Edge
TET	Turbine Entry Temperature
TG	Turbulence Grid
TI	Turbulence Intensity
TKE	Turbulence Kinetic Energy
TR	Temperature Ratio
TV	Trailing Vane
UHC	Unburnt HydroCarbon
UNIFI	Università di Firenze (University of Florence)
URANS	Unsteady RANS
VFD	Viewed From Downstream
VFU	Viewed From Upstream

This page is intentionally blank

This page is intentionally blank

1 | Introduction

Heavier-than-air flight has undoubtedly revolutionized the world as we know it today, and possibly represents the most significant breakthrough in transportation since the invention of the wheel. Since the Wright Flyer I first took to the skies in December 1903, aviation has come a long way to develop into the high-speed, safe, and affordable mode of transportation of the modern day. Despite having become a part of everyday life, flying continues to symbolize the pursuit of freedom in the limitless heavens above, inspiring awe in the minds of engineers and adventurers alike.

Recent years saw growing concern over the impact of aviation on the environment. Globally, aviation accounts for roughly 2.5% of greenhouse gas emissions by mass [1], primarily from the combustion of fossil fuels in aircraft engines. Although the aviation industry has a long track record of continuous improvements in fuel efficiency, technological advancements have consistently been outpaced by sector growth as a whole. This means that *absolute* emissions from aviation have nearly quadrupled since 1970, and are bound to continue increasing if not counter-balanced by a paradigm shift. In this vision, the industry has laid out a strategy to completely de-carbonize aviation by 2050 through a combination of sustainable aviation fuels (SAF), novel propulsion technologies, and carbon capture. While the de-carbonization of aviation is certainly a commendable endeavor, recent research suggests that non-CO_2 combustion products—namely nitrogen oxides (NO_x) and particulates (soot)—could play an equally important role in global warming [2]. Adjusting for this effect, aviation may account for as much as 5% of climate forcing. Mitigating the environmental impact of aviation therefore hinges on the development and adoption of combustor systems with low NO_x and particulate emissions.

Regulations on NO_x emissions were first introduced in the 1980s to combat their adverse effects on respiratory health. As the understanding of NO_x-driven climate forcing improved with time, emission standards became increasingly stringent and have recently been updated to include limits on non-volatile particulate matter (nvPM). Future tightening of emission standards is to be expected, which will require radical changes to the combustion process. Among several viable solutions [3], so-called *lean-burn* combustors have been identified as a particularly promising concept. As a natural development of implementing this technology, the associated risks need to be identified and adequately mitigated. This thesis contributes to this effort by performing experiments and simulations to examine the effect of lean-burn on the aerothermal performance of the high-pressure nozzle guide vane—the component immediately downstream of the combustor, and potentially most affected by a change in its architecture.

1.1 Research outcomes

This thesis examines the impact of lean-burn combustion on high-pressure nozzle guide vane (NGV) performance using a combination of experiments and simulations. The experiments were conducted in the Engine Component AeroThermal (ECAT) facility, which is a fully-annular NGV test facility capable of operating at engine-matched conditions of Reynolds number and Mach. The experimental assessment of lean-burn effects revolved around a purpose-built combustor simulator, which was shown to generate profiles of swirl and non-dimensional temperature similar to those of a recent lean-burn combustor prototype. In an effort to improve understanding of combustor simulator turbulence, a compact upstream traverse system was designed, manufactured, and used to survey the flow at vane inlet using split-fiber probes.

The evaluation of NGV performance under lean-burn built on a prior experimental characterization of the NGV flow under uniform inlet conditions, which was used as the performance baseline. The measurements with uniform inflow were initially analyzed in terms of aerodynamic wake development, thermal field mixing and integral loss, and would later serve as validation data in an investigation of the turbulence model sensitivity of NGV flows. Results with the k–ω shear stress transport (SST) model were undermixed—a common problem in flows where unsteady vortex shedding occurs but is not modeled. It was argued that some undermixing might be *unrelated to vortex shedding*, occurring instead due to excessively strict stress limiting conditions enforced in the vane passage. Responsiveness to freestream turbulence increased as the stress limiter was relaxed. For the current test case, this improved likeness with experiments slightly, although it remains unclear to what degree the behavior is conflated with mixing caused by unsteady vortex shedding.

NGV experiments with lean-burn investigated residual combustor swirl, thermal field development and kinetic energy loss in the downstream flow. Complementary simulations were performed to explore the strengths/limitations of numerical models in lean-burn environments, and to investigate the cooling system response to swirl. In both experiments and simulations, the downstream flow had mild residual swirl, persistent temperature distortion, and slightly increased integral loss compared to the baseline with uniform inflow. Simulations revealed significant internal flow redistribution on account of altered external loading. Combined with a modified surface streamline pattern, this led to a degradation of the film coolant coverage uniformity, ultimately resulting in a lower area-averaged film effectiveness. All in all, current NGV designs appear reasonably resilient to lean-burn, but may need adapted cooling for optimum performance.

1.2 Thesis outline

The top-level structure of the thesis is shown in Figure 1.1. Each box represents a chapter, with arrows indicating the flow of information. The content of each chapter is briefly summarized below.

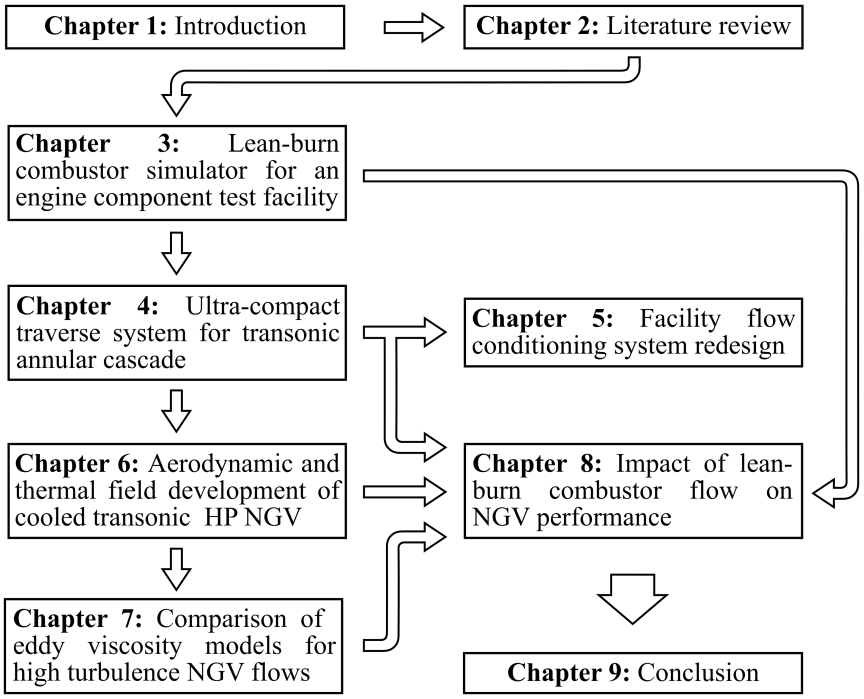


Figure 1.1: *Flow of information between the chapters of this thesis.*

Chapter 1: Introduction

The introduction touches upon recent developments and emerging trends in commercial aviation, and outlines how the current thesis contributes to related research efforts. You are currently reading this chapter.

Chapter 2: Literature review

The literature review considers the high-level performance optimization of civil turbofan engines, with an emphasis on low emission combustor architectures, and how these might impact the high-pressure turbine. In-depth literature reviews are included as part of the individual chapters.

Chapter 3: Lean-burn combustor simulator for an engine test facility

This chapter takes the form of a *peer-reviewed journal paper* [4], presenting the design and commissioning of a lean-burn combustor simulator for the ECAT facility. The study features detailed experimental measurements at combustor simulator exit, which are compared with predictions from computational fluid dynamics (CFD) simulations.

Chapter 4: Ultra-compact traverse system for transonic annular cascade

This chapter takes the form of a *peer-reviewed conference paper* [5], describing the design and commissioning of an ultra-compact traverse system for characterizing the mean-flow and turbulence upstream of the vanes. In subsequent chapters, the traverse measurements are used as reference conditions for NGV experiments, and as boundary conditions in complementary CFD simulations.

Chapter 5: Facility flow conditioning system redesign

This *conventional chapter* presents an improved design of the ECAT facility flow conditioning system. After identifying the causes of non-uniformity in the original design, the improved design is developed using fully-annular simulations of the facility working section. The new design features two perforated plates and a pair of flow guides, halving non-uniformity at vane inlet.

Chapter 6: Aerodynamic and thermal field development of cooled transonic HP NGV

This chapter takes the form of a *peer-reviewed journal paper* [6], which examines the aerodynamic and thermal field development downstream of high-pressure NGV sourced from a modern turbofan engine. The study is based on high-fidelity experimental data, which is used to assess the accuracy of CFD in terms of whirl angle, wake mixing rates, and integral loss. The analysis is deepened by comparing results with an earlier study, which used NGV from a different engine of the same family.

Chapter 7: Comparison of eddy viscosity models for high turbulence NGV flows

This chapter takes the form of a *peer-reviewed journal paper* [7], which explores turbulence model sensitivities of NGV flows under high-turbulence inlet conditions. The study examines the effects of various stress realizability limiters on aerodynamic/thermal field mixing, and integral loss.

Chapter 8: Impact of lean-burn combustor flow on NGV performance

This chapter takes the form of a *journal paper* (under review), which investigates the impact of lean-burn-representative swirl and inlet temperature distortion on the aerothermal performance of fully-cooled NGV. The study is based on highly engine-representative experimental data and CFD simulations of the fully-featured vane geometry. Key topics include hot streak migration, integral loss, and cooling performance.

Chapter 9: Conclusion

The conclusion summarizes key outcomes of the thesis, and offers an outlook on how the field of combustor–turbine interactions research might develop in the near future.

2 | Literature Review

With fuel costs accounting for nearly a third of operating expenses of a typical air carrier [8], reduced fuel consumption has long been a strong selling point of new aircraft. Historically, fuel consumption (measured in kilograms of fuel per tonne of payload per kilometer) has shrunk on average by 1.0% per year since 1960 [9]. This has been achieved *in-part* through optimized airframe designs with improved aerodynamic characteristics (e.g. wingtip devices; supercritical airfoils; rounded cockpit windows), and reduced weight (e.g. composites; additive manufacturing), but perhaps *more importantly* through the development of more efficient engines.

With climate change in the spotlight, the International Civil Aviation Organization (ICAO) [10] and the International Air Transport Association (IATA) [11] have set-out the goal to completely de-carbonize civil aviation by 2050. This plan relies on the widespread adoption of Sustainable Aviation Fuels (SAF), novel technologies, and further fuel efficiency gains. Low SAF usage thus far can be ascribed to its greater cost, compared to conventional kerosene fuel. In the United States, SAF adoption will be incentivized through a tax credit system, while the European Union plans to mandate minimum usage for all departing flights from 2025 onward [12]. Fuel efficiency gains, on the other hand, are likely to be derived from a combination of higher bypass ratio engines (i.e. greater propulsive efficiencies) and improvements in the thermal efficiency of the gas turbine core.

While pollutant emissions such as NO_x and particulates have been known to harm respiratory health since the 1970s, their role in climate forcing only came to light shortly before the turn of the century [13]. The recent estimates of Grewe et al. [2] go so far as to suggest that the cumulative warming effect of pollutants from aircraft engines may exceed that of CO_2 . This emphasizes the importance of harmonizing de-carbonization goals with low emission combustor technology. In response, regulators have imposed increasingly stringent limits on the permitted pollutant levels in aircraft engine exhausts. Several industry initiatives are underway to develop/mature so-called lean-burn combustors, which promise to deliver the necessary reductions in pollutant emissions.

The literature review begins by exploring the effects of component efficiency, cooling, and real gas effects on the fuel efficiency of modern aero-engines. This is relevant insofar interplay between fuel efficiency (i.e. CO_2 emissions) and pollutant emissions may require trading-off the turbine entry temperature. Low emission combustor architectures—past, present, and future—are reviewed in terms of their emission characteristics, and in terms of the resulting conditions of swirl, turbulence, and temperature distribution at combustor exit. The chapter concludes by examining the existing literature on the effects of lean-burn combustion on high-pressure turbine performance.

2.1 Brayton cycle with component losses

For an ideal Brayton cycle, thermal efficiency approaches unity asymptotically as the compressor pressure ratio (PR) tends to infinity. This relationship breaks down for real gas turbines, where the compression, combustion, and expansion processes are associated with irreversible total pressure losses. To illustrate this, a carpet plot of thermal efficiency and specific work with varying inlet-to-turbine-entry temperature ratio (TR) and compressor PR is shown in Figure 2.1 for representative polytropic compressor and turbine efficiencies of 0.90 and a combustion pressure loss of 3%. Ideal gas law and constant specific heats were assumed.

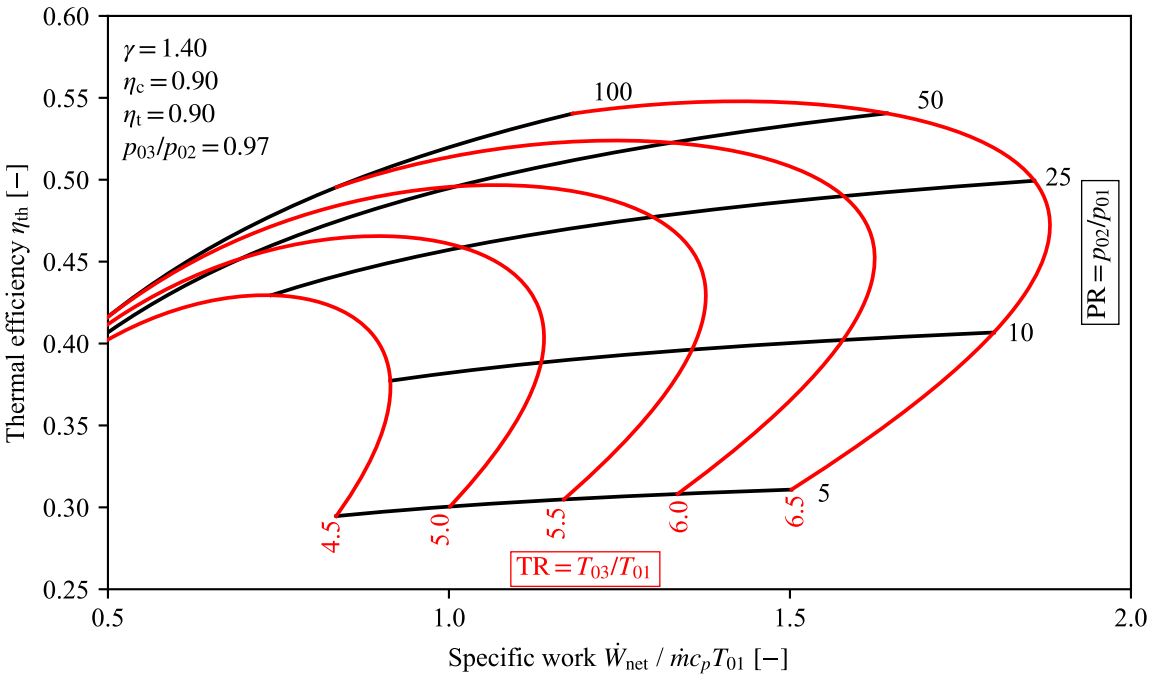


Figure 2.1: *Brayton cycle thermal efficiency (η_{th}) and specific work ($\dot{W}_{net}/\dot{m}c_pT_{01}$) as a function of temperature ratio (TR) and pressure ratio (PR).*

The graph shows that thermal efficiency and specific work of the non-ideal cycle depend on both PR and TR. Critically, the maximum attainable thermal efficiency increases with the TR, and occurs at a finite PR. Trends for specific work are qualitatively unchanged compared to an ideal cycle, with the maximum achievable value increasing with TR. As both specific work and thermal efficiency increase with TR, performance is chiefly limited by the ability of materials to withstand high temperatures. Modern gas turbines can operate at TRs up to 6.5, for which the maximum thermal efficiency based on the current assumptions occurs around PR = 73, and the maximum specific work output is achieved around PR = 18. In practice, the chosen PR for a certain TR is likely to fall *in between* these optima, based on a trade-off that takes into consideration the effects of overall efficiency and propulsion system weight on the fuel consumption of the whole aircraft.

2.2 Historic trends in turbine entry temperature

Ideal gas analysis of the Brayton cycle suggests that thermal efficiency and specific work can be improved indefinitely by increasing the turbine entry temperature (TET). Practical limits on the TET arise from mechanical requirements of material strength, and creep resistance, both of which deteriorate rapidly for temperatures approaching the melting point. Historically, increases in TET have therefore been facilitated by a combination of advancements in material capability and innovative cooling technologies. This trend is illustrated in Figure 2.2, using a number of landmark Rolls-Royce engines as examples (adapted from Cumpsty [14]).

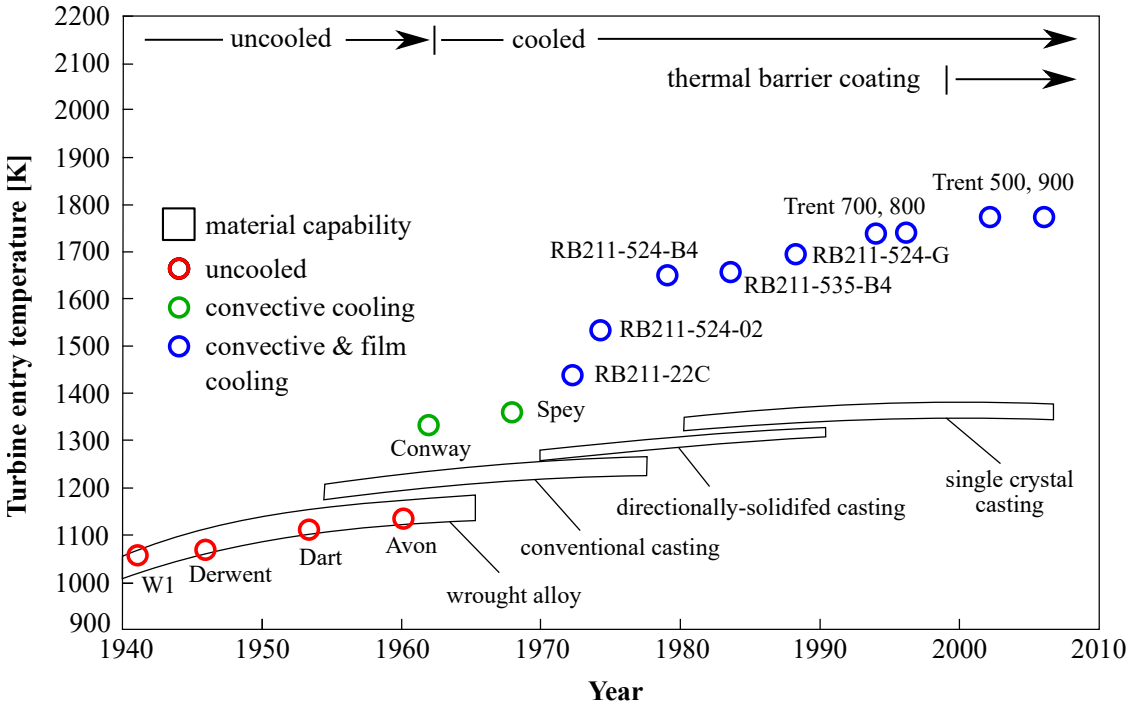


Figure 2.2: *Historic trends in the turbine entry temperature (TET) in the context of material and cooling technology advancements (adapted from Cumpsty [14]).*

Turbines in early engines such as the Dart and Avon were entirely uncooled, and therefore limited by their wrought alloy blades to TETs below 1200 K. With the introduction of the Conway, internal cooling passages allowed the turbine to operate at gas temperatures much closer to the material melting point. Cooling efficiency was improved drastically with the implementation and optimization of film cooling on the RB211, leading to a rapid increase in TET between 1970 and 1980 [15]. Since then, advanced manufacturing methods such as directionally-solidified and single crystal casting have been leveraged alongside thermal barrier coatings to further increase TET. Future increases in TET are likely to be derived from Ceramic Matrix Composite (CMC) materials, and from the maturation of transpiration cooling technology.

2.3 Brayton cycle: component efficiency, cooling flow, and real gas effects

While historic trends may initially lend credibility to the theoretical performance improvements afforded by increasing the TET, Horlock [16] demonstrated that thermal efficiency peaks at a finite temperature when incorporating real gas effects into the analysis. Building on this very significant outcome, Wilcock et al. [17] examined the effect of variable cooling flows and component efficiency in the context of the real gas Brayton cycle.

Although cooling is generally beneficial for the cycle efficiency in that it allows higher temperatures to be reached, Horlock [16] demonstrated that cooling incurs a small penalty in the thermal efficiency, compared to an uncooled cycle with the same TET. This can be explained by considering the coolant stream *in isolation*, noting that this fictitious cycle—consisting of a compression followed immediately by an expansion—yields net-negative useful power for non-ideal components. Cooling also reduces specific power, because a smaller fraction of the core flow participates in the main cycle. A key objective in turbine design is therefore to reduce the coolant flow as far as possible within the constraints of material capabilities and component design life. Additional reductions in thermal efficiency occur through thermal and kinematic mixing of the coolant with the hot stream.

The sensitivity of the real gas cycle to cooling flows, and component efficiencies was investigated by Wilcock et al. [17]. As expected, the maximum attainable thermal efficiency increased with both component efficiency and cooling effectiveness. Based on realistic ultimate limits on efficiency and cooling effectiveness, Wilcock et al. predict a maximum thermal efficiency slightly above 0.53, occurring for a TET around 2050 K [17]. By comparison, current civil engines operate at TETs up to 1900 K, reaching thermal efficiencies near 0.50.

In summary, the maximum achievable thermal efficiency of jet engines depends on the aerodynamic efficiency of components, and the fraction of the core flow which is used as coolant. The coolant flow, in turn, depends on material capability and the effectiveness of cooling. This emphasizes the importance of developing understanding in factors that affect component efficiency and the effectiveness of their cooling. While cycle analysis suggests that future increases in TET are warranted on thermodynamic grounds, there are environmental factors that render temperatures above 1900 K unattractive. Fortunately, cycle efficiency is not very *sensitive* to TET near the optimum, meaning that this constraint does not require significant sacrifices.

2.4 Emissions, air quality, and climate

The previous section focused on factors affecting the thermal efficiency of turbofan engines. This can be regarded both as an exercise in minimizing fuel costs, and as an effort in reducing the carbon footprint of aviation. Recent research indicates that pollutants such as NO_x and particulates may play an equally important role in climate change as CO_2 , despite accounting for a much smaller proportion of aircraft emissions by mass [2]. They also pose concern in terms of their impact on air quality around airports [18]. We review the most common pollutants from turbofan engines, consider their effects on climate and health, and discuss relevant environmental policies. This leads into a discussion of viable low emissions combustor architectures for turbofan engines.

Combustion process

Jet A-1 is by far the most widely-used fuel in civil aviation. It is composed of a mixture of hydrocarbons (paraffins, naphthenes, aromatic compounds), sulfur, and additives (anti-ice, static dissipators, corrosion inhibitors, etc.). When burned in an excess of air (N_2 + O_2 + inert Ar), the *primary* combustion products of Jet A-1 are carbon dioxide (CO_2) and water vapor (H_2O). The most abundant *secondary* combustion products are oxides of nitrogen (NO_x), oxides of sulfur (SO_x), carbon monoxide (CO), unburnt hydrocarbons (UHCs), and non-volatile particulate matter (nvPM; mainly black carbon). The unbalanced equation for this reaction is

$$\underbrace{\mathrm{N_2 + O_2}}_{\text{air}} + \underbrace{\mathrm{C_nH_m + S}}_{\text{fuel}} \rightarrow \underbrace{\mathrm{N_2 + O_2}}_{\text{air}} + \underbrace{\mathrm{CO_2 + H_2O}}_{\text{primary products}} + \underbrace{\mathrm{NO_x + SO_x + CO + UHC + nvPM}}_{\text{secondary products}} \tag{2.1}$$

Primary reaction products (CO_2 and H_2O) account for approximately 99.5% of non-air exhaust gases by mass [18]. As the controlling mechanism for their formation is the fuel flow rate, the scope for minimizing them is through the total efficiency of the engine. The remaining 0.5% of reaction products can arise from incomplete combustion (CO, UHC), temperature-sensitive secondary reactions (NO_x, CO, nvPM), and fuel composition dependencies (NO_x, SO_x, nvPM) [3]. The effects of combustion products on health and climate are now considered.

Effect on air quality and health

Aircraft emissions during taxi, departure, and approach affect the air quality in and around airports. This poses a health risk to chronically exposed individuals, particularly airport staff, and residents of nearby neighborhoods. On a much broader spatial scale, Barrett et al. [19] argued that recirculation of cruise emissions could have significant effects on ground-level pollutant concentrations. They estimated that of the 10,000 premature deaths attributable to aviation annually, approximately 80%

were caused by cruise emissions. The majority of these deaths are thought to occur in response to respiratory and cardiovascular conditions arising from exposure to fine particulate matter ($PM_{2.5}$; particles with diameters below 2.5 µm) and ozone (O_3) [20]. The effects of aviation on the complex atmospheric dynamics of particulates and ozone are now briefly considered.

Fine particulate matter is thought to be the primary driver of deaths from air pollution worldwide. Jet engines are not only a direct source of particulate matter (nvPM), but also emit gaseous aerosol precursors, which go on to develop into particulate matter through a complex series of atmospheric processes [18, 21]. An example of the latter mechanism is the conversion of NO_x and SO_x gases into nitrate and sulfate particulates. Simplistically, this occurs due to oxidation of NO_x /SO_x into nitric/sulfuric acid, respectively, which in turn react with ambient alkaline compounds (e.g. ammonia) to form solid particles (e.g. ammonium nitrate/sulfate). These particles grow through condensation of additional acid onto individual particles and through aggregation of multiple smaller particles into larger ones.

Ozone was identified as another important predictor of mortality from air pollution. Although no direct emissions of ozone are present in jet engine exhausts, both NO_x and carbon monoxide are known precursors to ozone [18, 22], and thereby *indirectly* contribute to further air pollution.

Unburnt hydrocarbons in aircraft engine exhausts were studied by Bendtsen et al. [23]. Many of the compounds are toxic in high concentrations, but their effects in dilute form are not well understood. Masiol et al. [18] argued that—although the effect of aviation on background concentration levels might be considered negligible compared to surface-level transportation—better understanding is required to accurately assess the potential health risks.

Effect on climate warming

The effect of human activity on climate is often expressed as an effective global-average heat flux. In the year 2005 for example (commonly-used reference point), overall anthropogenic radiative forcing (RF) from agriculture, industry, power generation, and transport combined to approximately 1600 mW/m^2 according to Lee et al. [24]. In comparison, the RF of CO_2 and water vapor *attributable to aviation* was estimated at +28.0 mW/m^2 and +2.8 mW/m^2, respectively, for the same year [24]. This is equivalent to 1.9% of overall RF, which is small but not insignificant.

While the climate warming effect of aviation CO_2 is widely acknowledged, the influence of pollutants is less well understood. This stems from their comparatively short lifetime, and complex interaction with atmospheric processes. The present state of knowledge is briefly summarized, with the purpose of highlighting the relative importance of pollutants, compared to that of CO_2 .

NO_x participates in a number of complex atmospheric processes. Most relevant to climate warming is its effect on concentrations of ozone (O_3) and methane (CH_4), both of which are potent greenhouse gases. In the short term, NO_x enhances photochemical ozone production (warming), and consumes methane (cooling). The reduction of methane has a delayed ozone depletion effect [25, 26], resulting in further cooling. This highlights that the RF associated with NO_x is transient, and depends on the time horizon in question. Considering opposing signs of ozone/methane contributions and uncertainty in their relative magnitude, it remains debated whether the *net* forcing effect of aviation NO_x ($\mathrm{RF}_{\mathrm{O_3}} + \mathrm{RF}_{\mathrm{CH_4}}$) is positive or negative. While Terrenoire et al. [26] have suggested that the long-term RF could be very slightly net-negative (–0.9 mW/m^2; i.e. cooling), other authors have predicted relatively strong warming effects ranging between +13.8 to +26.7 mW/m^2 [24, 25] (i.e. comparable to CO_2). The takeaway is that NO_x *could* impact climate to a similar degree as CO_2, with the caveat that current estimates have extremely high uncertainty owing to limitations in modeling microphysical processes on a global scale. In combination with the known adverse effects of NO_x on health, reducing emissions becomes a priority.

Sulfate and nitrate aerosols (forming as a result of SO_x and NO_x emissions) are thought to have a net-negative forcing (i.e. cooling) effect through scattering/reflection of incident radiation (see Prather et al. [27] and Zhang et al. [28]). Lee et al. [24] estimated sulfate aerosol RF around –4.8 mW/m^2. Nitrates were not considered, but may *in the future* overtake sulfates as the dominant effect, depending on background ammonia concentrations (see Hauglustaine et al. [29]). It has been suggested that—by intentionally increasing SO_x emissions—the sulfate cooling effect could be exploited to alleviate other forcing factors. This would unfortunately come at the expense of air quality, and is therefore not regarded a viable option [21] .

In contrast to sulfates/nitrates, which are optically reflective, black carbon particulates (nvPM) mostly absorb incident radiation [27], wherefore they are associated with a warming effect. Lee et al. [24] estimated a RF of +3.4 mW/m^2 at current emission levels.

By far the greatest uncertainty is associated with the effect of aviation on atmospheric cloud physics. Aircraft produce linear condensation trails (contrails; i.e. ice clouds), which can disperse and develop into contrail-induced cirrus. Contrary to the traditional low-level cumulus clouds, which are generally reflective and help cool the planet, linear contrails and contrail-induced cirrus are believed to have net positive RF (warming). This relates to their optical properties for short and longwave radiation (see discussion of Kärcher [30]). Moreover, there is concern that particulates—both as direct emissions and as products of atmospheric reactions—act as potential nucleation sites,

and therefore have the potential to promote natural cirrus formation. When combined with the direct effects of contrails and induced cirrus, Lee et al. [24] estimated that the RF of aviation induced cloudiness was +33.0 mW/m^2 (with a 90% confidence interval of +12 to +84 mW/m^2).

Overall, Lee et al. [24] predicted RF from aviation of +78 mW/m^2, with a 90% confidence interval of +38 to +139 mW/m^2. This corresponds to approximately 4.9% of overall anthropogenic forcing (vs. 1.9% from CO_2 alone). While much uncertainty remains about the role of NO_x and particulates in RF (particularly in their interaction with cloud formation), global air quality concerns alone should be reason enough to reduce emissions.

Climate policy and emission standards

Aircraft emissions are internationally regulated by the ICAO, which imposes limits on NO_x, CO, UHCs, and nvPM as part of engine certification [31]. A standardized landing and take-off (LTO) cycle is used to model pollutant emissions during taxi, departure, and approach, encompassing operations within 3000 feet above ground level. While there are currently no explicit limits on cruise emissions, the LTO cycle includes a wide range of engine power settings, and therefore *indirectly* addresses cruise contributions. In the understanding of adverse effects of pollutants on health and climate, the regulations have become increasingly stringent. Engine manufacturers therefore need to plan ahead to ensure that their product portfolios remain future-proof.

SO_x emissions are directly proportional to the fuel sulfur content, which is limited to a maximum of 3000 ppm. This contrasts with much stricter limits for automotive Diesel and gasoline, which currently stand at 15 ppm in the USA and 10 ppm in the European Union. A possible reason for relaxed regulation is that removing sulfur from crude oil has the undesirable side-effect of reducing fuel lubricity, thereby increasing component wear. In practice, concentrations generally vary between 500–1000 ppm [21]. Stricter limits on aviation fuel sulfur content have been considered by the European Aviation Safety Agency (EASA) [32], but these were ultimately tabled in favor of legislation that will encourage SAF usage. SAF tends to have very low sulfur and aromatic content, which helps reduce SO_x and soot formation [33, 34]. Pure SAF is not technologically feasible currently, because aromatic content is key to lubrication.

To accelerate SAF adoption, the European Commission has passed legislation that will mandate a minimum volume of SAF for all departing flights, starting at 2% in 2025 and ramping up to 70% in 2050. The USA has taken a more market-driven approach, by offering tax credits to incentivize SAF production. Similar policies governing the rapidly growing Asian market will be vital to effectively tackling the environmental impact of aviation [12].

2.5 Combustors

Aircraft pollutant emissions are driven by chemical reactions in the gas turbine combustor (see Equation 2.1). To satisfy ICAO emission standards for engine certification, they need to be controlled over a wide range of power settings. In this section, the mechanisms responsible for pollutant formation are discussed, and possible mitigation strategies are explored. Lean-burn combustors are identified as a particularly promising technology for addressing both NO_x and particulate emissions.

Conventional combustor

An example of a conventional combustor is shown in Figure 2.3 (adapted from Wulff and Hourmouziadis [35]). Its physical layout and operation are briefly considered with the purpose of exploring mechanisms responsible for pollutant formation.

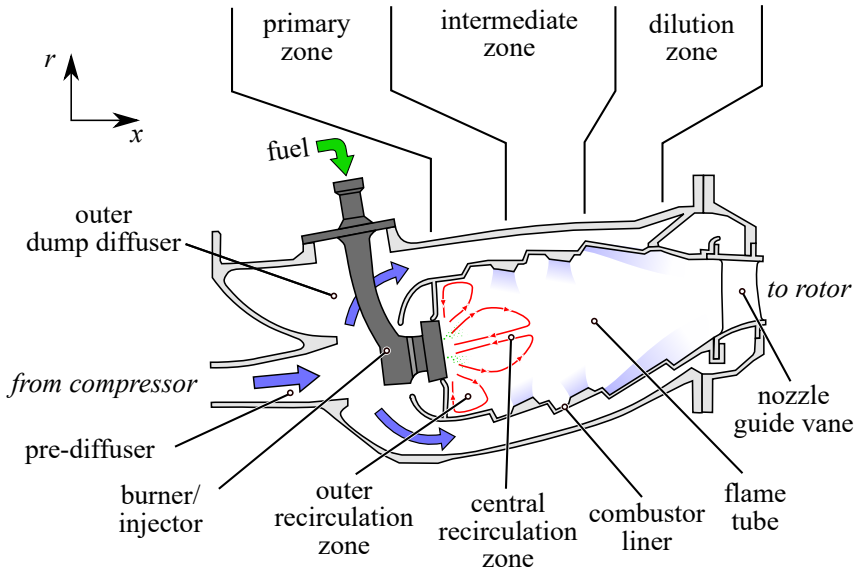


Figure 2.3: *Layout of a generic conventional combustor (adapted from Wulff and Hourmouziadis [35]).*

Similar to a lit matchstick extinguished by a gust of wind, combustors cannot sustain a flame at high flow speeds. For this reason, the compressor delivery air is decelerated through a pre-diffuser, and subsequently exhausted into a dump cavity. Approximately 30% of the incoming flow enters the flame tube through a burner/injector, which swirls the air and injects fuel. The remaining 70% of compressor delivery air is initially diverted around the flame tube, and gradually admitted through the combustor liner. Some of this air may bypass the combustor entirely, and instead re-enter the main gas path as turbine coolant. The combustor exit is marked by the nozzle guide vane (NGV).

Within the flame tube are three identifiable zones: primary, intermediate, and dilution. In the primary zone, strong swirl and subsequent vortex breakdown gives rise to a region of low-speed

recirculating flow, which anchors the flame to the injector. Fuel is introduced into the primary zone using an atomizer, which breaks up fuel into small droplets to accelerate vaporization. Vaporization occurs within the primary zone and is essential to obtaining a flammable mixture [36].

In the intermediate and dilution zones, air is injected through the combustor liner to control fuel-to-air mixture, and to shape the turbine inlet temperature profile. Gradual (as opposed to sudden) introduction is key to maintaining sufficiently high temperatures necessary for completing reactions of intermediate species, which would otherwise appear as pollutants in the exhaust stream [36]. Pollutant formation is now systematically reviewed.

Factors affecting pollutant emissions

With the exception of SO_x, which primarily depends on fuel sulfur content, pollutant emissions are driven by chemistry and aerodynamics in the combustor. The primary controlling parameter is the fuel-to-air ratio (FAR). FAR is commonly expressed as an equivalence ratio, ϕ, where a value of one corresponds to stoichiometric conditions, values above one indicate a fuel-rich mixture, and values below one indicate a fuel-lean mixture. Here we make a further distinction between overall equivalence ratio (which depends on fuel flow and defines the engine operating point), zonal equivalence ratio (which is dictated by fuel flow, air splits, and combustion progress), and local equivalence ratio (which depends on all of the above, and mixing phenomena).

Variation of pollutant emissions and flame temperature are shown in Figure 2.4 as a function of the primary zone equivalence ratio, ϕ (adapted from Wulff and Hourmouziadis [35]). Peak temperatures (right axis) occur at equivalence ratios slightly above unity (condition maximizing ratio of heat release to heat capacity), with flame temperatures decreasing in the rich and lean regime. The equivalence ratio therefore provides information regarding reactant proportions and average temperatures (controlling reaction rates).

In conventional combustors, overall ϕ varies between 0.1–0.3, as primary zone ϕ varies from approximately 0.3–1.0 [35]. Take-off power is characterized by a near-stoichiometric (slightly rich) mixture in the primary zone, with accordingly high temperatures. With the introduction of dilution air through the liner in the intermediate and dilution zones, temperatures and zonal equivalence ratios gradually decrease (see e.g. Saboohi et al. [37]). Idle power is characterized by lean primary zone equivalence (despite flow local to injector remaining fuel-rich), resulting in lower peak temperature along the axial direction, and rapid cooling in the intermediate and dilution zones [37]. The effects on carbon monoxide (CO), unburnt hydrocarbons (UHC), NO_x, and nvPM (smoke) formation are now considered.

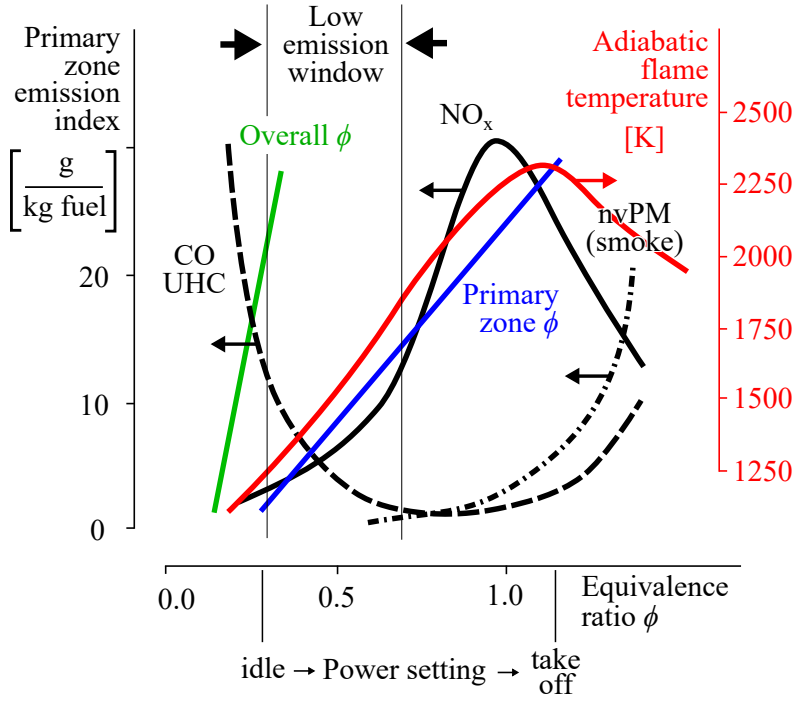


Figure 2.4: *Variation of carbon monoxide (CO), unburnt hydrocarbon (UHC), NO_x, and nvPM (smoke) emissions as a function of equivalence ratio (ϕ) for a conventional combustor (adapted from Wulff and Hourmouziadis [35]).*

CO and UHC emissions (dashed line; left axis) indicate incomplete combustion, and go hand-in-hand with low combustion efficiency. This typically occurs at very low (lean) primary zone equivalence ratios, due to low temperatures and accordingly slow reaction rates in the intermediate and dilution regions (see e.g. Diehl and Biaglow [38]), but can also happen at very high (rich) primary zone equivalence ratios, where limited oxygen supply prevents complete oxidation of CO. The latter pathway is rarely an issue, however, because rich mixtures only occur at higher power, where CO and UHC are mostly consumed in the then extremely hot intermediate zone. CO and UHC emissions can also occur due to poor fuel atomization in an otherwise well-proportioned combustor. At very high temperatures (i.e. equivalence ratios near unity), dissociation of CO_2 into CO may further contribute to emissions [3].

Non-volatile particulate matter (dash-dotted line; left axis) primarily forms in fuel-rich regions of the combustor, and therefore tends to increase at high power settings [39]. Lefebvre argued that higher pressures are likely to exacerbate soot formation, due to extended limits of flammability, which allow combustion (and soot formation) to initate closer to the fuel-rich injectors [40]. Similar to CO and UHC, nvPM can occur due to inadequate mixing of air and fuel (e.g. poor atomization) [36]. It is also recalled that nvPM increases with fuel aromatic content (see e.g. Bulzan et al. [39]). Negligible aromatic content is one of the many benefits of sustainable aviation fuels.

There are three mechanisms for the formation of NO_x : prompt, fuel-bound, and thermal [41].

Thermal NO_x formation is the dominant mechanism in gas turbines, and occurs at high temperatures when *normally* inert nitrogen dissociates and reacts with oxygen and hydroxyl radicals. The NO_x formation rate increases with both temperature and pressure (see [41]). The highest NO_x emissions (solid line; left axis) therefore tend to occur at high power settings [39], where the primary zone is operating near stoichiometric conditions, and average temperatures are greatest. This is reinforced by the correspondingly greater compressor delivery temperature. Thermal NO_x formation can be mitigated by operating fuel-rich or fuel-lean and by minimizing residence time in high temperature regions (>1900 K). Harmonizing cycle efficiency (which favors high temperature) with emission standards may therefore require a compromise in TET (see [42]).

Low emission strategy

The combination of high emissions of CO/UHC with decreasing ϕ, and high emissions of NO_x /soot with increasing ϕ leads to a "low emission window" around $0.3 < \phi < 0.7$. Ideally, the combustor would operate in this window over the full range of power settings. In practice, this is not possible however, because lean blow out margins at low power usually dictate the maximum air fraction that may pass through the fuel injector/swirler [35]. This also constrains the primary zone ϕ at high power, which is equal to overall high-power ϕ, divided by the constant primary zone air fraction.

One possible strategy for reducing low power CO and UHC emissions of conventional combustors is to switch off fuel flow to individual injectors. In this setup, the remaining fuel injectors receive proportionally greater fuel flow to achieve the same power setting. Because the injector air flow remains approximately constant, the number of active injectors can be modulated to achieve the desired primary zone ϕ. So-called "circumferential staging" is challenging, because it results in strong circumferential non-uniformity of combustor outlet conditions, which translates into degraded turbine performance (see Bahr [43]). Lefebvre also describes a "chilling" effect [40] at interfaces between operating and non-operating injectors, which may counteract the perceived benefits of operating active injectors at higher ϕ. Moreover, circumferential staging does not address high power NO_x and nvPM emissions, wherefore designers have developed more advanced staging strategies.

Overview of low emissions combustors

In this subsection, examples of low emission combustor architectures past and present are considered. These include configurations with additional fuel injectors, optimized versions of the conventional architecture, and internally-staged multi-concentric injectors.

Double Annular Combustor (DAC) and Axially Staged Combustor (ASC)

Early examples of combustors with staged combustion are Double Annular Combustors (DAC). An example of a CFM56 DAC is shown on the left side of Figure 2.5 (adapted from Foust et al. [44]). Recirculating regions are not explicitly drawn, but instead indicated using linear arrows.

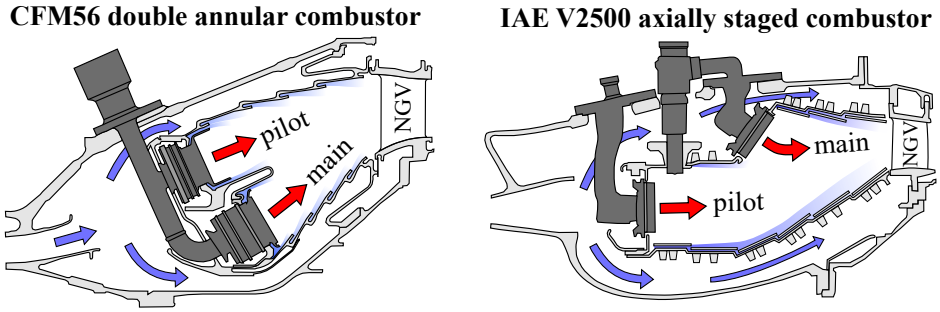


Figure 2.5: *CFM56-5B DAC (adapted from Foust et al. [44]); IAE V2500-A5 ASC concept (adapted from Lefebvre and Ballal [36]).*

The DAC is based on two radially-staged injectors: an outer pilot, and an inner main. The two injectors share approximately 46% of the incoming flow at a 1:2.5 pilot-to-main split ratio, with the remaining 54% used for dilution, and dome/centerbody/liner cooling (see Gleason and Bahr [45]). Because only about 13% the air passes through the pilot injector, its zonal equivalence ratio can be doubled compared to that of a conventional combustor with the same overall equivalence ratio [35]. At idle and low power, only the pilot zone is active, operating at $\phi = 0.8$ to ensure stability and reduce CO/UHC emissions [40]. At high power, both pilot and main are operated fuel-lean (with $\phi = 0.6$) to reduce NO_x emissions and soot formation [40]. The benefits of lean zonal equivalence are limited, however, because combustion is non-premixed (i.e. fuel-rich local to injectors) [46].

The introduction of DACs in the 1990s saw improved NO_x emissions, compared to contemporary single annular combustors. The resulting turbine inlet temperature profile was, however, deemed unfavorable for optimal work extraction, because of a strong dependence on the pilot–main injector fuel split at different staging conditions (see discussion of Liu et al. [3]). Moreover, the comparatively large wetted area made cooling challenging. Performance at intermediate power settings was poor, as both main and pilot zones were operating off-design [40].

An axially staged combustor (ASC) is shown on the right side of Figure 2.5 (adapted from Lefebvre and Ballal [36]). ASCs are conceptually similar to DACs, and were conceived around the same time, but ultimately never made it into service. Lefebvre [40] ascribed this to the greater axial length, and fuel coking risk (DAC uses the pilot fuel to cool the stagnant main fuel line at low power; this is not possible with separate injectors).

Rich-burn quick-quench lean-burn

Conventional combustors suffered from relatively high NO_x emissions at high power settings. Following the recommendations of Mosier and Pierce [47], some engine manufacturers optimized this architecture by operating the primary zone extremely fuel-rich, and adjusting liner hole placement. So-called *rich-burn quick-quench lean-burn* (RQL) combustors have been marketed under various names, namely the Technology for Advanced LOw NO_x (TALON X) developed by Pratt & Whitney for their Geared Turbo Fan, and the Rolls-Royce Phase 5 combustor, which features on Trent 1000 and XWB engines. The TALON X and Phase 5 combustors are illustrated in Figure 2.6 (adapted from McKinney et al. [48] and Haselbach and Parker [49]).

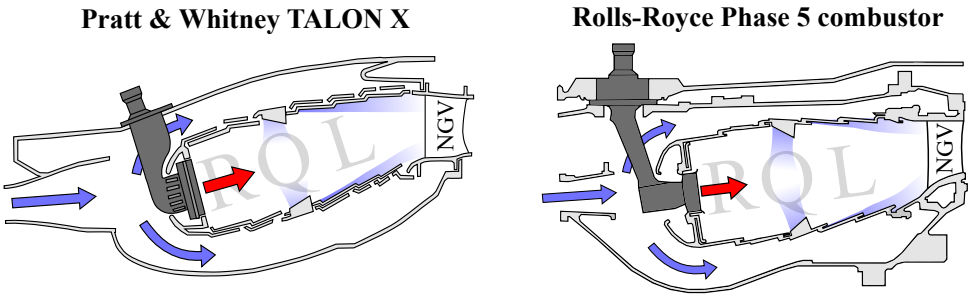


Figure 2.6: *RQL combustors: Pratt & Whitney TALON X (adapted from McKinney et al. [48]); Rolls-Royce Phase 5 combustor (adapted from Haselbach and Parker [49]).*

In RQL combustors, the primary zone is operated fuel-rich at high power ($\phi \approx 1.2$–1.6; see Wulff and Hourmouziadis [35]) with associated low thermal NO_x but high soot formation. The implication is that the air fraction admitted through the injector is lower than for conventional architectures, which operate at primary zone $\phi \approx 1.0$. To complete combustion, the zonally rich mixture is quickly quenched by cooling jets (formerly intermediate zone) to obtain a lean mixture. This transition inevitably results in *locally* stoichiometric conditions, giving rise to thermal NO_x formation. Minimizing residence time in the quench region is therefore key to reducing NO_x emissions. Additional cooling air is admitted for liner cooling, and temperature profile shaping. At idle power, the primary zone equivalence ratio is lean, but higher than for conventional combustors, which reduces CO/UHC emissions and improves combustion efficiency.

A limitation RQL inherits from conventional combustors is the inability to actively control primary zone equivalence ratio, therefore requiring compromises when considering emission characteristics across a wide range of power settings. The main drawback of RQL is extremely high nvPM formation at high power, due to a fuel-rich primary zone. Here, rapid quenching and shortened combustor length—intended to minimize peak temperatures, residence time, and NO_x formation—exacerbates the propensity for soot emission.

Lean-burn premixed combustors

A fairly recent innovation is lean-burn premixed combustor technology. A salient example is the GE Twin Annular Premixing Swirler (TAPS) combustor, which is currently flying on GENx engines, and was recently scaled-down for the CFM LEAP engine family. Comparatively little information has been publicly released about the competing Rolls-Royce Advanced Low Emission Combustion System (ALECSys), which is currently undergoing testing, and is rumored to feature on the upcoming UltraFan. The design might be expected to bear resemblance to an earlier lean-burn concept presented by Lazik et al. [50]. Both the GE TAPS and Rolls-Royce lean-burn concept are shown in Figure 2.7 (adapted from Foust et al. [44] and Lazik et al. [50]).

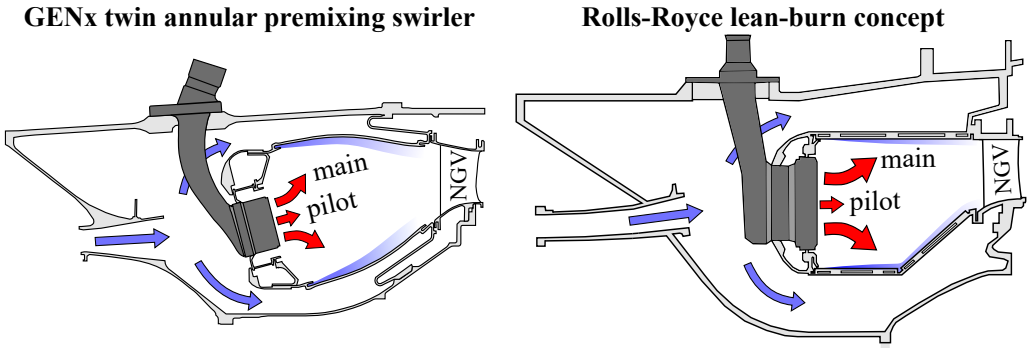


Figure 2.7: *Lean-burn combustors: General Electric GENx TAPS (adapted from Foust et al. [44]); Rolls-Royce lean-burn concept (adapted from Lazik et al. [50]).*

Lean burn combustors operate fuel-lean at high power. Approximately 70% of the incoming air passes through the injectors, which are proportionally larger diameter. Intermediate and dilution zones are completely eliminated, with the remaining 30% of air used for liner cooling. Staging is achieved within a single injector head, which features a central non-premixed pilot and a concentric outer premixed main stage [50]. At low power, only the pilot is used, resulting in emission characteristics comparable to those of an RQL combustor [50]. At high power, both the main stage and pilot are fired. In this way, NO_x /nvPM are substantially reduced by avoiding stoichiometric/rich conditions in the main stage—both zonally and locally by virtue of premixing. NO_x reduction is further aided by the shortened flame tube, which decreases residence time.

Premixing occurs within the injector head [44, 50]. Given the high operating pressure and compressor delivery temperature, auto-ignition in the injector is a major concern, which limits premixer length and mixing effectiveness [46]. Noting this limitation, the current generation of lean-burn is sometimes referred to as "partially-premixed". Combustion instabilities due to thermo-acoustic self-excitation also pose a design challenge, especially at high power settings [51].

Comparison of combustor architectures

NO_x, CO, and nvPM emissions of eight modern turbofan engines are shown as a fraction of current regulatory limits in Figure 2.8. The data were taken from the ICAO aircraft engine emissions databank [52]. The engines were specifically selected to have similar operating pressure ratios (OPR) with the purpose of isolating strengths and limitations of DAC, RQL, and TAPS technology.

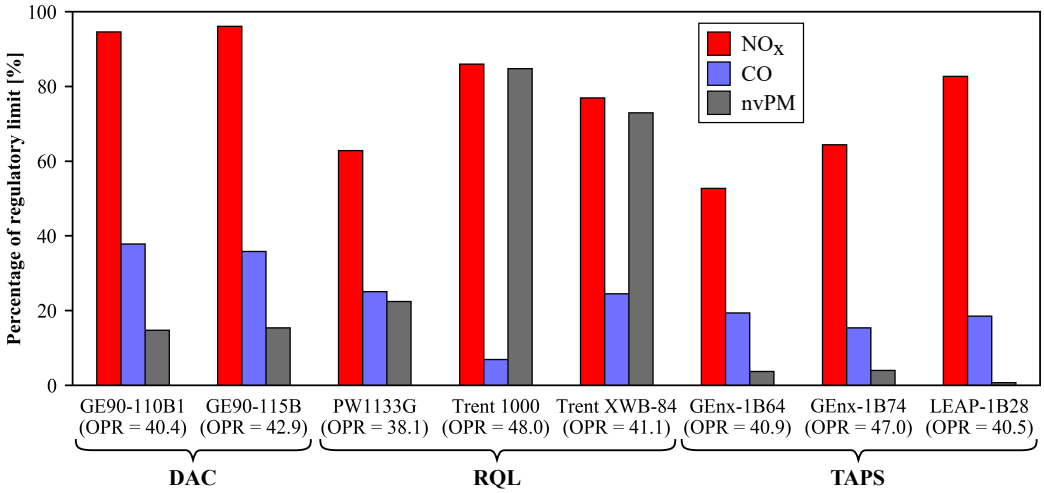


Figure 2.8: *Comparison of characteristic LTO emissions of DAC, RQL, and TAPS combustors as a percentage of current regulatory limits (CAEP/8 NO_x; CAEP/1 CO; CAEP/11 nvPM).*

If the GE90 engine were introduced today, its DAC combustor would have only about 5% margin to the current CAEP/8 NO_x standard. Significantly lower NO_x emissions were recently achieved with RQL technology, which boasts an average margin of 25%. TAPS has a slight edge, with an average margin of 33%. This gap widens to 42%, when only the wide-body GENx engines are considered.

CO emissions have also gradually improved. Even so, new stringency for CO is unlikely to be introduced in the near-future, wherefore this metric is not currently critical.

While nvPM emissions of DAC are surprisingly low (average margin of 85% to CAEP/11 new-engine standard), they are unusually high for RQL (with an average margin of only 40%). Extreme particulate emissions may be an isolated problem of the Phase 5 RQL combustor on Trent 1000 and XWB-84 engines (average margin of 21%), considering that the PW1133G has a more conservative 78% nvPM margin. As expected, lean-burn (TAPS) reduces nvPM emissions by an order of magnitude, with an average margin of 97% to new-engine standards.

All in all, lean-burn combustors appear extremely promising for mitigating the environmental impact of aviation. This is especially apparent when comparing architectures based on NO_x and nvPM emission characteristics at cruise power, which should arguably be given the greatest weight when assessing the impact of aviation on climate forcing and air pollution [2, 19].

2.6 Conditions at lean-burn combustor outlet

An important consideration of implementing lean-burn combustors in aero-engines is their interaction with other sub-systems. The high-pressure turbine is located immediately downstream of the combustor, and therefore most susceptible to radical changes in combustor design. The anticipated conditions at lean-burn combustor outlet (i.e. turbine inlet) are now discussed. This sets the stage for a review of the literature on lean-burn combustor–turbine interactions.

Residual swirl

It is recalled that gas turbine combustors almost universally use swirl to stabilize the flame in a region of recirculating flow [36]. A common metric used to quantify swirl intensity is the swirl number, S, which can be defined (following Gupta et al. [53]) as:

$$S = \frac{\int \rho V_x V_\theta r^2 dr}{\bar{r} \int \rho V_x^2 r dr} \tag{2.2}$$

where V_x, V_θ, and r are (respectively) the axial velocity, circumferential velocity, and radius in a cylindrical coordinate frame concentric with the swirler. The overbar represents area-averaging, and ρ is the density. The swirl number is typically calculated separately for the pilot and main stage, with limits of integration adjusted accordingly. The swirl number quantifies the ratio between the axial flux of angular momentum and the axial flux of axial momentum, which is considered a good predictor of whether a region of flow recirculation will develop (this generally requires $S > 0.6$; see Lucca-Neggro and O'Doherty [54]).

Following the conservation of angular momentum, swirl imparted by the injectors largely persists up to turbine inlet. Considering that relatively high swirl numbers are generally required to stabilize of the flame ($S > 0.6$), and that approximately 70% of core flow passes through the injector in lean-burn combustors, mass-averaged swirl is considerably greater than for conventional/RQL architectures [51]. At turbine inlet, this manifests as significant spatial non-uniformity of the swirl angle (α) and pitch angle (β), which can be defined as follows:

$$\alpha = \arctan \frac{V_\theta}{V_x} \tag{2.3}$$

$$\beta = \arctan \frac{V_r}{V_x} \tag{2.4}$$

where V_x, V_r, and V_θ are (respectively) the axial, radial, and circumferential components of the velocity in a cylindrical coordinate frame coincident with the machine axis—not the swirler.

Measurements of flow angles in reacting lean-burn combustors are scarce due to the difficulty of instrumenting such experiments. A welcome exception to this trend is the study of Schroll

et al. [55], which characterized the outlet flow of a single-sector lean-burn combustor simulator using particle image velocimetry and filtered Rayleigh scattering. Although flow angles were not explicitly discussed, the study provides a unique insight into the flow structure at turbine inlet, which resembles a large, and fairly mixed-out vortex at both low- and intermediate-power conditions.

Further insight can be gained from the work of Shahpar and Caloni [56], who optimized the geometry of a high-pressure turbine for a lean-burn combustor. Their turbine inlet conditions were based on a high-fidelity simulation of a reacting lean-burn combustor prototype, which predicted local swirl angles between ±25 degrees and pitch angles ranging from −20 to +40 degrees. Here, not too much emphasis should be placed on the large variation of pitch angles, as these are usually exaggerated by superposed bulk effects of the contracting duct. Interestingly, the preceding studies of Qureshi et al. [57, 58], which also appear to have been informed by real combustor simulations, aimed for much more aggressive inlet conditions, with swirl angles of approximately ±40 degrees. There are further instances where high intensity and relatively concentrated swirl cores were viewed as lean-burn representative, namely the target profiles of the Full Aerothermal Combustor–Turbine interactiOn Research project (FACTOR), which had peak swirl angles in excess of ±40 degrees (see Koupper et al. [59] and Chevrier and Bertrand [60]). Somewhat less aggressive targets were set by Beard et al. [61] as part of the Low Emission Core Engine Technology project (LEMCOTEC), which saw swirl angles between −25 and +33 degrees (see also Adams et al. [62]). The apparent variability might be explained by the fact that flow angles respond to a number of combustor design parameters, for example the pilot and main stage swirl intensities and the combustor liner contraction ratio. Interpretation of what constitutes lean-burn representative outlet conditions has therefore evolved with the advancement of this combustion technology, and may vary altogether from engine-to-engine.

An interesting complexity to consider is the sensitivity of swirl/pitch angles to the engine power setting. Following the ideal gas law, heat release during the (approximately) constant-pressure combustion process causes density to decrease. To satisfy one-dimensional continuity, the axial velocity must increase proportionally. The average swirl velocity, on the other hand, is governed by the conservation of angular momentum, and therefore relatively insensitive to heat release. This implies that swirl angles are greatest in the limit of isothermal operation (i.e. combustor flow without heat release; see Adoua and Page [63]). This effect must be carefully taken into consideration when investigating lean-burn in non-reacting environments.

Temperature distribution

On account of the altered injector-to-liner air splits, the turbine inlet temperature profile might also be expected to change with lean-burn. Temperature profiles at turbine inlet are often presented non-dimensionally in terms of an overall temperature distribution factor (OTDF) and a radial temperature distribution factor (RTDF), which are defined (following e.g. Cha et al. [64]) as:

$$\mathrm{OTDF} = \frac{T_{\theta,\max}(r) - T_{\mathrm{avg}}}{T_{\mathrm{avg}} - T_{\mathrm{c}}} \qquad (2.5) \qquad\qquad \mathrm{RTDF} = \frac{T_{\theta,\mathrm{avg}}(r) - T_{\mathrm{avg}}}{T_{\mathrm{avg}} - T_{\mathrm{c}}} \qquad (2.6)$$

where $T_{\theta,\max}(r)$ is the maximum temperature at a fixed radial location, $T_{\theta,\mathrm{avg}}(r)$ is the circumferentially-averaged (i.e. radial) temperature profile, T_{avg} is the mass-averaged temperature, and T_{c} is a cold reference temperature (typically the compressor delivery temperature).

In the lean-burn combustor simulations of Lazik et al. [50], high-power (pilot and main) operation resulted in an RTDF profile that peaked around the midspan, became colder towards the endwalls, and was approximately parabolic in shape. This was confirmed by experimental measurements in a reacting and fully-annular test facility. Low-power (pilot-only) operation was characterized by a relatively concentrated midspan hotspot—especially for injector designs with low pilot swirl (see also low-power measurements of Doll et al. [65]). Perhaps the most detailed survey of combustor exit conditions in the open literature was performed by Jianchen et al. [66]. Using a tri-sector reacting combustor, they found approximately parabolic RTDF profiles at both low- and high-power conditions. Increasing the pilot-to-main fuel ratio for a fixed overall FAR had the effect of increasing maximum OTDF and RTDF.

Somewhat more bucket-shaped RTDF profiles were reported by Insinna et al. [67], Mazzei et al. [68], and Adoua and Page [63]. Here, "bucket-shaped" implies approximately constant temperature in the freestream with radially mixed-out coolant layers near the endwalls. This might be expected on the assumption that pilot and main stage combustion products are well-mixed, and on the basis that the limited air available for liner cooling is likely injected tangentially to minimize mixing and film decay (see Figure 2.7). In contrast, quenching and dilution flows in conventional/RQL combustors tend to be injected radially to increase spanwise penetration distance and to promote mixing (see Figure 2.3). This typically results in quasi-parabolic RTDF (see Barringer et al. [69]), which was also seen in some lean-burn studies considered above [50, 66].

In practice, there is of course significant sensitivity to the geometry of the swirler (controlling the flame expansion angle and inter-zone mixing; see Huang and Yang [70], and Shi et al. [71]), the method of cooling (effusion, film, double-walled etc.), the flame tube shape (e.g. length-to-dome

ratio and contraction ratio), and the engine power setting (affecting the location of heat release depending on staging conditions; see Lazik et al. [50], Greifenstein et al. [72], and Jianchen et al. [66]). The point is that turbine inlet temperature distributions representative of lean-burn combustors are highly design-dependent and therefore not uniquely definable.

Unsteadiness and turbulence

Turbulence at lean-burn combustor outlet remains relatively poorly understood due to limited engine-representative data. The first such measurements were recently presented by Schroll et al. [55], who reported turbulence intensities between 8–16% at low-power (pilot-only) and between 8–20% at intermediate-power (pilot and main). By comparison, values between 10–30% are considered typical of conventional/RQL combustors (see Zimmermann [73] and Bicen et al. [74]). Of note, turbulence intensity at the outlet of RQL combustors has been shown to exhibit only limited sensitivity to combustion [74]. This observation led some investigators to argue that RQL combustor turbulence can be characterized using cold-flow tests (see e.g. Cha et al. [75] and Folk [76]). Adoua and Page [63] demonstrated that this does not hold true for lean-burn combustors, because heat release increases meridional velocities under reacting conditions *without* amplifying turbulence energy proportionally. Together, this has the effect of reducing turbulence intensity. This behavior was corroborated by the experiments of Hassa et al. [77], which showed that peak and mean turbulence intensities were approximately halved under reacting conditions.

A possible explanation is that turbulence kinetic energy in lean-burn combustors arises primarily from premixing *before* combustion, with intensity modulated by the effect of heat release on meridional velocities. This theory can be reconciled with opposing behavior in RQL combustors, considering that RQL turbulence is dominated by the dilution jets, which are introduced *after* most heating has already occurred (see discussion of Folk [76]).

Turbulence length scales at turbine inlet were studied by Hassa et al. [77] under isothermal and reacting conditions. Under isothermal conditions, circumferential variation of length scales peaked downstream of the swirler center. Along the spanwise direction, length scales were maximum near the midspan and decreased gradually approaching the walls. A slight decrease in this peak under reacting conditions was ascribed to damping of the precessing vortex core—a slowly-rotating helical vortex structure commonly encountered in high-swirl flows [78]. The precessing vortex core (PVC) is damped or even entirely suppressed by heat release [79, 80], and therefore tends to be more prominent in isothermal swirling flows. Indeed, unsteadiness associated with the PVC might be a contributing factor to the extremely high turbulence intensities measured in cold-flow tests.

2.7 Combustor simulators

Because it is impractical and costly to perform measurements at the extremely high pressure and temperature conditions present in modern engines, much of the experimental work on lean-burn combustor–turbine interactions has been based on so-called non-reacting *combustor simulators*. Combustor simulators reproduce *non-dimensional* conditions representative of real engines, and can be classified based on the type of conditions they simulate (swirl; RTDF/OTDF; turbulence).

Investigation of interactions between high-pressure turbines and RQL combustors, for example, mainly focused on the effects of radial temperature distortion and hot spots (see review of Povey and Qureshi [81]). A separate class of RQL combustor simulators has also been used to investigate the effect of turbulence on NGV loss (see e.g. Ames and Plesniak [82], and Folk et al. [83]).

As discussed earlier, lean-burn combustors differ from their RQL counterparts in that they produce significant residual swirl at turbine inlet. Early experimental work on lean-burn combustor–turbine interactions therefore focused on the effect of swirl. As part of this effort, swirl simulators were developed by Qureshi and Povey [57], Giller and Schiffer [84], Krichbaum et al. [85], Luque et al. [86], and Hong et al. [87]. A common feature of these studies was the use of swirlers in a contracting duct to tailor swirl angles at turbine inlet. Here, an interesting consideration is that—in the absence of heat release and the associated meridional acceleration—combustor simulators need to be designed with lower swirl numbers than those typically encountered in real engines so as to produce the same flow angles at their outlet.

A second generation of lean-burn combustor simulators incorporated both swirl and temperature profiling. A notable example is the tri-sector facility at the University of Florence [59, 88, 89], which was later integrated into the fully-annular Next Generation Turbine Research Facility (NG-Turb; [90]), and now complements an earlier rich-burn combustor simulator (see Wolf et al. [91]). In the tri-sector and NG-Turb facilities, air is preheated upstream of the swirlers to over 400 K; temperature profiling is then achieved by injecting cold air downstream of the swirlers. A similar design was used for the Oxford Lean-burn Combustor Simulator (OLCS; Hall and Povey [92]), with the difference that coolant was ejected from slots rather than through perforated liners. Adams et al. [62] later scaled the OLCS design for integration in the Oxford Turbine Research Facility.

General considerations of combustor simulator design are explored in the next Chapter, which details the integration of a combined swirl and temperature profile simulator in an annular NGV test facility. For completeness, we note that an entropy wave simulator was recently developed by Notaristefano and Gaetani [93] to study the effect of unsteady heat release on NGV performance.

2.8 Lean-burn combustor–turbine interactions

A single-stage high-pressure turbine (HPT) is illustrated in Figure 2.9 (adapted from Soares [94]). At a high level, the HPT consists of stationary nozzle guide vanes (NGV), and rotating turbine blades. Simplistically, the role of the NGV is to accelerate the flow onto the rotor, which in turn extracts work from the flow to drive the high-pressure compressor. Both NGV and rotor require heavy cooling to withstand the extreme temperatures exiting the combustor (see arrows). NGV typically also form the narrowest cross-sectional area of the engine, and therefore constrain the non-dimensional mass flow (i.e. capacity) of the engine. The capacity characteristic is particularly important for controlling turbine pressure ratios, which—together with turbine efficiency—can be used to calculate the compressor and engine operating line. The relevance of turbine efficiency also cannot be overstated, especially considering its impact on maximum achievable cycle efficiency, and the associated optimum compressor PR (see Wilcock et al. [17]). Understanding the impact of lean-burn on cooling performance, efficiency, and capacity is therefore of great engineering interest.

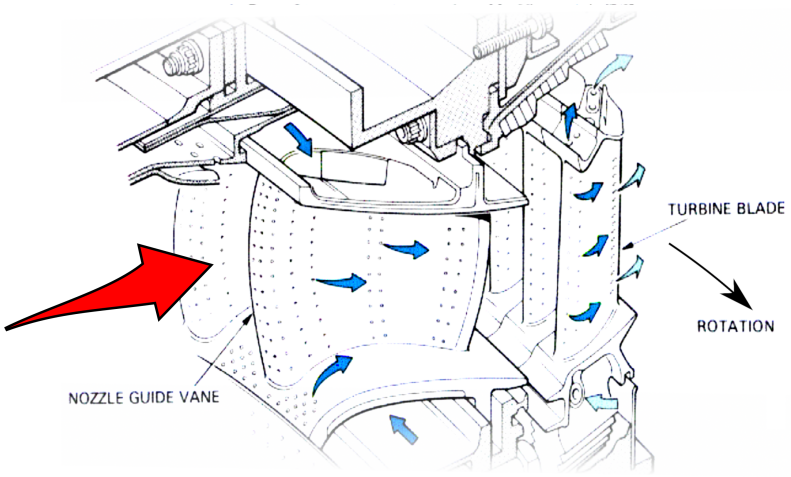


Figure 2.9: *High-pressure turbine layout and cooling flows (adapted from Soares [94])*

Definition of clocking and swirl direction

In engines where the number of NGV is an integer multiple of the number of fuel injectors, the question of optimum clocking (i.e. relative circumferential alignment) arises. Here, designers have freedom to align the swirler (or vortex) center either with the vane leading edge (LE), the passage, or anything in between. In principle, one might also independently consider the clocking of hot streaks in the temperature profile, though in practice it is usually assumed that their migration follows the vortex core. An interesting complexity is that *geometric* alignment of the swirler does not directly translate into *aerodynamic* alignment of the vortex. In particular, Insinna et al. [67] observed that the vortex core migrates circumferentially between the swirler and vane inlet. They

attributed this to a gyroscopic effect induced by asymmetric hub endwall contraction (i.e. mean radius increase). Noting however that the effect also occurred for a constant mean radius and symmetrically-contracting duct, Vagnoli and Verstraete [95] proposed an alternative mechanism. We develop further arguments for the migration phenomenon in Chapter 3.

Another important variable often considered in relation to combustor–turbine interactions is the vortex sense of rotation with respect to the NGV direction of turning. So as to discuss studies with opposing NGV turning in a unified manner, we refer to swirl as "co-rotating" in configurations where the angular momentum vectors (right hand rule) of combustor swirl and NGV outlet flow (and rotor rotation) point in the same direction, and as "counter-rotating" where they point in opposite directions. For NGV with an LE-clocked vortex, co-rotation tends to increase NGV incidence/loading at the hub, and to decrease incidence/loading at the casing, whereas the opposite is true of counter-rotation.

Effect of inlet swirl on NGV and turbine performance

The initial work on lean-burn combustor–turbine interactions focused on the effect of inlet swirl *in isolation*. Key findings from these studies are now briefly reviewed.

Qureshi et al. [58] investigated NGV aerodynamics and heat transfer for LE-clocked co-rotating swirl and compared this to uniform inflow. Swirl caused loading to increase at 10% span, whereas a decrease was measured at 90% span. The accompanying simulations revealed significant distortion of the surface streamlines on both airfoils, with strong radially-outward migration on the pressure side (PS), and amplified radially-inward motion on the suction side (SS). Consistent with the change in loading, secondary flows were amplified at the hub, and suppressed at the casing as reflected by downstream profiles of loss. As much as 17% enhancement of the circumferentially-averaged hub endwall Nusselt number was predicted by simulations, whereas the casing endwall Nusselt number decreased slightly on-average.

Soon thereafter, Beard et al. [96] performed experimental measurements and simulations for a full HPT stage, also with co-rotating LE-clocked swirl. Compared to axial inflow, swirl caused HPT stage efficiency to decrease by 1.06% in experiments, which was in excellent agreement with the corresponding numerical predictions (0.90% decrease). Another significant outcome was that NGV capacity decreased by approximately 2.0%, which the authors ascribed to increased NGV pre-throat loss and secondary-flow blockage, both from off-design operation. An additional consequence was that because NGV capacity fell by more than that of the rotor, inter-stage static pressure decreased, causing the corresponding Mach number to increase (see also Johansson et al. [97]) .

Around the same time, Schmid et al. [98] performed full-stage non-linear harmonic simulations, comparing LE clocking with passage clocking for both directions of swirl. This indicated between a 1.0 to 2.6% efficiency decrease relative to axial inflow, with the lowest loss occurring with co-rotation and LE-clocking (1.0%). Co-rotation was deemed advantageous because it maintained high turning and work extraction at the rotor casing. Consistent with the earlier experimental results of Qureshi et al. [58], the area-averaged NGV hub endwall heat transfer coefficient (HTC) increased by approximately 25% relative to axial inflow, with slightly lower values for counter-rotation but no obvious sensitivity to clocking.

The parallel experimental work of Werschnik et al. [99] in the Large Scale Turbine Rig (LSTR; see Krichbaum et al. [85]) considered aerodynamic losses, flow angles, and coolant migration through the NGV with counter-rotating swirl, and for both passage- and LE-clocked configurations. Mass-averaged NGV loss increased from 5.4% under axial inflow to 6.5% and 7.3% for passage and LE clocking, respectively. Downstream flow angles changed by up to 4 degrees, approximately following the direction of upstream swirl. A unique aspect of this study was that the temperature field downstream of the NGV was decomposed into individual contributions from the rotor cavity purge flow, NGV hub endwall coolant, and the NGV trailing edge (TE) slot. Overall, radial distributions of these three coolant streams were not significantly affected by swirl or clocking, but the elevated combustor simulator turbulence enhanced mixing in the circumferential direction (also seen in the aerodynamic wakes).

Werschnik et al. [100] also studied the effect of swirl on hub endwall heat transfer with varying cooling mass flow. Generally speaking, swirl had the effect of increasing the Nusselt number (by up to 30%), and decreasing adiabatic effectiveness (by 15–35%). Both individually and together, these effects are detrimental to cooling performance (see Sen et al. [101]). Increasing the coolant flow rate improved adiabatic effectiveness, reducing also its sensitivity to swirl clocking, but with the penalty of increasing the Nusselt number. Even so, adiabatic cooling effectiveness remained approximately 15% lower than for uniform inflow, even at the highest cooling mass flow condition.

As an extension to this work, Wilhelm et al. [102] used split-fiber probes to study turbulence migration through the NGV. They found that the LSTR combustor simulator produced approximately isotropic structures upstream of the NGV, with average and peak turbulence intensities of 25% and 45% (respectively) and length scales of approximately 34 mm—similar to geometric features of the swirler. Downstream of the NGV, average/maximum intensity decreased to 3.5/7.0% owing to flow acceleration, with length scales shrinking to 23 mm.

Effect of inlet swirl combined with temperature non-uniformity (hot streak)

As the understanding of NGV–swirl interactions evolved, it became increasingly clear that the altered flow field could also affect the migration of inlet temperature non-uniformities (sometimes called hot streak). Here, we invoke the Munk and Prim [103] principle, which states that the Mach number distribution and streamline pattern should remain unaffected when altering the inlet temperature profile, provided that the inlet total pressure distribution is kept the same (see also discussion of Adams et al. [104]). This suggests that—for the NGV at least—hot streak can loosely be treated as a passive scalar, which simply migrates along the streamline pattern set up by the NGV–swirl interaction. This is convenient because it suggests that NGV aerodynamics can continue to be studied without including inlet temperature profiling.

Importantly, however, this does not hold true for the rotor, because relative incidence angles for a fixed rotor speed depend on both the flow angle, Mach number, and total temperature (affecting absolute velocity triangles through the speed of sound; see [104]). In addition to this aerodynamic effect, radial temperature profiles are highly relevant in the context of rotor heat transfer, where it constitutes the time-averaged boundary condition. Circumferential non-uniformities of total temperature, on the other hand, could give rise to an unsteady temperature segregation effect, whereby cold fluid preferentially migrates onto the rotor SS (see Kerrebrock and Mikolajczak [105]). In an effort to characterize the likely effect of lean-burn on rotor inlet conditions, a second wave of experiments and simulations was carried out.

The simulations of Khanal et al. [106] revealed that an LE-clocked swirl core with hot streak bifurcates into two legs, which subsequently migrate into opposing radial directions. Flowing along the streamline pattern for co-rotating swirl, the SS leg migrates radially-inward, and the PS leg migrates radially-outward, whereas the opposite occurs for counter-rotating swirl. For passage clocking, the hot streak stretches radially so as to concentrate hot fluid towards the hub/casing for co/counter-rotating swirl.

Early experiments studying combined swirl and hot streak migration took place at the tri-sector NGV test facility at the University of Florence. Bacci et al. [107] investigated geometrically co-rotating LE-clocked swirl, but found that circumferential vortex migration in the combustor simulator caused the vane aerodynamics to be more characteristic of passage clocking. Accordingly, the hot streak preferentially migrated into the vane passages towards which the vortex was biased, where it resulted in peak temperatures towards the hub. Combustor liner coolant—originally near the casing—was drawn towards the midspan, whereas temperature in the

non-vortex passage was relatively uniform. The measurements would later be repeated in the NG-Turb facility [108] (implementing the same combustor simulator geometry) for both passage and LE-clocked configurations. In these experiments, a significant hot streak persisted downstream of the NGV for passage clocking, whereas LE-clocking saw the structure bifurcate (consistent with Khanal et al. [106]), resulting in more evenly distributed hot fluid between adjacent passages. The accompanying simulations of Gövert et al. [109] also reflect this in their adiabatic wall temperatures, which were more uniform from vane-to-vane with LE-clocking, but on-average higher (see also Flaszynski et al. [110]). It remains unclear why the behavior initially reported by Bacci [107] could not be replicated in the NG-Turb tests.

In the more recent study of Adams et al. [104], a somewhat weaker vortex and significantly less circumferentially-distorted inlet temperature profile was considered. In contrast to the results of Krumme et al. [108], the thermal field downstream of the NGV was therefore less significantly affected. More generally, studies should therefore be further classified in terms of their hot streak *shape*. Mansouri and Jefferson-Loveday [111] shared this view, identifying rounded, radial, and distorted hot streak types. Even so, this framework does not fully consolidate the other two studies, possibly pointing also to a dependence on the swirl intensity.

Although heat transfer can readily be studied by proxy of the HTC/Nusselt number and adiabatic effectiveness, the ultimate purpose is of course to predict metal temperatures. In this respect, Griffini et al. [112] performed conjugate heat transfer (coupled fluid and solid) simulations of film-cooled NGV with counter-rotating inlet swirl and temperature profiling for LE and passage clocking. The investigators found that passage clocking resulted in lower peak and average NGV temperatures by effectively *avoiding* the hot streak, noting however that this strategy might compromise rotor temperatures (see rotor heat-transfer analysis of Khanal et al. [106]). Another important outcome was that swirl-induced changes in the external pressure distribution caused significant internal redistribution of coolant between holes (previously also observed in the experiments of Giller et al. [84], and Bacci et al. [113]).

Geometry and clocking optimization

Having developed a basic understanding of the effects of lean-burn, mitigation is the logical next step. This effort was spearheaded by Shapar and Caloni [56], who optimized a modern HPT for LE-clocked counter-rotating swirl with a passage-aligned hotspot. They demonstrated that the penalty in stage efficiency from swirl could largely be recouped—possibly even improved—by radically modifying the airfoils. Cooling performance does not appear to have been considered as part of the optimization, wherefore it remains unclear whether the design would meet thermal requirements. Another significant challenge going forward was that some features of the optimum geometry were deemed difficult to manufacture due to high curvature.

For completeness, we also reference the study of Rahim et al. [114], which investigated an LE-clocked vortex with hot streak, and varying NGV lean, as well as the study of Jeon et al. [115], which did not include hot streak, but considered the impact of changing lean and sweep of the NGV/rotor on turbine capacity and efficiency. For brevity, the results are not rehearsed here.

Perhaps also with the intention of identifying optima in the design space, a few numerical studies examined HPT aerodynamic and thermal performance for different clocking and swirl configurations including hot streak. Khanal et al. [106] found that the lowest combined NGV+rotor heat load and highest efficiency were achieved for passage-clocked co-rotating swirl. Li et al. [116], on the other hand, reported that LE-clocking with counter-rotating swirl was the best compromise between turbine efficiency and thermal load. Pyliouras et al. [117] investigated yet another two turbine designs, one of which indicated that LE-clocking had a clear edge in terms of efficiency, slightly favoring the counter-rotating case, whereas no obvious sensitivity was found for the second turbine (less than 0.1% overall variation). The apparent lack of a clear trend precludes making general recommendations on optimum clocking and swirl direction.

Similar inconsistencies emerge when comparing the conjugate heat transfer and clocking optimization study of Griffini et al. [112] with that of Wang et al. [118], which recommended counter-rotating swirl with passage and LE clocking, respectively. Together, these studies exemplify the sensitivity of optimum clocking to both turbine geometry and the nature of the inlet profile (swirl intensity, hot streak shape, turbulence etc.). This re-iterates the importance of validating simulation tools with high quality experimental data so as to build confidence in future numerical predictions.

Nomenclature

Roman

c_p	Specific heat at constant pressure	[J kg^{-1} K^{-1}]
$\dot{m}$	Mass flow rate	[kg s^{-1}]
p	Pressure	[Pa]
PR	Compressor pressure ratio	[–]
r	Radius	[m]
S	Swirl number	[–]
T	Temperature	[K]
TR	Inlet-to-combustor-exit temperature ratio	[–]
V	Velocity	[m s^{-1}]
V_x	Axial velocity	[m s^{-1}]
V_r	Radial velocity	[m s^{-1}]
V_θ	Circumferential velocity	[m s^{-1}]
$\dot{W}_{\mathrm{net}}$	Useful power output	[W]

Greek

α	Swirl angle	[°]
β	Pitch angle	[°]
η_{c}	Compressor polytropic efficiency	[–]
η_{t}	Turbine polytropic efficiency	[–]
η_{th}	Thermal efficiency	[–]
ρ	Density	[kg m^{-3}]
ϕ	Equivalence ratio	[–]

Subscripts

0	Stagnation property
1	Condition at compressor inlet
2	Condition at compressor outlet
3	Condition at combustor outlet
avg	Area average
c	Cold reference (temperature)
θ, avg	Circumferential average
$\theta, \max$	Circumferential maximum at fixed radius

3 | Lean-burn combustor simulator for an engine component test facility

The computational and experimental assessment of a lean-burn low-NO_x combustor simulator for an engine component test facility is presented. The Engine Component Aero-Thermal (ECAT) facility is a full-scale engine-parts facility, designed for the study of the aero-thermal performance of fully cooled high-pressure nozzle guide vanes (NGVs). The facility operates with non-dimensionally matched engine conditions in terms of Reynolds number, Mach number and coolant-to-mainstream pressure ratio. The combustor simulator is designed to replicate lean-burn conditions of swirl and temperature distortion upstream of the nozzle guide vanes. The purpose is to allow the study of flow capacity, aerodynamic performance (with film cooling) and thermal performance (overall effectiveness) in the presence of engine-realistic inlet distortions.

The ECAT combustor simulator design builds on the work of Hall and Povey, who developed a full-scale low-speed atmospheric-pressure combustor simulator for the preliminary design of similar simulators later implemented in the Oxford Turbine Research Facility and ECAT. This pilot facility produced non-dimensional lean-burn combustor-exit conditions closely matched to target profiles representative of modern aero engines. This design was modified and scaled for compatibility with the annulus-line and higher pressure operating conditions of the ECAT facility.

In the present study, detailed experimental measurements with multi-hole probes and thermocouples (pressure profile and temperature field) are presented and compared to results from Reynolds-Averaged Navier–Stokes Simulations. Additional simulations were performed to understand how the elevated back pressure and vane potential field affect the non-dimensional profiles of pressure loss, residual swirl and temperature at the combustor-turbine interface. This is perhaps the most comprehensive study to date of a combustor simulator in an engine-scale research facility, providing unique insight into the known challenges of simulator design, scaling issues when moving from low to high Reynolds number and limitations of CFD in this flow environment. The results, which will serve as boundary conditions to understand the impact of this flow on components in future studies in this facility, demonstrate the fidelity with which lean-burn target conditions can be replicated in a non-reacting environment.

Context with other chapters

This Chapter describes the design, implementation, and subsequent characterization of a lean-burn combustor simulator in the ECAT facility. The current experimental data offers detailed insights into the mean flow upstream of the vanes, but does not include a quantification of combustor turbulence energy and scale. This motivated a second series of experiments using split-fiber (i.e. hot wire), Kiel, and thermocouple probes, inserted *radially* from a purpose-built traverse system. In contrast to the current study, which introduced probes *axially* from downstream, this permits surveying inlet conditions *with vanes installed*. The design of the new traverse system is summarized in Chapter 4, which also includes sample data from the lean-burn combustor simulator. This data is revisited in Chapter 8, when examining the effect of lean-burn on NGV aerothermal performance using the combustor simulator described in the current chapter.

Publication status and co-author contributions

The chapter takes the form of a *peer-reviewed journal paper*, which has been published in the ASME Journal of Turbomachinery [4]. The DPhil candidate was responsible for the setup and completion of simulations, data analysis, and paper writing. The candidate was not involved in the design of the combustor simulator or in the collection of experimental data, having taken over the project from two departing post-doctoral researchers: Roderick Lubbock, who is credited with performing the experimental work, and Francesco Ornano, who performed exploratory simulations of the combustor simulator. Thomas Povey supervised all aspects of the work. A statement of authorship is included at the end of the document.

3.1 Introduction

Lean-burn combustion has been shown to reduce emissions of carbon monoxide, nitrogen oxides (NO_x) and particulates by avoiding stoichiometric conditions, thus lowering peak temperatures. It is therefore regarded as advantageous over traditional rich-burn architectures.

In most modern turbofan combustors, flame-stabilization is achieved by swirling the flow, resulting in a region of recirculating flow (reversed axial flow). In lean-burn combustors, a far greater mass fraction of the engine core-flow is involved in this swirling motion, when compared to traditional combustor architectures, resulting in significant residual swirl, greater turbulence

intensity, and a bucket-shaped temperature profile (constant across most of the span; cold near walls) at the inlet to the high-pressure (HP) turbine.

Given these altered boundary conditions, the robustness of the aerodynamic and thermal design of the high-pressure nozzle guide vane to inlet swirl, thermal profiling and unsteadiness must be carefully considered. In particular, the likely impact on the vane loading distribution, the secondary flow structure, and the vane cooling systems, both due to the internal flow redistribution on account of the altered loading, and the external flow pattern as films develop on the surface, need to be quantified. The migration of temperature non-uniformities through the vane passage may also impact the thermal loading of downstream components because of the well-known temperature segregation effect in the rotor [119].

HP stage efficiency penalties due to combined swirl and temperature distortion [106] (sometimes referred to as hot spots or hot streaks), have already been demonstrated computationally. Experimental studies have primarily focused on half-stage (NGV only), non-reacting, low Reynolds number cases with simplified geometries, because more sophisticated experiments, particularly those involving real combustors, are extremely difficult to instrument, often resulting in sparse data (see e.g. [120]). On the other hand, transient simulations of combustor-turbine interactions, whilst not restricted in terms of the operating point, are notoriously resource intensive when modelling reaction kinetics at engine Reynolds numbers.

Non-reacting combustor simulators (CS) bridge the gap between high-temperature experiments and costly simulations, allowing for the collection of comprehensive high-quality data relevant to modern lean-burn engine design (see e.g. [81]). In this paper, the design and experimental characterization of such a lean-burn combustor simulator for the Engine Component Aero-Thermal (ECAT) facility [121] is presented. The simulator is being used to study the combined impact of inlet swirl and temperature distortion on the aerodynamics (wake traverse and capacity) and thermal performance (overall effectiveness) of fully-cooled nozzle guide vanes (NGVs).

3.2 Review of combustor simulators with combined swirl and temperature distortion

Much of the early work on turbine inlet distortion effects focused on temperature distortion (or, so-called, hot-streak) effects. This work has been comprehensively reviewed in the literature [81]. Other studies contributed understanding of the effect of turbulence [122, 123], because of increasing awareness of the significant non-uniformity of turbulence at the outlet of rich-burn combustors.

Swirl-stabilized lean burn combustors are a relatively recent innovation, and the literature is therefore limited. The first studies to develop swirl simulators for turbine experiments were focused on understanding the impact of swirl—in isolation—on turbine performance and heat transfer [57, 96, 124]. Understanding of the impact on secondary flows led to a realization that swirl and temperature distortion could not be dealt with by superposition (e.g. [106]), and this mandated the use of combined simulators in experiments. This second wave of experiments was aimed at understanding the combined impact (swirl and temperature profile) on turbine performance, and on the aerodynamic and heat transfer performance of NGVs and the HP turbine. As part of the analysis, the swirl-induced migration of the temperature pattern through the vane and rotor have been studied numerically [106, 125] and the results proved to be interesting, if disappointingly geometry-specific. The literature on combined simulators is briefly reviewed.

Investigators at the University of Florence (UNIFI) completed several studies on a tri-sector (3/20 annular sector) CS, which implemented the Full Aerothermal Combustor-Turbine InteractiOns (FACTOR) combustor geometry. The facility acted as a precursor to the fully-annular Next Generation Turbine Test Facility [126, 90], which integrates the same CS in a state-of the art 2.5 stage rotating test-rig. In both facilities, temperature distortion is introduced through multiperforated effusion cooled liners, closely mimicking how coolant is introduced in a real engine. The compact design of the tri-sector facility, first presented by Koupper et al. [59], was successfully validated with Large Eddy Simulations (LES), demonstrating sufficient similarity in outlet profiles obtained when using a tri-sector design as opposed to a full ring of swirlers. Surveys at combustor exit, using both thermocouples, multi-hole probes [88] and hot-wire anemometry [89], to study the unsteady flow field, showed promising similarity between the target and experimental swirl profiles. However, initial results highlighted the necessity for a cylindrical tube mounted at the exit of the swirler to prevent premature mixing of the heated mainstream flow with coolant streams to guarantee a lean-burn-representative non-dimensional temperature profile [88].

A similar topology was implemented in the Demonstrator Lean-burn Combustor Simulator (OLCS) [127], on which the present work is based. Whilst temperature distortion was introduced

through annular cold air bleed slots at hub and case (instead of the effusion cooled liner employed in the UNIFI tests), a diffusion tube, fitted at the exit of the flat blade swirlers, controlled the axial deceleration rate to reduce the likelihood of vortex breakdown as the flow mixes out to fill the annulus. Another innovative feature of the OLCS was the axial orifice at the center of each swirler, which was successfully used to generate a jet that suppresses the formation of a precessing vortex core (PVC) without disturbing the desired inlet total pressure field. A PVC is an undesirable large scale, asymmetric, corkscrew-shaped coherent flow feature, which is often associated with catastrophic hydrodynamic instability of the combustion process [79]. It is thus perhaps surprising that PVC suppression was not considered as part of the UNIFI experiment. In real engines such features are thought to be largely suppressed by a combination of combustion-induced volume dilation through heat-release and conscious design choices [80], thus necessitating an artificial means of eliminating them in non-reacting facilities such as the OLCS. The simulator was characterized experimentally [92], by conducting detailed traverse measurements at atmospheric exit pressure over three swirler pitches. Well-defined swirl and temperature profiles were achieved, which were a good match for the target profiles and pre-test unsteady-RANS simulations. In a similar upgrade program to that described in the current paper, a OLCS was implemented and commissioned [62] in the Oxford Turbine Research Facility. The facility was subsequently used to characterize the effect of lean-burn combustor flows on a 1.5-stage high pressure turbine [104].

Parallel work on the UNIFI CS included several LES investigations performed for the purpose of comparing turbulent timescales with the experimental hot-wire data [128] and for investigating the effect of swirler-vane clocking on the development of the swirl profile [129]. The latter investigation also addressed the impact of potential field effects and the presence of NGVs on the flow at the combustor-turbine interface. These effects are important in the context of experimental measurements at the combustor outlet because they are often carried out in the absence of NGVs for improved access. The LES studies were followed by an experimental evaluation of the effect of swirl and temperature distortion on NGV film cooling [113] and aerodynamic performance [107]. More recently, the tri-sector facility was used to examine the transport and dissipation of turbulence through the NGV under lean-burn-representative inlet swirl and temperature distortion [130], reporting substantial residual swirl and turbulence downstream of the NGVs (in the HP-rotor frame of reference).

3.3 The ECAT facility

The ECAT facility (for detail see [121]) is an engine-parts facility to study high pressure nozzle guide vanes. The parts are typically (depending on the test program) from a modern high-bypass-ratio civil turbofan engine and are operated at non-dimensionally engine representative conditions of Mach number (M), Reynolds number (Re), and coolant-to-mainstream pressure ratio. The facility has semi-transient operation (typically 40–60 s), operating in regulated-blowdown mode from compressed air tanks.

Table 3.1: *Operating conditions of the ECAT facility.*

Parameter	Nominal value
Vane inlet total pressure, $p_{0\mathrm{m}}$, bar	1.0–3.0
Vane pressure ratio, $p_{\mathrm{exit}}/p_{0\mathrm{m}}$	0.35–0.7
Vane exit M	0.7–1.3
Vane eixt Re	3×10^5–9×10^5
Mainstream mass flow, kg/s	6–17
Inlet total temperature, K	290–370

The mainstream flow is heated by electric heaters (2 MW) which in the current installation offer a hot-to-cold temperature ratio of approximately 1.2 (to be extended to 2.0 in an upgrade program [131]). There are auxiliary feeds to control coolant flow and dilution flow for the combustor simulator. Typical facility operating conditions are summarized in Table 3.1.

3.4 Design of the combustor simulator

The ECAT CS is based on the pilot studies of Hall and Povey [92] in the OLCS. This design was modified and scaled for compatibility with the annulus-line and higher pressure operating conditions of the ECAT facility. This required definition of the number of swirlers, blade geometry, and coolant slot areas at hub and case, based on target profiles.

The geometry of the ECAT combustor simulator is shown from a meridional view in Figure 3.1a. A compact swirler assembly and diffuser (to suppress vortex breakdown by controlling the rate of axial diffusion, see [127]) is mounted in a contracting annulus line that represents the relevant engine geometry. As shown in Figure 3.1b, the swirlers feature a central jet orifice to suppress the formation of a PVC (see [127]). The temperature profile is generated by controlled injection of coolant through annular hub and case slots. The coolant mass flow rates and coolant slot areas were optimized to achieve the target profiles of total temperature and pressure at the reporting plane, which is located 0.5 axial chords upstream of the vane leading edge at midspan (see Figure 3.1a).

The target profiles of total pressure, non-dimensional total temperature (or effectiveness), swirl angle, and pitch angle were loosely defined based on those by Shahpar and Caloni [56]. Their profiles were obtained from a simulation of a lean-burn combustor prototype under reacting conditions and are hence a suitable approximation of the non-dimensional fields anticipated at the combustor-turbine interface.

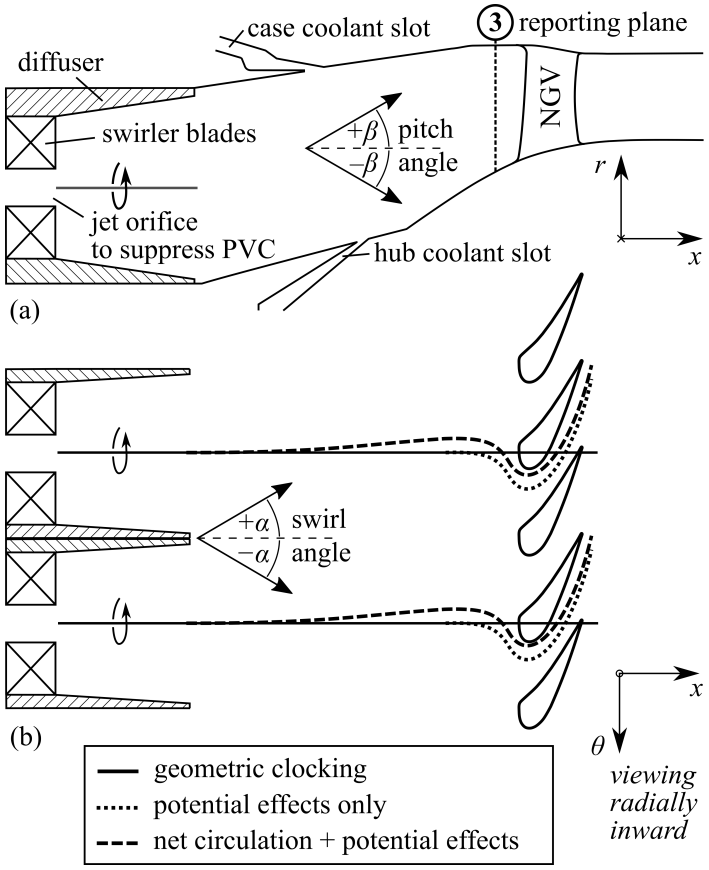


Figure 3.1: *Geometry of the combustor simulator showing: (a) hub and case coolant injection slots and pitch angle convention; (b) migration of the bulk flow, clocking relative to vanes, and swirl angle convention.*

Combustor simulator design optimization

The optimization of the system is covered in [127, 132]. So far as the temperature profile is concerned considerations included:

i) enthalpy balances in the upper and lower halves of the annulus to match the required temperature deficits for the non-dimensional profile (discussed in [132]);

ii) the axial position of the outlet of the coolant slots with respect to the reporting plane, which controls the amount of mixing and the non-dimensional shape of the profile at the reporting plane;

iii) the temperature ratio of the hot and cold gas at the point of injection;

iv) the outlet areas of the hub and case coolant injection slots which controls the velocity difference between streams (controls initial shear) and the dynamic head, which controls the total pressure profile at the point of mixing, assuming continuity of static pressure at the interface between streams.

These parameters must be optimized simultaneously, and their interaction is interesting and subtle. An example of the complexity of the optimization is that a given enthalpy deficit can be achieved with a given mass flow rate of very cold gas or a larger mass flow rate of a relatively warmer gas, with the simultaneous optimization of the injection point allowing a variety of shape factors and max-to-min temperature differences in the resulting profile. Such considerations are well-covered in [132].

So far as the swirl profile is concerned, the following must be considered:

v) the peak angle of the individual vanes of the swirlers;

vi) the swirler total pressure loss at the reporting plane;

vii) the rate of axial deceleration in the diffuser tube, which can reduce the likelihood of vortex breakdown, and complete mixing out of the profile;

viii) the contraction ratio between swirler exit and the reporting plane, which controls the swirl angle at the reporting plane through the axial velocity;

ix) the rate of axial acceleration in the downstream annulus, which has an impact on the peak swirl angles at the reporting plane (stretching effect on vortex [133]);

x) the axial distance between the swirler and the reporting plane.

In the ECAT facility, the maximum hot-stream temperature is limited by heater power. The cold-stream air is drawn directly from a high-pressure tank at ambient temperature. Mass fractions (enthalpy balance considerations) and associated stream temperatures (practical considerations) and axial injection locations were chosen (based on CFD simulations and prior experiments) to define the desired profile. At the point of injection, it is possible to design for matched velocity or matched total pressure. The first is a minimum shear condition (chosen in our case to delay mixing, but resulting in slightly elevated total pressure in the coolant layer) and the second a design requirement for studies requiring flat inlet total pressure.

Swirler count and geometry

The CS contains 20 flat vane swirlers (vs. 40 NGVs), which were designed according to the initial work of Kilik [134]. As implemented in the OLCS [127], a cylindrical orifice at the center of the swirler was used to suppress the formation of the PVC. The vane angles were estimated using a free vortex assumption between the swirler and reporting plane. Each swirler is comprised of 10 vanes, angled at 20° relative to the axial direction, yielding a swirl number of 0.26. The swirl number, S, was defined by

$$S = \frac{\int_0^{r_{\mathrm{sw}}} V_x V_\theta r^2 dr}{r_{\mathrm{sw}} \int_0^{r_{\mathrm{sw}}} V_x^2 r dr} \tag{3.1}$$

where the radius, r, the axial velocity, V_x, and the tangential velocity, V_θ, are defined in a swirler-centered coordinate frame. This parameter is commonly used to characterize the intensity of a vortex (see, e.g. [135]) and the value it takes can be considered a good predictor of whether a recirculating region might develop [54]. For $S < 0.60$ and hence for the ECAT CS ($S \approx 0.26$), the axial pressure gradient is too weak to cause flow recirculation [54]. Whilst in most modern combustors S is greater than 0.60 (to anchor the flame), the absence of volume dilation-induced acceleration in the ECAT CS mandated a lower swirl number to achieve the target swirl angles at the reporting plane, given the fixed contraction ratio of the annulus line and physical dimension of the NGVs. The swirlers were clocked as in the engine, such that the central axis of each swirler was geometrically aligned with the midspan stagnation point of alternating NGVs. This is illustrated in Figure 3.1b. The integer-multiple periodicity simplifies the CFD setup.

3.5 Combustor simulator commissioning

Geometry and hardware

An engine-scale, high pressure CS was designed and manufactured for the ECAT facility. A photograph of the hardware is shown in Figure 3.2. Five struts support the test section core, which houses the hub feed lines for the combustor simulator and the vane ring.

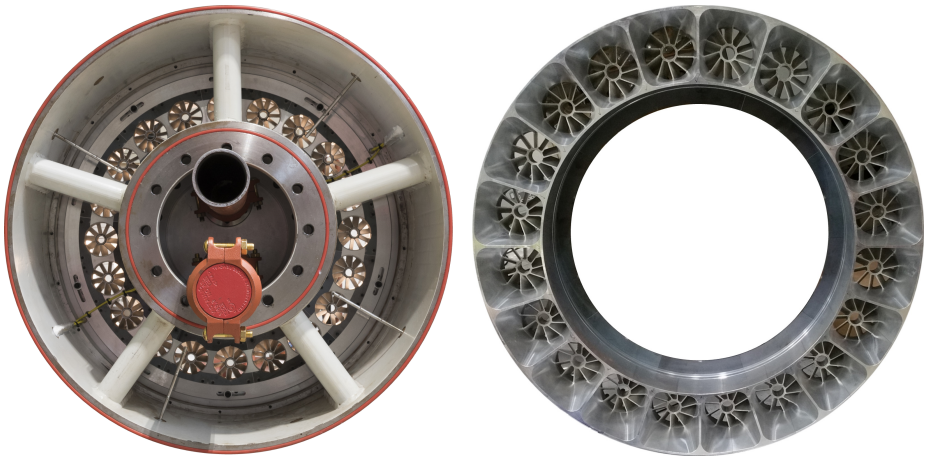
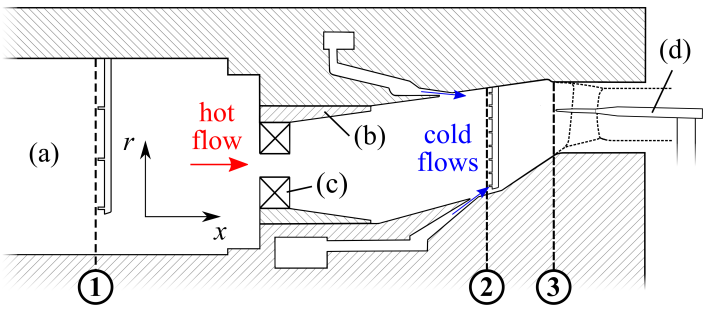


Figure 3.2: *Photograph of the combustor simulator viewed from upstream (left) and downstream (right). The upstream struts, swirlers, and diffusers are visible.*

Instrumentation

A schematic of the general arrangement of the test section is shown in Figure 3.3. Heated mainstream air from the axial stiffener passes through the swirlers and the diffusers. Further downstream, cold air is introduced from annular slots at hub and casing before the contraction shapes the swirl profile. Also indicated in Figure 3.3 are the locations of the three key measurement planes. A detail of measurement planes 2 and 3 is presented in Figure 3.4. The instrumentation at each of the three planes is now briefly outlined.



(a) axial stiffener (b) diffuser (c) swirler (d) probe

Figure 3.3: *Schematic of the general arrangement of the combustor simulator, showing the hot and cold feeds. The position of the measurement planes 1, 2 and reporting plane 3 are shown, as is the outline of the (removed) vane ring.*

At plane 1 and 2, two pairs of Pitot probe and bare bead thermocouple rakes are used for routine monitoring. At plane 1, probes in two circumferential locations measured a total of six pressures and six temperatures, which serve as reference conditions for the temperature and pressure normalization. At plane 2, probes with eight radially staggered measurement points were located

at four circumferential positions (each for pressure and temperature) giving a total of 32 pressure and 32 temperature measurements within the combustion chamber. The hub and case coolant plena pressures and temperatures were measured using two pressure and temperature points located diametrically opposite to one another (two of each type per plenum).

At plane 3 (reporting plane), aerodynamic traverse measurements were taken with a five-hole probe, a ducted three-hole probe (sensitive to swirl but not pitch), and a bare-wire thermocouple probe (25 μm bead diameter). The five-hole probe was used to survey the central 80% span, whilst a three-hole probe was used for the top and bottom 10% of span, allowing measurements of yaw angle very close to the walls (the three-hole probe does not report pitch angle). The hub-mounted traverse equipment has been described in [121, 136, 137]. The traverse was configured to cover an annular sector of 40 degrees in a single run but can be clocked at 36 degree increments allowing the entire annulus to be traversed. To determine acceptable traverse speed, the pressure probe-system time constant was determined using the methods discussed in [138], whilst the thermocouple probe was designed according to [139]. The effective bandwidth of the pressure and temperature signals were estimated to be around 50 Hz. Pneumatic tubing lengths were minimized by mounting the transducers on the traverse. A digital zero-phase filter was applied to the signals, both sampled at 500 Hz. The probes were traversed circumferentially (constant spanwise position) at 4 degrees per second, giving a passing time of 4.5 s for a single swirler pitch. This is equivalent to a spatial resolution of 0.5 mm in the circumferential direction, or 225 samples per swirler pitch. The effect of the traverse motion on the measurements was verified to be negligible by performing several sweeps in alternate directions and overlaying the left and right–passing events to ensure zero positional offset between them. The radial resolution (step height) was set to 4.5% of passage height over most of the span (3.1 mm) reducing to 2.3% (1.6 mm) for the upper and lower 10% span.

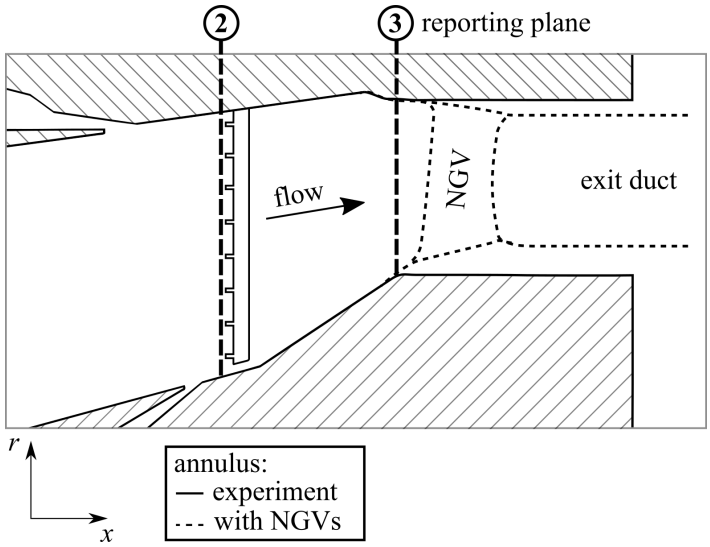


Figure 3.4: *Detail of measurement planes 2 and 3, showing the NGV position (removed in these experiments).*

Experimental conditions for commissioning experiments

To allow detailed traverse measurements at the reporting plane, experiments were conducted without NGVs installed, and with a modified exit duct to improve probe access (illustrated in Figure 3.4). If the NGVs had been installed, the extremely low dynamic-to-total pressure ratio in the combustor simulator would result in an unacceptable signal-to-noise ratio for five-hole probe measurements. Without NGVs, the backpressure during testing was approximately atmospheric (compared to an absolute pressure of 1.80 bar at nominal conditions, with NGVs installed). Further experimental conditions are summarized in Table 3.2.

Table 3.2: *Operating conditions for experiments.*

Parameter	Value
Mainstream (hot) mass flow, $\dot{m}_{\mathrm{h}}$, kg/s	11.60
Coolant mass flow, $\dot{m}_{\mathrm{c}}$, kg/s	1.54
Case coolant mass fraction	0.58
Hub coolant mass fraction	0.42
Inlet total temperature, $\dot{T}_{0\mathrm{h}}$, K	330–350
Coolant total temperature, $\dot{T}_{0\mathrm{c}}$, K	290–295
Exit plane absolute static pressure, bar	1.0

Typical inlet pressure (p_{01}) and temperature (T_{01}), measurements at plane 1 and in the coolant plena ($p_{0\mathrm{c}}$ and $T_{0\mathrm{c}}$) are shown in Figure 3.5. The coolant and mainstream mass flow rates are slowly increased by opening a valve (24 s to 30 s). To prevent accidental damage, the heaters are only switched on once the mass flow is sufficiently high, leading to a sudden increase in T_{01} (34 s).

Although maximum power is reached in less than 2 s, the mainstream temperature characteristic during the heated part of the run is asymptotic, on account of the thermal mass of the pipework and settling tanks between the heaters and plane 1 (this is modelled in [131]). Once the heaters are at full power and p_{01} is stable, the traverse is started manually at 41 s. The flow at plane 1 (at the outlet of the settling tank) and in the coolant plena is well-mixed and can be assumed to be spatially uniform, though varying in time. Throughout the run, the coolant temperature decreases slightly owing to the expansion of gas in the high-pressure tank. At 84 s, the heaters are switched off automatically, followed shortly by closure of the main valve at 87 s.

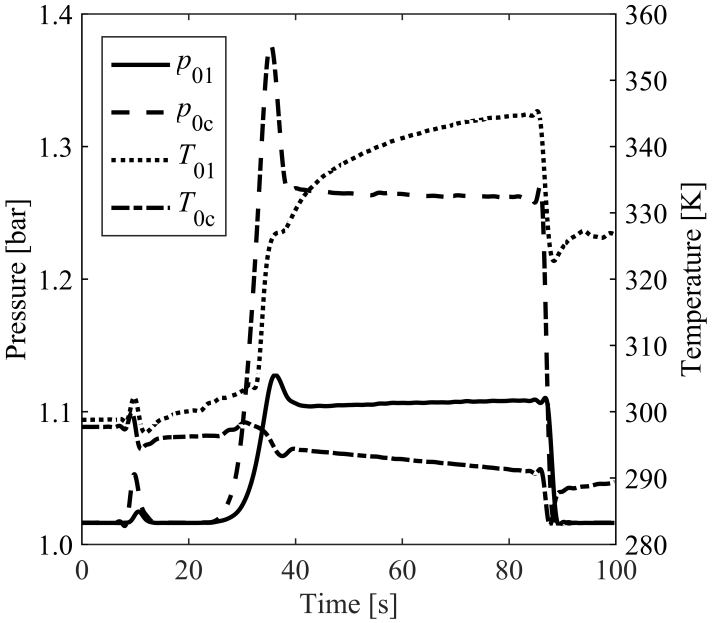


Figure 3.5: *Typical inlet pressure and temperature measurements at plane 1, and in the coolant plena.*

The temperature measured at the reporting plane, T_{03}, is presented as effectiveness, η^*, defined by

$$\eta^* = \frac{T_{03} - T_{0c}}{T_{01} - T_{0c}} \tag{3.2}$$

where the hot reference temperature, T_{01}, is measured at plane 1 (upstream of the swirler), and the cold reference temperature, T_{0c}, is that measured in the coolant plenum. This definition is convenient for combustor simulators because the hot and cold temperatures are easy to measure.

In principle, therefore, the non-dimensional temperature could be calculated—in real time—at the reporting plane. The issue arises, however, that there are additional thermal masses (the metal walls), with associated heat transfer from the hot gas to the cool walls, between plane 1 measurements and the reporting plane measurements. To understand the data at fixed thermocouple locations at plane 2, and to correctly normalize the traverse data at plane 3, it is

necessary to account for the inter-plane heat losses. This is particularly true for traverse data at plane 3, because, in addition to the transients due to the thermal mass between planes 1 and 3, the probe is moving through a spatial field of temperature (from coolant injection). Thus, decoupling the two effects is impossible without a transient heat transfer correction. This correction is discussed in the following section.

Transient effectiveness correction

The experimental effectiveness, η^*, is corrected based on the expectation that the mid-span region at plane 3—being devoid of coolant—will experience an effectiveness of unity under adiabatic conditions (as observed in complementary CFD simulations), such that any deficit may be attributed to transient convective heat loss. A scalar, time dependent correction factor, k_{corr}, is defined based on a curve fit to an ensemble average of the uncorrected reporting plane effectiveness in the 30–70% span region across all runs. Thermal traverse data is aligned in time using a run-specific temporal offset, δ_i, to ensure that the instant at which the heater switches on coincides between runs. The correction factor is obtained by fitting an analytically-based 1D solution to the ensemble average of the time-aligned traverse data:

$$k_{\mathrm{corr}}(t-\delta_i) = 1 - ae^{|b(t-\tau)|}\mathrm{erfc}\left(\sqrt{|b(t-\tau)|}\right) \tag{3.3}$$

The generic form corresponds to the non-dimensional fluid outlet temperature under a step change in inlet temperature at time τ, assuming a constant heat transfer coefficient for convective heat loss to a one-dimensional, semi-infinite wall [140]. Symbols a, b, and τ represent the least-squares optimization parameters. The averaged traverse data and correction factor curve are shown in Figure 3.6.

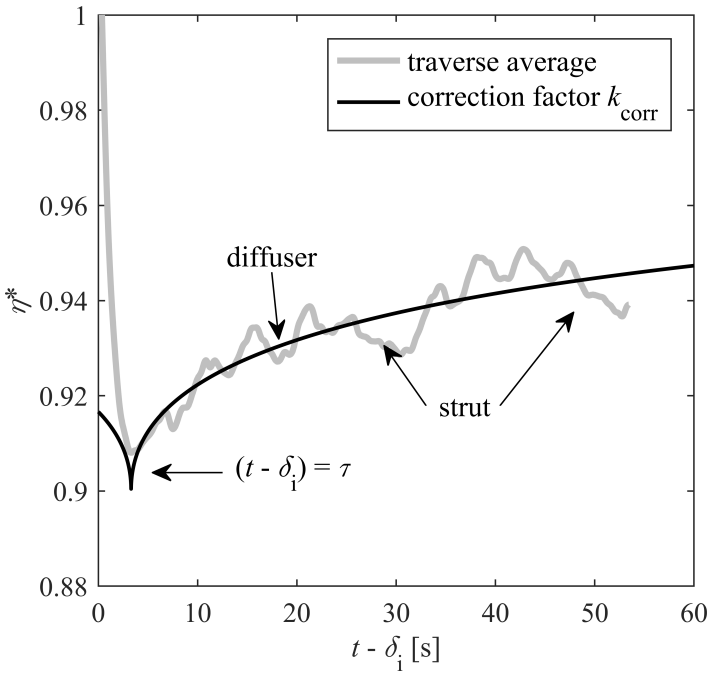


Figure 3.6: *Correction factor fit to average of reporting plane thermocouple traverse runs in the 30–70% span range.*

In Figure 3.6, the traverse average effectiveness increases throughout the run because the test section heats up, thus reducing the driving temperature difference, which causes heat loss between plane 1 and plane 3. Despite averaging the traverse data across multiple runs, minor oscillations persist due to a strong correlation between the circumferential position of the probe, θ, and pseudo-time, $t - \delta_i$, resulting in simultaneous exposure to the same circumferential thermal non-uniformities (albeit at different radii). The high frequency oscillation is caused by the thermal wakes of diffuser walls between adjacent swirlers whereas the lower frequency but higher amplitude oscillation arises from the thermal wake of a large upstream strut (see Figure 3.2). Both features are absent in adiabatic CFD simulations but were successfully reproduced in constant (cold) wall temperature simulations (not presented), confirming they are purely a consequence of transient heat transfer. The wake of the upstream strut is discussed further in the results section.

We define the corrected equivalent mainstream effectiveness, η^*_{corr}, by

$$\eta^*_{\mathrm{corr}}(t) = \frac{\eta^*(t - \delta_i)}{k_{\mathrm{corr}}(t - \delta_i)} \tag{3.4}$$

The instantaneous effectiveness from each individual run—including those outside of the 30–70% span range—is scaled by dividing by factor k_{corr} (with run-specific temporal offset δ_i). Radial profiles of corrected and uncorrected effectiveness at the reporting plane are compared to results from an adiabatic CFD simulation in Figure 3.7.

It is evident that the correction method effectively eliminates the overall enthalpy deficit as well as saw-tooth discontinuities in radial profiles at the interface between adjacent area traverses. The similarity between adiabatic CFD and experimental results in the near-wall region is also improved. Minor oscillations persist in the corrected data because the transient heat loss is a function of both space and time. Spatial variations in heat loss cannot be captured by the scalar, time-dependent correction factor, because insufficient data is available to construct a higher order correction model.

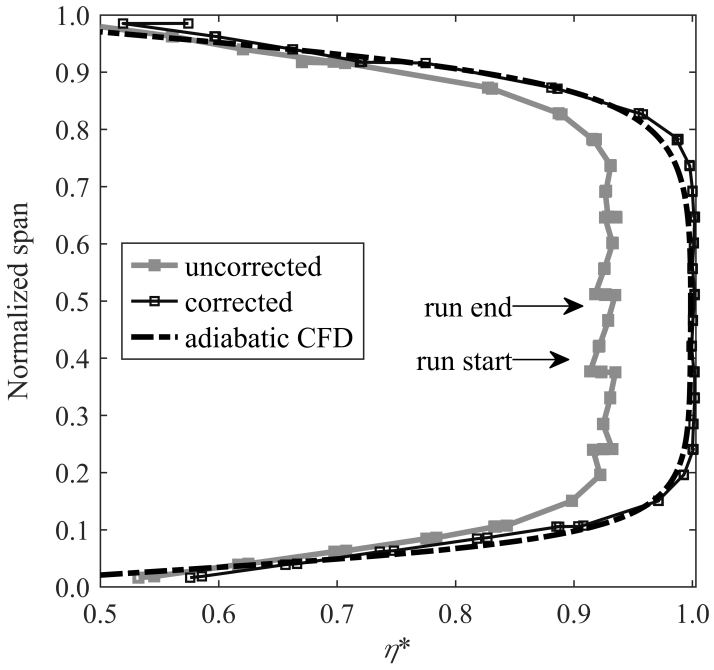


Figure 3.7: *Uncorrected experimental vs corrected experimental vs low pressure CFD k–ϵ radial effectiveness (adiabatic simulation).*

3.6 Numerical methods

In this section, the CFD analysis performed to investigate the effect of increased back-pressure as well as that of the vane potential field on the swirl profile and circumferential flow migration is described.

CFD domains

For the detailed CFD analysis, two computational domains were generated: one excluding and another including vanes. Together, they enable assessment of the validity of using the present experimental results at vane inlet as a reference condition in future studies *with vanes*.

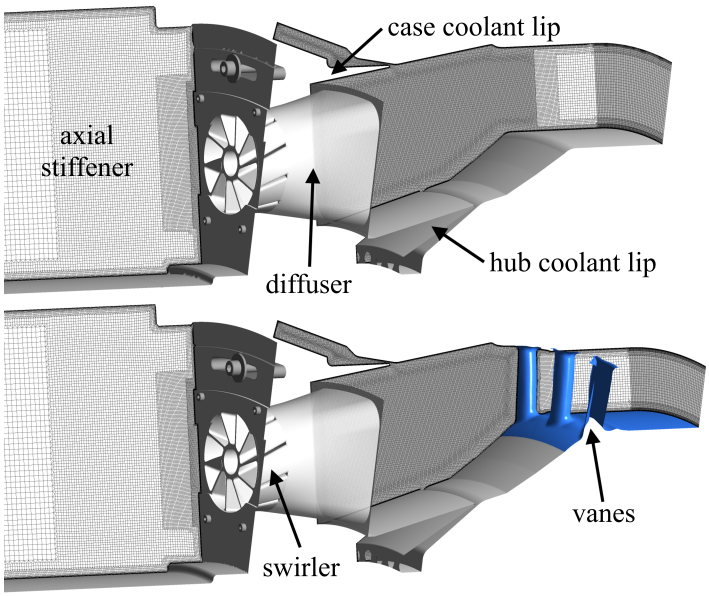


Figure 3.8: *Meshed flow domains with and without NGVs.*

The domain extends to the inlet of the axial stiffener (see Figure 3.8) because swirler lip separations, which would otherwise not be captured, were observed to have important effects on the development of loss within and downstream of the swirler passage. This approach was seen to offer an improved prediction of total pressure loss over a circular duct-fed swirler approach. Circumferentially, the computational domains span two vane passages or one swirler pitch. The geometric differences between the two domains (presence of the vanes and altered exit duct geometry) are shown in Figure 3.8.

Numerical test matrix

The three CFD cases that were run are summarized in Table 3.3. They are now briefly described. The first case replicates the experimental conditions, enabling direct comparison of profiles at the reporting plane whilst also establishing a baseline for the accuracy of various turbulence models. The measured profiles were obtained without NGVs installed and with atmospheric pressure at the rig exit. The second case also excludes the NGVs but was performed at elevated exit pressure to emulate the increased back-pressure that would arise in the presence of downstream vanes. The third case is both at elevated pressure and includes vanes. In combination with the second case, it serves to isolate vane potential field and back-pressure effects.

Table 3.3: *Description of CFD cases.*

CFD Case	Domain + exit pressure	Purpose
1	without NGVs, at low exit pressure (1 atm)	for direct comparison with ECAT combustor commissioning experimental results
2	without NGVs, at high exit pressure (2 atm)	to decouple potential field and back-pressure effects
3	with NGVs, at low exit pressure (1 atm)	to predict effects of the presence of NGVs on inlet profiles

Mesh and boundary conditions

A hybrid meshing approach, which included the generation of hexahedral elements in the freestream region, tetrahedral element around complex features, and prisms within the boundary layer regions, was particularly suited to the complex geometry of the combustor simulator. The meshes without and with NGVs, comprised of 67 million and 87 million cells respectively, are effectively identical upstream of the vanes. Both grids were refined near the walls, featuring 24 prism layers with an expansion ratio of 1.2. The grid sensitivity was evaluated by refining both meshes globally by decreasing the background cell size of the octree mesh. This is discussed in Appendix 3.A. Results are shown for the most refined meshes.

For all cases, the mainstream and coolant mass flows applied at the inlets are matched to the experimental conditions in Table 3.2, with corresponding total temperatures set to 350 K (mainstream) and 290 K (coolant feeds). Having carried out a sensitivity study and concluded no significant dependence of the flow on the inlet turbulence, the intensity was set to 5% at all inlets. A 1:1 rotational periodic interface was used at the circumferential extents of the domain. For cases 1 and 3, the exit pressure was atmospheric, whereas the back-pressure for the second case (without NGVs) was determined from the pressure which naturally develops in the plenum of case 3 (approximately 2.0 bar, depending on the turbulence model). The local pressure at the outlet was calculated from the radial equilibrium equation. All walls were modelled as smooth and adiabatic.

Models and solver settings

All CFD simulations were performed in ANSYS CFX 20.2. Simulations were run in double-precision with a steady, compressible solver. Simulations for three turbulence models—k–ϵ [141], k–ω SST [142], and the SSG Reynolds Stress Model (RSM) [143]—were performed. Scalable wall functions were used for k–ϵ and SSG RSM, whereas the k–ω SST model utilizes enhanced wall functions to adaptively switch between a wall-resolved and wall function

approach, depending on the local value of y^+. This approach allowed the use of the same grid for all three models. For k–ϵ and k–ω SST, a second-order blended discretization was employed for both the momentum equations and turbulence. The SSG RSM model was only stable using first order turbulence numerics.

3.7 Experimental and numerical results

In this section, we compare experimental and numerical results at the experimental condition (atmospheric exit pressure without NGVs installed).

The measured total pressure maps are presented in terms of a swirler total pressure loss coefficient, $C_{p,\mathrm{sw}}$, defined by

$$C_{p,\mathrm{sw}} = \frac{p_{01} - p_{03}(r,\theta)}{q_{\mathrm{sw}}} \qquad (3.5) \qquad\qquad q_{\mathrm{sw}} = \frac{\dot{m}_{\mathrm{h}}^2}{2A_{\mathrm{sw}}^2 \rho_1} \qquad (3.6)$$

Here, p_{01} and p_{03} are the total pressures at plane 1 and 3, respectively. The denominator, q_{sw}, is the reference dynamic pressure, which is defined in Equation 3.6, using the hot mass flow, m_{h}, the swirler reference area, A_{sw}, and the density at plane 1, ρ_1. The expression follows from the one-dimensional continuity equation, assuming incompressible flow. Experimentally, the pressure difference $p_{01} - p_{03}(r,\theta)$ was measured with a differential transducer setup to reduce the bias uncertainty of the total pressure loss coefficient (estimated to be ±3.8% to 2σ).

The temperature normalization has previously been described in Equation 3.2. All effectiveness data in this section has been corrected according to the definition of η^*_{corr} in Equation 3.4. The 2σ (95%) confidence interval for the experimental effectiveness was estimated at ±3.5%, assuming temperature measurements have a standard error of ±0.73 K.

The swirl angle, α, and the pitch angle, β, are defined as follows:

$$\alpha = \arctan\frac{V_\theta}{V_x} \qquad (3.7) \qquad\qquad \beta = \arcsin\frac{V_r}{V} \qquad (3.8)$$

where V is the local velocity magnitude and V_r, V_x, and V_θ the radial, axial and circumferential components, respectively, in the machine reference frame. The sign convention for flow angles is indicated in Figure 3.1b. The 2σ confidence interval for flow angles was estimated to be ±1.6°, based on the alignment uncertainty during probe calibration and testing (both were assumed to be uniformly distributed between ±1°).

Figure 3.9 is a side-by-side comparison of the experimental results and the k–ϵ CFD simulation for the low back pressure case (without NGVs), showing profiles of total pressure loss coefficient, equivalent mainstream effectiveness, swirl angle and pitch angle.

Distributions of loss, temperature, pitch and yaw

Consider first the total pressure loss coefficient distributions. In both the experiment and CFD, oval-shaped regions of relatively high loss are observed near the midspan, peaking approximately 1/5th of a swirler pitch (or 3.6°) to the left of the swirler geometric centerlines. Both experiment and CFD have elevated total pressure (reduced $C_{p,\mathrm{sw}}$) close to the end walls due to the slot-injection of coolant.

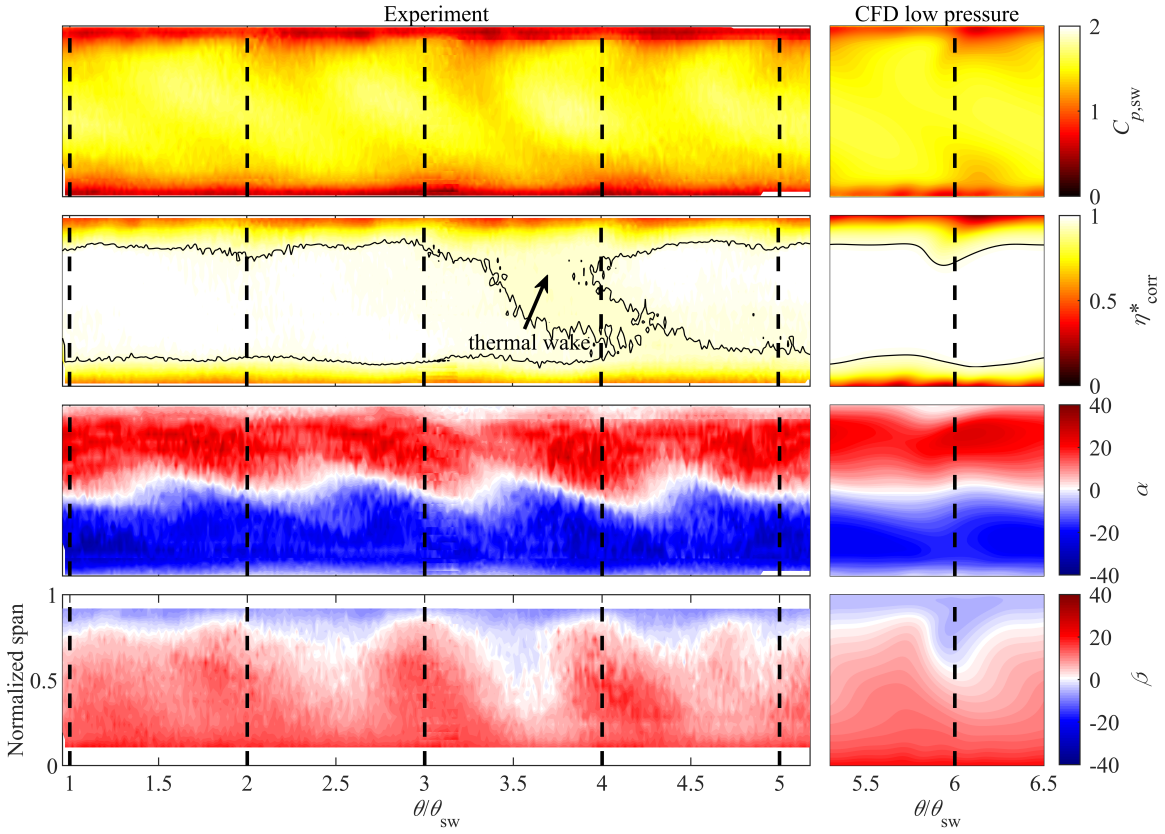


Figure 3.9: *Experimental and CFD results (k–ϵ low pressure case) at reporting plane 3 for: loss coefficient, $C_{p,\mathrm{sw}}$, corrected equivalent mainstream effectiveness, η^*_{corr}, swirl angle, α, and pitch angle, β. Results are viewed from upstream to downstream. Dashed lines indicate radial lines passing through swirler centerlines.*

At the casing, immediately to the right of the swirler centerlines, this region protrudes slightly into the mainstream. A corresponding, but less distinct feature can be seen at the hub. The most natural explanation for this effect would be upwash of the (relatively) high-pressure coolant at the vortex-vortex interface. CFD streamlines indicate, however, that the feature originates from the root region of the swirler blades. The streamlines passing through this region experience lower than average total pressure loss because the flow at the root region of the swirler remains attached, whereas large-scale flow separation occurs along the outer span of the swirler vane suction side well as the shroud. Overall, there is an excellent match between the experimental and CFD data.

Consider now the corrected equivalent mainstream effectiveness (η^*_{corr}) data. The dominant feature in both experimental and CFD data is the relatively cold (low η^*_{corr})) flow near the hub and case walls, indicating well-behaved near-wall coolant flow. The coolant layer at the case is slightly thicker than that at the hub due to higher injected coolant mass fraction. There is a periodic thickening in the coolant layer at both the hub and case, with the same periodicity as the swirler count, and the thick regions largely coinciding with regions of elevated total pressure. This is in line with the argument that the high-density coolant is the primary influence on the total pressure field in the near-wall regions. Overall, the CFD matches the experimental effectiveness profile extremely well, producing a nearly identical radial profile (see Figure 3.7). The only significant dissimilarity is the region marked as "thermal wake" at approximately $\theta/\theta_{\mathrm{sw}} = 4$. This is caused by convective heat loss to an upstream radial strut (see Figure 3.2, and discussion regarding the transient correction to equivalent mainstream temperature). The strut is aligned with the swirler geometric center $\theta/\theta_{\mathrm{sw}} = 4$, and the cold thermal wake appears to be "processed" by the swirler into a diagonal strip approximately downstream of that swirler. This feature is not captured in the CFD, because the domain covers a single swirler sector, and the radial strut is not modeled.

We now consider the swirl angle (α) distribution (sign convention in Figure 3.1). The experimental swirl angle distribution is very periodic, confirming well behaved vortex cores with minimal non-periodic interaction between them. The iso-line of zero swirl has a quasi-sinusoidal profile, characteristic of distorted (non-circular) vortex cores. The CFD results are similar in general form, with rather less distortion from a regular (circular) vortex than the experimental data.

Finally, consider the pitch angle distributions. As expected, the trend is for mildly negative pitch at the casing and positive pitch at the hub, in line with the annulus hade angles (see Figure 3.4), with the classical quasi-sinusoidal variation of the iso-line of zero pitch associated with the interaction of the vortex with the annulus hade. The general pattern was reasonably well matched by CFD. The experimental data for pitch angle only extends to within 10% span of the hub and case walls (probe size restriction).

In the next section the radial profiles of loss coefficient, equivalent mainstream effectiveness, yaw angles and pitch angles are considered.

Radial profiles of pitch and yaw

Experimental and CFD-predicted radial distributions of circumferentially-averaged total pressure loss coefficient, effective mainstream effectiveness, yaw angle, and pitch angle are presented in Figure 3.10. CFD data are presented for three simulations using k–ϵ, k–ω SST, and RSM SSG

turbulence models using experimental boundary conditions (see case 1 description in Table 3.3).

First consider the radial loss coefficient ($C_{p,\mathrm{sw}}$) profiles in Figure 3.10a. In the experimental profile, the peak loss is at approximately mid-span, but with fairly uniform loss distribution between 20 and 80% span. Significantly lower loss near the walls is associated with the coolant layers, which have higher density and higher velocity than the mainstream flow (see also the distributions of Figure 3.9). Predicted mass-averaged loss coefficients differ significantly between the three turbulence models, with values of 1.40 for k–ϵ, 1.54 for k–ω SST, and 1.78 for RSM SSG. It is interesting to note that although both k–ω SST and k–ϵ models use the k–ϵ equations in the freestream, the k–ϵ model predicts a 10% lower mass-average freestream loss, yielding a better match with experimental results.

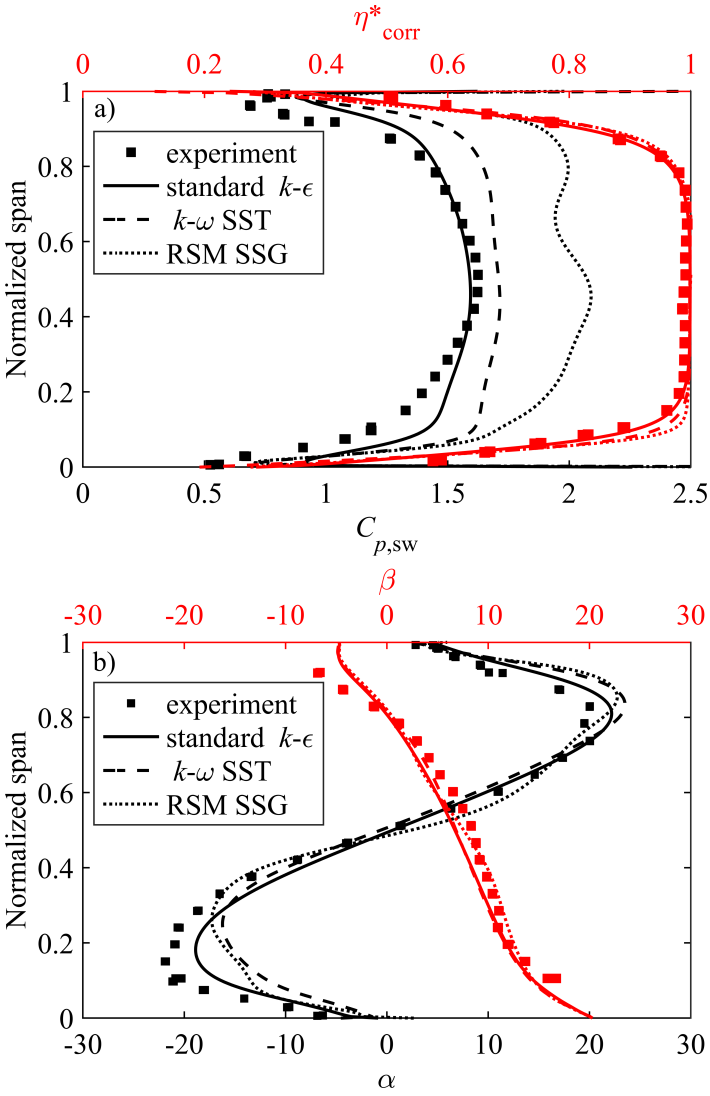


Figure 3.10: *Experimentally-measured and CFD-predicted radial profiles of circumferentially averaged: (a) pressure loss coefficient and corrected equivalent effectiveness; (b) swirl and pitch angle.*

Now consider the radial effectiveness (η^*_{corr}) profiles in Figure 3.10a. The experimental profile is uniform between 20 and 80% span, where the effectiveness is unity (hot stream temperature). Above 80% span and below 20% span the effectiveness falls rapidly through the mixing coolant layer, to a value of approximately 0.4 at the walls. All three radial distributions from CFD simulations are a reasonable match to the experimental distribution, with slightly closer agreement in the hub region for the k–ϵ model than for k–ω SST and RSM SSG models, both of which underpredict mixing.

Now consider the radial swirl angle (α) profiles of Figure 3.10b. The experimental profile tends to zero whirl at the walls (due to axial injection of coolant at hub and case), and at the vortex center (approximately 50% span) with maxima and minima of approximately +20° and −22° at span fractions of 0.15 and 0.83 respectively. This represents a good match to the target profile [56] (swirl angles between −20°and +15°). The k–ϵ CFD simulations produce a good match with the experimental data, agreeing to within 4° of the measured profile across the entire span. The CFD simulations using the k–ω SST and SSG RSM turbulence models under-estimated mixing, as evidenced by a distinct vortex dipole at the reporting plane, which is not seen in the experimental data. Swirl-number-dependent accuracy of RSM has been observed by Escue and Cui [144]. At the relatively low ECAT CS swirl number (0.26), the standard k–ϵ model appears to offer the best overall match to experiments among the models tested.

Finally, consider the pitch angle (β) profiles of Figure 3.10b. As expected, the trends are broadly linear (long-range potential field disturbance of the endwalls) with limits at the hub and case walls matched to the pitch angle of the annulus lines. Note that in our definitions of angle—Equation 3.8—ratios of velocity are with respect to absolute flow velocity not axial velocity, so the good match of pitch angle to the annulus pitch angle is only true in the limit of zero swirl angle at the walls (a condition that is met in the current study). The predicted pitch angle distributions were similar for all three turbulence models, and were in agreement with the experimental profile to within 3°.

3.8 Effect of Mach number mismatch and vane potential field

It will be recalled the experimental data was collected with the facility operating without vanes (to allow a large sector of data to be taken at fine resolution) and with atmospheric back-pressure (improved dynamic head to total pressure ratio). These are clear compromises, but avoid the problems seen in previous studies [62, 57] leading to sparse data, or data with high error, namely: low dynamic to total pressure ratio leading to high absolute error; transducer-line frequency

response issues [138]; and access. Avoiding these problems in the experimental design allowed extremely accurate data to be taken. In this section, we assess the scaling compromises associated with running the facility in this way. In particular, the sensitivity of the flow distributions to back-pressure and NGV potential field are investigated.

Reynolds and Mach number scaling

The combustor simulator survey data were taken at the same nominal mass flow rates as a typical ECAT experiment (high back pressure) but at lower back pressure. We now consider how this affects swirler Re and M. Here we define these relevant to the flow through the swirler vanes.

The relationship between Re and mass flow rate is given by

$$\mathrm{Re} = \frac{\rho V D_{\mathrm{sw}}}{\mu} \propto \frac{\dot{m} D_{\mathrm{sw}}}{\mu} \tag{3.9}$$

where ρ and μ represent the fluid density and dynamic viscosity, respectively. D_{sw} is the swirler diameter (an arbitrary swirler reference length) and $\dot{m}$ the swirler mass flow rate. The proportionality is valid for fixed area (relevant to all our experiments and CFD). The conclusion is that flow pattern should be similar between the low and high-pressure cases, and that the loss coefficient, $C_{p,\mathrm{sw}} = f(\mathrm{Re})$, would be the same in both cases. Here we reference incompressible arguments. For completeness we note that for fixed $\dot{m}$, halving the absolute pressure has the effect of doubling ρV^2. That is, the absolute loss is twice as high for the low pressure case.

In the simplest model of free-jet loss (dynamic head mixing out) this problem could be regarded as quasi-incompressible. Certainly, the flow is well-outside the range in which shock waves would enter consideration. Interestingly, however, although the mass-flow-averaged Mach numbers at the swirler exit for the high-pressure and low-pressure k–ϵ cases were 0.20 and 0.42 respectively (i.e. fairly incompressible for a problem of this type), the corresponding peak Mach numbers (evaluated from CFD) were 0.26 and 0.62. This non-uniformity arises because of two effects. Firstly, the relatively low-pressure vortex core at the center of the swirler draws in high pressure upstream air through the axial orifice, thus increasing the Mach number of the jet. Secondly, separation-induced blockage in the swirler passages reduces the effective flow area (for a fixed mass flow), thus leading to greater flow speeds to satisfy continuity. For the low-pressure case this represents a deviation between the impact pressure (difference between total and static pressure in a compressible flow) and incompressible dynamic pressure of 9.6% at the peak Mach number. A modified definition of the loss coefficient, $C'_{p,\mathrm{sw}}$, is introduced to reconcile the results for the high and low pressure cases by accounting for local compressibility. The modified definition is given by

$$C'_{p,\mathrm{sw}} = \frac{p_{01} - p_{03}(r,\theta)}{q'_{\mathrm{sw}}} \tag{3.10}$$

where q'_{sw} is the CFD mass flow-averaged impact pressure at the exit of the swirler. The modification decreases the loss coefficient for the low-pressure k–ϵ case by approximately 10%, relative to the equivalent high pressure case, when compared to the incompressible definition. In the following section, we compare the profiles at the reporting plane for the three CFD cases outlined in Table 3.3.

Effects of back-pressure (on M) and the vane potential field

Figure 3.11 serves as a direct comparison between the profiles at the reporting plane, with the three CFD cases summarized in Table 3.3 arranged by columns. The mass-flow-averaged Mach number at the swirler exit is indicated at the top of each column. Due to limited space, only the results for k–ϵ are shown, considering this model was seen to achieve the best match with experiments.

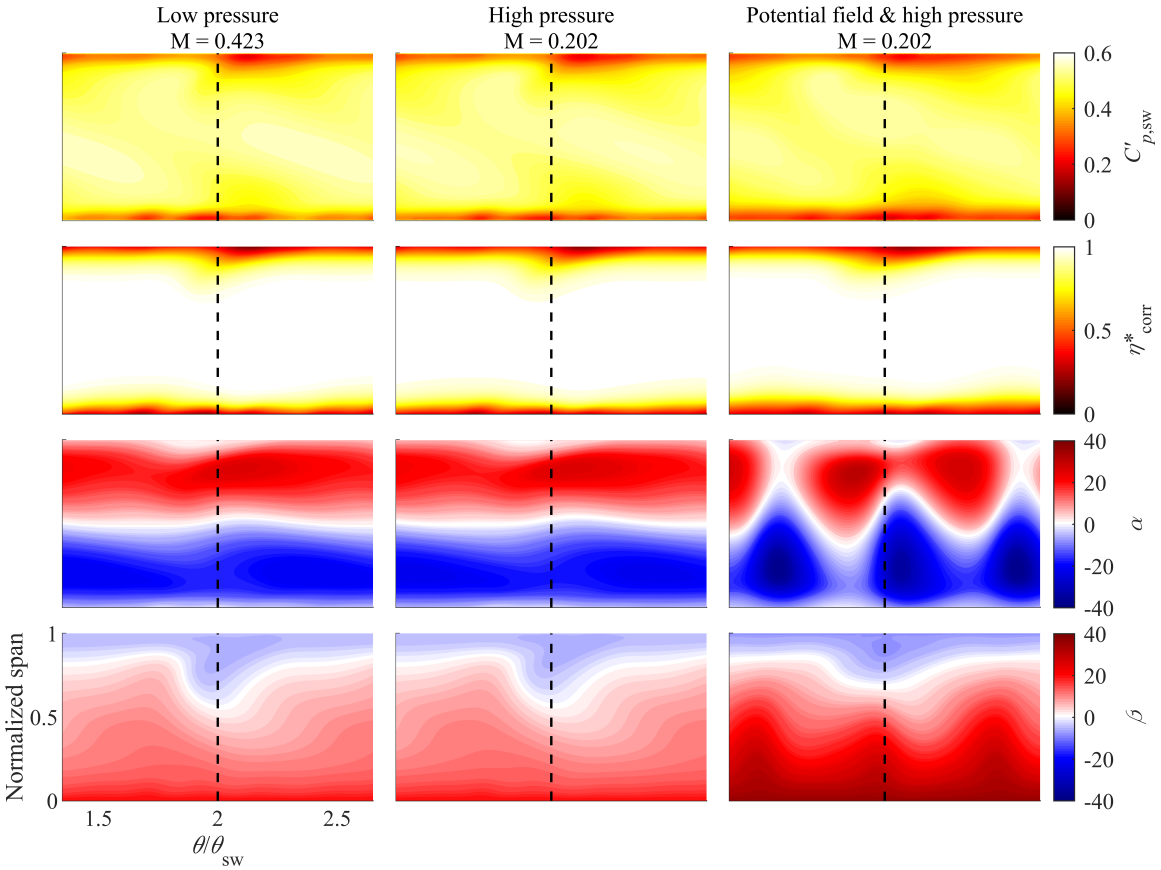


Figure 3.11: *Comparison of CFD predictions with k–ϵ model of the modified loss coefficient, $C'_{p,\mathrm{sw}}$, corrected equivalent effectiveness, η^*_{corr}, swirl angle, α, and pitch angle, β, at the reporting plane (viewed from upstream) for three simulations: (left) low exit pressure; (middle) high exit pressure; (right) high exit pressure with potential field caused by vanes. Dashed lines indicate swirler centerlines.*

The first row of Figure 3.11 shows contours of the corrected swirler total pressure loss coefficient, $C'_{p,\mathrm{sw}}$. Comparing the low back-pressure case (column 1) to the high-pressure ones (columns 2 & 3), no obvious difference in the loss is apparent, and the distribution of the flow features matches well. This is consistent with the earlier argument that at subsonic speeds, the loss coefficient is expected to scale only with the Reynolds number (which is identical for all three cases). The mass flow averaged total pressure loss coefficient is 0.485 for the low pressure case, 0.479 for the high pressure case without vanes and 0.466 for the case with NGVs (also at high back pressure). Here it should be noted that the back-pressure for the second case was set based on the combustor pressure from the third case, which was simulated with atmospheric exhaust pressure (but with vanes), allowing the back-pressure in the combustor simulator to develop naturally. With both Re and M matched, any differences between cases two and three are thus due to potential field effects only. Compared to case 2, the mass flow average total pressure loss coefficient of the k–ϵ simulation is 2.7% lower for case 3. Reduced losses might be expected with a favorable pressure gradient [145], but the result is inconclusive noting variability in loss prediction depending on the grid refinement level.

The second row of Figure 3.11 shows the non-dimensional total temperature (or effectiveness), η^*_{corr}. Whilst the distribution is virtually identical for cases 1 and 2, the prediction for the third case exhibits enhanced coolant penetration at the hub, which is thought to be associated with the differing annulus line. This is also reflected by the corresponding loss profile for the case with NGVs, which—due to coolant penetration—features a slightly thicker high total pressure region towards the hub.

The third and fourth rows of Figure 3.11 show the swirl angle, α, and pitch angle, β, respectively. The flow-angles seem unaffected by the Mach number difference, with nearly identical distribution of swirl and pitch angle for cases 1 and 2.

When considering the case with NGVs (column 3), it is evident that the potential field dominates the flow-angles at the reporting plane. Features are periodic in accordance with the vane locations, not those of the swirlers. Relative to the case with low back pressure, the area-averaged swirl angle is lower by 2.5°. This leads to increases of the same magnitude in the incidence angle to the NGVs (see swirl angle sign convention in Figure 3.1).

Turning our attention to the pitch angle (bottom row), a slight deviation from the cases without vanes arises due to two distinct effects. First, the annulus downstream of the reporting plane differs between the two domains, contracting further for the case with vanes (see annuli comparison in Figure 3.4). Even though the flow path up to the reporting plane is almost identical, the potential

field of the contracting NGV end walls cause the pitch angle to respond upstream. The second effect is the potential field of the vane airfoils, generating circumferentially periodic heterogeneities of the pitch angle. These are however less prominent than the azimuthal variations witnessed for the swirl angle, as already noted in a similar study [129].

3.9 Circumferential flow migration

Clocking of NGVs relative to the swirlers has previously been shown to affect the heat transfer and aerodynamic performance under lean-burn stage inlet conditions [106]. In designs with integer NGV-to-swirler count ratio, the question of optimum circumferential clocking position arises. Here the definition of circumferential position must be carefully considered, however, as there are two mechanisms by which circumferential migration of the vortex center between the swirler exit and the reporting plane can occur, leading to a difference between the geometric and effective positions. The first is the well-known potential field migration effect [129]. The second is due to net circulation around the machine axis due to net vorticity of the flow. Each effect is now briefly described.

The potential field effect is—simplistically—the migration of the vortex along the streamline pattern set up by the NGVs, though of course in any sophisticated analysis there is some degree of interaction of the two potential fields. In [129], this effect is described for the leading edge and passage-aligned clocking configurations. This effect is also shown in the simulations of Figure 3.11: for the case with the vane potential field (right column) there is a significant reduction in average swirl angle, resulting in increased incidence to the vanes.

The migration effect associated with net-circulation appears not to have been discussed in the literature. Here we refer to net circulation around the machine axis (i.e. non-zero mass average circumferential velocity) resulting from the net angular momentum of the field of individual vortices. As the vortices mix out (intra-vortex free shear or vortex-vortex interactions) this can lead to migration around the annulus. There are three contributing mechanisms for this effect, which we develop arguments for in Appendix 3.B.

Exaggerated trends of the anticipated trajectories resulting from the potential field effect in isolation, as well as in superposition with net circulation are illustrated in Figure 3.1b.

3.10 Numerical study on circumferential flow migration

In experimental data the vortex migration effect can only be inferred from the flowfield at the reporting plane: the circumferential location of the loss peak and the deformation of the thermal wake, for example, which are offset from the swirler centerline by 3° to 4° (CCW VFU). In CFD,

however, the location of maximum pressure loss does not always coincide with other vortex identification criteria such as the Q-criterion, or the peak turbulence intensity. To provide insight into the relationship between these identification criteria, and the likely flow migration in practice, the circulation effect was investigated using CFD by calculating the mean circumferential flow migration between the settling plenum and the reporting plane from a parameter we call the *bulk yaw angle*, α_{bulk}. We define α_{bulk} as the ratio of the mass flow averages of the circumferential and the axial velocities (as opposed to the mass average of the yaw angle, which is not conservative)

$$\alpha_{\text{bulk}} = \arctan \frac{\int \rho V_x V_\theta dA}{\int \rho V_x V_x dA} \tag{3.11}$$

where ρ is the fluid density, V_x the axial velocity and V_θ the circumferential velocity (both in the machine reference frame). The integral is performed over a plane dA with an axial normal direction. The circumferential migration between two axial planes can then be calculated by integration:

$$\Delta\theta(x) = \int_{x_1}^{x_2} \left[\frac{\tan \alpha_{\text{bulk}}}{r_{\text{ref}}} \right] dx \tag{3.12}$$

where $\Delta\theta$ is the cumulative change in circumferential machine coordinate, x_1 and x_2 are the axial coordinates of the planes, r_{ref} is a constant reference radius (equal to 360 mm), and α_{bulk} is the bulk yaw angle. The term in square brackets is recalculated at each sampling plane. The expression can be discretized as required.

Figure 3.12 shows the circumferential migration, $\Delta\theta$, as a function of the axial coordinate, relative to the NGV leading edge (at x/C_{ax} = 0) for the CFD simulations with the k–ϵ turbulence model (best similarity to experimental results). Results are shown for the three test cases in Table 3.3. An additional test case was performed with the diffuser removed to investigate its impact on flow migration.

Positive values represent migration in the counter-clockwise (CCW) direction, when viewed from upstream (VFU). For all cases with a diffuser, a positive bulk yaw angle (positive gradient of $\Delta\theta$) initially develops in the swirler passages (x/C_{ax} between −11 and −10; see Figure 3.12), where free-shear dissipation within each vortex contributes to net circulation. Surprisingly, the expected direction of migration persists only until approximately mid-way through the diffuser passage (approximately $x/C_{\text{ax}} \approx -9$; see Figure 3.12), where the bulk circumferential flow direction changes from CCW VFU to clockwise (CW) VFU. This behavior is explained by a net negative circumferential pressure gradient (i.e. pressure tending from positive to negative in the

CW VFU direction) that develops within the diffuser. The origin of this is not clear, but it appears to be associated with asymmetric interaction of the vortex with the left-hand and right-hand radial walls of the diffuser, following initial migration of the vortex core. What is surprising is that the vortex is turned from CCW VFU, through a stationary point, to CW VFU. This could be explained by the potential field being primarily *developed* in the higher Mach number upstream region, but persisting even into the lower Mach number downstream region (result of diffusion), where the flow has the ability to be overturned as a result of its lower axial momentum. We coin the term 'vortex reflection' to describe this behavior. Once the flow exits the diffuser, the vortex–vortex and intra-vortex free shear appears to result in transfer of individual vortex angular momentum to net circulation around the annulus. This results in a monotonic increase in α_{bulk} for $x/C_{\mathrm{ax}} > -7$, which results in an increase in the gradient of $\Delta\theta$, ultimately resulting in net circulation reversal between $x/C_{\mathrm{ax}} = -4$ and -1, depending on the test case.

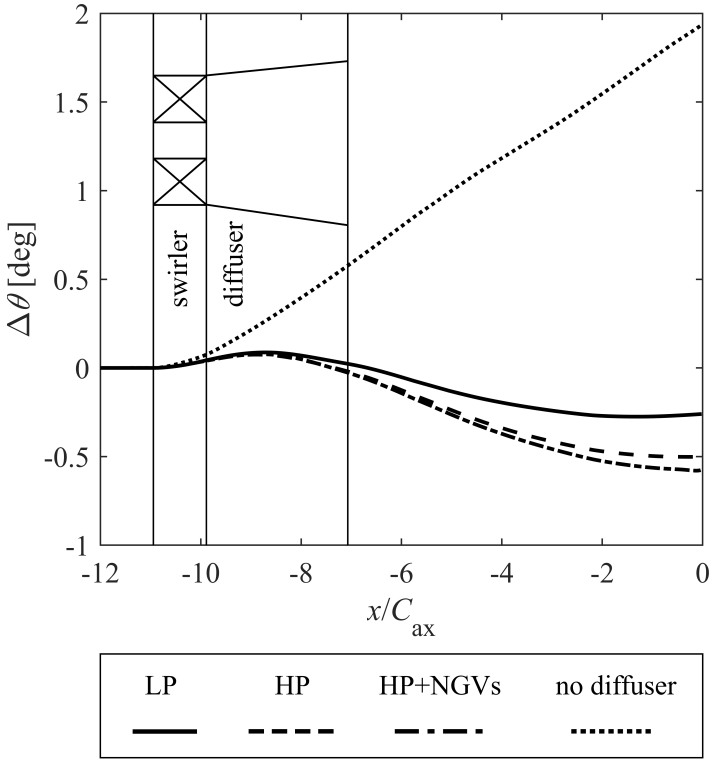


Figure 3.12: *Circumferential flow migration calculated from integral of bulk yaw angle (α_{bulk}) for the k–ϵ turbulence model for: low back-pressure; high back-pressure; NGV test case (with high back-pressure); no diffuser.*

Under low exit pressure conditions, the net circumferential flow migration at the reporting plane (x/C_{ax} = −0.5) was approximately −0.25°, i.e. mild migration in the opposite to sense of rotation of the swirlers. For the high back pressure case, CFD predicts −0.50°. This result is approximately the same with and without NGVs, suggesting the vortex migration effect is relatively insensitive to the vane potential field. The swirler Mach number appears to have a mild influence on the net migration.

To understand the influence of the diffuser, an additional low back-pressure CFD case was run with the diffuser removed (using k–ϵ). This is marked as the *no diffuser* case in Figure 3.12. Immediately upon entering the swirler (x/C_{ax}= −11), the flow begins to migrate CCW VFU. An approximately linear CCW trend develops downstream of the swirler, which persists up to the reporting plane and the vane leading edge. Minor inflections in the $\Delta\theta$ trend are caused by the introduction of coolant jets, which cause blockage and an increase in the mean axial flow velocity, both of which decrease the bulk yaw angle. Without the diffuser, the net circumferential migration at the reporting plane was 2.0° CCW VFU, which is equivalent to approximately 0.22 NGV pitch spacings. These values are very large in comparison to the cases with diffuser, highlighting the importance of performing simulations with realistic geometry when designing combustor simulators.

Net circumferential flow migration *as a measure of vortex migration* has the advantage of being a robustly defined parameter (see Equation 3.12) that can be computed at every axial plane. This allows comparisons of migration trends of the form shown in Figure 3.12. It is worth nothing, however, that there are other measures of flow migration (for example, the location of peak Q-criterion, peak turbulence intensity or minimum total pressure) and all of these give slightly different measures of the vortex center location, and therefore the vortex migration. These inconsistencies highlight the complexity of uniquely defining the vortex center.

3.11 Conclusions and recommendations

The design and experimental commissioning of a fully annular lean-burn combustor simulator for the Engine Component Aerothermal Testing Facility at the University of Oxford has been presented. The facility is an engine-parts cascade used for aero-thermal performance analysis of fully cooled nozzle guide vanes, and the combustor simulator allows studies of combustor turbine interaction effects on NGV capacity and aerothermal performance.

The combustor simulator has been characterized by measuring exit flow profiles of total pressure, total temperature, swirl angle, and pitch angle. The measurements were performed by

removing the NGVs and traversing a four-swirlers sector (72°) from downstream. To validate CFD design methods, and provide further insight into the flow mechanisms, complementary CFD studies were performed using k–ϵ, k–ω SST and SSG RSM turbulence models. The general flow profiles at the reporting plane were well-predicted by all methods. The best agreement in absolute total pressure loss, and in coolant stream mixing and swirl profiles was achieved with the k–ϵ model. We recommend this model for future design of similar systems. The SSG RSM model was found to underpredict mixing, compared to experiments, resulting in a different vortex structure at the reporting plane: we conclude that this method is probably unsuitable for design work.

The impact of acquiring profiles without vanes installed was assessed in CFD studies with and without vanes. Changes in back-pressure alone were found to have a negligible impact on the flow, but—as expected—the introduction of the vane potential field caused the area-averaged yaw angle to increase by approximately 2.5° at the reporting plane (located 0.5 NGV axial chords upstream of the NGV leading edge).

To understand design for particular clocking orientations, we study the flow migration effect in some detail. Two effects have been discussed, which include: the vane potential field effect and a net-circulation effect. The first of these effects (vane potential field) was shown to cause a local increase in NGV incidence angles, without significantly impacting circumferential flow migration. The second effect (net circulation) has not been discussed in the literature but results in circumferential flow migration of 0.22 NGV pitches in the absence of a diffuser. For the ECAT CS, the net-circulation effect is largely suppressed by the diffuser, but this is thought to be highly geometry specific. The importance of accurate CFD design simulations with realistic geometry is emphasized by this study.

Both the experiments and simulations suggest that the ECAT combustor simulator achieves a lean-burn-representative temperature distortion and swirl intensity at the NGV inlet plane. The new module will be used for investigating the impact of lean-burn combustion profiles on NGV mass-flow (capacity), overall effectiveness, and aerodynamic performance.

Nomenclature

Roman

$C_{p,\mathrm{sw}}$	Pressure loss coefficient	[–]
D	Diameter	[m]
k_{corr}	Effectiveness correction factor	[–]
$\dot{m}$	Mass flow rate	[kg s^{-1}]
M	Mach number	[–]
p	Pressure (total or static)	[Pa]
q	Dynamic pressure	[Pa]
Re	Reynolds number	[–]
r	Radius	[m]
S	Swirl number	[–]
t	Time	[s]
T	Temperature	[K]
V	Velocity magnitude	[m s^{-1}]
V_r	Radial velocity	[m s^{-1}]
V_x	Axial velocity	[m s^{-1}]
V_θ	Circumferential velocity	[m s^{-1}]
x	Axial coordinate	[m]
y^+	Normalized wall distance	[–]

Greek

α	Swirl angle	[°]
β	Pitch angle	[°]
δ_i	Temporal offset	[s]
η^*	Effectiveness	[–]
η^*_{corr}	Corrected effectiveness	[–]
θ	Circumferential coordinate	[°]
μ	Dynamic viscosity	[Pa s]
ρ	Density	[kg m^{-3}]
σ	Standard error	[variable]

Subscripts

0	Total property
1	Quantity measured at plane 1
2	Quantity measured at plane 2
3	Quantity measured at plane 3
c	Cold stream inlet
exit	Vane exit
h	Hot stream inlet
m	Property as measured on R57 plane
sw	Swirler property

Appendix 3.A Grid sensitivity study

In this section we consider the sensitivity of the numerical results to the resolution of the computational grid.

Refinement strategy and test cases

The grids with and without vanes were both refined by successively decreasing cell sizes globally. In the combustor simulator, cell sizes (based on approximate edge length) were decreased from 0.80 mm to 0.60 mm to 0.48 mm, resulting in cell counts of 20, 39, and 67 million (respectively) for the case *without* vanes. Corresponding grid sizes for the case *with* vanes were 27, 52, and 87 million. For the low pressure case, grid sensitivity was studied for the k–ϵ, k–ω SST, and SSG RSM turbulence models. The grid sensitivity study for the case with NGVs was completed for the k–ϵ model only.

Low pressure case grid sensitivity

Variables of interest are the swirl/pitch angle distribution, loss coefficient, and temperature profile at the reporting plane. Our preliminary analysis showed that temperature and pitch angle were relatively insensitive to mesh refinement. We therefore report only the—more critical—loss and swirl angle distributions. Reporting plane profiles of the loss coefficient (Equation 3.10) and the swirl angle (Equation 3.7) are shown in Figure 3.13 for the k–ϵ, k–ω SST, and SSG RSM models.

For k–ϵ, some grid-sensitivity of loss coefficient can be seen, with mass-flux-averaged loss ranging between 0.497 (20M cells) and 0.485 (67M cells). For swirl angle, the first refinement step (20M to 39M) caused the vortex to move radially downward, whereas the profiles for the intermediate (39M) and most refined mesh (67M) are essentially identical. This suggests that the intermediate and most refined grids are adequate for k–ϵ.

For k–ω SST, mass-flux-averaged loss varies between 0.463 (67M) and 0.468 (20M). The radial profiles of the loss coefficient are generally similar, with a gradual reduction in loss around midspan as the mesh is refined. Area averaged y^+ values range between 1.52 (20M) and 0.93 (67M) with a maximum around 6.6 for all three cases. Despite the relatively high degree of mesh refinement, the swirl angle profile does not appear to be fully grid independent, with differences of approximately 1° for the maximum and minimum swirl angles between subsequent refinement steps.

For SSG RSM both the loss and swirl profiles changed significantly between both refinement steps. Mass flux averaged loss changed from 0.535 (20M) to 0.499 (67M cells). Swirl angle extrema changed by as much as 5°.

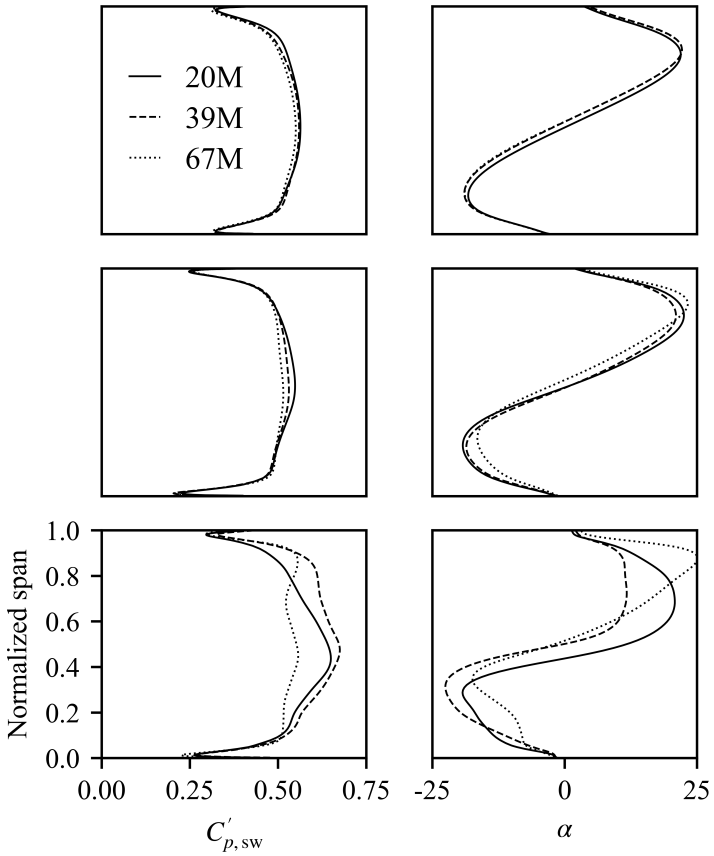


Figure 3.13: *Grid sensitivity of the loss coefficient, $C'_{p,\mathrm{sw}}$, and the swirl angle, α, at the reporting plane for the low pressure case using the k–ϵ, k–ω SST, and SSG RSM models.*

Overall, the grid sensitivity study shows that even for relatively fine grids, neither k–ω SST or SSG RSM achieve the same degree of grid independence as the k–ϵ model. This demonstrates the challenges of simulating this type of flow.

Case with vanes grid sensitivity

Reporting plane profiles of loss coefficient and swirl angle for the case with vanes using k–ϵ are shown in Figure 3.14. The mass flux averaged loss coefficient ranges between 0.470 (27M) and 0.466 (87M). The swirl angle profiles are effectively identical, with all three solutions falling within 0.5° of each other.

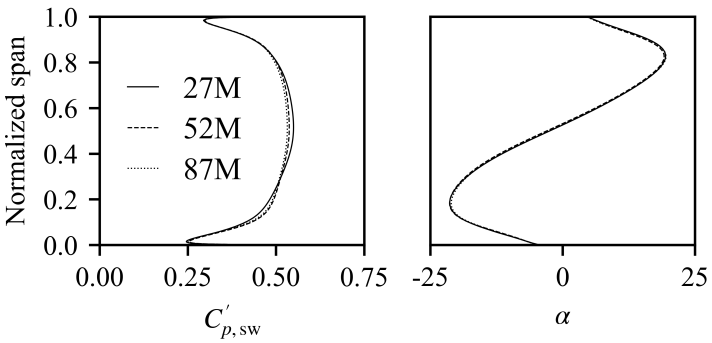


Figure 3.14: *Grid sensitivity study of the loss coefficient, $C'_{p,\mathrm{sw}}$, and the swirl angle, α, at the reporting plane for the case with NGVs using the k–ϵ turbulence model.*

Appendix 3.B Effect of net-circulation on flow migration

Effect 1: Conservation of angular momentum about machine axis

Imagine an annulus with N discrete swirlers, A, B, C ... N, as shown in Figure 3.15. We argue as follows:

1) Swirler applies torque on the flow giving rise to net angular momentum both about the individual swirler axes A, B, C, etc. and—as a consequence—about the machine axis x.

2) If the vortices suffer no internal (free shear), or external (wall) shear, and noting there is net angular momentum about the machine axis, it is possible for the vortices to persist indefinitely along an axial path S_1.

3) As the vortices interact and mix out, the angular momentum terms associated with individual decaying vortex cores (A, B, C etc.) reduce (no local conservation required). The angular momentum about the machine axis must be conserved. As individual vortices decay the entire flow must therefore start to rotate about the machine axis. The mean flow therefore follows trajectory S_2, not S_1.

4) In the absence of external shear & pressure, the flow initially mixes out such that it satisfies the convention of angular momentum about x, and radial equilibrium.

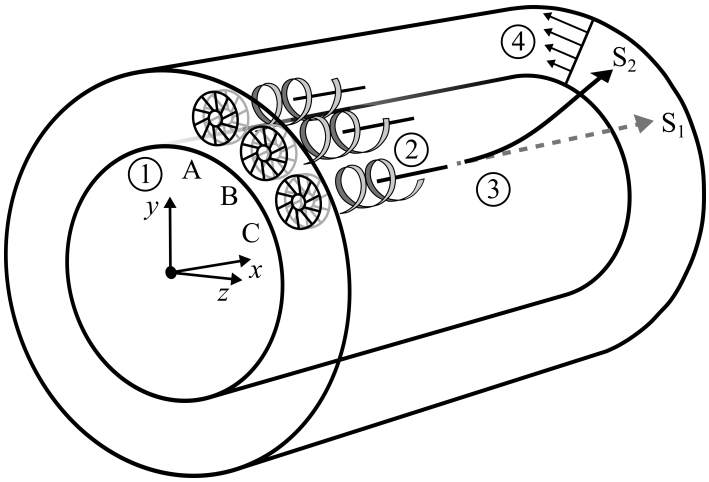


Figure 3.15: *Net migration due to the conservation of angular momentum alone.*

Effect 2: External shear

Now consider the same problem but with wall shear forces acting on the vortices, as shown in Figure 3.16. We argue as follows:

1) During the decay process, external shear (hub and case walls) acts both with (τ_2) and against (τ_1) the direction of net rotation. The direction (+ or −) of this secondary influence on net migration is ambiguous.

2) In the "initially mixed" state, the external shear forces τ_3 and τ_4 both act to oppose the net migration. The secondary influence of external shear is to reduce net migration. The path is changed from S_2 to S_3.

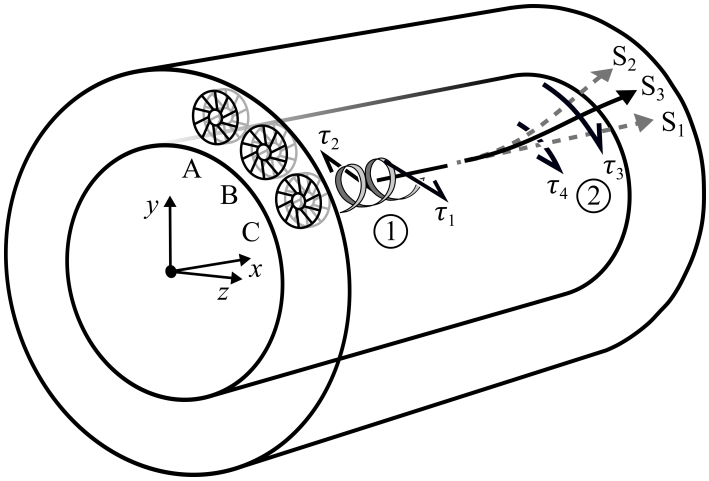


Figure 3.16: *Influence of wall shear on net migration.*

Effect 3: Pressure distribution in diffuser

Finally, consider an effect associated with the swirler diffuser (if present), the geometry for which is illustrated in Figure 3.17. We argue as follows:

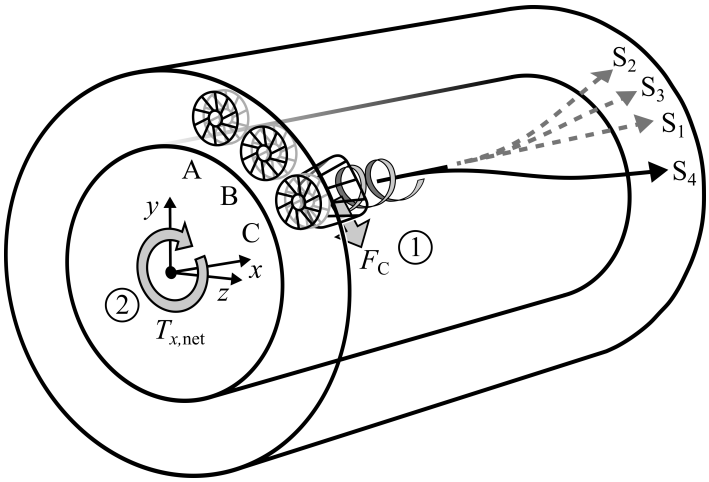


Figure 3.17: *Effect of diffuser on net migration.*

1) If the swirler is provided with a diffuser, the interaction of the individual vortices with their respective diffuser walls will, in general, give rise to pressure thrust terms F_{A}, F_{B}, F_{C}, etc.

2) Circular symmetry implies that the net force (entire annulus) in the z–y plane (see diagram) on the entire flow is zero, but in general there could be a net axial thrust F_x and a net torque about the machine axis, $T_{x,\mathrm{net}}$. This may result in a full reversal of the general trend described under effects 1 and 2, changing the trajectory from S_3 to S_4.

4 | Ultra-compact traverse system for transonic annular cascade

This chapter describes the design and commissioning of an ultra-compact traverse system for the Engine Component Aerothermal (ECAT) facility at the University of Oxford, an engine-parts facility operating at engine-representative Mach and Reynolds numbers. The traverse system was required to be unusually compact to integrate within an existing upstream cassette system. The system has been used to perform detailed surveys of inlet total pressure, temperature, flow angles, velocity, and turbulence. The design and commissioning are described in detail. Example data is also provided. It is hoped that the novel design will be useful for other engineers involved in facility design.

Context with other chapters

An ultra-compact traverse system was designed with the purpose of characterizing the mean-flow and turbulence generated by the lean-burn combustor simulator of Chapter 3, and by a generic turbulence grid (see Chapter 5). This data feeds into performance analyses of NGV under uniform and lean-burn-representative inflow—considered in Chapters 6 and 8, respectively—where it serves as reference conditions for experimental data taken *downstream* of turbine vanes, and as inlet boundary conditions for complementary simulations. The measurements of the turbulence grid flow uncovered a mild circumferential non-uniformity, which motivated the redesign of the ECAT facility flow conditioning system described in Chapter 5.

Publication status and co-author contributions

The chapter takes the form of a *peer-reviewed conference paper*, which has previously been presented at the Global Power and Propulsion Society Chania22 conference in Chania, Crete, Greece [5]. The DPhil candidate was responsible for the mechanical design, and commissioning of the traverse system, as well as data processing and paper writing. Thomas Povey supervised all aspects of the work. A statement of authorship is included at the end of the document.

4.1 Introduction

The Engine Component Aero-Thermal (ECAT) facility [121] is a nozzle guide vane (NGV) test facility designed to characterize the aero-thermal performance of engine parts. The facility operates at engine-matched Mach and Reynolds numbers and has been used for studies of NGV capacity [136], heat transfer [146], and aerodynamic performance [147, 137]. The inlet flow can be conditioned to be uniform in total temperature and pressure, or to operate with an upstream combustor simulator [121]. For heat transfer testing the facility can operate at mainstream-to-coolant temperature ratios of 1.2 using air heaters, or ratios up to 2.0 using a secondary heated-tank supply system [131].

The facility operates in semi-transient blow-down mode, with air stored initially in air receivers at 27.5 bar. Large civil engine stages can be operated at steady state conditions (achieved using pressure regulators upstream of a choked nozzle) non-dimensionally matched to the cruise condition for approximately 60 seconds. This mode of operation is used for traverse measurements. It is also possible to operate the facility in blow-down mode, in which the operating condition (Mach number) varies through a range of quasi-steady states during a 60 second period (see work by Kirollos et al. [121]): this mode is typically used for measuring NGV capacity characteristics.

The NGV inlet conditions are measured approximately three axial chords upstream of the NGV leading edge, using probes mounted in a radial-cassette system (four equally spaced cassettes). This is illustrated in the meridional view of Figure 4.1a (build configuration showing the combustor simulator).

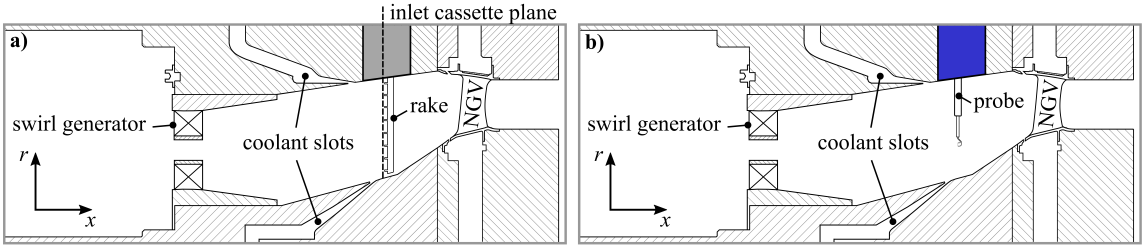


Figure 4.1: *Meridional view of the ECAT facility test section with: (a) the rake-fitted cassette installed; (b) the new upstream ultra-compact cassette-based traverse system installed.*

Each cassette can hold up to 4 rake probes, with typically eight measurement points per probe for total pressure or temperature. Offset probes have been used to increase the effective radial resolution to 16 points. This data is used to set the row pressure ratio, and to establish the temperature boundary conditions for overall effectiveness measurements. When operating with non-uniform inlet conditions (temperature distortion and swirling flow) traverse measurements have been performed using a hub-mounted downstream traverse system (see Burdett and Povey

[147], Kirollos et al. [121], and Michaud et al. [137]). This system has the advantage that it can be used to survey the entire 360° annulus (in 40° segments), but the disadvantage that it necessitates removal of the NGVs to survey the inlet cassette plane, shown in Figure 4.1a. Because of the highly haded endwalls, near-wall measurements are complicated in this measurement configuration, and swan neck probes are required. This paper describes an upgrade to that system: the development of an ultra-compact cassette-based traverse system for the NGV inlet flow. This two-axis motorized r–θ traverse system is shown in Figure 4.1a, and operates over the complete radial range of the annulus, and with a circumferential range of 35°. Example data is presented in later sections.

4.2 Literature review

In this section, the literature relating to traverse systems for annular turbomachinery experiments is briefly reviewed.

In very short duration facilities (< 1 s), probe response times often mandate fixed-position instrumentation. To build up an area-survey it is common to use indexable rakes (Adams et al. [62]; Atkins et al. [148]; Cernat and Lavagnoli [149]). These are typically manually repositioned in-between runs.

Facilities with longer run times generally use automated traverse systems, allowing finite areas to be surveyed with a single probe in a given run. Several systems have successfully deployed rotating stators paired with a radial traverse system (Dahlqvist et al. [150]; Wolf et al. [151, 91]). In the Test Turbine Rig at KTH Stockholm (Dahlqvist et al. [150]), stator rotation was achieved by attaching the stator disc to a hollow shaft, concentric with and opposite the rotor shaft.

An alternative way of achieving circumferential movement is via a rotating casing. For example, the Purdue Small Turbine Aerothermal Rotating Rig (Cuadrado et al. [152]) uses an electric linear actuator to turn a ring on which are mounted three independent radial traverse gears. The Purdue Big Rig for Aerothermal Stationary Turbine Analysis (Bhatnagar et al. [153]) may also broadly be classified as a rotating casing facility, even though only a small brass carriage moves circumferentially. The carriage is guided by a track and is powered by an industrial robotic arm. Both Purdue facilities feature an additional axis for yawing the probe. A rotating casing ring, driven via a worm gear, was implemented in the 4-stage turbine facility at RWTH Aachen (Bohn et al. [154]), although in this implementation four rakes (spaced at 90° intervals) were used instead of a dedicated radial axis. The Air Force Research Laboratory Turbine Research Facility (Anthony and Clark [155]; Barringer et al. [69]) uses the same approach.

Hub mounted systems have been used in the ECAT facility (Burdett and Povey [147]; Kirollos et al. [121]; Michaud et al. [137]), the von Karman Institute CT3 facility (Sieverding and Arts [156]) and the Chalmers University LPT-OGV facility (Jonsson et al. [157]; Jonsson [158]). The existing ECAT facility downstream traverse system (Michaud et al. [137]) mounts onto a backing plate downstream of the NGV ring. The system features a large central bearing on the machine axis, around which the traverse system rotates. A separate linear motion unit allows radial motion. The system was primarily designed for downstream surveying but has been used for inlet surveying with the NGV ring removed. The CT3 facility (Sieverding and Arts [156]) at the von Karman Institute is equipped with a similar system, but with the distinction that the probe is introduced radially through a hole in a rotating hub exit duct, with rotation actuated by pneumatic piston instead of a geared stepper motor. The LPT-OGV facility (Jonsson [158]) hub-mounted traverse uses a large disc mounted on a geared ring guide with four individually controllable radial traverse axes. The facility also features an independent downstream traverse system, using an ABB IRB-1400 6-axis robotic arm to directly manipulate probes, as well as a radial and axial traverse system, introduced from the casing.

Two designs with some similarity to the present system are those used in the Oxford Cold Heat Transfer Tunnel (CHTT) (Martinez-Botas et al. [159]), and the new Next Generation Turbine Test Facility (NGTurb) at the German Aerospace Center (Krumme et al. [90]). In the CHTT the traverse system was integrated into an upstream cassette, with the radial traverse gear inside the pressure vessel, driven circumferentially by a piston attached to the cassette exterior. The inner radial gear was mounted on a carriage constrained to move in an arc by two circular slots. The NGTurb facility uses a similar concept, with fixed and eccentric cam rollers running inside a circular slot.

Commercial traverse systems for cylindrical coordinate frames are offered by Aerodyn Ltd, Rotadata Ltd, and Quadratec Ltd. Several patents for turbomachinery traverse systems have also been registered (Mashburn et al. [160]; Singh et al. [161]; Wittig [162]). A top-mounted cassette allowing for 3-axis rectilinear motion as well as probe pitch and yaw is summarized by Wittig [162]. The system is intended for radial operation in turbomachinery, but it is noted that only a limited circumferential range is accessible with this design. The traverse gear patented by Mashburn et al. [160] is a hub-mounted system, allowing for radial, and circumferential motion as well as probe yaw. It features an aperture for passing a rotor shaft. A generic rotating casing, driven via a ring gear mechanism is described by Singh et al. [161].

4.3 Traverse plane location

The axial location of both the existing cassette-based rakes and the new traverse system (subject of this paper) was approximately three axial chords upstream of the vane leading edges (see Figure 4.1). Here the flow is relatively unaffected by the vane potential field, allowing the same traverse data to be used—with a high degree of accuracy—for vanes of similar aerodynamic design in any clocking position, provided there is limited change in the downstream annulus line.

4.4 Traverse system overview

The new cassette-based traverse system is shown in Figure 4.2. Two custom linear motion units driven by stepper motors allow for radial and circumferential motion of the carriage frame and probe (see Figure 4.2). To translate linear motion into cylindrical motion, the radial gear assembly is mounted on a four-wheeled carriage frame assembly that is guided by circular-arc slots machined into the inner walls of the lower cassette assembly. The interface between the carriage frame and the lower cassette is symmetric, allowing the radial gear to be reversed. This extends the total circumferential range from approximately 20° to 35°. The circumferential and radial traverse gear assemblies are connected via a sliding pin-slot arrangement. The two stepper motors have encoders allowing for closed-loop control. The ECAT facility run time is approximately 60 seconds, and therefore the system was designed for relatively high maximum acceleration and velocity, to maximize the traverse area in each run. A particular design challenge was ensuring the cassette was sealed, with a design pressure of 10 bar. This required power cables, probe signals and encoder feedback to be passed through sealed connectors. Key parameters of the traverse system are summarized in Table 4.1.

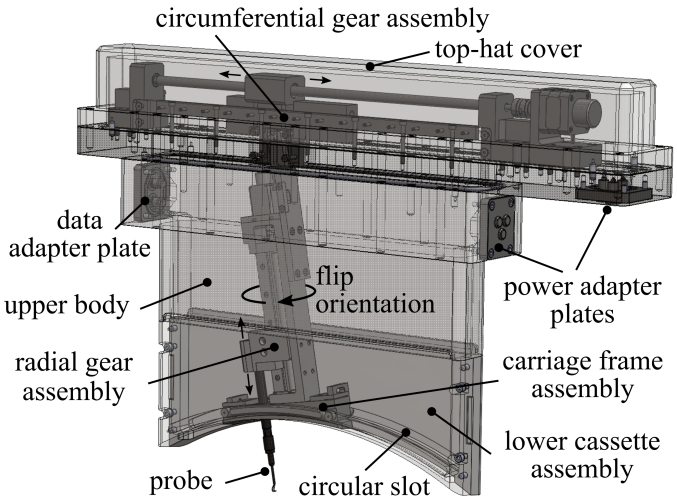


Figure 4.2: *Visualization of assembled traverse showing internal mechanisms.*

Table 4.1: *Details of traverse system.*

Parameter	Nominal value
Angular range (single orientation) [°]	35 (20)
Radial travel [mm]	115
Circumferential axis acceleration [mm s^{-2}]	600
Radial axis acceleration [mm s^{-2}]	300
Circumferential axis velocity [mm s^{-1}]	32.0
Radial axis velocity [mm s^{-1}]	22.5
Circumferential backlash [mm]	±0.2
Radial backlash [mm]	±0.1
Axial backlash [mm]	±0.3
Pressure rating [barg]	10.0
Minimum safety factor at rated pressure [–]	5.7
Assembly mass [kg]	29.7

4.5 Subsystems and interfaces

In this section the traverse assembly is described in greater detail and key design issues are discussed.

Cassette housing assembly

The cassette housing assembly is shown in Figure 4.3a. It is comprised of the upper cassette body (single part with through-slot), and the lower cassette body with two clamshell parts. The interface between the upper and lower cassette (detail A) is a shallow (1 mm) interlocking rail/slot assembly to minimize wall thicknesses in the axial direction (eliminating screws on most surfaces). The internal walls of the lower cassette clamshell parts have circular-arc slots which guide the carriage frame through two pairs of cam rollers (detail B). To ensure accurate alignment, precision machining and dowel-pin assembly was used throughout this assembly. The upper cassette body was made from 6082-T6 aluminium. The lower cassette parts are manufactured from 304 steel.

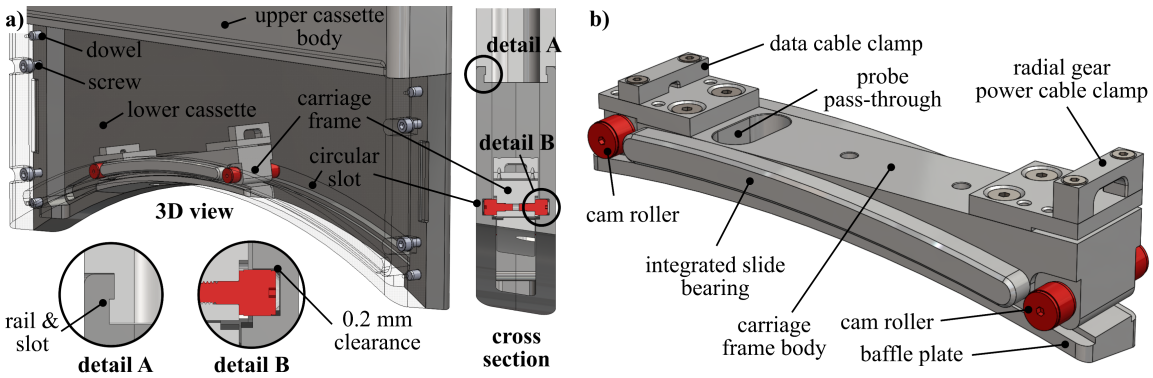


Figure 4.3: *(a) Cassette housing clamshell assembly showing the opposing circular-arc slots and carriage frame assembly with cam rollers; (b) carriage frame assembly close-up.*

Carriage frame assembly

The carriage frame assembly is shown in Figure 4.3b. Four cam rollers (Ø10.00 mm) mate within circumferential slots in the lower cassette housing clamshell. Low radial clearance (0.2 mm; see detail B in Figure 4.3a) between the rollers and slot reduces backlash, but clearance must be sufficient to avoid binding of the cam rollers. Integrated slide bearings along the length of the carriage frame (see Figure 4.3b) constrain axial position within ±0.2 mm. Dry friction at the sliding interface between the integrated slide bearing and the lower cassette is minimized by pairing steel (lower cassette) with phosphor bronze (SAE660; carriage frame). This eliminates the need for lubrication, thus reducing the likelihood of probe contamination. A baffle plate attached to the lower side of the carriage body matches the gas path annulus. Based on the design clearances, the maximum positional probe tip uncertainty was estimated to be ±0.2 mm circumferentially, ±0.1 mm radially, and ±0.3 mm axially. This is within the probe measurement size for all probes used in the ECAT facility.

Radial traverse gear assembly

The radial traverse gear assembly is shown in Figure 4.4a. The sled (see Figure 4.4a) is mounted on a linear guide, and its radial position is controlled via a leadscrew, which is powered by a stepper motor (with encoder). The sled also features a modular probe clamp that can accommodate shafts diameters up to 10 mm. Limit switches serve to set a datum for the incremental encoder and to prevent damage if the control system is incorrectly coded. A stop-block acts as a hard-stop, should the limit switch fail. The radial traverse gear assembly is mounted directly to the carriage frame assembly (Figure 4.3b) and thus follows a circular arc. The interface with the circumferential traverse gear assembly (next section) is a pair of sliding pins (see Figure 4.4a) at the end of the connector arm, that engage with a slot in the circumferential traverse gear.

Circumferential traverse gear assembly

The circumferential traverse gear assembly is shown in Figure 4.4b. A stepper motor (with encoder) drives a sled assembly via a leadscrew. The sled assembly has a vertical slot into which the radial traverse gear sliding pins engage: this is shown in detail C.

Entire traverse assembly

A photograph of the entire traverse gear assembly is shown in Figure 4.4 (c), with one of the lower cassette body clamshell parts removed to expose the internal systems. The phosphor bronze carriage frame assembly and radial traverse gear are clearly visible. The reversible asymmetric

head (to extend the circumferential range) can also be seen. The entire assembly has a mass of approximately 30 kg.

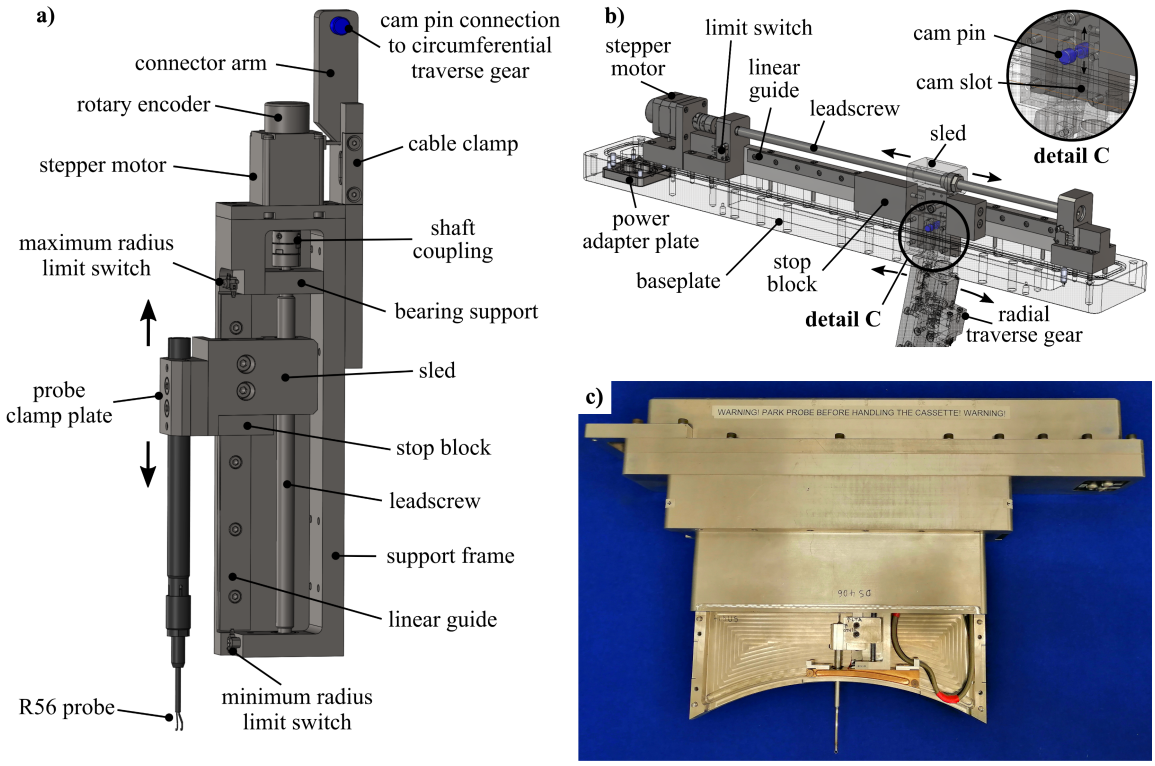


Figure 4.4: *(a) radial traverse gear assembly showing the sliding pin interface with the circumferential traverse gear; (b) circumferential traverse gear assembly showing the sliding pin interface with the radial traverse gear assembly; (c) photograph of the entire traverse assembly with one lower cassette body clamshell part removed to reveal the carriage frame assembly and radial gear.*

4.6 Traverse electronics and control

Traverse system electronics box

The power supplies, stepper motor drives, encoder wiring and limit switch wiring were integrated into a bespoke 19 inch rack unit, which runs as a module along other ECAT facility control equipment. The stepper motors are driven by a 300 W (48 V) switch mode power supply unit. Limit switches operate at 24 V. Encoder signals (5 V) are interference protected using braid and foil-shielded twisted pair cable. A braided shield around the power and limit switch cables further reduces noise.

Communication and control

The traverse is controlled through a LabView serial interface (115.2 kBaud s^{-1}). LabView reads a user-generated traverse pattern file and verifies that the desired trajectory falls within the operable

range. Before each run, the traverse performs a homing routine to establish a datum for the incremental encoders. The position history and configuration are automatically written to an output text file.

4.7 Experimental methods

Overview of probes

Five probes were used in the first measurement campaign using the new traverse system: R56 and R57 split-fiber probes for turbulence measurement; Kiel and pitot probes for total pressure measurement; and a thermocouple probe for temperature measurement. Photographs of these probes are shown in Figure 4.5a.

The split-fiber probes measure flow inclination and flow velocity on a plane orthogonal to their sensor axis (R56 has a circumferentially-aligned sensor; R57 has a radially-aligned sensor). Together, they yield the mean-flow direction and magnitude, as well as turbulence statistics, including five (of six) Reynolds stresses, integral timescales, and power spectra. An excellent overview of the operating principle of split-fiber probes has been written by Lepicovsky [163].

For pressure measurements, the Kiel probe was used between 6% and 100% span (improved incidence tolerance, but larger size) with the Pitot probe being used between 2% and 6% span (less incidence tolerance, but smaller size). The Kiel and Pitot probes were found (direct calibration) to have time constants of 14 and 10 milliseconds, respectively. The time constant of the thermocouple (K-type; 0.127 mm diameter) was estimated to be on the order of 100 milliseconds (method of Paniagua et al. [139]).

Build configuration for reported data

The most common build configuration for the ECAT facility includes four equally spaced cassette ports in the inlet duct, as shown in Figure 4.5b (see also Figure 4.1). For the tests reported in this paper, two cassettes of fixed rakes were used in addition to the traverse cassette, with a blank cassette in the fourth port. All cassettes are interchangeable. Fixed information is used for scaling and normalization of the traverse data (e.g. to account for small variations in inlet total pressure). The traverse covered a 34.4° sector, between 297.4° and 331.8° clockwise from top dead center (TDC). The build configuration was with a lean-burn combustor simulator, described by Hall et al. [127] and Hall and Povey [92] with the ECAT facility implementation discussed by Kirollos et al. [121]. The combustor simulator can operate with both radial temperature distortion and high inlet swirl. The swirler count was 20, equivalent to 18° sectors.

For the split-fiber and pressure measurements, the traverse was operated with intermittent motion, stationary at each grid point for 0.75 seconds. Radial and circumferential grid spacings were set to 5 mm (at midspan), with radial refinement to 1.5 mm near the walls. Temperature data was acquired during continuous traverse motion at 10 mm s^{-1} circumferentially, which corresponds to an effective circumferential resolution of 3 mm, assuming a 500 ms settling time (equal to five time constants). The radial step size was set to 3 mm over most of the span, and 0.75 mm near the walls in regions of high temperature gradient.

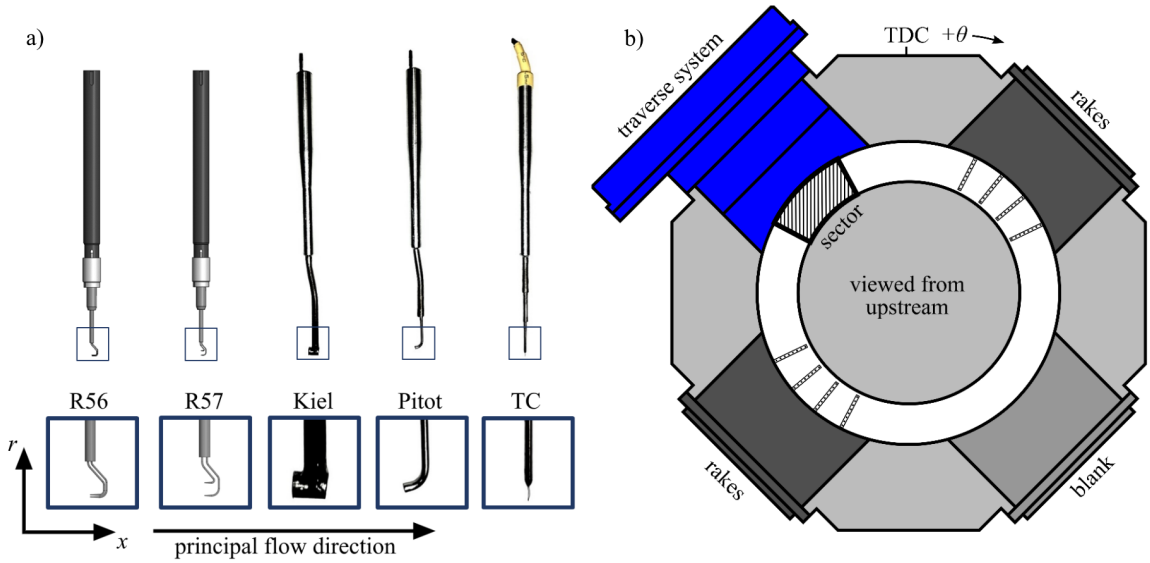


Figure 4.5: *(a) photographs of the five traverse probes used in the first experimental campaign; (b) cassette configuration (viewed from upstream) showing the location of the traverse sector and the fixed rakes; all four cassettes can be interchanged.*

Constant temperature anemometer setup and calibration

The constant temperature anemometry (CTA) method uses a high-frequency electrical feedback loop to maintain a thin wire (high thermal frequency response) at a constant temperature (around 200°C in this experiment), irrespective of the convective cooling flux. Under conditions of constant temperature difference between the sensor and the flow, voltage squared (i.e. power dissipation) is approximately proportional to the square root of the flow Reynolds number (King [164]). With careful calibration, this method can be used to determine the real-time flow velocity.

Because the convective cooling flux scales approximately with the square root of the Reynolds number, the sensor voltage calibration map is expressed as a function of the mass flux (i.e. the product of density and velocity). This ensures that the differences between air pressure during calibration (ambient pressure) and experiments (approximately 1.8 bara) are considered when reducing the data.

The probes were calibrated over an inclination range of ±90° in increments of 5° across 20 different mass fluxes distributed evenly between 6 and 140 kg m–2 s–1. Equations 4.1 and 4.2 are used to translate sensor voltages, E_1 and E_2 into two coefficients, c_1 and c_2, which decouple the effect of flow velocity and flow inclination.

$$c_1 = E_1^2 + E_2^2 \tag{4.1}$$

$$c_2 = \frac{E_2^2 - E_1^2}{c_1} \tag{4.2}$$

The sum of squares of the voltages, c_1, is an expression for the total power dissipation in the sensors and should be a function of the mass flux, ρV, which drives the heat transfer rate (see arguments of Lepicovsky [163]). The coefficient c_2 (difference in the squares of the sensor voltages) is sensitive to flow inclination. Figure 4.6 shows contours of the calibration coefficients c_1 and c_2 as a function of mass flux and the probe yaw angle, α, for the R57 probe. Coefficient c_1 is almost entirely independent of yaw angle and is approximately quadratic in mass flux. The directional coefficient, c_2, is monotonic in yaw angle from –90° to +85°, with limited (undesirable) dependence on mass flux.

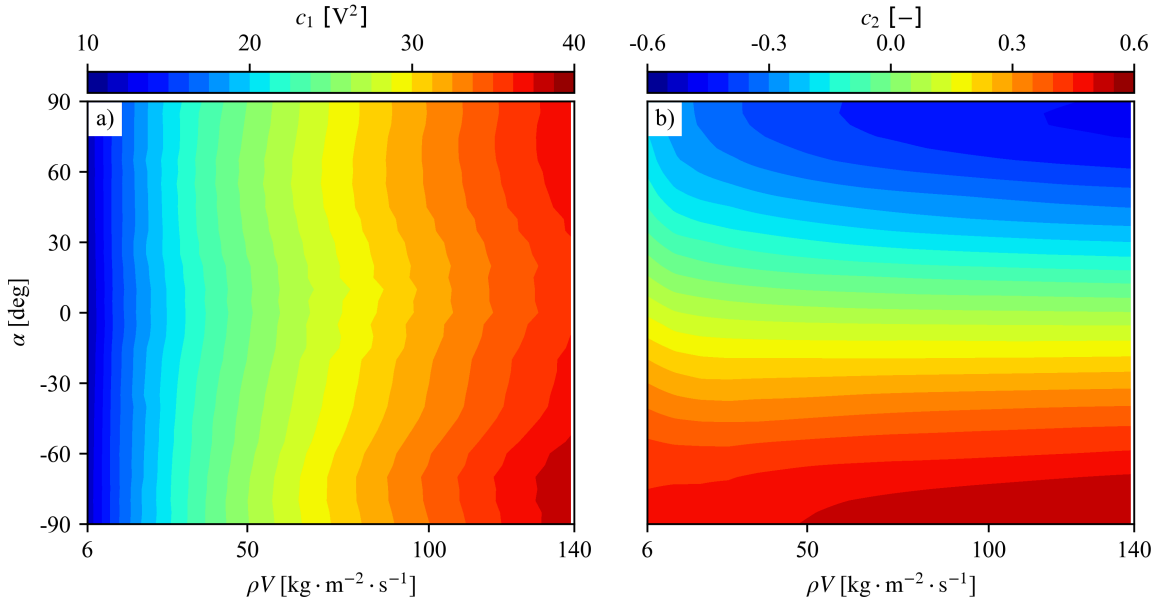


Figure 4.6: *R57 split-fiber probe calibration maps for coefficients: (a) c_1; (b) c_2.*

Hotwire data reduction

CTA data was acquired with synchronous sampling at 250 kHz, using an analog 100 kHz lowpass filter. Small differences in flow temperatures between the facility and calibration environment were corrected for using the Bearman correction method [165]:

$$E_{\text{corr}} = E_{\text{m}} \left(\frac{T_{\text{w}} - T_{\text{c}}}{T_{\text{w}} - T_{\text{m}}} \right)^{b} \tag{4.3}$$

where T_{w} is the temperature of the sensor (independent of the ambient temperature), T_{c} is the flow temperature during calibration, T_{m} is the flow temperature during measurements (from fixed thermocouple rakes), E_{m} is the measured voltage, E_{corr} is the corrected voltage, and b is an exponent for model fitting (nominal value of 0.5 unless calibrated). The time series of corrected voltages is fed into an iterative solver (using a method similar to that described by Lepicovsky [163]) to obtain mass flux and flow angle.

Decomposition & turbulence statistics

Time-resolved flow angles and mass fluxes can be decomposed into axial, radial, and circumferential mass fluxes, as shown in Equations 4.4 to 4.7.

$$\rho V_x = (\rho V)_{\mathrm{R56}} \cos\beta \qquad (4.4) \qquad \rho V_r = (\rho V)_{\mathrm{R56}} \sin\beta \qquad (4.5)$$

$$\rho V_x = (\rho V)_{\mathrm{R57}} \cos\alpha \qquad (4.6) \qquad \rho V_\theta = (\rho V)_{\mathrm{R57}} \sin\alpha \qquad (4.7)$$

Based on the sensor orientation and directional sensitivity, $(\rho V)_{\mathrm{R56}}$ represents the mass flux components on the x–r plane, whereas $(\rho V)_{\mathrm{R57}}$ encompasses the mass flux components on the x–θ plane. The yaw angle, α, and the pitch angle, β, are used to project the probe mass fluxes onto the principal axes. If desired, the time resolved experimental velocities can be recovered by dividing the respective mass flux by the time average density inferred from inlet rake measurements. Reynolds stresses, R_{ij}, can be calculated using Equation 4.8

$$R_{ij} = \frac{\sum_{n=1}^{N} \left(\rho V_i(n) - \overline{\rho V_i}\right) \cdot \left(\rho V_j(n) - \overline{\rho V_j}\right)}{N \left(\overline{\rho_{0,\mathrm{rake}}}\right)^2} \qquad (4.8)$$

where i and j represent the index of three orthogonal components (x,r and θ) and $\overline{\rho_{0,\mathrm{rake}}}$ is the total density inferred from rake measurements. The overbar represents the ensemble average across N samples at each grid point. When $i = j$, the equation reduces to the root mean square of ρV_i divided by the density squared. Since synchronized pairs ρV_x–ρV_r and ρV_x–ρV_θ are available, the Reynolds shear stress terms R_{xr} and $R_{x\theta}$ may also be determined.

The turbulence kinetic energy, k, can be calculated from the sum of the principal stresses (Equation 4.9), which—in combination with the absolute velocity—can be used to determine the turbulence intensity, I (Equation 4.10).

$$k = \frac{1}{2}\left(R_{xx} + R_{rr} + R_{\theta\theta}\right) \qquad (4.9) \qquad I = \frac{\sqrt{2k/3}}{\sqrt{\left(\overline{V_x}\right)^2 + \left(\overline{V_r}\right)^2 + \left(\overline{V_\theta}\right)^2}} \qquad (4.10)$$

Since the both the R56 and R57 probe yield results for ρV_x and R_{xx}, the values were averaged at overlapping points.

Pressure and temperature data processing

Pressure and temperature data were both acquired at 500 Hz. The effective time constants of the pressure and temperature probes were approximately 10 ms and 100 ms, respectively, and therefore the data were low-pass filtered to 100 Hz and 10 Hz, i.e. one time constant. Average pressure at each traverse sampling point was normalized by the ensemble average of the fixed-rake Pitot pressures over the respective sampling period. The traverse temperature measurements were normalized by the filtered instantaneous ensemble average of the fixed-rake thermocouples.

Traverse patterns

The run duration is approximately 60 seconds (Kirollos et al. [121]; optimized for capacity testing, heat transfer testing, and downstream area traverse testing) allowing upstream full area traverse maps to be built up in approximately 20 runs. Figure 4.7a shows the traverse pattern used for pressure and split-fiber probes, and Figure 4.7b shows the traverse pattern for the thermocouple probe. In all, 22 and 20 runs were used respectively.

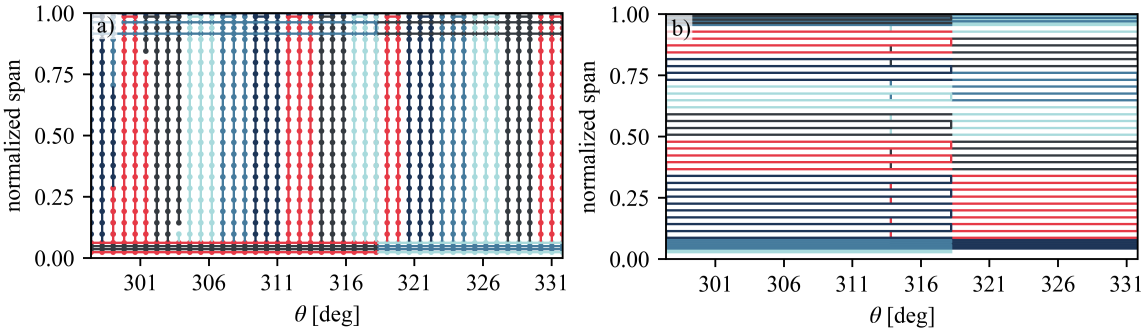


Figure 4.7: *Examples traverse patterns for: (a) split-fiber and pressure probe; (b) thermocouple probe.*

4.8 Sample data

In this section, examples of data collected with the new traverse system are shown. Distributions of axial mass flux, normalized total pressure, yaw angle, pitch angle, turbulence intensity and normalized total temperature are shown in Figure 4.8a–f respectively. The purpose here is simply to show the quality of the data that can be obtained with the traverse.

All six distributions exhibit good resolution, and periodicity at the swirler pitch (18°). In the near-casing region of Figure 4.8a, b and f a region of high mass flux, slightly elevated total pressure (by approximately 2%) and low total temperature can be observed. This is the coolant layer introduced by the combustor simulator, directly downstream of the injection location before

partial mixing with the main flow. Yaw and pitch angle distributions characteristic of a well-behaved vortex (see work by Hall et al. [127] and Hall and Povey [92]) can be seen in Figure 8c and d respectively. The turbulence intensity distribution is shown in Figure 4.8e, with a mean of 15%, and a peak of 24% at a location near the vortex core. Interestingly, turbulence intensity in the coolant jet is low, but with slightly elevated values in the shear layer that develops at the interface with the freestream.

This pilot demonstration of the traverse system shows that detailed flow field maps can be obtained downstream of the ECAT facility combustor simulator, allowing improved understanding of combustor–turbine interaction effects, and more accurate CFD boundary conditions.

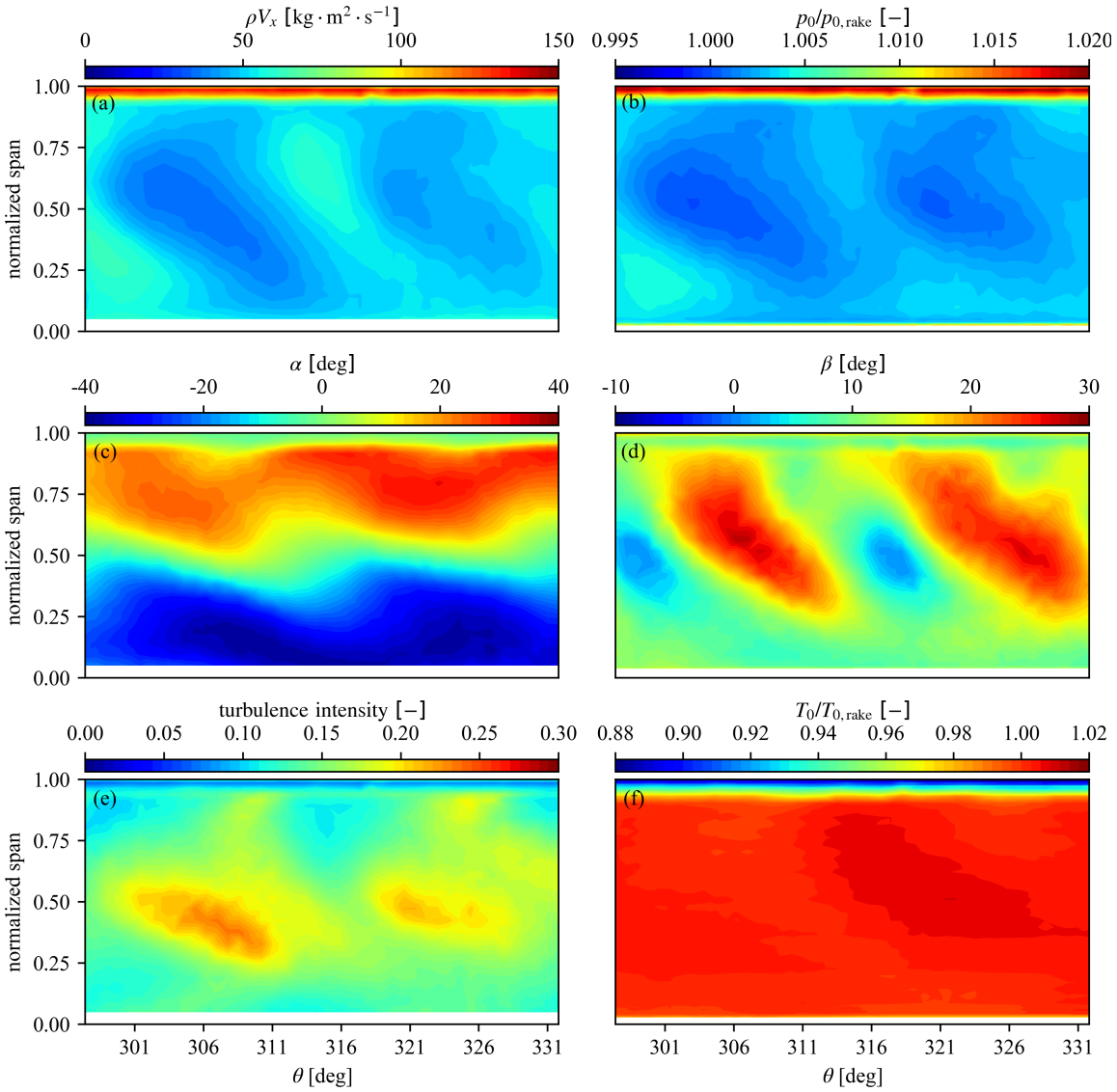


Figure 4.8: *Distributions (viewed from upstream at the inlet cassette plane) of: (a) axial mass flux; (b) normalized total pressure; (c) yaw angle; (d) pitch angle; (e) turbulence intensity; and (f) normalized total temperature.*

4.9 Uncertainty and repeatability

In this section we estimate the bias and precision errors associated with the measured properties.

Bias uncertainty

Let us first consider the bias error of the variables measured by the split-fiber probes (ρV, α, and β). An overview of common sources of error for constant temperature anemometry is given by Jørgensen [166]. For the current setup, the 2σ (95% confidence interval) bias uncertainty of the split-fiber probe local mass flux (ρV) measurement was estimated to be ±3.0%. This arises from the propagated bias uncertainty of the local mass flux during calibration (±1.0%; 2σ; normally distributed) and the uncertainty in the temperatures used for the temperature correction of the voltages (±2.8%; 2σ; normally distributed). The remaining error sources affecting ρV are negligible by comparison: calibration curve-fitting uncertainty was essentially eliminated by measuring the non-linear calibration curve directly at high resolution (20 different mass flux conditions); uncertainty in the gas density was essentially eliminated by calibrating against ρV instead of the velocity; the voltage quantization resolution was 0.15 mV. For the split-fiber-measured flow angles (α and β) the 2σ bias uncertainty was estimated to be ±1.6°. This was calculated by propagation from the combined alignment uncertainty during calibration and testing (both were assumed to be uniformly distributed between ±1.0°).

The bias uncertainty of the normalized total pressure was determined from the standard error of the Kiel/Pitot probe pressure transducers (0.02% of the 2 bar full-scale output or equivalently ±40 Pa), and the standard error of the rake pressure transducers (0.05% of the 5 bar full-scale output or equivalently ±250 Pa). At an operating pressure of 1.80 bara, the 2σ bias uncertainty was ±0.28% of the normalized total pressure.

Finally, we consider the bias uncertainty of the normalized total temperature. The temperature probe uses a specialized thermocouple with a standard error of ±0.37 K (1σ), whereas the rake uses standard K-type thermocouples (±0.73 K; 1σ). At an operating temperature of 340 K, the 2σ bias uncertainty for normalized total temperature was estimated to be ±0.48%.

Precision uncertainty

We now consider the precision uncertainty of the measurements. We calculate standard error using the sample standard deviation and the effective sample size. For the split-fiber probe time-series data, the effective sample size (function of sampling period, sampling frequency, and integral time scale) was estimated using the method of Sciacchitano and Wieneke [167]. For the pressure

probes, the effective sample size is a function of the sampling period, sampling frequency, and probe time constant. The typical estimated 95% confidence intervals for precision error were ±1.7% for mass flux, ±0.9° for flow angles, ±1.2% (absolute) for the turbulence intensity, and ±0.026% for normalized total pressure (5% of mean dynamic head). Temperature precision uncertainty is undefined because the probe moves continuously.

Repeatability in practice

We now benchmark the repeatability of the traverse measurements by comparing two R57 probe datasets. The two datasets were acquired several days apart and were separated by a rebuild of the traverse, including the removal and re-alignment of the probe (see traverse system overview; normal/reversed orientation). Radial profiles of ρV_x, α, R_{xx}, and $R_{\theta\theta}$ are shown in Figure 4.9 for the region of overlap between the normal and reversed cassette configurations (312.6–318.2°). The profiles of axial mass flux and yaw angle are shown in Figure 4.9a, and b, respectively. The agreement between the two datasets is excellent, with maximum differences of 2.4 kg m^{-2} s^{-1} (approximately 5%) and 1.0° respectively. The profiles of the Reynolds stresses R_{xx} and $R_{\theta\theta}$ are shown Figure 4.9c, and d, respectively. The agreement is good for both variables, with maximum differences of 1.8 m^2 s^{-2} (approximately 10%) and 1.0 m^2 s^{-2} (approximately 7%) respectively. As expected, the convergence level of the turbulence statistics is slightly lower than that of the mean flow variables. Overall, the comparison shows excellent repeatability of the traverse measurements in practice, demonstrating good calibration, and well-controlled facility operating conditions between runs.

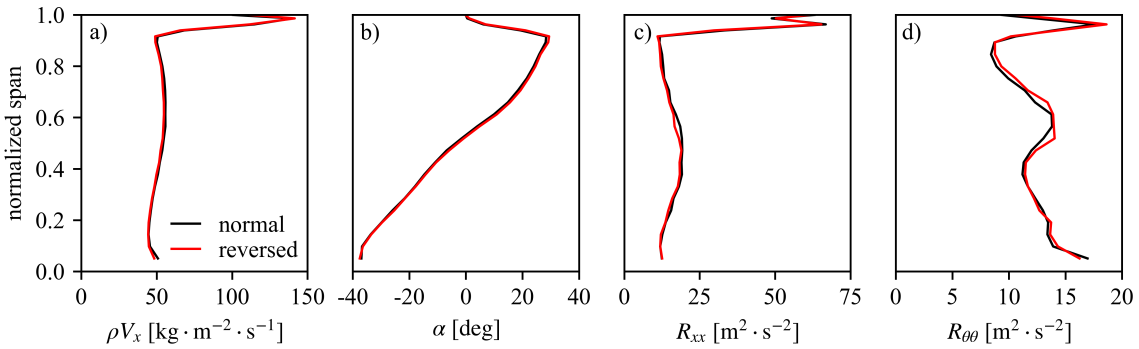


Figure 4.9: *Comparison of datasets from two R57 probes in the range 312.6°–318.2°, measured for normal and reversed cassette configurations: (a) ρV_x; (b) α; (c) R_{xx}; (d) $R_{\theta\theta}$.*

4.10 Conclusions

The design and commissioning of an ultra-compact traverse system to survey the inlet flow of a transonic annular cascade system has been presented. The system is unusual in that it was necessary to accommodate it within a 30 mm axial gap within an existing cassette architecture, and that it had to be rated to a design pressure of 10 bar. With the use of split-fiber, Kiel, and thermocouple probes, it has been demonstrated that the system is capable of delivering high-quality inlet traverse data, acquired across a series of semi-transient (approximately 60 s) runs. It is hoped that the detailed design information will be of use to those designing similar systems for turbomachinery test facilities.

Nomenclature

Roman

c_1	Mass flux coefficient	[V^2]
c_2	Yaw/pitch directional coefficient	[–]
E_1, E_2	Split-fiber sensor voltage	[V]
I	Turbulence intensity	[–]
k	Turbulence kinetic energy	[m^2 s^{-2}]
n	Summation number	[–]
N	Number of samples	[–]
p	Pressure	[Pa]
r	Radial coordinate	[m]
R_{ij}	Reynolds stress	[m^2 s^{-2}]
T	Temperature	[K]
V	Velocity magnitude	[m s^{-1}]
V_r	Radial velocity	[m s^{-1}]
V_x	Axial velocity	[m s^{-1}]
V_θ	Circumferential velocity	[m s^{-1}]
x	Axial coordinate	[m]

Greek

α	Yaw angle	[°]
β	Pitch angle	[°]
θ	Circumferential coordinate	[°]
ρ	Density	[kg m^{-3}]
σ	Standard error	[variable]

Subscripts

0	Total property
c	Value during calibration
corr	Temperature-corrected value
i,j	Indices
m	Measured value during experiments
rake	Ensemble average across the rake
R56	Property as measured on R56 plane
R57	Property as measured on R57 plane
w	Split-fiber sensor property (temperature)

5 | Facility flow conditioning system redesign

The ultra-compact traverse system, described in Chapter 4, was used to survey the mean-flow and turbulence conditions at NGV inlet. Two test section configurations were considered: a lean-burn combustor simulator and a turbulence grid. For the turbulence grid, traverse measurements revealed a mild but undesirable non-uniformity of total pressure, turbulence intensity, and yaw angle at vane inlet. After identifying the underlying causes using CFD, the ECAT facility flow conditioning system was redesigned, with the objective of improving flow uniformity at vane inlet. According to simulations, the modified design approximately halved the spatial non-uniformity of total pressure and turbulence intensity at the NGV inlet plane, whereas the amplitude of yaw angle variations was largely unchanged. The detailed mechanical design and manufacture were led by Matthew Stokes (another student), after the DPhil candidate completed the aerodynamic optimization work.

This *conventional thesis chapter* describes the original design, the causes of non-uniformity at vane inlet, and the steps taken to mitigate these effects. The current improvements were limited in scope, due to financial constraints and time limitations. Recommendations for possible future upgrades to the facility flow conditioning system are discussed at the end of the chapter.

5.1 Original design

In this section, the mechanical design of the ECAT working section and the aerodynamic design of its original flow conditioning system are described. The mechanical design is considered first, because structural elements supporting the working section core are immersed in the main gas path.

Working section mechanical design

Photographs of the original ECAT working section assembly are shown in Figure 5.1. During testing, the working section is suspended from a gantry frame via roller bearing carriages, which run along a guide rail on the underside of the gantry frame main beam (see Figure 5.1a). At a high level, the working section consists of a settling plenum bulkhead (see Figure 5.1b) and a test module (see Figure 5.1c), which are securely bolted together during testing, but independently attached to the gantry frame. When the test module is detached from the settling plenum bulkhead, the test module core (i.e. the assembly of hub components) is suspended from five "axial stiffener struts", which are exposed in Figure 5.1d. This design facilitates the rapid installation, and repositioning of infra-red cameras, which are typically mounted in between the axial stiffener struts.

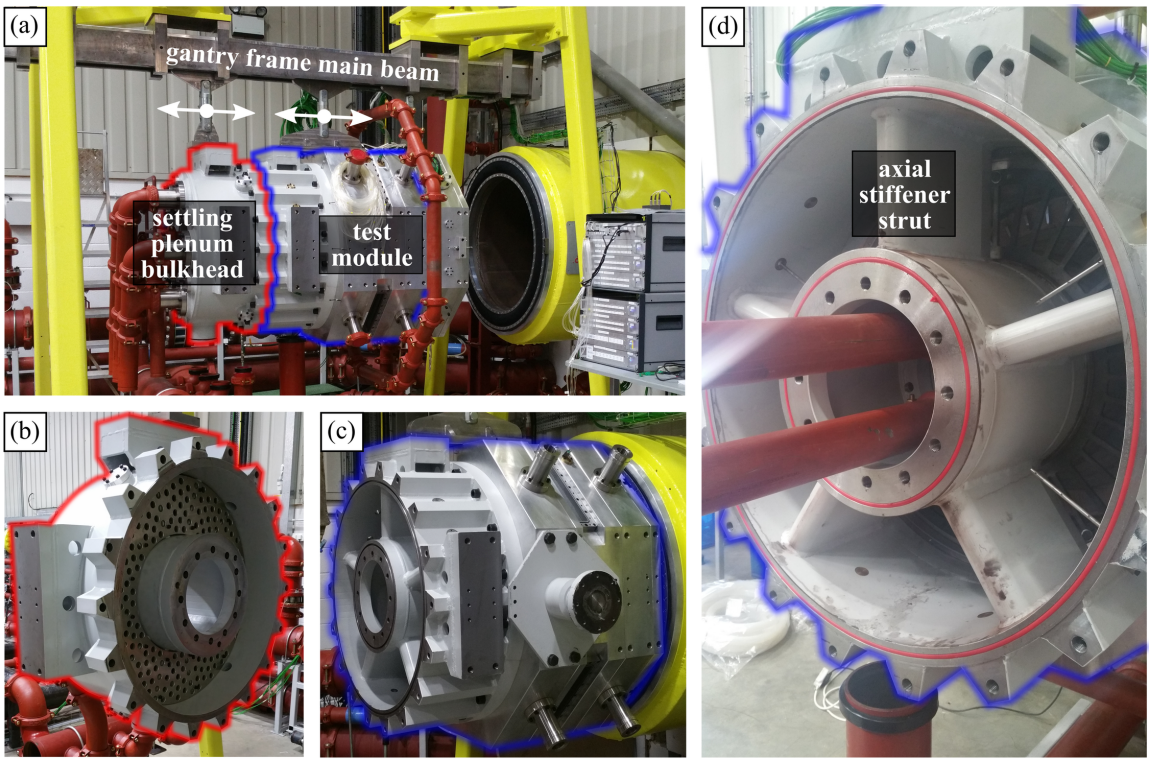


Figure 5.1: *Photographs of the ECAT facility working section: (a) settling plenum and test module; (b) settling plenum; (c) test module; (d) close-up of axial stiffener struts.*

Flow conditioning system aerodynamic design

The original flow conditioning system of the ECAT facility is illustrated in Figure 5.2, showing a meridional view (top) and a three-dimensional cutaway view (bottom). The mainstream flow enters the working section through six "injectors", which feed into a settling plenum. Twelve structural "ribs" divide the settling plenum into alternating compartments *with* and *without* injectors. Each rib features a "window", allowing the settling plenum flow to freely distribute around the annulus. The flow is subsequently ejected from the settling plenum through a "perforated plate", which is mounted axially onto the ribs. Downstream of this location, the five "axial stiffener struts" suspend the working section core by the casing (see also Figure 5.1d). Finally, the flow passes through a "turbulence grid" consisting of 40 radial bars (matching the number of NGVs), before accelerating through a combustor-like contracting duct towards the NGV.

It is recalled that the axial stiffener struts are necessary because the working section is assembled in two main parts, which need to *individually* support their respective cores. The two-part design was largely mandated by the system requirement to rapidly access the axial stiffener region to install and reposition infra-red cameras during testing. Placing additional perforated plates *downstream* of the axial stiffener struts was not an option, considering optical access requirements.

In the course of a CFD analysis of the flow conditioning system, profiles at five axial stations are considered. These are indicated as planes 0, 1, 2, 3, and 4 in the meridional view of Figure 5.2. Experimental measurements using the ultra-compact traverse system (UCTS; see Chapter 4) were carried out at plane 4. Photographs of the hardware are shown in Figure 5.3, with individual parts highlighted according to the color scheme from Figure 5.2.

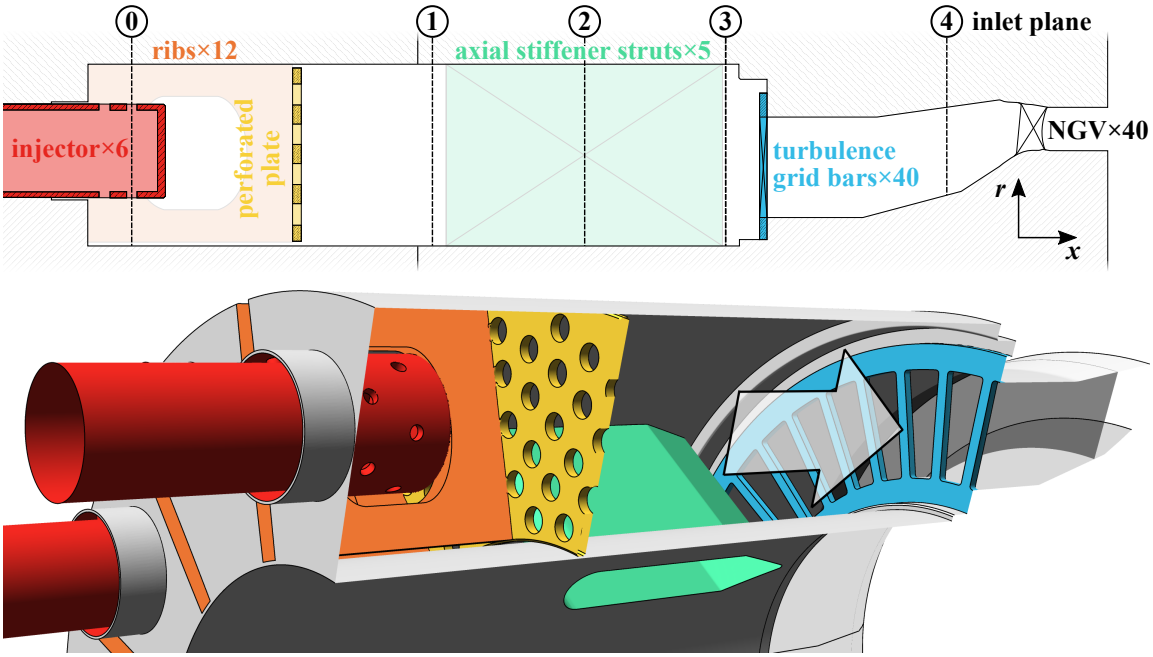


Figure 5.2: *Original ECAT facility flow conditioning system: meridional view (top); three-dimensional cutaway view (bottom).*

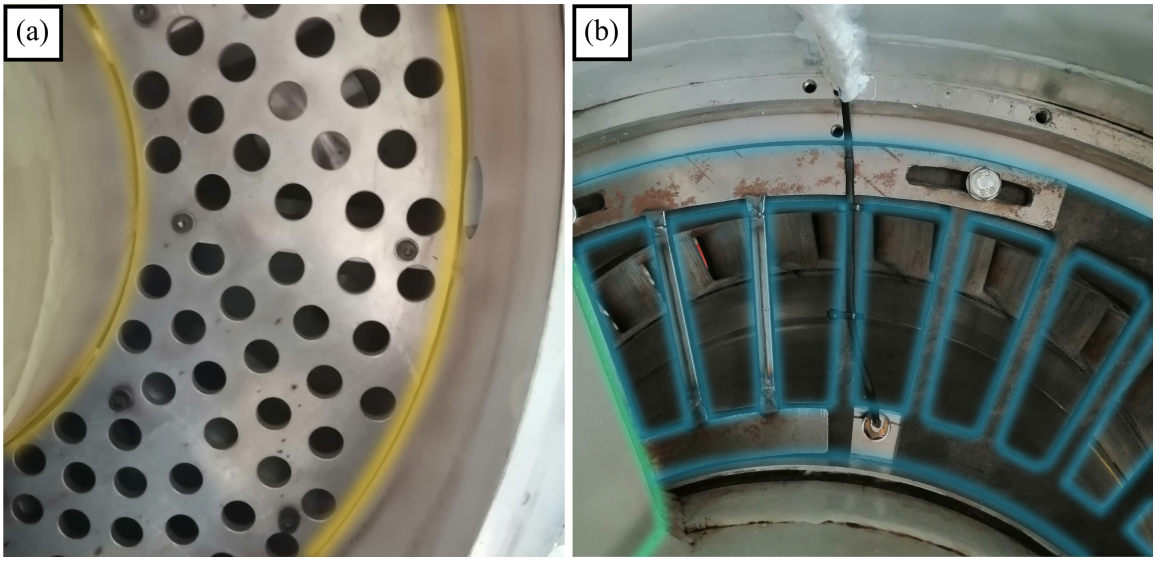


Figure 5.3: *Photos of original flow conditioning system showing: (a) perforated plate; (b) turbulence grid. Parts are highlighted according to the color scheme in Figure 5.2.*

5.2 Experimental methods

The turbulence grid flow at the NGV inlet plane (see plane 4 in Figure 5.2) was characterized across the full span radially, and over a 34.4° sector circumferentially using a combination of split-fiber, Pitot, and thermocouple probes. The circumferential location of the traversed sector is indicated in Figure 5.4, with the axially-projected locations of injectors, axial stiffener struts, and turbulence grid bars superimposed. Angles are defined relative to top dead center (TDC), measuring clockwise (CW), when viewing from upstream (VFU). Traverse measurements of total pressure and total temperature were normalized by the arithmetic average from an array of Pitot and thermocouple rakes at the same axial plane but at a different circumferential location (see "rakes" in Figure 5.4). The data processing method for split-fiber probe signals is extensively described in Chapter 4.

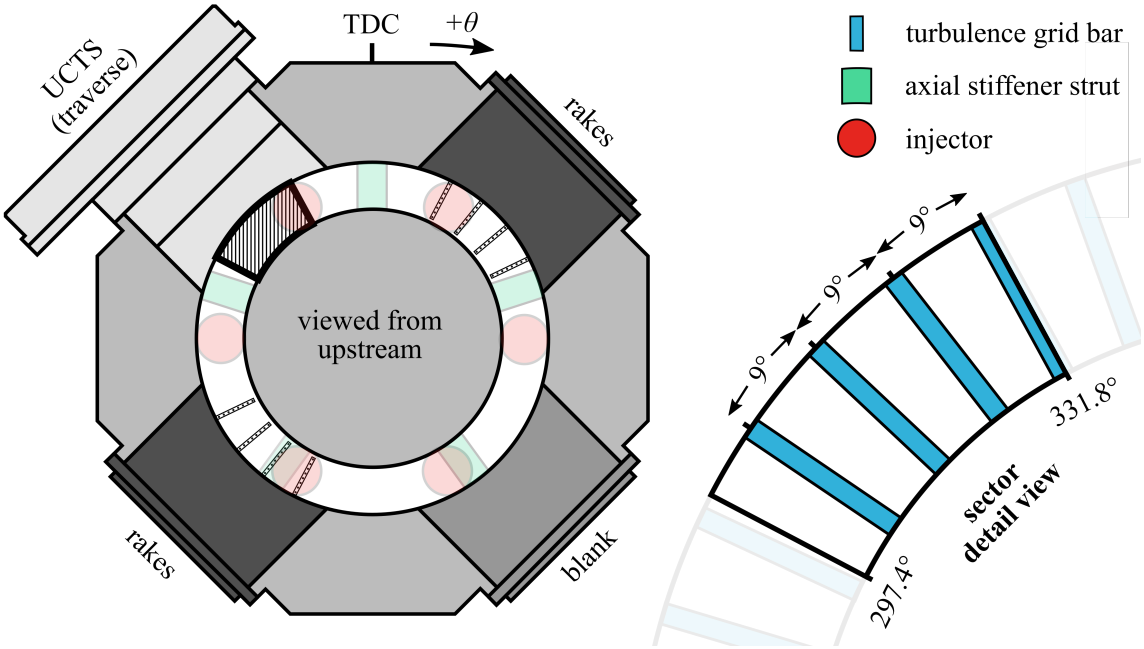


Figure 5.4: *Circumferential location of experimentally-surveyed sector, with axially-projected injector, axial stiffener strut, and turbulence grid bar locations superimposed.*

5.3 Numerical methods

Exploratory CFD simulations of the ECAT facility flow conditioning system were performed to inform the spatial sampling resolution required for experiments. These early simulations spanned one periodic sector of the turbulence grid circumferentially, and extended axially from plane 2 to one axial chord upstream of the NGV. Because the experimentally-measured distributions deviated from exploratory simulations, the domain was later expanded to the full annulus. The purpose was to determine why the real flow field did not follow the turbulence grid pitch of 9°.

Domain and mesh

The fully-annular CFD domain is shown in the cutaway view in the lower half of Figure 5.2. There are six domain inlets, located in the cylindrical ducts leading up to the injectors. The outlet is located approximately two axial chords downstream of plane 4, or equivalently one axial chord upstream of the hypothetical location of the NGV leading edge. The NGVs themselves were not modeled to reduce computational cost, resulting in a mesh size of approximately 100 million cells.

Boundary conditions

The injector inlet condition was specified as a constant mass flow rate of 10.82 kg s^{-1} (distributed evenly over six injectors) combined with a total temperature of 285 K, a turbulence intensity of 5%, and a viscosity ratio of 10. The mass flow rate corresponds to the average during experiments. The outlet condition was that of radial equilibrium with an average back-pressure of 1.81 bar (absolute). All remaining boundaries were treated as hydraulically smooth, adiabatic, no-slip walls.

Model and solver settings

Simulations were performed in ANSYS CFX 20.2 with a second-order discretization for the mean-flow and turbulence. The working fluid was dry air, which was assumed to behave as an ideal gas with constant transport properties of dynamic viscosity, thermal conductivity, and specific heat capacity. Turbulence was modeled using the standard k–ϵ model [168].

5.4 Non-uniformity at inlet plane

Distributions of experimentally-measured and CFD-predicted mass flux (ρV_x), normalized total pressure ($p_0/p_{0,\mathrm{rake}}$), yaw angle (α), pitch angle (β), turbulence intensity (TI), and normalized total temperature ($T_0/T_{0,\mathrm{rake}}$) at plane 4 are shown in Figure 5.5. Vertical dashed lines indicate axially-projected turbulence grid bar locations. Distributions of these quantities have previously been presented for a lean-burn combustor simulator configuration (see Figure 4.8 in Chapter 4). The reader is referred to Chapter 4 for the conventions used when defining these parameters. For CFD data in particular, total pressure and total temperature are normalized by the area average at plane 4 instead of the arithmetic average of the rake. Turbulence intensity (TI) is calculated from the turbulence kinetic energy (TKE), k, and the velocity magnitude, V, assuming isotropic turbulence (i.e. $\mathrm{TI} = \sqrt{2k/3}/V$).

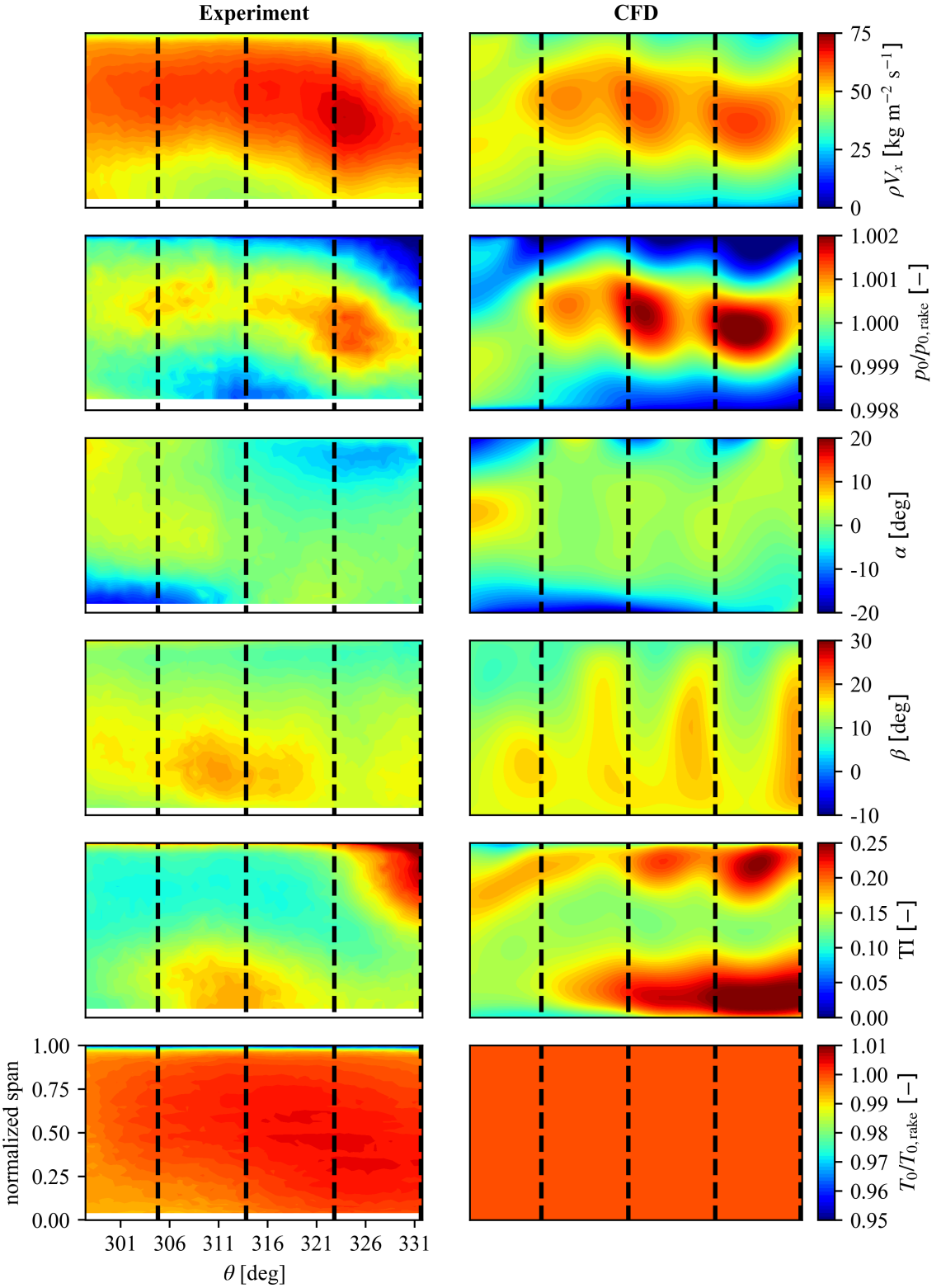


Figure 5.5: *Experimentally-measured and CFD-predicted plane 4 distributions of: axial mass flux (ρV_x); normalized total pressure ($p_0/p_{0,\mathrm{rake}}$); yaw angle (α); pitch angle (β); turbulence intensity (*TI*); normalized total temperature ($T_0/T_{0,\mathrm{rake}}$) with original flow conditioning system and turbulence grid installed. Viewed from upstream; vertical dashed lines indicate turbulence grid bars.*

Experimental results

First consider the *experimentally-measured* area maps shown in the first column of Figure 5.5. It is noted that a small radial band near the hub could not be traversed due to probe size limitations. As expected, spatial distributions of mass flux (ρV_x; first row) and normalized total pressure ($p_0/p_{0,\mathrm{rake}}$; second row) are relatively similar to each other, with generally higher momentum around the midspan than near the walls. Both profiles feature a global maximum near the midspan around 325°, and a distinct minimum in the upper right corner of the traversed region. Another large but less intense region of low momentum extends from 300° to 320° circumferentially and from 0% to 30% span radially. Importantly, neither the mass flux nor total pressure field is periodic according to the turbulence grid pitch (9°; see vertical dashed lines), indicating that the turbulence grid is not the dominant influence on the flow at the inlet plane. This is also reflected by the yaw angle (α) distribution in the third row, which varies non-periodically in the circumferential direction, with values ranging between −16° and +7°. The pitch angle (β) distribution, shown in the fourth row, is perhaps the best behaved, resembling an approximately radial profile. This was expected, because pitch angle is primarily dictated by the annulus hade angles, and the long-range potential field of the contracting inlet duct. The distribution of turbulence intensity (TI) is shown in the fifth row, and was 14% on average with regions of high intensity coinciding with regions of low total pressure. The high TI in these regions is caused both by elevated TKE, and by low velocity (i.e. the denominator of TI). The normalized total temperature ($T_0/T_{0,\mathrm{norm}}$) field is shown in the sixth and last row. It is approximately uniform in the freestream (5–95% span), with a thermal boundary layer developing near the casing on account of transient heat transfer from the hot flow to the test section walls.

Numerical results

Now consider the *CFD-predicted* area maps, shown in the second column of Figure 5.5. Although the simulations were fully-annular, only the region corresponding to the experimentally-surveyed sector is shown. The distributions of mass flux, total pressure, yaw angle, and pitch angle are qualitatively similar to the corresponding experimentally-measured profiles, confirming that the flow conditioning system output is not truly uniform. The CFD-predicted TI has a slightly higher average of 16% (versus 14% in experiments), but with similar "hotspots" towards the walls. The CFD-predicted normalized total temperature profile is uniform, because walls were modeled as adiabatic.

5.5 Cause of non-uniformity

The full-annulus CFD simulation showed good qualitative likeness with experimental data, thus corroborating that significant circumferential heterogeneities exist at vane inlet. Using the fully-annular CFD simulation, the origin of the circumferential distortion was traced to the facility settling plenum. Both simulations and experiments also identified a radial distortion component at the inlet plane, which is associated with flow separation from the forward facing steps at the interface between axial stiffener and contracting inlet duct. These phenomena are now discussed in detail.

Circumferential distortion

CFD-predicted distributions of Mach number (M) at plane 0, and plane 1 are shown in Figure 5.6. First consider the distribution at plane 0, which is located in the settling plenum, intersecting the injectors and the rib window (see overview of planes in Figure 5.2). The Mach number distribution at plane 0 shows that the jets exiting the injector are deflected towards the endwalls by the ribs, with only a small proportion passing through the windows. Mass flow therefore becomes biased towards rib compartments which feature injectors. The circumferential distortion seemingly persists downstream of the perforated plate, as evidenced by the alternating 30° regions of high and low Mach number (60° periodicity) at plane 1, shown on the right side of Figure 5.6. These interact *non-periodically* with the five axial stiffener struts (72° periodicity), and the 40 turbulence grid bars (9° periodicity). This explains why preliminary simulations including *only* the turbulence grid did not yield a good match with experimental data.

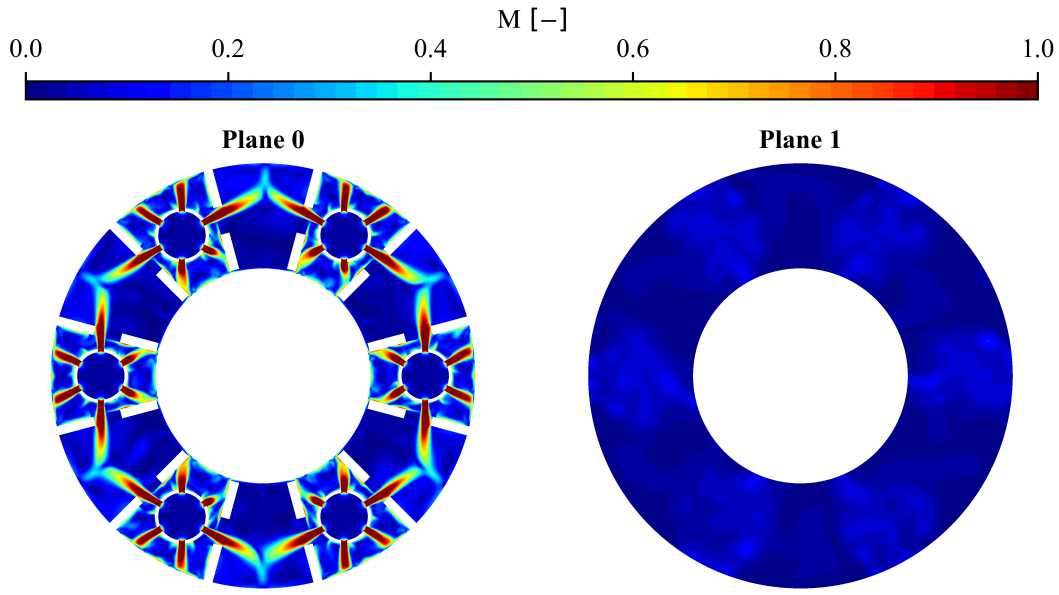


Figure 5.6: *Mach number (M) distributions for axial sections in the settling plenum (plane 0), and downstream of the perforated plate (plane 1). Viewed from upstream.*

For the *real* geometry, additional contributing factors to circumferential non-uniformity at the inlet plane are the variable hub and casing clearances of the perforated plate due to eccentricity of the settling plenum bulkhead (a fabricated part). This is of particular concern, because Figure 5.6 shows that the mass flow exiting the injectors accumulates near the endwalls.

Of note, when configured with the lean-burn combustor simulator described in Chapter 3, the periodicity at plane 4 is improved (see Figure 4.8), presumably because the swirlers produce sufficient total pressure loss and turbulence to outweigh the influence of any upstream distortion. The drawback is that optical access is obstructed in this configuration.

Radial distortion

Now consider the distributions of normalized total pressure ($p_0/p_{0,\mathrm{rake}}$) and turbulence intensity (TI) shown for a local meridional section in Figure 5.7. The plane is located 327.3° CW from TDC when VFU—midway between two turbulence grid bars. The CFD simulation reveals a separation from the forward facing step between the axial stiffener and contracting inlet duct, giving rise to low total pressure in the separated region and high turbulence in the shear layer. The low total pressure fluid is partially entrained following reattachment, which explains why high TI regions are co-located with local minima of total pressure. The implication is that reducing the separation *intensity* would improve the radial uniformity of mass flux, total pressure, and turbulence.

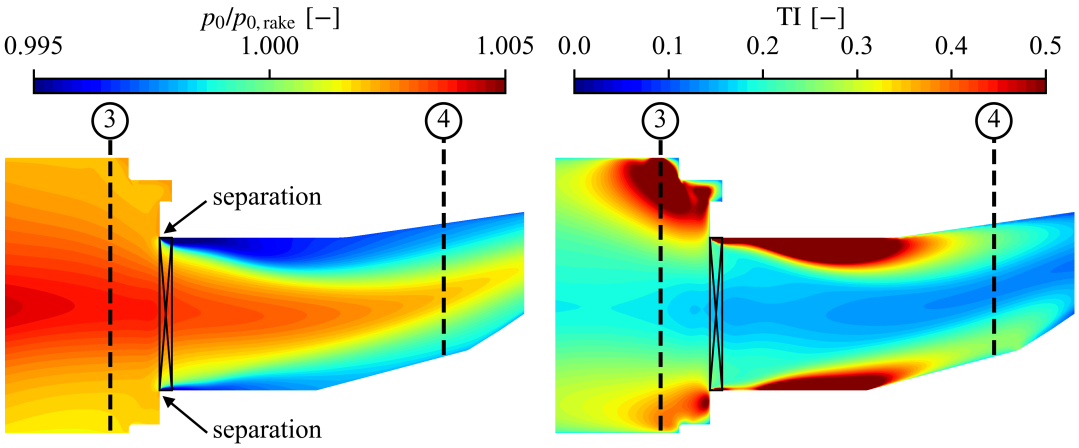


Figure 5.7: *Distributions of normalized total pressure ($p_0/p_{0,\mathrm{rake}}$) and turbulence intensity (TI) for a local meridional section midway between turbulence grid bars (327.3° CW from TDC when VFU).*

5.6 Redesign process

Modifications to the ECAT facility flow conditioning system were evaluated using full-annulus CFD simulations. The design-space was constrained by the limitation that large parts such as the settling plenum bulkhead (including the injectors and ribs; see Figure 5.1b), and the axial stiffener (see Figure 5.1d), could not be re-designed within the required timescale and available budget. Having identified a significant periodic component associated with the injectors, the practical way forward was to mix this out across a series of perforated plates. It is also recalled that installing additional grids downstream of the axial stiffener struts was not possible, because optical access for infra-red cameras was a key requirement of an upcoming test program. In total, nine design concepts were simulated. The chosen design is now considered.

5.7 Revised design

The revised design of the flow conditioning system is shown in Figure 5.8. It retains the injectors and ribs of the original system (design constraint), but replaces the single perforated plate (see Figure 5.2) with two in-series perforated plates. The first plate has relatively low porosity, and therefore generates fairly high loss. This helps balance out the upstream distortion, because the dynamic pressure (and therefore absolute loss) *through the plate* scales with the local excess in upstream total pressure. The second perforated plate (downstream) has higher porosity, with radially-variable hole diameters, and seals at the hub and casing. High porosity and radially-variable hole diameters help distribute the flow evenly. The seals prevent the occurrence of circumferentially-variable leakage flows due to eccentricity of the fabricated parts. Both perforated plates feature smaller holes, compared to the original design. Smaller holes were considered favorable because the non-uniformity local to the hole has a shorter wavelength and therefore mixes out more rapidly as a function of the axial distance. As in the original design, the first perforated plate is mounted onto the ribs, with the downstream perforated plate offset axially using stand-off bars.

A second major modification was the addition of flow guides. The flow guides form a bell-mouth contraction, which smoothly bridges the interface between the flow conditioning system and the contracting inlet duct. This reduces the intensity of flow separation compared to the original design which had a step contraction, thereby improving flow uniformity at NGV inlet (plane 4). Photographs of the new hardware are shown in Figure 5.9 (credit to Matthew Stokes), with individual parts highlighted according to the color scheme from Figure 5.8.

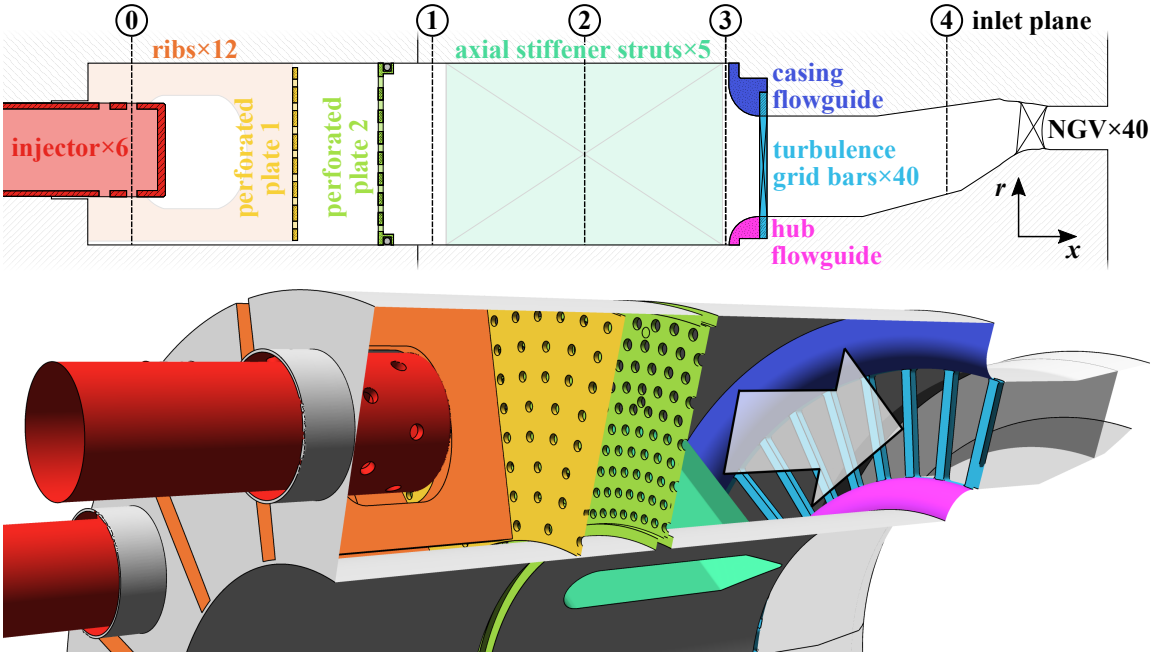


Figure 5.8: *Revised ECAT facility flow conditioning system: meridional view (top); three-dimensional cutaway view (bottom).*

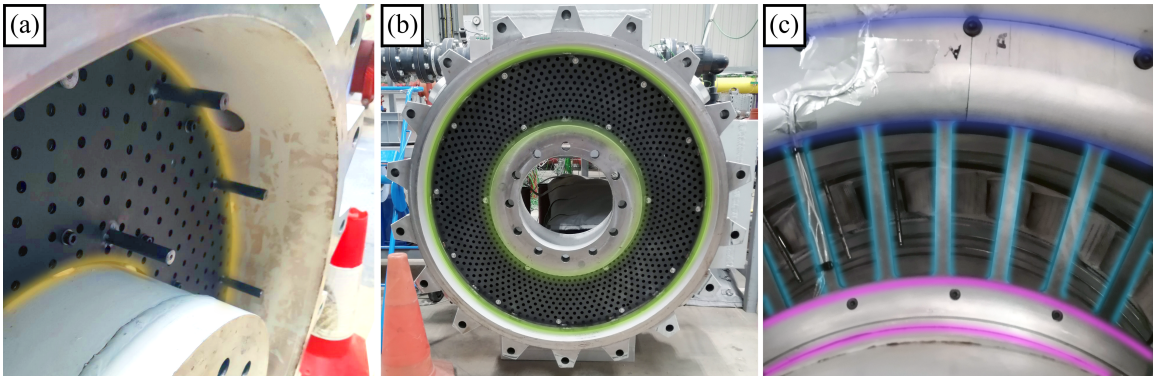


Figure 5.9: *Photos of revised flow conditioning system showing: (a) first perforated plate and stand-off bars; (b) second perforated plate; (c) flow guides mounted onto the turbulence grid. Parts are highlighted according to the color scheme in Figure 5.8.*

5.8 Flow field comparison of original and revised design

In this section, the performance of the original and revised flow conditioning systems are systematically compared using CFD. We begin by examining axial sections of the full annulus, analyzing the streamwise evolution of circumferential non-uniformities. It is also demonstrated that flow guides improve the radial uniformity of total pressure and TI at vane inlet.

Circumferential distortion

CFD-predicted profiles of total pressure (normalized by the local area-average, $p_{0,\mathrm{avg}}$), and turbulence intensity (TI) for the original and revised design are shown in Figure 5.10. The axial

evolution of these parameters is studied using data at planes 1, 2, 3, and 4 (see Figure 5.8). For brevity and because the injector and rib geometries were unchanged, the profiles at plane 0 (inside the settling plenum) are not shown.

First, consider the profiles downstream of the perforated plate(s) (plane 1; first row). For the original design, injector-aligned sectors exhibit elevated total pressure (first column), and therefore relatively low turbulence intensity (third column). The revised design almost completely eliminates circumferential distortion of total pressure from the injectors (see second column), but introduces regions of low total pressure near the hub and casing. This is caused by the non-porous region occupied by the radial seals. The turbulence intensity for the revised design is shown in the fourth column: TI is more uniform circumferentially, and on-average lower.

Now consider the profiles at the mid-chord of the axial stiffener struts (plane 2; second row). For the original design, the total pressure and TI non-uniformity persists albeit with reduced intensity and superimposed distortion from interaction with the axial stiffener struts. For the revised design, the radial distortion—caused by the seals—has largely mixed-out. Turbulence intensity is also lower on average, consistent with the shorter length scales and therefore faster turbulence decay resulting from smaller holes in the perforated plate(s).

Next, consider the profiles immediately downstream of the axial stiffener struts (plane 3; third row). The magnitude and wavelength of total pressure non-uniformity is significantly improved compared to the baseline design and the radial uniformity from the seals is almost fully mixed-out. The average turbulence intensity is reduced and its uniformity is improved. The regions of high TI near the hub and casing are artifacts due to stagnation of corner flows (i.e. low denominator V; see plane location in Figure 5.8).

Finally, consider the profiles at NGV inlet (plane 4; fourth row). For the original design, the total pressure non-uniformity persists up to vane inlet, with superimposed modulation from the turbulence grid bar wakes, and radial distortion due to separation from the forward facing steps. The revised design improves the uniformity of total pressure, with remaining distortion mostly related to the turbulence bar wakes. Notably, by virtue of the flow guides, hotspots of turbulence and the associated minima of total pressure at the casing are almost completely eliminated, while those at the hub are noticeably weakened. As a result, the average CFD-predicted TI at plane 4 falls from 16% to 12%.

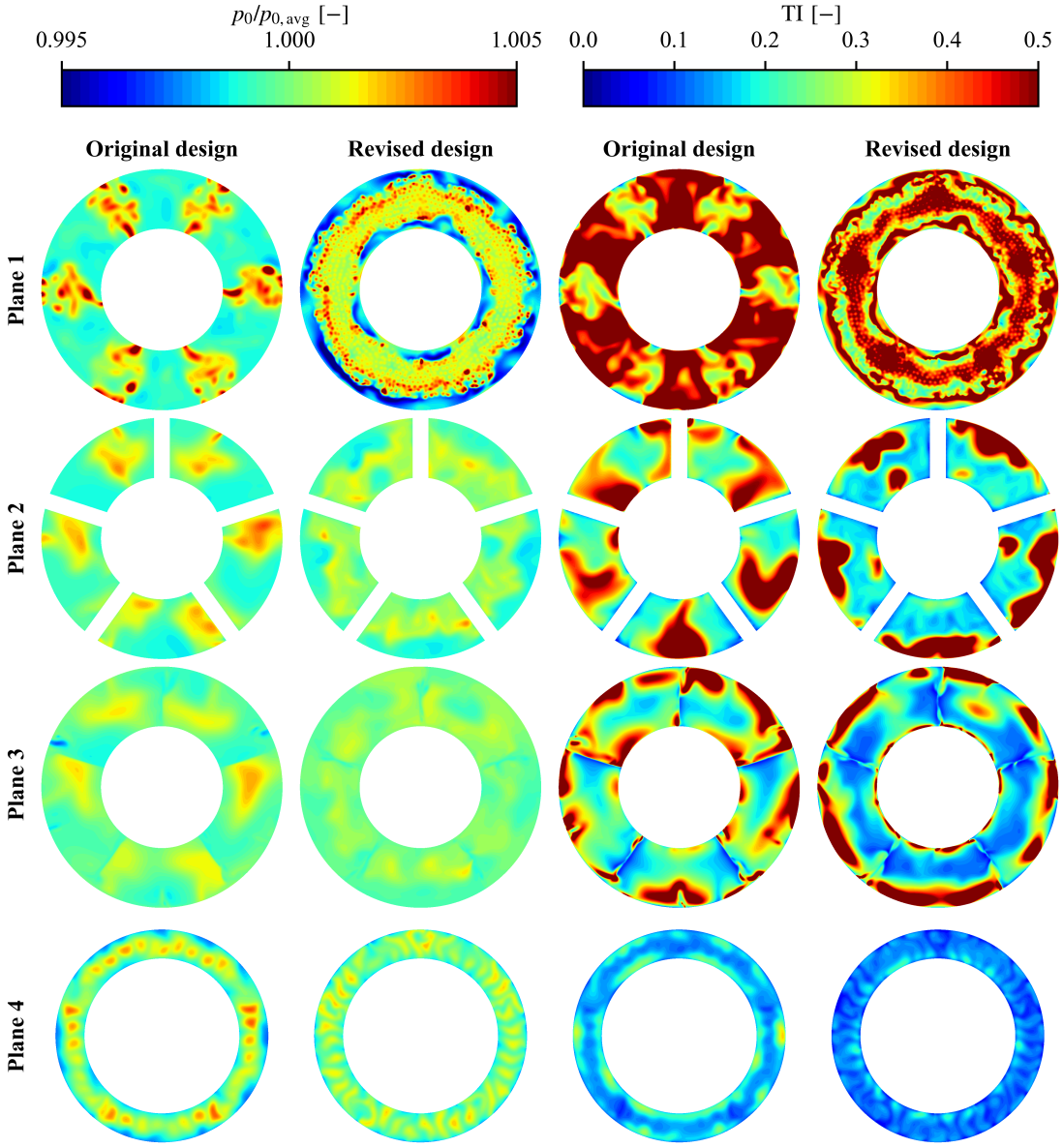


Figure 5.10: *Axial evolution of normalized total pressure ($p_0/p_{0,\text{avg}}$) and turbulence intensity (*TI*) for the original and revised flow conditioning systems.*

Yaw angle non-uniformity (not shown) was regrettably neither improved nor degraded. A plausible explanation is that the circumferential variability of yaw is primarily caused by non-zero incidence onto the turbulence grid in the wake of the axial stiffener struts. Fortunately, mixing and axial acceleration between the nominal inlet plane and the NGV reduces the *actual* incidence range to approximately ±6°.

Radial distortion

Distributions of normalized total pressure, and TI in a local meridional plane are shown for the original and revised designs in Figure 5.11. The plane is located 327.3° CW from TDC when

VFU, which is midway between two turbulence bars. The distributions for the original design (first row) have already been discussed in relation to Figure 5.7, and are only shown for comparative purposes. For the revised design, shown in the second row, both the distributions of normalized total pressure ($p_0/p_{0,\mathrm{norm}}$; first column) and TI (second column) suggest that flow separation intensity is dramatically reduced, if not entirely suppressed. Of note, there is a sudden reduction of total pressure accompanied by a sudden increase of TI slightly downstream of the flow guides. This might be mistaken for a late separation, but is in fact caused by the advection of the turbulence grid bar wake into the section plane from a different circumferential location.

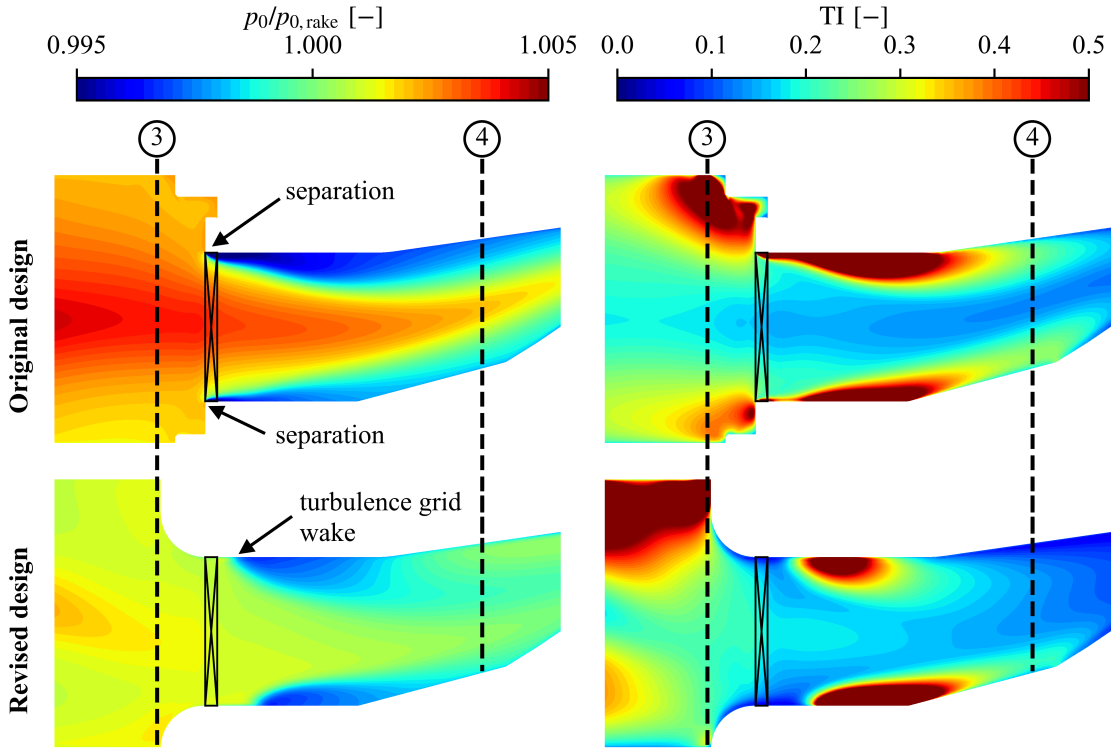


Figure 5.11: *Effect of flow guides on separation intensity: comparison of normalized total pressure ($p_0/p_{0,\mathrm{rake}}$) and turbulence intensity (*TI*) distributions on a local meridional section (327.3° CW from TDC when VFU) for the original and revised flow conditioning systems..*

5.9 Conclusions

A new flow conditioning system for the ECAT facility has been presented. The project was undertaken in response to unexplained circumferential non-uniformity in experimental data taken at vane inlet. In a first instance, the cause of non-uniformity was investigated using a full-annulus CFD simulation of the original flow conditioning system. This confirmed the initial experimental observations, and revealed that circumferential distortion was caused by an interaction of the incoming flow with structural ribs in the settling plenum, resulting in an unexpected circumferential variation of mass flux.

An improved flow conditioning system was developed using CFD, with the constraint that many large parts could not be modified within the allocated budget and time. The new design mitigates the settling plenum non-uniformity by mixing-out the flow through two perforated plates. Compared to the original design, this approximately halved total pressure non-uniformity at vane inlet. The new design also incorporates flow guides, which smoothly bridge what was previously a forward-facing step contraction in the hub and casing radii. The flow guides were shown to prevent large-scale separation, significantly improving the radial uniformity of both total pressure and turbulence intensity immediately upstream of the vanes. The new design was successfully built and commissioned in the ECAT facility by Matthew Stokes (another DPhil candidate).

Perhaps most importantly, this chapter highlights that seemingly insignificant geometric details can have a strong influence on the flow at NGV inlet. Therefore, any future redesign work of the flow conditioning system should be guided by CFD simulations spanning the *full axial and circumferential extent* of the ECAT facility working section, and including the injector(s).

5.10 Recommendations

Given more time and funding for upgrades, the ECAT facility might benefit from replacing the *discrete injector* configuration that is currently used, with an *annular injector* design. This would eliminate the underlying cause of circumferential non-uniformity at the source. It may also be desirable to reduce the number of axial stiffener struts from five to either four (combined with an octagonal injector ring) or three (combined with a hexagonal injector ring). This would avoid the problem whereby the interaction between the injector flow and the struts is non-periodic (requiring full-annulus simulations), with the added benefit of reducing blockage. In the same vein, the distance between the trailing edge of the axial stiffener struts and the turbulence grid should be increased to reduce interactions likely responsible for non-uniform yaw angles. Similar modifications have already been implemented in the related high-temperature ECAT+ facility [169], namely an octagonal injector ring and a three-strut axial stiffener.

For studies *not requiring* optical access from upstream, it may be beneficial to use a less porous turbulence grid with circular holes instead of radial bars. This would likely improve flow uniformity at vane inlet, and might offer finer control over turbulence length scales.

For studies *including* infra-red measurements, future investigators may want to examine the effect of cameras installed upstream of the NGVs in terms of the blockage, and in terms of the disturbance from the camera wake felt at vane inlet.

Nomenclature

Romans

k	Turbulence kinetic energy	[m^2 s^{-2}]
M	Mach number	[–]
p	Pressure	[Pa]
r	Radial coordinate	[m]
T	Temperature	[K]
TI	Turbulence intensity	[–]
V	Velocity magnitude	[m s^{-1}]
V_x	Axial velocity	[m s^{-1}]
x	Axial coordinate	[m]

Greeks

α	Yaw angle	[°]
β	Pitch angle	[°]
θ	Circumferential coordinate	[°]
ρ	Density	[kg m^{-3}]

Subscripts

0	Total property
rake	Ensemble average across the rake
avg	area average

6 | Aerodynamic and thermal field development of cooled transonic HP NGV

In this chapter we present detailed aerodynamic and thermal field measurements downstream of an annular cascade of fully-cooled nozzle guide vanes (NGVs). The experiments were conducted in the Engine Component Aerothermal (ECAT) facility at the University of Oxford, at engine-matched conditions of Reynolds number and Mach number, and high turbulence intensity. The experimental data are unusually high-fidelity and allow for detailed comparison with modern computational fluids dynamics (CFD) methods. We compare the experimental data to simulations of fully-featured geometry (resolved internal geometry and film cooling holes). We analyze distributions of whirl angle, kinetic energy loss, and non-dimensional temperature at three axial planes downstream of the NGVs. The aerodynamic and thermal wakes are also characterized in terms of their spreading and decay rates. The analysis is deepened with detailed comparison to a previous data-set for a different design of heavily-cooled NGV. The analysis is a useful reference point for assessing the accuracy of the current state-of-the-art numerical methods used in the engine design process.

Context with other chapters

This chapter examines the aerodynamic and thermal field development of cooled transonic NGVs. The unusually high-fidelity experimental data is used as a benchmark for numerical methods commonly used during turbine design. Inlet conditions for simulations of the NGV flow were informed by the detailed measurements taken at vane inlet, which are presented in Chapter 5. The comparison of experimental results and CFD predictions was later extended into a turbulence model sensitivity study, which is covered in Chapter 7. The NGV data under uniform inlet conditions serve as the baseline when studying the effect of lean-burn in Chapter 8.

Publication status and co-author contributions

The chapter takes the form of a *peer-reviewed journal paper*, which has recently been accepted for publication in the ASME Journal of Turbomachinery [6]. The DPhil candidate was responsible for carrying out aerodynamic experiments, running simulations, processing data, and ultimately writing the paper. Roderick Lubbock acquired the thermal field data, and Francesco Ornano performed preliminary simulations. Nafiz Chowdhury supported facility operation throughout the experimental work. Thomas Povey supervised all aspects of the project. A statement of authorship is included at the end of the document.

6.1 Introduction

Preliminary turbine design is usually performed using mean-line calculations and through-flow codes, followed by design optimization using Reynolds-averaged Navier–Stokes (RANS) and unsteady RANS (URANS) codes. The very early correlations (e.g. Ainley and Mathieson [170]) on which the original mean-line and through-flow codes were built have since been updated to account for secondary flows and tip losses (e.g. Dunham and Came [171]) and for off-design operating points (e.g. Benner et al. [172]), but there is still limited data for transonic designs with significant cooling flow. This leads to inaccuracy in the design starting point, which would be improved by re-benchmarking these codes against data from more current engine components. Likewise, known errors in RANS and URANS methods can lead to inaccurate performance prediction. The most significant contributors to error are generally the limitations associated with artificially modelling the effects of turbulence rather than explicitly resolving it, with models relying on calibration against experimental datasets that are not particularly representative of most real engine environments. The original calibration datasets are often from low-speed experiments with lower-than-engine turbulence levels (see, for example: Launder and Spalding [168], Wilcox [141], Spalart and Allmaras [173], and Menter [142]). Obtaining turbulence closure coefficients from such tests might yield acceptable results in environments similar to the calibration environment, but at the sacrifice of good performance in engine-like environments. It is well-established that optimum closure coefficients depend on both the flow and the location within the flow (see, for example: Chambers et al. [174], Georgiadis and Yoder [175], and Costa Rocha et al. [176]). For high-accuracy simulations, application-specific model recalibration becomes a priority. This point is adequately demonstrated by considering recent comparisons of nozzle guide vane (NGV) flows at engine-realistic conditions (transonic and fully-cooled) with corresponding uncalibrated RANS and URANS. We review this literature now.

Yasa et al. [177] and Burdett and Povey [147] investigated kinetic energy loss and mixing rates downstream of fully cooled NGVs, and compared results to RANS simulations using the k–ω shear stress transport (SST) model. In Burdett and Povey, RANS simulations overpredicted profile loss by 22%, when compared to experiments [147]. This was largely attributed to over-estimation of loss local to the film cooling holes, which arose as a result of incorrect film momentum flux ratio due to the use of a point-source method, which is common in design practice. The recommendation was to use fully resolved cooling hole geometries to mitigate this problem. The simulations of Yasa et al. [177] overpredicted profile losses by approximately 40%. Here, it is

noted that film cooling was not considered as part of the CFD model; a better match in loss predictions may have been achieved had this been included. In both studies the spreading and decay rates of the wake were investigated. On average, Burdett and Povey reported a 31% underprediction in wake width and a 91% overprediction of wake depth at midspan. The corresponding values for Yasa et al. were a 12% underprediction in wake width and 32% overprediction of wake depth. Overall, CFD overestimated loss and under-predicted mixing rates when compared to experiments. These differences are important for correct estimation of the unsteady aerothermal load on the rotor.

Trailing edge (TE) dynamics are complex (see review of Sieverding et al. [178]), with significant unsteady vortex shedding. The difference between RANS and URANS for mixing rates in the near and far-wake were investigated by Kopriva et al. [179] for a transonic linear cascade with TE cooling, comparing CFD to the experimental data of Kapteijn et al. [180]. Kopriva et al. [179] did not report integral loss, which we have estimated here using simple area-weighted integrals of the extracted wake profiles. In line with Yasa et al. [177] and Burdett and Povey [147], in the study of Kopriva et al. [179] RANS overpredicted overall loss by 27% on average, across 4 measurement planes, whilst under-predicting mixing rates of both the aerodynamic wake and the thermal wake. When compared to the experiment, the RANS aerodynamic and thermal wake depths were overpredicted by 60% and 119% respectively, with corresponding wake widths 18% and 38% narrower. URANS showed a similar 35% overprediction of overall loss but an improved match of mixing rates when compared to the experiment, both in terms of the peak intensity and the wake width of aerodynamic and thermal wakes. The improved accuracy of URANS was attributed to the modeling of unsteady vortex shedding, though the underlying mechanism was not explicitly addressed. The performance of RANS and URANS was also compared by Burdett and Povey [147], with URANS closing the gap on experimental data by on-average 12% for the peak aerodynamic loss and 14% for the wake width. In both studies [147, 179], URANS led to an improved match with experiments in terms of mixing characteristics but had little effect on the overall loss.

Although URANS has been shown in the literature to be able to reproduce vortex shedding behavior for nozzle guide vanes with some success (see e.g. Leonard et al. [181]), and has been shown to improve the match of the wake profiles with experimental data [147, 179], there is some debate as to the mechanism by which the improvement is achieved. Fadai-Ghotbi et al. [182] argue that for problems without external forcing, RANS and time-averaged URANS should

converge to the same solution. We might therefore attribute the enhanced mixing that has been observed in URANS to numerical diffusion from the time space discretization. The point is that, whilst phenomenologically URANS appears to give closer match to experimental data than RANS for many examples of TE flows, the fundamental basis for the improvement is questionable. This has led some authors (e.g. Fadai-Ghotbi et al. [182] and Spalart [183]) to question whether URANS should be preferred over RANS for statistically-stationary problems—noting the attendant increase in computational cost—or whether effort would be better devoted to improving turbulence models for use in steady-RANS and hybrid solvers combining RANS with Large Eddy Simulations. Whatever position one takes on this unresolved question, there is little disagreement about the importance of high-fidelity experimental work for validation of particular methods, particularly the question of turbulence modelling.

In this study we consider the aerodynamic and thermal field development for a fully-cooled transonic NGV from a modern aero-engine. The parts were tested at engine-representative Mach and Reynolds number. In addition to a comprehensive analysis of the aerodynamic wake in terms of loss and whirl angle, the axial evolution of the thermal field downstream of the vanes is studied experimentally and via RANS simulations of the fully resolved NGVs. The aim is to explore the strengths and limitations of RANS solvers for this environment, and to quantify and understand the differences between the CFD and experimental data. Comparisons against high-fidelity data of this type are rare, and provide an opportunity to test commonly used methods against a relevant experimental benchmark. We compare results to the earlier work of Burdett and Povey [147], noting that the engine-parts of the current study are from an earlier generation engine of the same family.

6.2 Experimental methods

The experiments in this study were conducted in the Engine Component AeroThermal (ECAT) facility, described by Kirollos et al. [121]. The ECAT facility is a transonic annular cascade configured for testing high-pressure NGVs at engine-matched conditions of Mach number, Reynolds number, and coolant-to-mainstream pressure ratio. The vanes used in this study were from a modern turbo-fan engine. In this section we describe the layout and instrumentation of the facility working section.

Test section layout and instrumentation

The layout of the working section is illustrated in Figure 6.1. The inlet measurement plane, NGV, and three exit measurement planes are marked. The flow exhausts through a parallel annular duct

to a silencer at atmospheric pressure.

At plane 1, both total temperature and total pressure were measured using rakes (8 radial measurement points) at each of four circumferential locations (32 measurements for each). Hub and case coolant plena feed conditions were measured using 4 total temperature and 4 total pressure probes per plenum.

The NGV exit static pressure was measured with 32 static pressure tappings on the hub and casing platform overhangs of the NGV, approximately 0.3 axial chords downstream of the midspan TE. The tappings were evenly distributed over four vane platforms (8 tappings per platform). The axial location of the static pressure tappings is indicated in Figure 6.1.

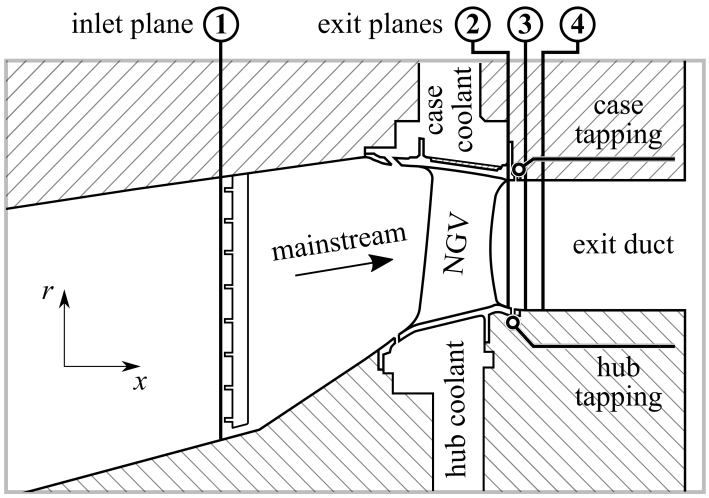


Figure 6.1: *Schematic of test section, showing the NGV, exit duct, hub and case coolant feeds, and the upstream rake. The inlet measurement plane, three exit measurement planes, and pressure tapping locations are marked.*

Exit measurement planes 2, 3 and 4 are located 0.25 C_x, 0.50 C_x, and 0.75 C_x downstream of the midspan TE. They were surveyed with a five-hole aerodynamic probe (total pressure; pitch; yaw; static pressure) and a thermocouple probe (dual-sensor; K-type; shielded and vented; 25 µm wire diameter). The near-wall regions, defined as within 10% of the hub and case walls, were traversed with a Pitot probe. All probes were pre-yawed by 68° and pre-pitched by between −5° and +10°, depending on the location.

The frequency response of the five-hole probe was measured to be approximately 50 Hz using an exploding balloon impulse response experiment. The thermocouple time-constant was estimated to be around 10 milliseconds using Paniagua et al. [139]. The traverse speed was 6 deg s^{-1} for the five-hole probe and Pitot measurements, and 3 deg s^{-1} for the thermocouple measurements, giving effective spatial resolutions in the circumferential direction (five time constants) of 0.4 mm and 0.5

mm at midspan, respectively. The radial traverse resolution was 1.6 mm (3.0% of span) for the five-hole probe, and 0.8 mm (1.5% of span) for the Pitot probe. For the thermocouple probe, the radial step size was approximately 3.2 mm (6.0% of span), except within 15% of span of the hub or casing walls, where an increment of 1.6 mm was used.

Accurate measurement of flow angles using multi-hole aerodynamic probes can be challenging in flows with strong pressure gradients. To increase the accuracy of the pitch and whirl angle measurements, flow-angles were corrected using a method similar to that of Vinnemeier et al. [184]. The recovery factor for the downstream total temperature probe was taken to be 0.975, a value typical for a shielded bare-bead thermocouple at transonic conditions (see e.g. Paniagua et al. [139] and Glawe et al. [185]). Experimental measurement uncertainty is covered in Appendix 6.A.

Experimental operating conditions

Aerodynamic and thermal traverse measurements were performed at conditions of Mach number, Reynolds number and coolant-to-mainstream mass flow rate ratio matched to the engine conditions at cruise. These conditions are summarized in Table 6.1. Aerodynamic measurements were performed with ambient flow temperature. Measurements of the downstream thermal field were performed at a mainstream-to-coolant temperature ratio of 1.20 (using a 2 MW heater).

Table 6.1: *Summary of experimental operating conditions.*

Parameter	Value
Vane Mach number	0.92
Vane Reynolds number based on axial chord	7.5×10^5
Coolant-to-mainstream mass flow rate ratio	0.14–0.15
Case coolant mass fraction	0.37
Hub coolant mass fraction	0.63
Mainstream total temperature, K	285–350
Coolant total temperature, K	285–290
Plane 1 mean turbulence intensity	13%
Plane 1 mean length scale, mm	28

Experimental inlet profiles

Inlet measurements (plane 1; see Figure 6.1) of total pressure and total temperature were conducted using both fixed rakes and an automated two-axis traverse system, which has been described by Amend and Povey [5]. The fixed pressure probes were beveled-inlet Pitot probes, and the traverse probe was of Kiel-head design. The thermocouple probes on the rake were 125 µm diameter K-type butt-welded wire. An Omega 125 µm diameter K-type thermocouple with improved error was used for the traverse probe. Circumferentially averaged profiles are shown in Figure 6.2. Data were real-

time-normalized against average instantaneous values from the fixed rakes (32 measurement points for each). We refer to these normalized measurements as $p_{01,\mathrm{norm}}$ and $T_{01,\mathrm{norm}}$.

First, consider the normalized total pressure in Figure 6.2a. The profiles measured by both rake and traverse system have a peak at approximately mid-span, with a variation of approximately ±0.1% from the mean: i.e. the radial trend is very flat. The two profiles agree extremely well with maximum variation between the two trends of approximately 0.04%, which is within the combined bias error of the transducers of 0.06% (see Appendix 6.A).

The normalized total temperature is shown in Figure 6.2(b). The profiles are gently peaked towards midspan between 10% and 90% span with a variation of ±0.2% from the mean in this range. Towards the casing, a thermal boundary layer, which was measured with the traverse only, develops due to convective heat transfer from the hot flow to the relatively cold test section walls. The peak deficit here was roughly 5% (16 K) of the nominal value (T_{01} = 340 K). In this region the probe could be traversed to the casing wall (retractable probe). The hub thermal boundary conditions are essentially identical to the casing. Because of this, and because the measured profile was symmetric about midspan in the region measured, the hub thermal deficit was assumed to be the same magnitude as that measured at the casing. Measurements from the fixed rakes and traverse system agree to within 0.3%, which is well within the bias error of the measurement (0.49%; see Appendix 6.A).

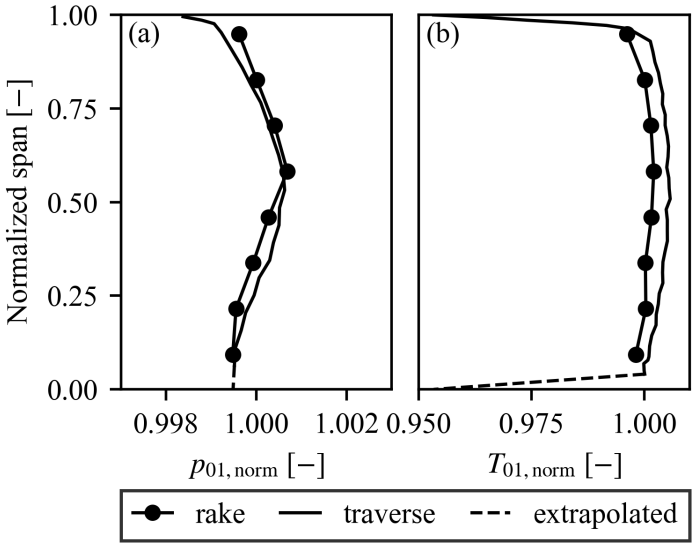


Figure 6.2: *Inlet plane radial profiles of: (a) normalized total pressure; (b) normalized total temperature for the fixed rakes.*

Turbulence was characterized at plane 1 by traversing the inlet with a pair of split-fiber probes [5]. Profiles of turbulence intensity, I, and normalized turbulence length scale, ℓ/C_x, are shown in Figure 6.3. Turbulence intensity was calculated from turbulence kinetic energy and velocity magnitude. Finite probe size meant that the 0–5% span region could not be surveyed. A k–ϵ CFD simulation of the turbulence grid was used to inform extrapolation of the experimental profiles to the walls.

First consider the radial profiles of turbulence intensity, which are shown in Figure 6.3a. The experimental traverse profile (solid line) is relatively flat (average of 13%) with a slight bias for being higher in the lower half of the span (average of 14%) than the upper half of the span (average of 12%). The turbulence intensity rises sharply near the casing (95–100% span) but this is thought to be caused by a local interaction between mainstream and traverse probe access port, resulting in disturbed cavity flow. As this is local to the probe and at a single circumferential location (vane wakes were surveyed at a different circumferential location) we use a CFD-informed extrapolation in the 95–100% span region. The CFD-predicted profile of turbulence intensity (dotted line) has a similar general trend to experiments, but with a slightly higher average value (16%) and two moderate peaks (maximum of 21%) at 10% and 87% span. At the hub and casing, CFD predicts turbulence intensities of 15% and 13%, respectively. Low gradient of turbulence intensity in the approach to the wall is a common feature of k–ϵ CFD predictions because the inner boundary layer is not resolved. Extrapolations of the experimental data at the hub and case are shown as dashed lines.

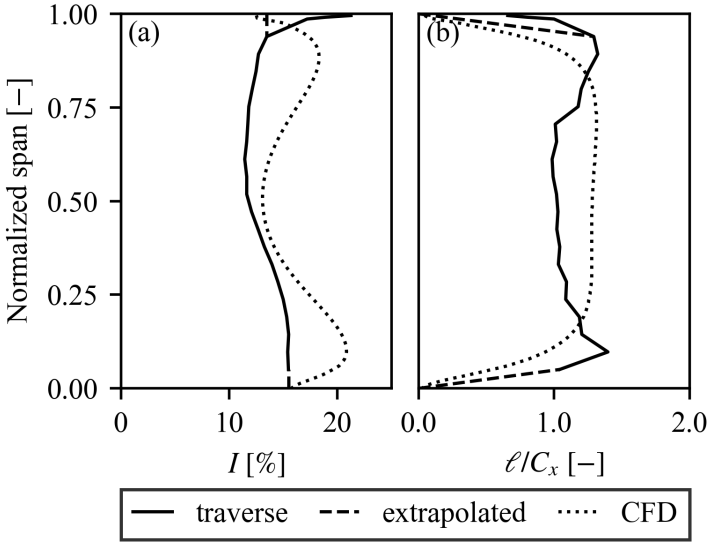


Figure 6.3: *Inlet plane radial profiles of: (a) turbulence intensity; (b) normalized integral length scale.*

Consider now the profiles of normalized turbulence length scale, ℓ/C_x, which are shown in Figure 6.3b. For the traverse data, ℓ was calculated from the product of the time-averaged velocity magnitude and the integral time scale (average of three principal components). Time scales were determined using the method of Nix et al. [186], integrating the normalized autocorrelation function up to the first zero crossing. CFD time scales were calculated from turbulence kinetic energy, k, and turbulence dissipation rate, ϵ, using the well-known relation $\ell \propto k^{1.5}/\epsilon$. Both the traverse and CFD profiles of turbulence length scale are relatively flat in the 20–80% span range, with values of approximately 1.10 C_x and 1.26 C_x, respectively. The traverse data has two moderate peaks (maximum value 1.40 C_x) at 10% and 89% span. These are not seen in the CFD and are thought to originate from flow separation at a step contraction of the duct, at the interface between the feed manifold and the test section. In the approach to the wall both the experimental and CFD data show reducing length scales, as we expect. It was not possible to perform measurements at the hub wall due to a probe size restriction, and the casing measurements were disturbed by cavity flow interaction. For this reason, in the near-wall region a patching method was used for this experimental data, informed by CFD and the proportionality between length scale and wall distance in the log-layer [141]. Patched data is shown by the dashed line.

Overall, the agreement between traverse data and CFD is good, especially as RANS frequently fails to predict the length scale parameter correctly.

6.3 Numerical methods

To complement the experimental measurements, back-to-back CFD simulations were performed in ANSYS CFX (version 22.2). The computational model was based on the engine geometry with fully-resolved internal features. Steady simulations were performed at the nominal rig operating point. We now describe the computational domain, grid, boundary conditions and solver settings.

Computational domain

The computational domain includes two vanes (designed in pairs, with slightly different cooling schemes for *leading* and *trailing* vanes) and both external and internal flows. This is shown in Figure 6.4. The internal features include all vane internals, fully resolved cooling holes and the coolant feed plena. The upstream domain extent is the inlet cassette measurement plane (plane 1; see Figure 6.1), and the downstream extent is approximately three axial chords downstream of the NGV TE (parallel duct). The domain exit is approximately co-incident with the exit of the annular duct downstream of the vanes in the experiment.

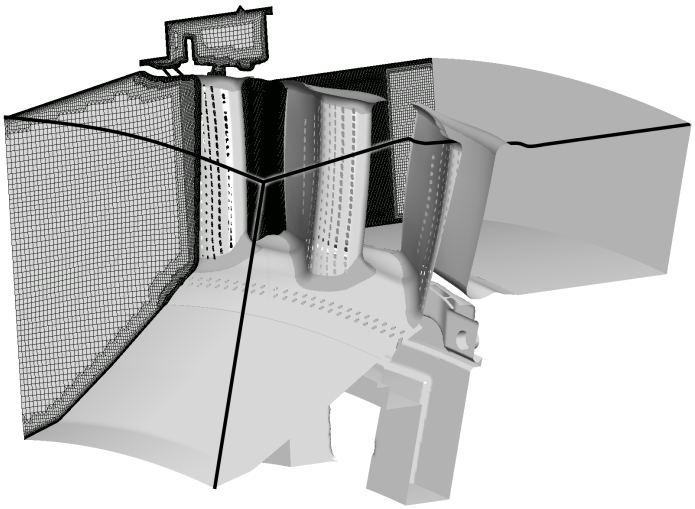


Figure 6.4: *Flow domain showing the vanes, cooling holes, and the coolant feed plena.*

Computational grid

A hybrid grid was generated with Boxermesh (version 3.8.3). The mesh consists primarily of unstructured hexahedra, with variable grid refinement near the walls and in the wake. A 23 layer inflation region was used near the walls, giving average y^+ values of 0.7, 1.3, 0.6, and 0.8 on the pressure side, suction side, endwalls, and internals of the vane, respectively. Local mesh refinement around small features was down to 0.04 mm, giving approximately 35 cells across a cooling hole diameter. The overall mesh had approximately 312 million cells. Detail views of the TE/wake refinement, film cooling holes, and internal rib turbulators are shown in Figure 6.5. Sensitivity to grid refinement was evaluated by refining the mesh globally. This is discussed in Appendix 6.B. Results are analyzed and discussed using data from the most refined grid.

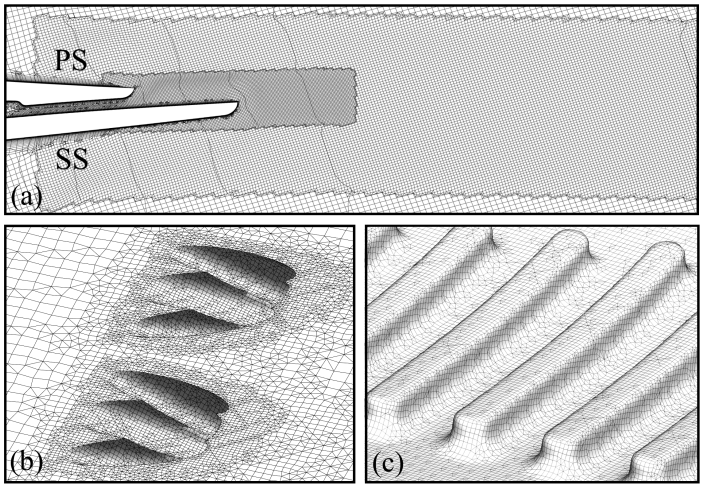


Figure 6.5: *Mesh detail views showing: (a) TE/wake refinement; (b) film cooling holes; (c) internal rib turbulators.*

Boundary conditions

The mainstream inlet boundary conditions of total pressure, total temperature, turbulence intensity, and length scale were set to the extrapolated traverse profiles at plane 1 (see Figure 6.2 and Figure 6.3). The hub and case coolant feeds were mass flow rate boundary conditions; 5% turbulence intensity and a viscosity ratio of 10 were specified. A radial equilibrium condition was used for the outlet static pressure, with the average outlet pressure adjusted iteratively to match the experimental vane pressure ratio (inlet total to platform static). A conformal periodic rotational interface was used for the circumferential boundaries of the domain. All remaining boundaries were modeled as adiabatic no-slip walls.

Solver settings

Simulations were steady-state using the k–ω SST turbulence model, with a turbulent Prandtl number of 0.50, which is optimized for free shear thermal mixing layers (see e.g. Chambers et al. [174]). The *high-resolution* discretization scheme, which is formally *second-order-accurate*, was employed for both the momentum equations and the turbulence closure method. The convergence criteria were that residuals had entered a limit cycle, with monitors of inlet pressure and outlet entropy oscillating around a constant average value. At convergence, domain imbalances were oscillatory, with a maximum amplitude of 0.02% for mass and enthalpy.

6.4 Performance metrics

In this section, we summarize the performance metrics for our analysis of the aerodynamic and thermal field downstream of the NGVs.

Whirl angle definition

To compare flow angle distributions downstream of the vane we define whirl (yaw) angle, α, by

$$\alpha = \arctan \frac{V_\theta}{V_x} \tag{6.1}$$

where V_x, and V_θ are, respectively, the axial, and circumferential components of velocity in a cylindrical coordinate frame coincident with the machine axis.

Kinetic energy loss coefficients

As measures of the aerodynamic efficiency of the NGV, we define four kinetic energy (KE) loss coefficients: a *local* KE loss coefficient, a *circumferentially-averaged* KE loss coefficient, a *plane-averaged* KE loss coefficient, and a *mixed-out* KE loss coefficient.

The *local* kinetic energy loss coefficient, $\zeta_1(r,\theta)$, is defined by

$$\zeta_1(r,\theta) = 1 - \frac{1 - \left(\frac{p_2(r,\theta)}{p_{02}(r,\theta)}\right)^{\chi}}{1 - \left(\frac{p_2(r,\theta)}{p_{01}}\right)^{\chi}} \tag{6.2}$$

where p_{01} is a reference inlet total pressure, p_{02} is the downstream total pressure (measured at plane 2, 3 or 4, in our experiments), and p_2 is the corresponding static pressure. The exponent χ is defined by $\chi = (\gamma - 1)/\gamma$, where γ the ratio of specific heats of air, which was assumed constant and equal to 1.40. Here the reference inlet total pressure (p_{01}) is calculated in real-time from the arithmetic mean of the fixed-rake total pressures ($p_{01,\mathrm{rake}}$) using a fixed, linear scaling factor k_p, which is derived from the rake data and the more detailed area survey data. That is: $p_{01} = k_p p_{01,\mathrm{rake}}$, where $p_{01,\mathrm{rake}}$ is the instantaneous average of the pressure measurements from fixed rakes. The local KE loss coefficient represents the ratio of the local kinetic energy deficit and the energy associated with an isentropic expansion from the mainstream total pressure, p_{01}, to the downstream local static pressure, p_2. We use it as a measure of the local aerodynamic inefficiency of the expansion.

Next, we define a *circumferential-average* KE loss coefficient (see discussion of Burdett and Povey [147]), $\zeta_3(r)$, as

$$\zeta_3(r) = 1 - \frac{1 - \left(\frac{\overline{p_2}(r)}{\overline{p_{02}}(r)}\right)^{\chi}}{1 - \left(\frac{\overline{p_2}(r)}{p_{01}}\right)^{\chi}} \tag{6.3}$$

where p_{01} and p_{02} have the same meaning as in the preceding equation. Overbars represent mass-flux averaging in the case of p_{02}, and area averaging in the case of p_2. The area and mass-flux averages were evaluated across two vane pitches in the circumferential direction, with the circumferential limits arranged to track the same wakes at each axial location downstream of the vanes. When reporting midspan data, averages were taken between 45% and 55% span.

A *plane-averaged* KE loss coefficient, ζ_4, is defined according to the definition of Lawaczeck [187]:

$$\zeta_4 = 1 - \frac{(\dot{m}_{\mathrm{m}} T_{01} + \dot{m}_{\mathrm{c}} T_{0\mathrm{c}}) \left[1 - \left(\frac{\overline{p_2}}{\overline{p_{02}}}\right)^{\chi}\right]}{\dot{m}_{\mathrm{m}} T_{01} \left[1 - \left(\frac{\overline{p_2}}{p_{01}}\right)^{\chi}\right] + \dot{m}_{\mathrm{c}} T_{0\mathrm{c}} \left[1 - \left(\frac{\overline{p_2}}{p_{0\mathrm{c}}}\right)^{\chi}\right]} \tag{6.4}$$

where $\dot{m}_{\mathrm{m}}$ and $\dot{m}_{\mathrm{c}}$ denote the mainstream and coolant mass flow rates respectively, and $p_{0\mathrm{c}}$ is the coolant total pressure. The overbars represent mass-flux averaging for p_{02}, and area averaging for p_2, both over the full span. T_{01} is the total temperature at plane 1, and $T_{0\mathrm{c}}$ is the mass-weighted average total temperature of the hub and case coolant feeds. This plane-averaged KE loss

coefficient represents the kinetic energy deficit of the bulk flow, relative to the mass flow rate-weighted kinetic energy of hypothetical isentropic expansions of both coolant and mainstream flow to the area-average downstream static pressure, $\overline{p_2}$. We use it as a single scalar measure of the inefficiency of the entire expansion, accounting for excess pressure in the coolant stream. For cold testing, $T_{01} = T_{0c}$ such that the temperature terms cancel out, and the definition of plane-averaged KE loss coefficient used by Burdett and Povey [147] is recovered.

We also define a *mixed-out* KE loss coefficient, ζ_5, using the Dzung mixing model [188] (see also discussion in [147]), by

$$\zeta_5 = 1 - \frac{(\dot{m}_{\mathrm{m}} T_{01} + \dot{m}_{\mathrm{c}} T_{0\mathrm{c}}) \left[1 - \left(\frac{\widetilde{p_2}}{\widetilde{p_{02}}}\right)^{\chi}\right]}{\dot{m}_{\mathrm{m}} T_{01} \left[1 - \left(\frac{\widetilde{p_2}}{p_{01}}\right)^{\chi}\right] + \dot{m}_{\mathrm{c}} T_{0\mathrm{c}} \left[1 - \left(\frac{\widetilde{p_2}}{p_{0\mathrm{c}}}\right)^{\chi}\right]} \tag{6.5}$$

where averages of p_{02} and p_2 (indicated with tilde) are performed according to the Dzung-method [188] in which a mixed-out state is calculated from the local flow field according to one-dimensional conservation laws for mass, momentum in the meridional plane, angular momentum around the machine axis, and energy. The equations for this are summarized by Pianko and Wazelt [189]. The mixed-out KE loss coefficient considers the loss to a hypothetically mixed state, and so accounts for loss that would arise from the complete mixing out of existing secondary flow. This allows comparison between flows which are mixed to different degrees, for example, a comparison between planes 2, 3 and 4 in the experiment, or between experiment and CFD at a particular plane.

Finally, we introduce the concept of the secondary kinetic energy coefficient (SKE), which is defined as the difference between mixed-out and plane-averaged KE loss coefficients, i.e.

$$\mathrm{SKE} = \zeta_5 - \zeta_4 \tag{6.6}$$

A reduction in SKE indicates the mixing out of a non-uniform flow, with a value of zero corresponding to the fully-mixed state. In real flows, over finite length scales, SKE may decay to a stationary, but non-zero value. This occurs if the real flow does not mix-out to the same equilibrium conditions as the mixing-model used to estimate ζ_5 (see comparison of mixing models by Burdett and Povey [190]).

Flow effectiveness: the non-dimensional flow temperature

The thermal field downstream of the vane results from mixing of the hot mainstream and coolant flow. To non-dimensionalize the total temperature field we define a *flow effectiveness*, Θ, by

$$\Theta = \frac{T_{02}(r,\theta) - T_{0c}}{T_{01} - T_{0c}} \tag{6.7}$$

where T_{01} is a *reference* inlet total temperature, T_{02} is the downstream total temperature to be measured, and T_{0c} is the mass-weighted-average total temperature of hub and case coolant feeds. In similarity to the reference total pressure, the reference total temperature is calculated in real-time from the arithmetic mean of the fixed-rake total temperatures ($T_{01,\mathrm{rake}}$) using a small, fixed, linear scaling factor k_T, which is derived from the rake data and the more detailed area survey data. That is $T_{01} = k_T T_{01,\mathrm{rake}}$, where $T_{01,\mathrm{rake}}$ is the instantaneous average of the temperature measurements from fixed rakes. A physical interpretation of the flow effectiveness, Θ, is that the related variable $\lambda = 1 - \Theta$ is equal to the cold gas mass fraction.

6.5 Experimental and numerical results

In this section we compare and analyze the experimental and numerical results. Estimates of the experimental measurement uncertainty are summarized in Appendix 6.A.

NGV exit circumferential static pressure profiles

Experimentally-measured and CFD-predicted circumferential distributions of NGV platform overhang pressure are presented in Figure 6.6. The purpose is to validate the operating pressure ratio in CFD. Static pressures are normalized by the upstream total pressure. Flow over two passages is shown, with the circumferential coordinate, θ_{NGV}, normalized by the vane pitch, s. The vane TE positions correspond to θ_{NGV}/s = 0, 1.

Overall the CFD prediction is in reasonable agreement with the experimental data, with the radial equilibrium component well-matched, but with an exaggerated circumferential potential field disturbance in the CFD when compared to the experiment. Minima in the pressure distribution occur at approximately θ_{NGV}/s = −0.6 and θ_{NGV}/s = 0.4, at the point of peak-suction on the uncovered suction side. Maxima occur at approximately θ_{NGV}/s = −0.1 and θ_{NGV}/s = 0.9, corresponding to the TE region where the PS and SS flows meet. These can be explained with reference to the CFD-predicted potential field at midspan, which is shown in Figure 6.7. The axially-projected TE locations (at θ_{NGV}/s = 0.0 and 1.0) are marked TE1 and TE2. Regions around these lines

are associated with high-pressure disturbances. These modify the whirl angle as the flow passes through them. We consider this effect in the next section.

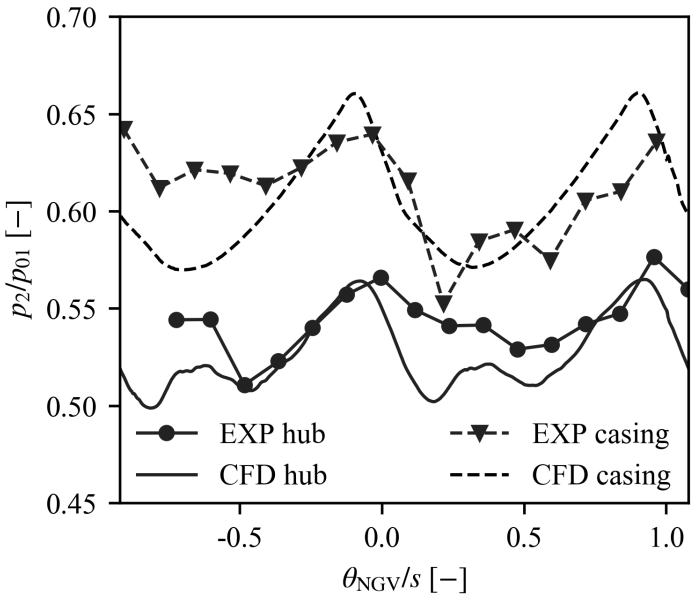


Figure 6.6: *Experimentally-measured and CFD-predicted circumferential distributions of NGV platform overhang pressure, presented as ratio to inlet total pressure.*

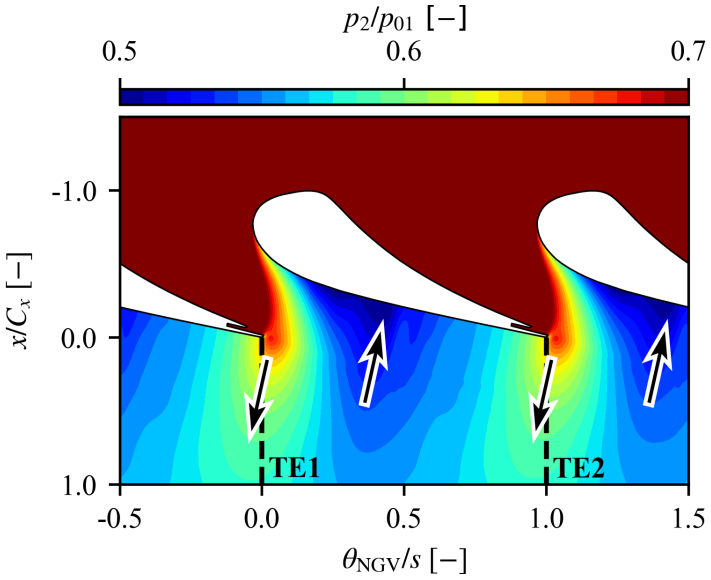


Figure 6.7: *CFD-predicted static pressure distribution at midspan. Data are normalized by upstream total pressure. Arrows indicate the direction of flow deflection in response to pressure gradients in the streamline-normal direction.*

Whirl angle profiles

Experimentally-measured and CFD-predicted whirl angle (α) distributions at downstream planes 2, 3, and 4 are shown in Figure 6.8. The data are datumed to the mean midspan metal angle of the vane, α_{TE}, which is in the typical range for a modern transonic turbine with approximately 50% reaction; i.e. we present $\alpha - \alpha_{\mathrm{TE}}$ in Figure 6.8. The experimental traverse data and CFD analysis consider the same two wakes at each plane. That is, the data analysis region moves around the annulus following the wakes. We differentiate between the NGV-fixed-reference-frame circumferential coordinate, θ_{NGV}, and the wake-following-reference-frame circumferential coordinate θ_{wake}. The wake-following circumferential coordinate translates around the annulus at the same rate as the mass-mean flow. This is shown diagrammatically in the lower half of Figure 6.8. The wakes, located around θ_{wake}/s = 0.0 and 1.0, are marked W1 and W2, respectively. In the upper half of Figure 6.8, a contour line of normalized local KE loss corresponding to $\zeta_1/\zeta_{\mathrm{ref}}$ = 0.5 is shown, where ζ_{ref} is defined as the experimentally-measured mixed-out KE loss coefficient at plane 4. Axially projected locations of the NGV TEs are marked TE1, TE2 and TE3. The regions axially downstream of the TE are associated with a high-pressure perturbation in the vane potential field (see Figure 6.7).

First, consider the experimental whirl angle distribution at plane 2. The radial distribution of flow-angles is primarily dictated by spanwise metal-angle distribution, which is approximately 3° higher in the near-casing region than the near-hub region. Comparing the CFD to the experiment, we see very good agreement between the distributions, with a maximum local difference of approximately 5°.

Downstream of the TE, *local* whirl angle modulation can be introduced by the vane potential field. As the flow passes through the vane potential field, it is deflected towards the axial direction in a positive axial pressure gradient (i.e. towards lower pressure) and away from the axial direction in a negative axial pressure gradient. The direction of deflection is indicated with arrows in Figure 6.7. The effect explains the slightly lower whirl angles on the immediate right of the high-pressure regions axially downstream of the vane TEs (aligned with TE1, TE2 etc.) and slightly higher whirl angles axially downstream of the vane SS (midway between vane TEs). The result is a slightly sinusoidal distribution of whirl angle with circumferential displacement.

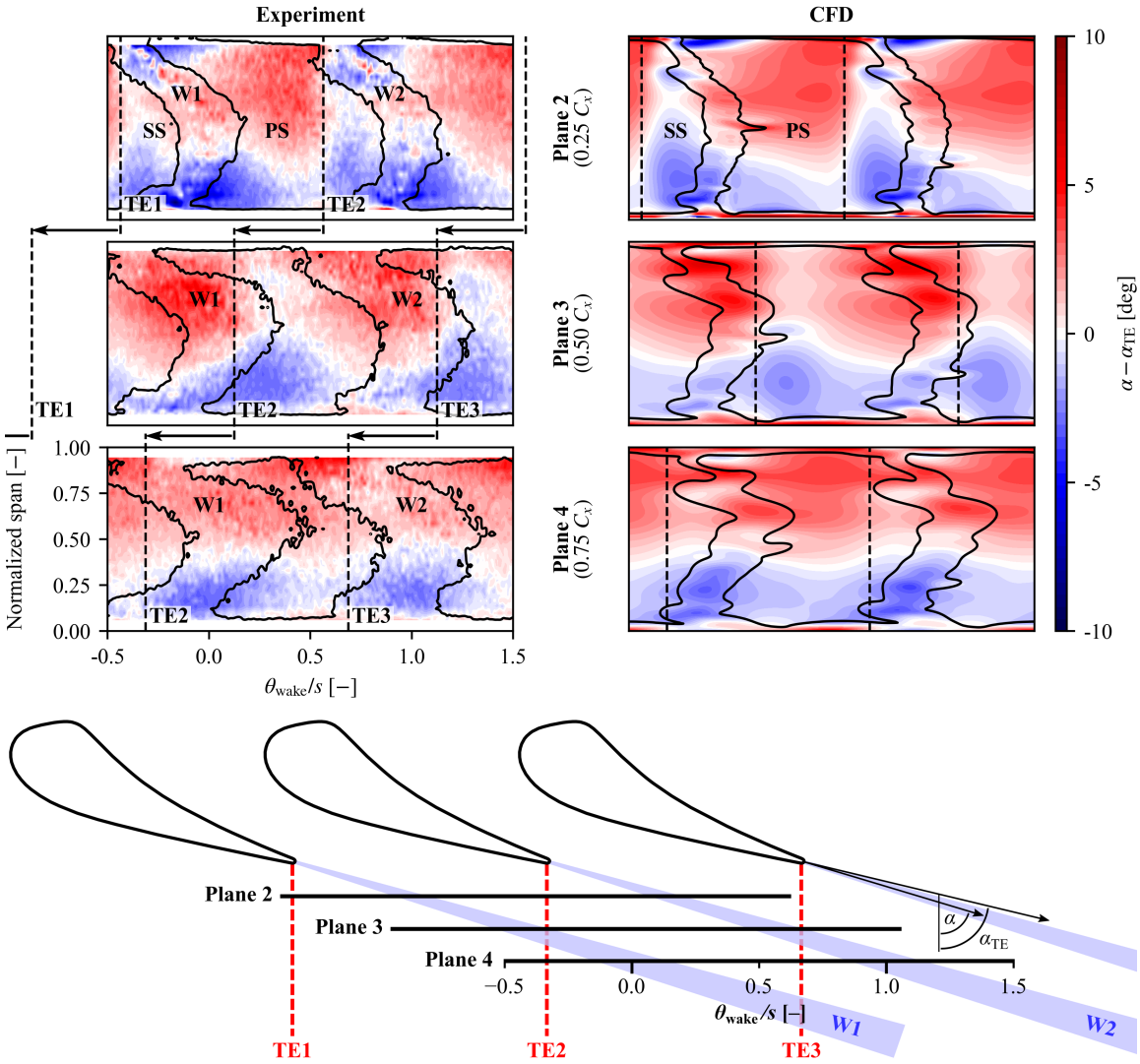


Figure 6.8: *Whirl angle (α) distributions at planes 2, 3, and 4 for experiments and CFD. Axially projected TE locations are marked TE1, TE2 and TE3. Wakes are marked W1 and W2. The contour of normalized local KE loss corresponding to $\zeta_1/\zeta_{\text{ref}} = 0.5$ is superimposed.*

Now consider the experimental whirl angle at plane 3. Here the flow is partially mixed-out, with lower local variation. As we move downstream in the wake-following reference frame, the vane-fixed potential field moves towards the left. This is indicated using arrows in Figure 6.8. The high-pressure perturbations now intersect plane 3 at approximately $\theta_{\text{wake}}/s = 0.1$ and 1.1. Corresponding regions of low whirl appear at approximately around $\theta_{\text{wake}}/s = 0.4$ and 1.4. At plane 3 the high whirl location (approximately half a vane pitch out of phase with the low whirl region) coincides with the wakes ($\theta_{\text{wake}}/s = -0.1; 0.9$), resulting in an interesting interaction with the potential field: in the upper half of the span, the peak whirl angle is higher than at plane 2. This local *decrease* in uniformity relative to plane 2 appears to occur because the relatively low momentum fluid in the wake is more strongly affected by the potential field, which acts to increase whirl angle. A similar—but reversed—effect can be seen at plane 4, where the whirl angle in the lower half of

the wake is lower than at plane 3 (increasing non-uniformity) due to the low momentum wake fluid being overturned towards the axial direction by the positive axial pressure gradient in this circumferential location at this plane. The effect is particularly pronounced for the CFD results.

Radial profiles of circumferentially-averaged (mass-flux-weighted) whirl angles are shown in Figure 6.9. The general trend is a decrease in whirl angle in the direction from casing to hub with excursions from this trend in the near-wall secondary-flow regions. Between 25% and 75% span the CFD-predicted profiles are in excellent agreement with the experimental data, with maximum differences of only 0.5° between the two data. Above 75% and below 25% span, in the near-wall regions there is greater disagreement between CFD and experiment, with CFD predicting higher turning than measured by up to 1.6°. As a result, mass-flux-weighted whirl angle was slightly greater in CFD (evaluated over the area common with experiments), with values (relative to experiments) of +0.65, +0.20, and +0.02 degrees at planes 2, 3, and 4, respectively. Discrepancies of the mass-flux-weighted whirl angle are similar in magnitude to the bias uncertainty of the experimental data, which we estimate to be around ±0.8° (95% confidence interval; see Appendix 6.A).

An increase in absolute mass-flux-averaged whirl angle between planes 2 and 3 is seen for both the experimental data (+0.51°) and numerical results (+0.16°). This is thought to occur due to a slight reduction in axial velocity caused by a slight increase in passage area in the downstream direction (see Figure 6.1), with approximate conservation of angular momentum of the bulk flow.

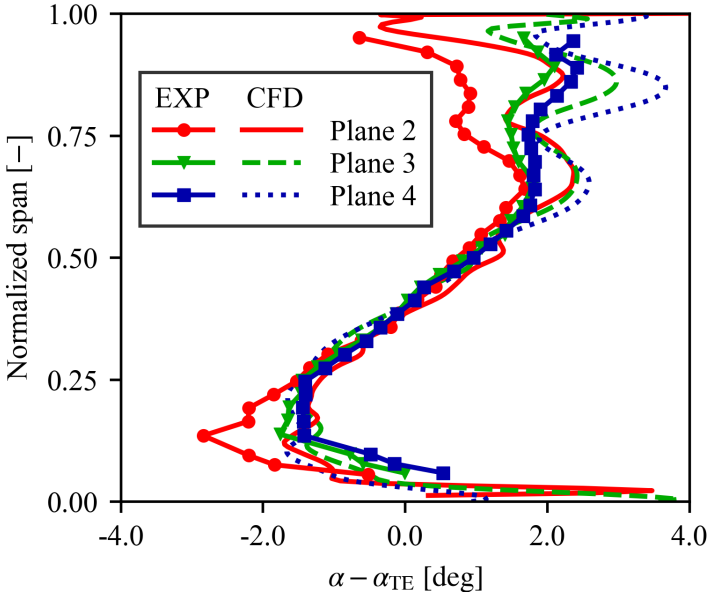


Figure 6.9: *Whirl angle (α) radial distributions at planes 2, 3, and 4, for experiments and CFD.*

A notable feature of both experimental and numerical results is the double-peak whirl angle pattern between 55% and 90% span. Here, the flow angles are distorted by a clockwise-rotating (when viewed from downstream) vortex centered at approximately 80% span, which raises whirl angle around 85% span and reduces whirl around 75% span. The minimum at approximately 75% span gives rise to a weak second peak at approximately 60% span. The vortex develops near the leading-edge SS, seemingly as a result of an interaction between the casing endwall cooling flow and the vane leading-edge potential field. Noting the location of origin and direction of rotation, it is interesting that the vortex is not identifiable as either a conventional *passage vortex* or a conventional *counter-vortex* according to the generally-accepted terminology. This highlights the complexity of secondary flows for heavily cooled vanes. Similar modulations of the whirl angle, visible around 10%, 30%, and 55% span in the CFD data, correspond to smaller vortex structures in the flow.

Local kinetic energy loss

Experimentally-measured and CFD-predicted distributions of local KE loss coefficient at downstream planes 2, 3, and 4 are shown in Figure 6.10. The wakes are marked W1 and W2. Both experimental and CFD-predicted values of local KE loss coefficient, ζ_1, have been normalized by the experimentally-measured *mixed-out* KE loss coefficient at plane 4. We refer to this value as the reference KE loss coefficient, ζ_{ref}.

First, consider the normalized experimental local KE loss coefficient at plane 2. The wakes have the shape of the positively compound leaned TE, with relatively uniform peak KE loss coefficient across the span. Local peaks at approximately 12% and 79% span correspond to hub and casing secondary flows, respectively. The casing endwall BL is marked by a region of low momentum fluid which is thicker towards the SS corner of the vane due to the cross-passage migration effect. A similar pattern can be observed at the hub, but with—on average—greater BL thickness than at the case. This likely results from a combination of higher speed flow near the hub wall, and local separation caused by diffusion on the lee side of a high-curvature blend in the aft hub platform just upstream of plane 2 (see Figure 6.1). The CFD predictions are in good agreement with the experiment, with similar overall distributions of loss, but with evidence of undermixing in several regions: narrower wakes with higher peak values; thinner BL regions near the endwalls. This results from undermixing in the CFD method, a seemingly common problem when simulating transonic NGV flows using turbulence models (see, e.g. [147, 179]).

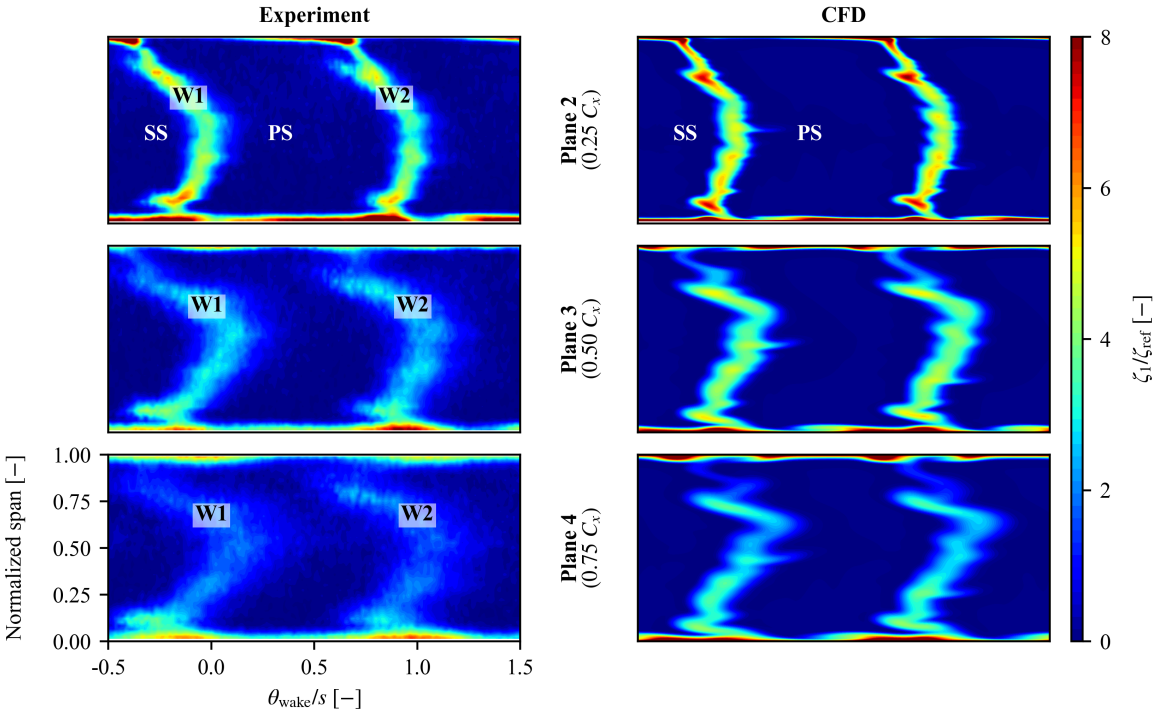


Figure 6.10: *Normalized local KE loss coefficient ($\zeta_1/\zeta_{\mathrm{ref}}$) distributions at planes 2, 3, and 4 for experiments and CFD.*

Now consider the experimental KE loss at plane 3 and plane 4. As expected, the wakes and secondary flow features mix out as the flow progresses downstream. The wakes also become stretched-out in the circumferential direction due to radial variation in the progression of the wake. That is, radial variation in the ratio of angular displacement to axial displacement, which depends on the local whirl angle and radius as $d\theta_{\mathrm{NGV}}/dx = \tan(\alpha)/r$. The stretching-out of the CFD-predicted and experimentally-measured wakes is similar, but with greater local variation in the shape for CFD than experiment in the near-casing region (70% to 100% span) for planes 3 and 4. This is explained by the greater local angle variation in the CFD than experiment. The CFD wake also becomes slightly more asymmetric in appearance at planes 3, and 4 (i.e. less swept-back near the casing). This indicates greater angular displacement in CFD than in the experiment, which is consistent with the overprediction of whirl angles in this region (see Figure 6.9).

Radial profiles of circumferentially-averaged kinetic energy loss coefficient, ζ_3, are shown in Figure 6.11 for planes 2, 3 and 4 for both experiment and CFD. The values are normalized by ζ_{ref}.

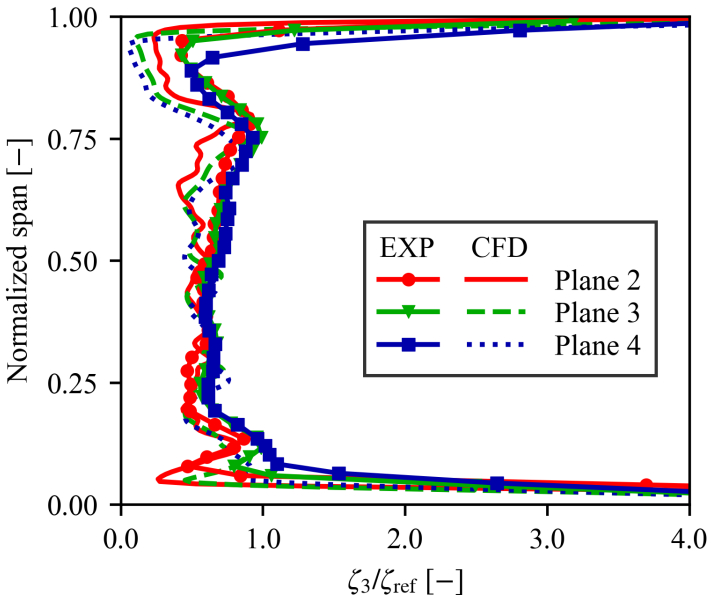


Figure 6.11: *Experimentally-measured and CFD-predicted radial distributions of normalized circumferentially-averaged KE loss coefficient (ζ_3/ζ_{ref}) at planes 2, 3, and 4.*

First consider the experimental data at plane 2. The experimental profiles of KE loss are relatively flat between 20–60% span, with local peaks around 15% and 75% span, which are associated with the secondary flow loss cores. Near the walls, KE loss increases steeply on account of the endwall boundary layers. In the corresponding CFD prediction for plane 2, the radial distribution of KE loss—including the secondary flow peaks—is captured reasonably well. In the *profile loss region*, which we define to be the central 80% of the span, the profile KE loss is slightly lower in the CFD simulation than the experiment. The CFD-predicted boundary layers are also thinner than for the experiment.

Moving axially downstream, to planes 3 and 4, we observe boundary layer growth in both experiments and CFD. We also note an increase of KE loss in the 20–60% span range. This is associated with the conversion of secondary kinetic energy (SKE) into realized losses (i.e. the generation of loss through mixing-out of non-uniform flow). We consider mixing characteristics quantitatively in the next section by examining the change with streamwise distance of wake widths, peak loss and integrated loss.

Circumferential kinetic energy loss distributions at midspan: wake width, peak loss, and integrated loss

In this section we consider the wake development with streamwise distance in more detail. Midspan distributions of normalized KE loss at planes 2, 3, and 4 are shown in Figure 6.12 for

both experimental measurements and CFD predictions. The wakes are marked W1 and W2. We analyze these distributions in terms of wake width, peak loss, and integrated loss. We determine wake width and peak loss from the radially mass-flux-weighted average profile of ζ_1 between 45% and 55% span, where the width is the full width at half maximum. Similarly, integrated midspan loss is calculated using Equation 6.3, where area and mass averages are evaluated between 45–55% span. Reported values are the average of both W1 and W2. An important result of Burdett and Povey [147] is that apparently disparate trends of these parameters when presented as a function of downstream axial distance from a nominal TE plane collapse extremely well when presented as a function of *real streamwise distance* from a local TE position. For this reason, we present trends of these parameters as a function of streamwise distance. In the calculation of streamwise distance constant whirl angle is assumed between the downstream measurement planes. The resulting trends are shown in Figure 3.13. For the current experiment, midspan data at planes 2–4 have equivalent streamwise distances, d, of approximately $0.99C_x$, $1.99C_x$, and $3.00C_x$.

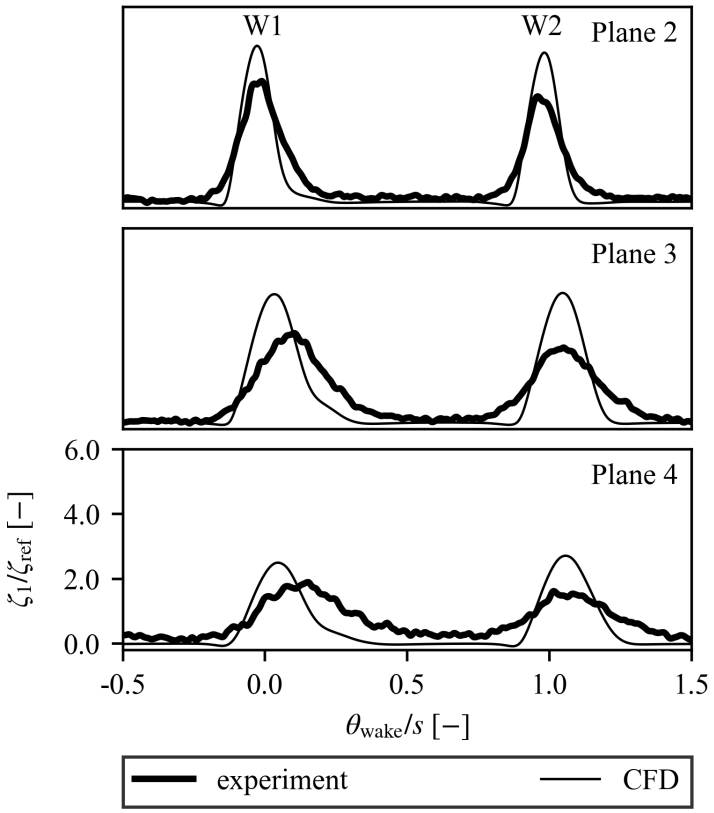


Figure 6.12: *Circumferential distributions of normalized KE loss coefficient at midspan (45–55% span) in planes 2, 3, and 4 for experiments and CFD.*

First consider the experimental and CFD data in Figure 6.12 at downstream plane 2. The most striking feature is the undermixed CFD wake in comparison to the experiment. Here the peak KE loss coefficient exceeds that of the experiment by 30% for W1 and 43% for W2. The CFD wake is correspondingly narrower: we analyze the relationship between peak loss and wake width in the following paragraphs. In the experimental data, W1 and W2 are broadly similar, but peak loss for W2 is 13% lower than for W1. This is thought to be an artefact of spanwise loss redistribution resulting in a radial variation in the wake depth. An example of this can be seen at approximately 50% span for W2 in both the plane 2 and plane 3 data of Figure 6.10, where there is a *pinch* in the wake. This can occur by local streamline divergence on the vane surface, causing boundary layer redistribution, which is a common effect particularly for the SS flow. Similar effects can be seen in all three planes of the CFD-predicted distributions of Figure 6.10, with distinct radial variation along the wake centerline. Another interesting feature of the experimental data is the non-zero loss in the freestream ($\theta/\theta_{\text{wake}} \approx 0.5$ and 1.5). Ames and Plesniak [82] showed that these so-called *background losses* occur at elevated inlet turbulence intensities, but their origin is not fully understood. Looking now at the CFD-predicted data in Figure 6.12, W1 and W2 have *peak* loss within 4% of each other. This lends credibility to the earlier theory that the 13% difference in the experimental peak intensities is an artefact from loss redistribution, likely due to hardware variations. The CFD data do not show background losses.

Data at plane 3 and plane 4 show the general trend of wakes broadening with peak loss coefficient values reducing, as the wakes mix out. The rate of mixing is higher in the experiment than in CFD. We now quantitatively analyze these mixing rate trends.

The trends of wake width, peak loss, and integrated loss (Equation 6.3) with streamwise distance, d, are shown in Figure 6.13. The CFD and experimental trends from the current study are compared to experimental and CFD-predicted data from Burdett and Povey [147]. This is an interesting reference point because it is a second example of a heavily cooled NGV from a modern aero-engine. The study [147] was conducted two years before the current experimental campaign, using a different working section, with largely independent instrumentation, and a separate processing team. This is relevant because it shows the independence of the two datasets. Although both engines had identical vane count, and were from the same family, an important difference between [147] and the current study is that [147] used a centered-ejection TE design (see Burdett and Povey [191]) whereas the current study used a SS-overhang TE design. As we will see, the centered-ejection design has higher overall loss, higher wake thickness, and lower peak loss: the

reasons for this are complex and are influenced by the size of the TE *base region* and the unsteady shedding in this region, which is itself influenced by the TE coolant ejection design and momentum flux [191]. For both studies, we consider the restacked-wake-average between 45% and 55% span in which before averaging, each radial band of data is shifted circumferentially so that the peaks are aligned. The reason for comparing restacked data is that there can be significant lean of the mid-span wake, which in a direct averaging approach would lead to artificial mixing of misaligned peaks.

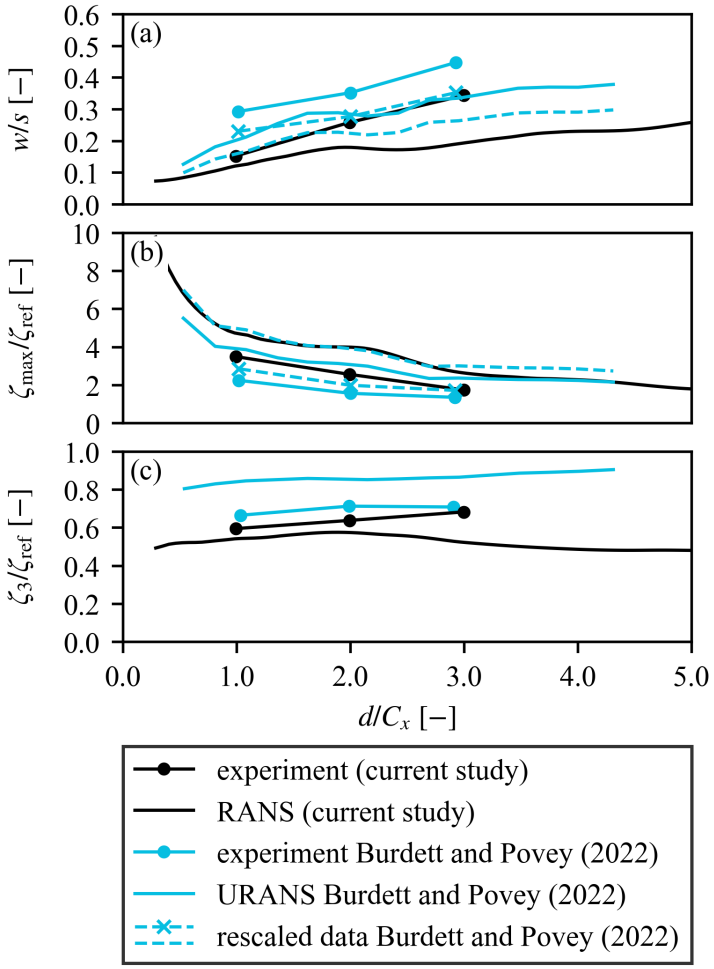


Figure 6.13: *Trends with streamwise distance of: (a) wake width; (b) normalized peak KE loss coefficient; (c) circumferentially averaged normalized KE loss coefficient. Experimental and CFD data from Burdett and Povey [147] are presented on the same axes for comparison.*

In the study of Burdett and Povey [147] the non-dimensional TE thickness (TE thickness normalized by the axial chord) was 1.27 times thicker than the current study. To facilitate closer comparison of the *streamwise trends* on a like-for-like basis with the data of the current study, in Figure 6.13 we also present *rescaled* trends of wake width and peak intensity from the study Burdett and Povey [147]. Wake width is divided by 1.27 and (to preserve the product of

normalized width and normalized peak loss) normalized peak loss is multiplied by 1.27. This is a crude rescaling method but allows first-order correction for the difference in geometries.

Consider first the evolution of wake width with streamwise distance, which is shown in Figure 6.13a. The wake width, w, has been normalized by the vane pitch, s. In the current experimental data, the wake successively grows from approximately $0.15s$ at plane 2, to $0.26s$ and $0.34s$ at planes 3, and 4 respectively. The trend is approximately linear with streamwise distance. The slightly decreasing gradient of wake width with streamwise distance is consistent with the self-similarity solution for the far-wake, where the halfwidth is proportional to the square root of the streamwise distance (see e.g. Wilcox [141]). Now consider the experimental data of Burdett and Povey [147]. In this data the wake widths were higher ($0.29s$, $0.35s$, and $0.45s$, at planes 2, 3, and 4, respectively) than the current experiment by—on average—a factor of 1.45. The greater wake width for the experimental results of Burdett and Povey [147] can be explained in part by the 27% greater non-dimensional TE thickness, considering that we might—simplistically—expect the wake width at the TE to be proportional to the sum of SS and PS momentum thickness and the TE metal thickness. Indeed, the rescaled trends of experimental wake width, which are shown with cross markers in Figure 6.13a, indicate that the experimental trends of the current study and those of Burdett and Povey [147] almost collapse once the differences in TE thickness are adjusted for. At $d/C_x \approx 1$, rescaling closes the gap to $0.08s$, whereas for $d/C_x \approx 2$, and $d/C_x \approx 3$, the difference is reduced to $0.02s$, and $0.01s$, respectively. The significantly greater discrepancy at the first plane might be expected, considering the effects of centered-ejection on wake spreading characteristics [191].

Now consider the CFD results for both studies. Predictions of wake spreading rates have a number of implications for engine design, for example in terms of establishing the unsteady aerothermal load on the downstream rotor. The trends of CFD-predicted wake width with streamwise distance are broadly similar to the experimental data but with two distinct differences.

Firstly, there are a number of distinct plateaus in the rising trend, which are explained by interaction of the potential field and the wake, which periodically increases or decreases the wake whirl angle, leading to modulation in the wake width as measured on an axial plane. This behavior cannot easily be captured in the experimental data, due to the comparatively large spacing between the measurement planes. Secondly, an offset of the CFD-predicted wake width from the experimental data, with the wake width being underpredicted on average across three experimental planes by 34% in the current study, and by 23% in the study of Burdett and Povey [147]. This

effect arises because of undermixing in the CFD solution. To take account of the larger TE thickness in [147], rescaled CFD trends from [147] are shown in Figure 6.13a as dashed lines. This closes the gap with the current study by approximately half the initial difference. Overall, the experimental and CFD trends in these—essentially—independently constructed studies show remarkably similar characteristics.

Now consider the trends in the peak value of KE loss coefficient. These are shown in Figure 6.13b. For the current study, both CFD and experimental wake depth follow a trend of quasi-exponential decay with similar proportional streamwise decay *rates*. The peak CFD loss coefficient was consistently higher than the experiment (undermixing), with an average value (across three experimental evaluation planes) 45% higher. The experimental results of Burdett and Povey [147] have similar trends, though normalized peak intensity was on average only 66% of that in the current data. For the rescaled trend (i.e. multiplied by the non-dimensional TE thickness ratio), this figure is improved to 84%.

For the CFD data of [147], the trend was, on average, 77% higher than the corresponding experimental trend. Higher peak loss is—of course—concomitant with lower wake width. For the current study and the study of Burdett and Povey [147] we might crudely consider that the 34% and 23% deficits, respectively, in wake width, might—for the same overall loss—be accompanied by a corresponding excess in wake depth of 52% and 30% (inverse percentages). The former value (current study) is in good agreement with the difference in wake width between CFD and experiment. That is, we expect CFD to predict integrated loss relatively accurately, even though the flow is undermixed. The latter value (Burdett and Povey [147]) accounts for only half of the excess wake width predicted by CFD. The remainder is accounted for by an overestimate in integrated loss. In this case the CFD is both undermixed and overestimates integrated loss. We now consider this in more detail.

Trends of integrated midspan loss with streamwise distance are shown in Figure 6.13c. For the current study, experimental loss increases slightly with axial distance, from 0.60 ζ_{ref} at plane 2 to 0.68 ζ_{ref} at plane 4, along a shallow linear trend. The CFD trend is consistently lower, with an average difference of 14% across three measurement planes. Based on the 34% under-prediction of wake width and the 45% over-prediction of wake depth, an underprediction of integrated loss of 4% would have been expected. The additional 10% deficit can be explained by non-zero freestream loss, which is significant for the experimental data only (see circumferential profiles in Figure 6.12). As we have mentioned, these so-called background losses have been observed to occur at high levels

of inlet turbulence [82]. Now consider the CFD trend of integrated loss with streamwise distance. CFD-predicted midspan KE loss increases approximately linearly, reaching a maximum around $d/C_x \approx 2$, after which it begins to reduce again. A reduction indicates redistribution of loss to other radial positions. This occurs due to the tendency of low momentum fluid in the wake to migrate radially-inward. This highlights the limitations of using a narrow radial band as a proxy for profile. The experimental data of Burdett and Povey [147] are relatively similar in both magnitude and form to the current study. This is not unexpected as the engine parts were taken from engines of the same family (but different generations). So far as the CFD comparisons of Burdett and Povey [147] are concerned, the trend is similar to the experimental data (approximately constant), but the integrated loss is overestimated by on average 23%. Presumably, this is related to the excess loss, which arises from modeling film cooling holes using point-sources as opposed to resolving them, as was done in the current study.

Mixed-out and plane-averaged kinetic energy loss coefficients

In this section we consider the mixed-out (ζ_5) and plane-averaged (ζ_4) KE loss coefficients for the entire flow. These are presented in Figure 6.14 as a function of the normalized axial coordinate for both the experimental data (three planes) and CFD (evaluated at axial intervals of 0.4 mm). The data are normalized by the experimentally-measured mixed-out loss coefficient at plane 4, ζ_{ref}. We also decompose the plane-averaged loss coefficient into a profile-region loss coefficient, ζ_{p} and an endwall-region loss coefficient, ζ_{e}. A common approach is to define endwall loss as the difference between plane-averaged loss, and profile loss (see e.g. Coull [192]). A profile-region KE loss coefficient was evaluated by calculating the mass-flux-weighted total pressure over the central 80% span and substituting this value for $\overline{p_{02}}$ in Equation 6.4. Because the choice of span range for calculating profile loss is somewhat arbitrary, it has been verified that the sensitivity of profile KE loss to the span range is acceptable. For averaging windows that include 40% to 90% of the *total span* but arranged symmetric about the midspan, the profile loss varied with averaging window size by less than ±3% at any one axial plane.

First, consider the CFD-predicted normalized mixed-out KE loss coefficient (solid line). At the TE plane, normalized mixed-out KE loss coefficient takes a value of 0.90. The trend with axial distance is that it decreases to a minimum of 0.80 at approximately x/C_x = 0.2, before rising approximately linearly to 0.88 at x/C_x = 0.75. In principle, we would expect the mixed-out loss coefficient to remain constant by definition. The initial *decrease* occurs because of continued flow turning at the hub and casing, where the airfoils extend up to $0.2C_x$ (recall the TE datum,

x/C_x = 0.0, is defined at midspan). In the context of the Dzung mixing framework, the additional flow turning reduces mixed-out loss, because it increases the downstream KE. A quasi-linear *increase* of mixed-out loss—starting around 0.20 C_x—is the result of KE dissipation through friction at the endwalls. Over the axial range of experimental data, the CFD-predicted mixed-out KE loss trend is similar to the corresponding experimental trend (triangular markers), but with CFD underpredicting mixed-out loss by 12% on average across three measurement planes. The fact that the trends are similar indicates that the *rate* of endwall loss production is accurately captured by CFD, this being the only mechanism for increasing mixed-out KE loss for a constant-area horizontal duct.

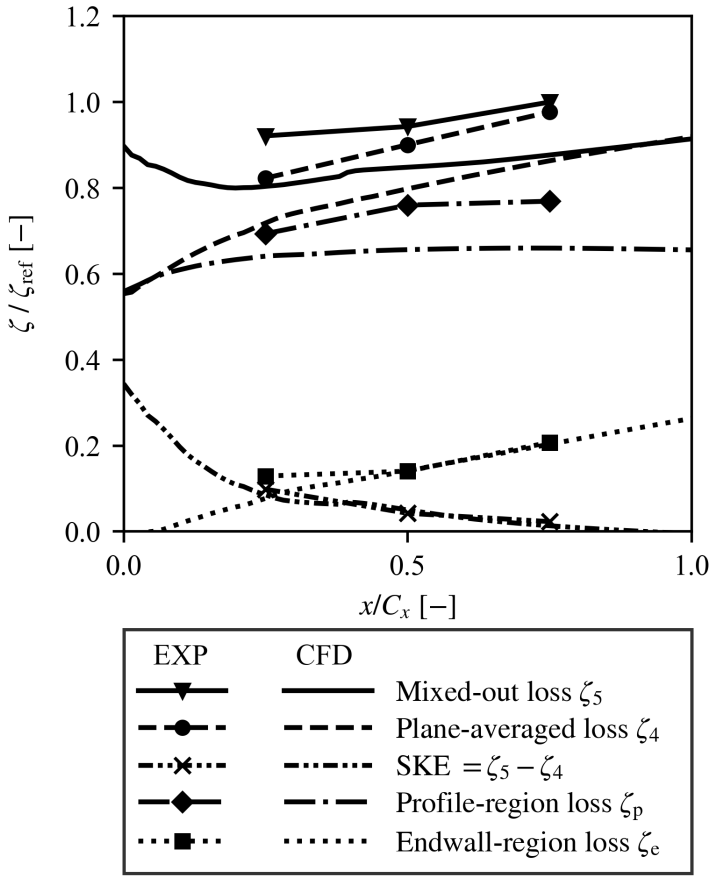


Figure 6.14: *Axial evolution of the mixed-out loss coefficient (ζ_5), plane-averaged loss coefficient (ζ_4), SKE coefficient (SKE), profile-region loss coefficient (ζ_p) and endwall-region loss coefficient (ζ_e) for experiments and CFD. Data are normalized by the reference KE loss coefficient (ζ_ref).*

Now consider the CFD-predicted normalized plane-averaged loss coefficient (dashed line). At the TE (x/C_x = 0.0) plane-averaged KE loss increases steeply due to mixing of the PS, SS, and TE coolant streams, which are all initially at different velocities. The plane-averaged loss approaches the CFD-predicted mixed-out KE loss trend (solid line) quasi-asymptotically, as secondary kinetic

energy (SKE) is converted into realized losses. Around x/C_x = 0.9, the lines representing CFD-predicted mixed-out and plane-averaged KE loss intersect such that $\zeta_4 > \zeta_5$. This is surprising because it implies that SKE is negative, which is *conceptually* non-physical. Mathematically, however, SKE—calculated using Equation 6.6—can adopt small negative values, because mixed-out loss depends on the *assumed* mixed-out velocity profile (see e.g. comparison of free and forced vortex models in [190]). The fact that SKE can only be guaranteed everywhere-positive when the real flow mixes out to the same conditions as assumed by the mixing model points to the limitations of mixing models, and the arbitrariness of the definition of SKE.

Now consider the experimentally-measured normalized plane-averaged KE loss coefficient (circular markers). In close similarity to the CFD trend, the experimental plane-averaged KE loss also approaches the corresponding (experimental) mixed-out KE loss asymptotically. The CFD-predicted plane-averaged KE loss is 12% lower than the corresponding experimental trend, on average across three measurement planes. This is interesting because the difference is very similar to that for the CFD-predicted mixed-out KE loss, which is lower than the experimentally-measured mixed-out KE loss by on average 12%. As a result, the SKE coefficients (dash-dot-dotted line for CFD; cross markers for experiments) for experiments and CFD are exceptionally well matched, even though the absolute mixed-out and plane-averaged KE loss are not.

To further explore the numerical under-prediction of KE loss, we decompose plane-averaged KE loss into profile-region and endwall-region KE loss coefficients. By definition, profile-region KE loss and endwall-region KE loss coefficients are summative to the plane-averaged KE loss coefficient.

CFD-predicted profile-region loss (dash-dotted line) rises sharply with axial distance before leveling off at a value equal to 0.66 times ζ_{ref}, at approximately x/C_x = 0.55. Experimentally-measured profile-region loss (diamond markers) is consistently greater than the CFD prediction, with values of 0.69, 0.76, and 0.77 ζ_{ref}, at planes 2, 3, and 4, respectively. The average underprediction of profile-region loss by CFD was 12%, which accounts almost precisely for the deficit of mixed-out and plane-averaged loss.

Trends of normalized endwall-region KE loss (square markers for experiments; dotted line for CFD) are very similar to each other, increasing approximately linearly with axial distance. This is expected because circumferentially-averaged skin friction is relatively constant downstream of the vanes (see dissipation coefficient correlations of Denton [145]). A minor deviation from the linear

trend is evident for the experimental data at x/C_x = 0.25, where accurate experimental characterization of the endwall flow is particularly challenging due to extremely thin boundary layers.

The trends of mixed-out loss, plane-averaged loss, SKE, and profile loss from the study of Burdett and Povey [147] are plotted alongside those from the current study in Figure 6.15. Results from [147] were also normalized by the experimental mixed-out KE loss coefficient at a location equivalent to plane 4.

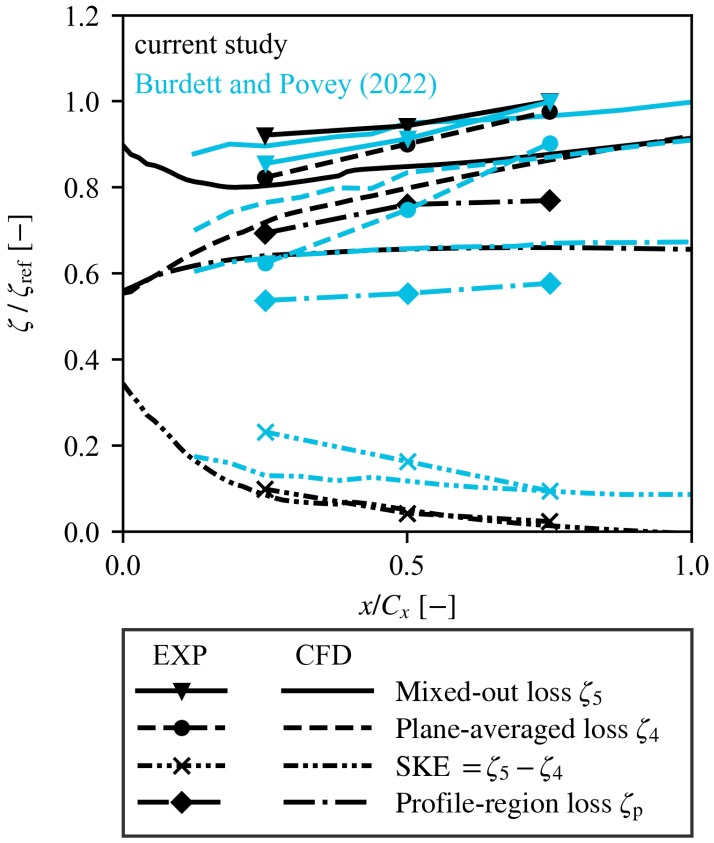


Figure 6.15: *Axial evolution of the mixed-out loss coefficient (ζ_5), plane-averaged loss coefficient (ζ_4), plane-averaged profile-region loss coefficient (ζ_p) and SKE coefficient (SKE). Comparison of the current study with data from Burdett and Povey [147].*

First consider the comparison of normalized mixed-out KE loss. We recall that downstream of the vanes, endwall-region losses are the only driver for an increase of mixed-out loss with axial distance. The experimental data of [147] have a slightly steeper gradient of mixed-out KE loss with axial distance than the current study, indicating a higher rate of KE loss production in the endwall boundary layer. This might be caused by a small endwall flow separation bubble in the experimental data of [147], with accordingly higher losses.

The trend of CFD-predicted plane-averaged KE loss from [147] has a trend which runs in parallel to—but below—the mixed-out KE loss from [147]. It is surprising, perhaps, that the plane-averaged loss does not approach the mixed-out loss asymptotically. The corresponding CFD-predicted SKE coefficient (dash-dot-dotted line) decays to a constant value of approximately $0.11\zeta_{\mathrm{ref}}$ (around $0.75C_x$). As discussed earlier, constant non-zero SKE indicates that the real flow does not mix-out to the same equilibrium state as the mixing model. The relatively high value ($0.11\zeta_{\mathrm{ref}}$) suggests a significant difference for this particular flow. Whilst the trends indicate important truths about the mixing rate, we note the difficulty of finely ranking different NGV designs with absolute values of SKE coefficient.

Finally, we consider the profile-region loss coefficient. Experimentally-measured normalized profile loss in both studies increases monotonically with axial distance, accounting on average for 56% of mixed-out loss in [147] and 78% in the current study. One possible explanation for the significantly lower *proportion* of profile loss in [147] is the greater rate of boundary layer growth, which increases endwall losses thus inflating the normalizing reference KE loss, ζ_{ref}. Indeed, the *absolute* value of the reference KE loss coefficient, ζ_{ref}, was approximately 1.45 times greater in the study of Burdett and Povey [147]. Therefore, the average *absolute* profile KE loss coefficient in [147] exceeds that of the current study by only 4%, as a fraction of the current profile loss coefficient. A slightly greater *absolute* profile loss coefficient for the centered-ejection design [147] might be expected due to the non-dimensional TE thickness being 1.27 times greater than the current study. We now consider CFD predictions of normalized profile-region KE loss coefficient. Compared to experiments, CFD under-predicted profile loss by 12% in the current study, whereas the CFD of [147] over-predicted profile loss by 18%. Burdett and Povey [147] hypothesize that their over-prediction of loss is associated with the point-source method used for modeling film cooling. This hypothesis is compatible with the current CFD study giving lower-than-experimental losses with fully-resolved film-cooling holes. The 12% underprediction of KE loss in the current study (±3% bias uncertainty; see Appendix 6.A) might be explained in part by surface roughness effects, which were not modeled in CFD, or turbulence modelling. Surface roughness is known to increase skin friction and KE loss for NGV flows, as demonstrated in the studies of Erickson et al. [193] and Michaud et al. [137].

Downstream thermal field

A unique feature of the current experiments was that both the downstream loss distribution and the associated thermal field were measured in detail. This data is important for establishing rotor-frame

boundary conditions, which dictate the thermal and aerodynamic forcing of the parts, and unsteady temperature segregation effect within the rotor row.

Non-dimensional temperature distributions, or flow effectiveness maps, Θ, for experiments and CFD at planes 2, 3, and 4 are shown in Figure 6.16. For completeness we note that the thermal traverse was taken downstream of a different vane pair than the pressure traverse data in previous sections, but for nominally identical parts. Aerodynamic data (KE loss, flow angles etc.) was also collected for this vane pair, and to compare locations of the thermal wake and the momentum wake we superimpose contour line of KE loss corresponding to $\zeta_1/\zeta_{\text{ref}} = 0.5$ on the data in Figure 6.16. The same data were not used in the pressure analysis sections because it did not extend all the way to the endwalls. We recall that a physical interpretation of the effectiveness, Θ, is that its complement $\lambda = 1 - \Theta$ is equal to the cold gas mass fraction.

As expected, the experimental effectiveness distributions at plane 2–4 are similar in general form to the KE loss distributions but with generally broader wakes. This is expected because—up to the TE at least—the *thermal mixing layer* is (in general) thicker than the aerodynamic boundary layer for a *film-cooled part* because of both the mass-displacement effect (coolant entering the domain) and because of direct mixing of the coolant and mainstream (coolant jet mixing). Although both of these effects contribute to total pressure loss, the primary mechanism for total pressure loss—up to the TE—is friction with the wetted surface: i.e. the classical aerodynamic boundary layer. This classical aerodynamic boundary layer has an attendant thermal boundary layer for the case of cooled parts, this latter being slightly thicker (for air; Prandtl number of 0.71). Importantly, it is the direct mixing of coolant—however—which is responsible for most of the thermal mixing layer temperature deficit. As discussed, this occurs at greater scale than both the aerodynamic and thermal boundary layers.

For the case of film cooled parts with TE coolant ejection the situation becomes complex. The TE can be seen as a direct and significant source of both pressure loss (base pressure drag) and temperature deficit (slot injection of coolant) followed by enhanced mixing in the vortex street downstream of the TE, which enhances the mixing of both the thermal mixing layer (now a thermal wake) and the aerodynamic wake (now enhanced by the base pressure drag). In this region, there are, of course additional thermal diffusivity terms, but these might be expected to be small in comparison to the effective momentum diffusivity terms (large scale vortex structures). That is, in this region, we might expect the thermal wake and pressure wake to mix at similar rates dominated by large scale vortex structures.

To confirm that the experiment was quasi-steady during the test period, we compare the expected (energy conservation based on hot and cold mass flow rates) mass-averaged effectiveness to that measured (based on full-plane mass flow-averages) at the three planes. The theoretical value of flow effectiveness was 0.868 for all three planes, compared to values of 0.871, 0.865, and 0.868 at planes 2, 3, and 4, respectively. The discrepancies are within 0.17 K (or ±0.3%) of the 55 K hot-to-cold stream temperature difference, which is well within the measurement uncertainty of K-type thermocouples (see uncertainty propagation in Appendix 6.A). This points to excellent conservation of energy, indicating effectively-steady flow. For CFD, the mass-average effectiveness was exactly 0.872 at all three planes; this was very slightly higher than for experiments because the coolant-to-mainstream mass flow ratio was not directly constrained (mainstream inlet was specified using a total pressure boundary condition).

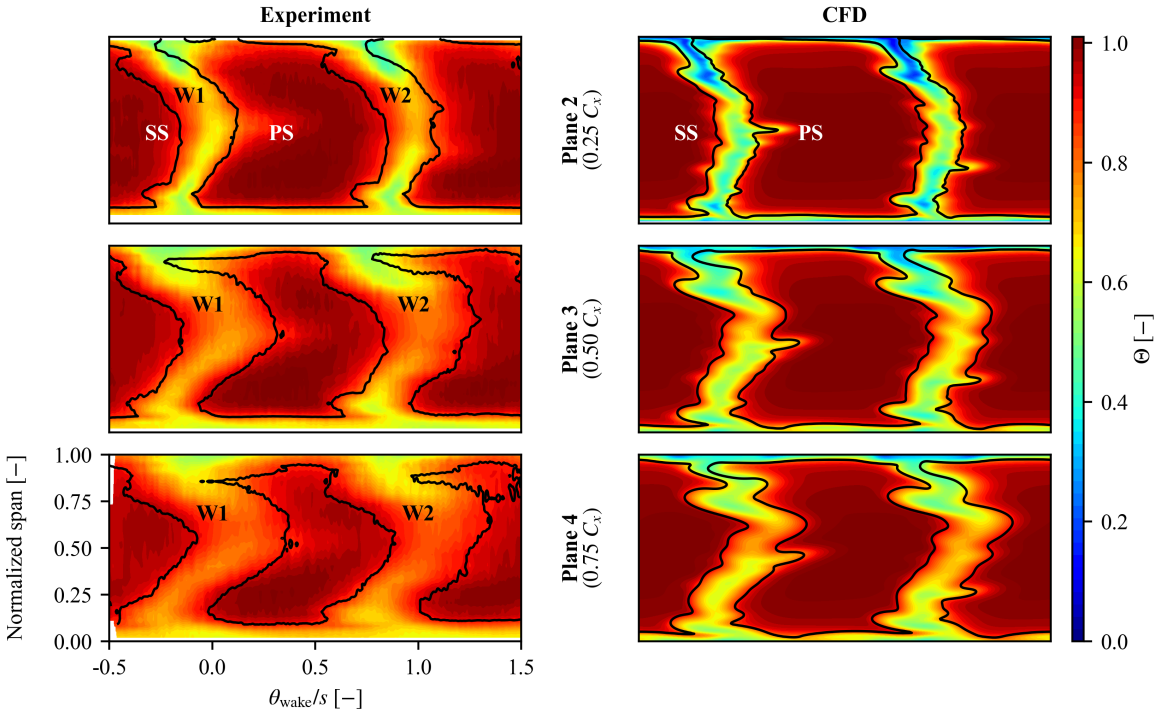


Figure 6.16: *Flow effectiveness (Θ) distributions at planes 2, 3, and 4 for experiments and CFD. The contour of normalized local KE loss corresponding to $\zeta_1/\zeta_{ref} = 0.5$ is superimposed.*

Radial profiles of circumferentially-averaged (mass-flux-weighed) effectiveness are shown in Figure 6.17 for experimental measurements and CFD predictions. Both experimental and CFD profiles have a relatively constant value between 20% and 70% span, with lower values towards the endwalls because of the endwall cooling flows. In the hub region (0% to 20% span) the experimental and CFD results are in reasonable agreement, but peaks and troughs in the CFD profile are not seen in the experimental data. These arise because of undermixed near wall cooling flow and undermixed secondary flows with entrained cold gas in the CFD solutions. This

manifests as a distinct cold core at approximately 12% span at plane 2 in the CFD data of Figure 6.16, where the near-wall flow is significantly undermixed. In the casing region between 70% and 100% span, there is greater difference between the experiment and CFD: the experimental distributions are well-mixed in the near-wall region, with the region of substantial temperature deficit extending to 70% span, suggestive of casing secondary flows spreading the cold endwall flow away from the casing wall (see Figure 6.16 experimental data at plane 2). In contrast the CFD predictions are substantially undermixed, both for the near wall flow, suggesting less entrainment of the cooling flow into secondary flows, and the wake flow than expected, leading to distinct low temperature core at 75% span (see Figure 6.16 CFD data at plane 2, and the corresponding Figure 6.10 KE loss core).

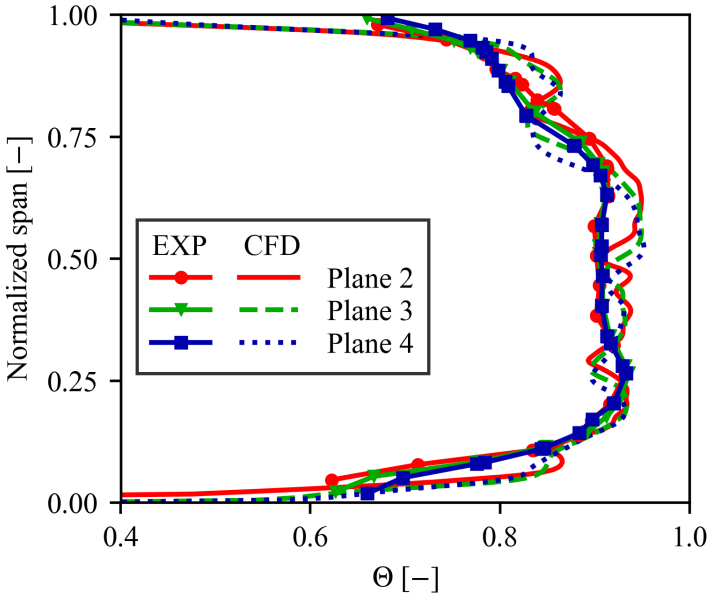


Figure 6.17: *Experimentally-measured and CFD-predicted radial distributions of flow effectiveness (Θ) at planes 2, 3, and 4.*

For both the experimental and CFD data, as we progress from plane 2 to plane 4 the effect is for the profiles to become slightly more radially uniform, as gradients in the flow mix out (see near-wall regions). The effect is slight because the majority of the gradients and associated mixing are in the circumferential direction.

Mixing rates of thermal field

The circumferential distributions at midspan (average between 40% and 60% span) of the cold gas mass fraction, λ, at planes 2, 3, and 4 are shown for experiments and CFD in Figure 6.18. The corresponding distributions of normalized KE loss coefficient at midspan from Figure 6.12 have been superimposed for comparison. Here, the aerodynamic wake has been scaled such that average

experimental peak values of KE loss and cold gas mass fraction across all three planes are equal. The wakes are marked W1 and W2.

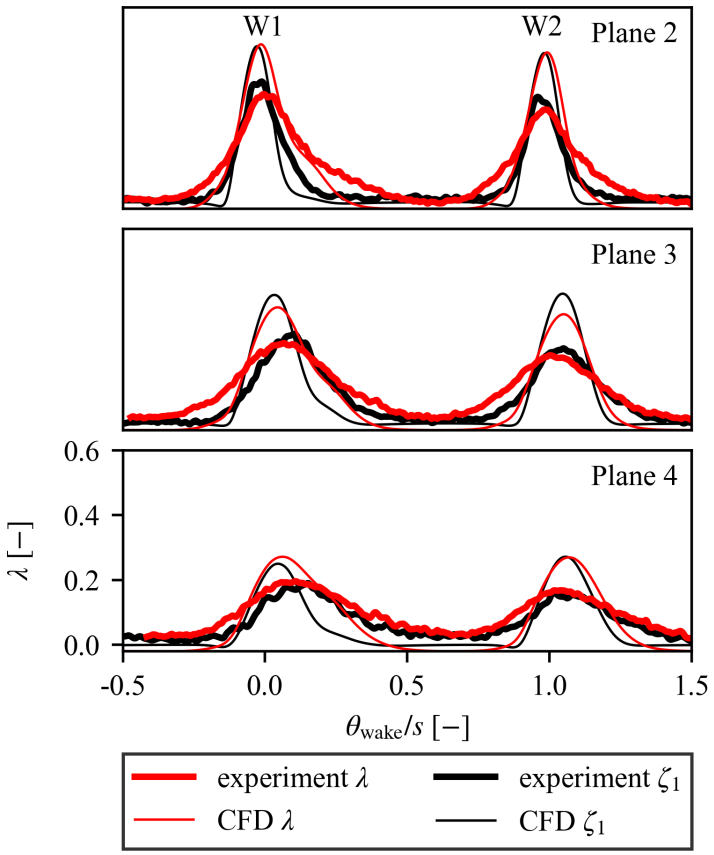


Figure 6.18: *Experimentally-measured and CFD-predicted circumferential distributions of cold gas mass fraction, λ, at midspan (40–60% span), and rescaled KE loss (45–55% span) at planes 2, 3 and 4.*

The distributions are similar in general form to those for kinetic energy loss coefficient distributions, but with broader wakes for both the experimental and CFD distributions. As with the kinetic energy loss coefficient distributions the wake broadens, and the peak reduces with streamwise distance. The CFD data offer an interesting insight into the relative locations of peak cold gas mass fraction and peak rescaled KE loss coefficient. On average, the aerodynamic wake trails the thermal wake by $0.02s$ in the circumferential direction. This is consistent with the fact that streamlines of peak KE loss originate from the base pressure region of the SS overhang (far left of TE; see Figure 6.5a), whereas streamlines of peak cold gas mass fraction originate from the TE coolant slot (center of TE). We now analyze the thermal wake distributions in terms of wake width, w, and peak cold-gas mass fraction, $\lambda_{\max}$, as a function of streamwise distance, d. These trends are shown in Figure 6.19, and compared to the corresponding trends for KE loss coefficient (data of Figure 6.13). To compare the decay rate of both thermal and pressure fields, absolute

values of the peak cold-gas mass fraction ($\lambda_{\max}$) were normalized by the arithmetic average of this parameter for the *experimental* data across planes 2–4 ($\overline{\lambda_{\max}^{\exp}}$): i.e. we present $\lambda_{\max}/\overline{\lambda_{\max}^{\exp}}$. In the same manner, the maximum KE loss coefficient values ($\zeta_{\max}$) were normalized by the experimental average of peak values across planes 2–4 ($\overline{\zeta_{\max}^{\exp}}$).

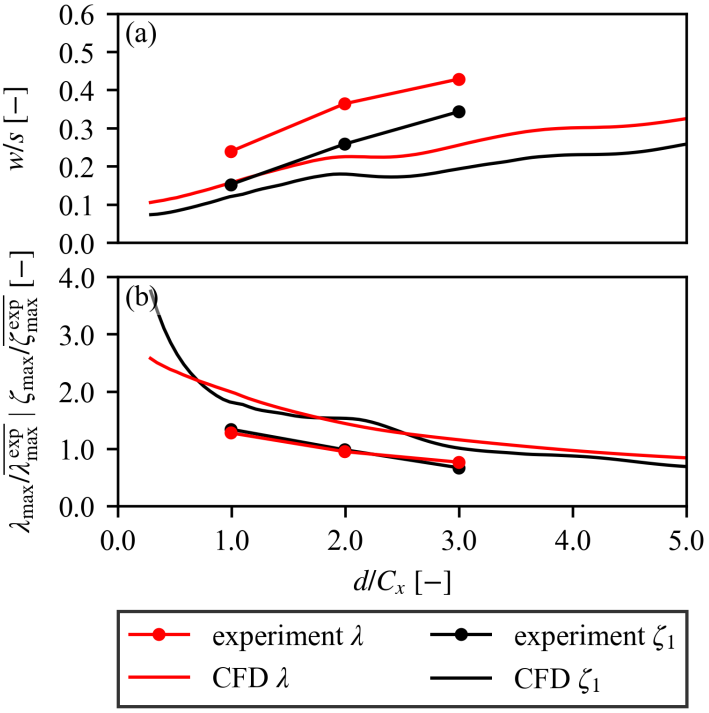


Figure 6.19: *Trends with streamwise distance of: (a) midspan pressure and thermal wake widths; (b) midspan peak values of rescaled cold-gas mass fraction, $\lambda_{\max}/\overline{\lambda_{\max}^{\exp}}$ and rescaled KE loss coefficient, $\zeta_{\max}/\overline{\zeta_{\max}^{\exp}}$.*

Consider first the streamwise evolution of the thermal wake width. This is shown in Figure 6.19a, in which we also compare to the pressure wake width. Both wakes were restacked prior to radial averaging. The experimentally-measured thermal wake widths were $0.24s$, $0.36s$, and $0.43s$ at planes 2, 3, and 4 respectively, on average 37% wider than the experimental pressure wake widths. This is in line with our earlier argument that the mass displacement resulting from coolant injection causes the thermal mixing layer on the vane surface to generally be thicker than the aerodynamic boundary layer, resulting in greater exposure to, and mixing with the turbulent freestream. The proportional growth rates of momentum and thermal wakes are similar, with factor increases in momentum/thermal widths of 1.69/1.52 from plane 2 to 3, and 1.33/1.18 between planes 3 to 4. So far as CFD results are concerned, both the initial width and the spreading rate of the thermal wake were lower than in experiments. At planes 2, 3 and 4 the CFD-predicted widths were $0.16s$, $0.23s$ and $0.26s$, respectively: an average underprediction of 38%. As we have discussed in the context of

Figure 6.13, CFD under-predicted the aerodynamic wake width by 34% on average. The suggestion is that an improved turbulence model is likely to address undermixing of both the aerodynamic and thermal wakes.

The streamwise evolutions of rescaled peak cold gas mass fraction and rescaled peak KE loss coefficient are shown in Figure 6.19b. The normalized experimental trends of thermal and pressure wake intensity are remarkably similar. Likewise, there is excellent agreement between the two CFD data in the range of streamwise distance $1 < d/C_x < 5$, but with differences from the experimental data of—on average—53% and 45% for the thermal and pressure wakes. The similar trends in the far-field, when the flow is already partially mixed out, presumably arise because both mixing of the pressure and thermal fields is dominated by turbulent transport rather than laminar thermal diffusivity (i.e conduction). In the near-wake ($d/C_x < 1$), the normalized decay rate of the aerodynamic wake intensity is significantly greater than for the thermal wake. Presumably, the greater rescaled intensity of the aerodynamic near-wake is related to the viscous dissipation of kinetic energy. Viscous dissipation scales with the square of the strain rate, which explains why the effect is strongest in the near-wake. The viscous dissipation effect is twofold, because it represents both a significant source of KE loss, and a *redistribution* of total enthalpy away from the wake centerline (see discussion by Kopriva et al. [179]). This is likely compounded by a small spatial difference in origin of streamlines with peak KE loss and peak cold gas mass fraction (rooted at the SS overhang base pressure region, and the TE coolant slot, respectively), which causes the aerodynamic and thermal wakes to experience differing levels of shear stress.

A second interesting difference between the decay trends of the thermal and aerodynamic wakes is the absence of plateaus in the CFD trend of thermal wake intensity. This is surprising because the modulation of CFD-predicted thermal wake *width* (see Figure 6.19a) is very similar to that of the aerodynamic wake. Following Thomas and Liu [194], the decay rate of peak KE loss is influenced by the *streamwise* pressure gradient, which varies due to the downstream potential field (see Figure 3.7 and associated discussion). Burdett and Povey [147, 190] attributed both the wake width and wake intensity modulation to streamwise pressure gradients. The absence of plateaus in the thermal wake intensity data of the present study suggests, however, that the modulation of aerodynamic wake width and wake intensity could be separate—but associated—effects, driven by the pressure gradient perpendicular, and parallel to the streamline, respectively. Firstly, the *streamline-normal* pressure gradient deflects the wake, with the modulation of wake width resulting from the projection of a wake with varying whirl angle onto an axial plane (affecting both pressure and thermal wake

width). Secondly, the *streamwise* pressure gradient affects the decay of peak aerodynamic loss only (see Thomas and Liu [194]). We hope that the understanding of similarities and differences between the development of aerodynamic and thermal wakes that arises from this study will be useful in future turbine design.

6.6 Conclusions

Aerodynamic and thermal traverse measurements downstream of a transonic annular cascade of heavily cooled NGVs have been presented. The experimental data were complemented by k–ω SST RANS simulations. In these simulations both the internal cooling passages and the film-cooling holes were fully resolved. Detailed pressure and temperature traverses were conducted at an upstream plane and three downstream planes, with clocking to track particular vane wakes. This allowed the streamwise development of whirl angle, kinetic energy loss, and thermal field to be studied. The data are for an NGV with a trailing-edge-cutback design (suction side overhang), but are compared to a similar dataset from the same facility for a centered-ejection trailing edge design [147]. This comparison is interesting because it allows us to compare common aspects of the datasets. We consider results for whirl angle, kinetic energy loss, and the thermal field in turn.

Whirl angle. We have presented area maps of whirl angle at three downstream planes for both experimentally measured data and CFD predictions. The general trend was an almost linear increase in whirl angle from hub to casing (dictated by the spanwise metal-angle distribution), with slight excursions on account of secondary flows. The distributions of whirl angle in CFD were generally well-matched to experiments, with CFD predicting marginally higher turning. Relative to experiments, mass-flux-weighted whirl angles were +0.65, +0.20, and +0.02 degrees, at planes 2, 3, and 4, respectively, with a maximum local difference of 1.6 degrees in the radial profiles. Area maps of whirl angle indicate a strong influence of the TE potential field, which periodically increases/decreases the whirl angle. This effect modulates the width of the wake, when evaluated on an axial-plane-projection.

Kinetic energy loss coefficient. Experimentally-measured and CFD-predicted area maps of KE loss at three downstream measurement planes were presented and analyzed. The NGV wakes showed the compound lean of the TE (as viewed on an axial cross-section). With increasing axial distance, the wakes deformed and mixed-out, whilst endwall boundary layers gradually grew in thickness. Mixing characteristics were investigated in terms of the streamwise development of wake width and the decay of peak KE loss at midspan. For experiments, aerodynamic wake width

increased approximately linearly from 0.15 to 0.34 vane pitches between $0.25C_x$ and $0.75C_x$, and wake depth (i.e. peak KE loss) decreased approximately inverse-linear over the same distance. The current experimental data for wake width and peak loss was found to correlate reasonably well with another study of NGV loss using cooled engine parts (Burdett and Povey [147]), with good collapse when accounting for differences in non-dimensional TE thickness. This suggests that trends of NGV wake spreading, and peak-loss decay rates are—to first order—applicable for a broad range of TE designs. Compared to experiments, CFD data in both the current study and the study of Burdett and Povey [147] were undermixed, with significantly narrower and more intense aerodynamic wakes. In the current study, wake width was underpredicted by 34%, and wake intensity was over-predicted by 45% (on average), with corresponding under- and over-predictions of 23%, and 77% in [147]. We also considered mixed-out and plane-averaged KE loss. CFD (k–ω SST model) underpredicted the mixed-out and plane-averaged loss by 12%, on average, primarily due to an underprediction of profile-region KE loss rather than a difference in the endwall-region loss, which was well-matched between CFD and experiment. By comparison, the CFD of Burdett and Povey [147] over-predicted profile-region loss by 18%. An over-prediction of KE loss (as opposed to the under-prediction in the current study) is presumably related to the method of modeling film cooling: Burdett and Povey [147] used point sources, whereas the film cooling holes were fully resolved in the current study.

Thermal field. Detailed experimental area-traverse data of the thermal field at three downstream axial planes have been analyzed. The thermal wake was wider than the pressure wake by 37% on average across three planes. This is caused by the mass-displacement effect of injecting film coolant on the vane surface, such that the thermal mixing layer is on average much thicker than the attendant aerodynamic boundary layer. The effect is likely compounded by greater resulting exposure to freestream turbulence, which then enhances mixing. Whilst the thermal wake was wider in *absolute* terms, *proportional* spreading and decay rates were very similar to those of the aerodynamic wake. Compared to experimental data, the CFD-predicted thermal field was undermixed, having on average a 38% narrower and 53% deeper wake (versus 34% and 45%, respectively, for KE loss). The fact that the aerodynamic and thermal fields behave similarly suggests that an improved turbulence model could address undermixing of both the aerodynamic and the thermal wakes.

In this study we have compared the loss and thermal field development downstream of two sets of heavily cooled engine parts operating at near-engine conditions including high turbulence

intensity. The experimental data are unusually high-fidelity and allow for detailed comparison with modern CFD methods. The k–ω SST model gave rise to undermixing in simulation results, but with reasonably good match with experiment for mass-averaged exit conditions. The data provide a robust benchmark for assessing current CFD design methods.

Nomenclature

Roman

C_x	Axial chord length	[m]
d	Streamwise path length	[m]
I	Turbulence intensity	[%]
k	Turbulence kinetic energy	[m^2 s^{-2}]
k_p	Pressure scaling constant	[–]
k_T	Temperature scaling constant	[–]
ℓ	Turbulence length scale	[m]
$\dot{m}$	Mass flow rate	[kg s^{-1}]
M	Mach number	[–]
p	Pressure (total or static)	[Pa]
Re	Reynolds number	[–]
r	Radius	[m]
s	NGV pitch	[°]
T	Temperature	[K]
V_x	Axial velocity	[m s^{-1}]
V_θ	Circumferential velocity	[m s^{-1}]
w	Full angular wake width at half maximum	[°]
x	Axial coordinate	[m]
y^+	Normalized wall distance	[–]

Greek

α	Whirl angle	[°]
ϵ	Turbulence dissipation rate	[m^2 s^{-3}]
ζ_1	Local kinetic energy loss coefficient	[–]
ζ_3	Circumferentially-averaged kinetic energy loss coefficient	[–]
ζ_4	Plane-averaged kinetic energy loss coefficient	[–]
ζ_5	Mixed-out kinetic energy loss coefficient	[–]
ζ_p	Profile-region kinetic energy loss coefficient	[–]
ζ_e	Endwall-region kinetic energy loss coefficient	[–]
ζ_ref	Reference kinetic energy loss coefficient	[–]
θ	Circumferential coordinate	[°]
Θ	Flow effectiveness (non-dimensional total temperature)	[–]
λ	Cold gas mass fraction	[–]

Subscripts

0	Total condition
1	Quantity measured upstream of NGV
2	Quantity measured downstream of NGV
c	Coolant stream property
m	Mainstream property
max	Peak value at midspan
norm	Normalized quantity
rake	Quantity as measured by upstream rake

Appendix 6.A Measurement uncertainty

Estimated experimental bias uncertainties for upstream normalized total pressure and temperature, downstream flow angle, KE loss, and flow effectiveness are summarized in Table 6.2. Values are given with 95% confidence interval (CI).

Whirl angle bias uncertainty was estimated from alignment uncertainties during calibration and testing. Uncertainties of pressure-based measurements were calculated from the manufacturer-quoted bias uncertainties of the transducers. A special effort was made to reduce uncertainty by performing accurate calibrations of all transducers in an appropriate range (1–2 bar absolute). Uncertainties of temperature-based measurements were calculated assuming a bias uncertainty of ±1.50 K (95% CI) for most thermocouples, and ±0.75 K (95% CI) for the upstream traverse thermocouple with improved error (see Nakos [195]).

Table 6.2: *Bias uncertainties of experimental measurements.*

Parameter	**95% CI**
Normalized total pressure, $p_{01,\mathrm{norm}}$ [–]	±0.06%
Normalized total temperature, $T_{01,\mathrm{norm}}$ [–]	±0.49%
Whirl angle, α, [deg]	±0.8 (absolute)
Kinetic energy loss coefficients, ζ, [–]	±0.03 $\times\zeta_{\mathrm{ref}}$
Flow effectiveness, Θ, [–]	±0.04 (absolute)

Appendix 6.B Grid sensitivity study

In this section we examine the sensitivity of the CFD solutions to the resolution of the computational grid. In the context of the experimental validation of simulation results, a grid sensitivity study allows us to differentiate between model and discretization errors.

Grid refinement strategy

Starting from a *coarse grid* comprised of 110 million (110 M) cells, the mesh was globally refined by successively decreasing the background cell size of the octree mesh. This was performed in two refinement steps, with corresponding relative cell edge lengths (i.e. normalized by that of the 110 M grid) of 0.72 (*intermediate grid*), and 0.62 (*fine grid*) with respective cell counts of 221 million (221 M), and 312 million (312 M). The internal cooling passages and film cooling holes of the NGVs account for approximately half of the cells. We examine the sensitivity of local flow properties, wake mixing characteristics, and integral KE loss to grid resolution.

Grid sensitivity of circumferential profiles at midspan

Circumferential midspan profiles (radially mass-flux-averaged between 40% and 60% span) of whirl angle, local KE loss, and cold gas mass fraction at plane 2 are shown in Figure 6.20.

First consider the circumferential profiles of whirl angle shown in Figure 6.20a. Values of whirl angle, α, are datumed to the midspan metal angle, α_{TE}. The maximum local variation across the three grids is 0.22 degrees. Relative to the fine grid (312 M), differences in mass-flux-averaged whirl angle were −0.058 degrees (112 M), and −0.010 degrees (221M). These values are extremely small, and much lower than the estimated experimental measurement bias uncertainty for whirl angle (±0.8 degrees).

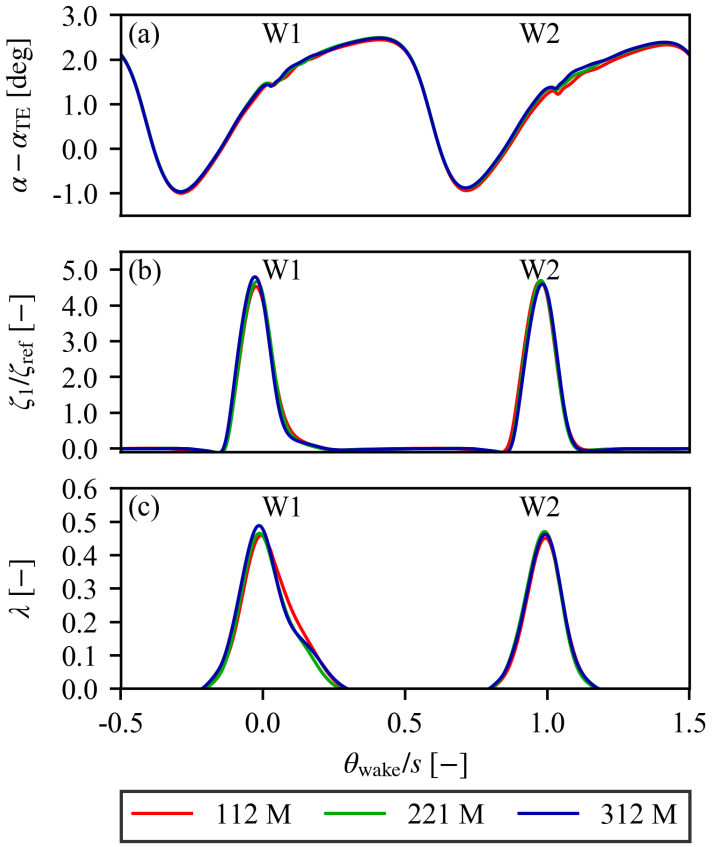


Figure 6.20: *Midspan (40–60% span) circumferential profiles in plane 2 of radially-averaged (mass-flux-weighted) properties for three grid sizes of: (a) whirl angle; (b) normalized local kinetic energy loss coefficient; (c) cold gas mass fraction.*

Next, consider the circumferential profiles of local KE loss coefficient, which are shown in Figure 6.20b. The values of local KE loss, ζ_1, have been normalized by the reference KE loss coefficient, ζ_{ref}. Peak normalized local KE loss, averaged across wakes W1 and W2, was 4.602 for the coarse grid, 4.678 for the intermediate grid, and 4.697 for the fine grid (difference of 2.0% across all

three grids). A somewhat surprising result is that—contrary to what we might expect based on arguments of numerical diffusion—the peak KE loss intensity of W2 does not increase with grid refinement, whereas W1 does. This behavior could be related to the mixed numerical order of accuracy, when using the high resolution advection scheme of the CFX solver. Roy has shown that oscillatory convergence can occur when truncation errors from blended first-order and second-order discretization interfere constructively or destructively, depending on the grid spacing [196].

Finally, consider the circumferential profiles of cold gas mass fraction, which are shown in Figure 6.20c. We recall that the cold gas mass fraction, λ, is related to effectiveness, Θ, by $\lambda = 1 - \Theta$. Peak cold gas mass fraction (average of W1 and W2) was 0.455 for the coarse grid, 0.468 for the intermediate grid, and 0.476 for the fine grid (difference of 4.4% across all three grids). Although the general trend is for an increase in peak cold gas mass fraction as the grid is refined, in similarity to the aerodynamic wake, only the thermal wake depth for W1 increases monotonically as the grid is refined.

Grid sensitivity of streamwise trends of aerodynamic and thermal wake properties

We now consider the grid sensitivity of the streamwise trends of aerodynamic and thermal wake properties. Width and peak heights for the aerodynamic wake and thermal wakes are shown as a function of normalized streamwise distance in Figure 6.21. These trends show the sensitivity of *mixing characteristics* to grid refinement. The method for determining wake width and peak intensity is described by Burdett and Povey [147] (direct averaging approach; without restacking). Average values for wakes W1 and W2 are reported.

The streamwise evolution of aerodynamic wake width is shown in Figure 6.21a. Here, the wake width, w, has been normalized by the vane pitch, s. Over the experimental range of streamwise distances ($0.99 < d/C_x < 3.00$), the aerodynamic wake width is effectively identical for all three grids (maximum local variation of $0.013s$). Above $3.0C_x$, the trends diverge slightly. At d/C_x = 5, the aerodynamic wake widths on the *coarse grid* and *intermediate grid* are $0.061s$ and $0.007s$ greater (respectively) than on the *fine grid*. This is consistent with the expectation that grid refinement reduces artificial diffusion.

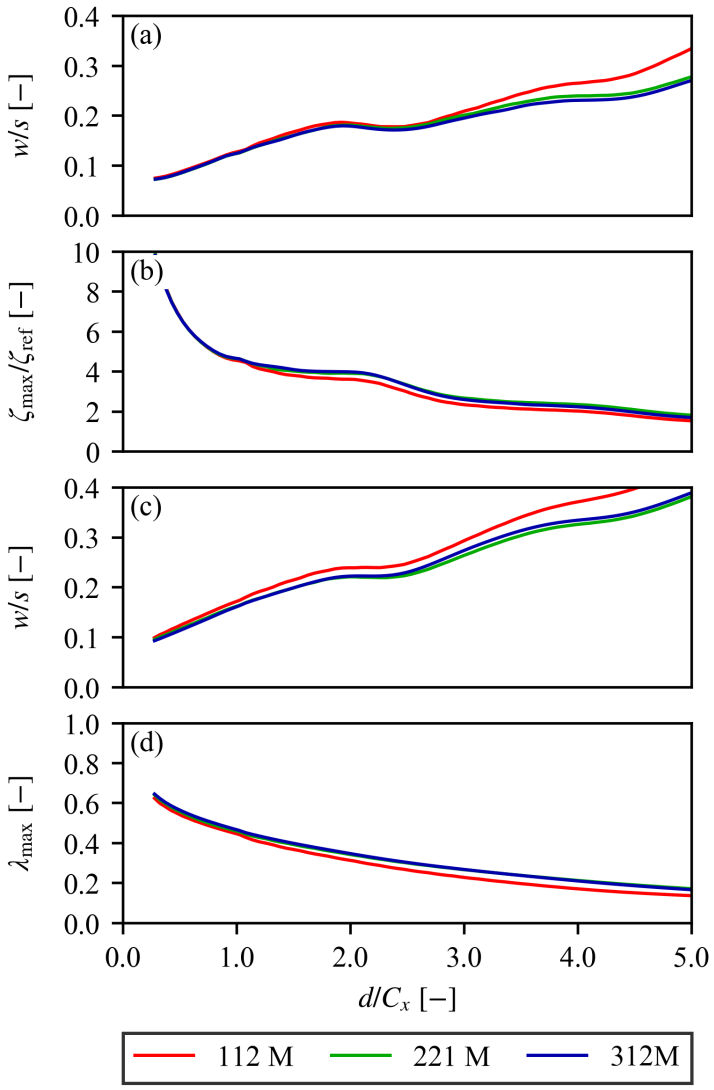


Figure 6.21: *Streamwise variation of wake properties for three grid sizes: (a) aerodynamic wake width; (b) aerodynamic wake peak intensity; (c) thermal wake width; (d) thermal wake peak intensity.*

Let us now consider the grid sensitivity of the peak KE loss coefficient, which is shown in Figure 6.21b. Compared to the *fine grid*, peak intensities of normalized local KE loss are on average 7.3% lower on the *coarse grid*, and 2.1% greater on the *intermediate grid*. We reference the earlier argument of Roy [196] to explain the non-monotonic decrease of peak loss. Overall, the observations are consistent with the expectation that numerical diffusion will tend to increase wake width and decrease wake depth.

The corresponding trends of thermal wake width and peak cold gas mass fraction with grid refinement are shown in Figure 6.21c and d, respectively. Relative to the *fine grid*, thermal wake width was on average 9.0% greater on the *coarse grid*, and 1.2% lower on the *intermediate grid*. Peak cold gas mass fraction was on average 12.4% lower and 0.2% greater for the *coarse* and

intermediate grids, respectively. Approximately inverse percentage error for wake width and peak intensity are expected, because the mass-flux-averaged cold gas mass fraction is a conserved quantity.

Grid sensitivity of integral measures of loss

Finally, we consider the development of mixed-out KE loss, plane-averaged KE loss, and SKE, which are shown as a function of normalized axial location in Figure 6.22 for three grid sizes. These trends are indicative of the grid sensitivity of *integral loss*.

As the grid is refined, both mixed-out KE loss (shown as solid lines), and plane-averaged KE loss (shown as dashed lines) reduce monotonically. On the first refinement step (112 M to 221 M), mixed-out and plane-averaged loss are reduced by 2.8% and 3.3%, respectively (ratio of ensemble averages between 0.0 and $1.0C_x$), with corresponding reductions of 0.7% and 0.3% on the second refinement step (221 M to 312 M). Using Richardson extrapolation, this translates to a predicted error of approximately 0.8% on the *fine grid* for plane-averaged KE loss. Because both mixed-out and plane-averaged loss change by a similar amount with grid refinement, SKE (dotted lines) is essentially unchanged. This suggests that integral *mixing* characteristics are less grid-sensitive than the *absolute* levels of KE loss.

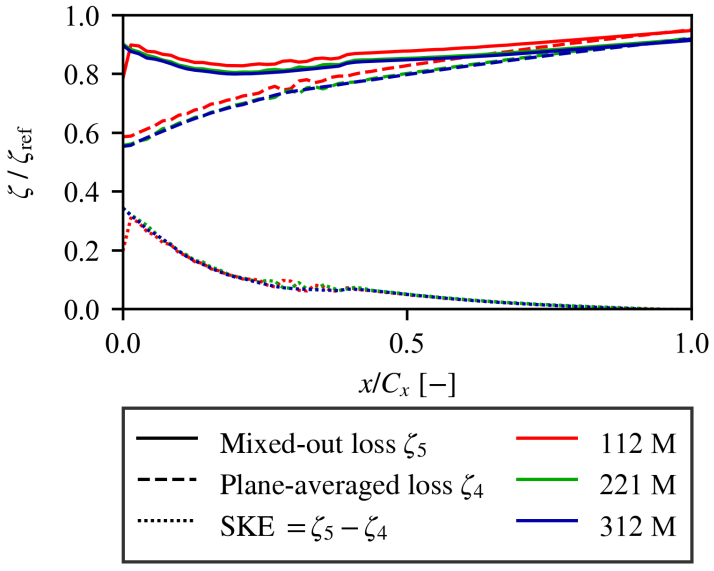


Figure 6.22: *Mixed-out KE loss, plane-averaged KE loss, and SKE coefficient as a function of axial location for three grid sizes.*

This page is intentionally blank

7 | Comparison of eddy viscosity models for high turbulence NGV flows

In this chapter we investigate the performance of eddy viscosity turbulence models for high-pressure nozzle guide vane (NGV) flows with engine-realistic turbulence. Using metrics such as integrated kinetic energy (KE) loss and mixing rate, we compare simulation results using turbulence models with high-fidelity experimental data from fully-cooled NGVs, operating at engine-matched conditions of Reynolds number and Mach. For the widely-used k–ω shear stress transport (SST) model, the aerodynamic and thermal wakes of the NGVs were undermixed. We compare simulation results with those using other common turbulence models including the standard k–ω, baseline k–ω, Spalart–Allmaras, and baseline explicit algebraic Reynolds stress model. Alternative turbulence models formulations are explored, with an emphasis on modifications to the implementation of the shear stress limiter. We also investigate the sensitivity of models to the specified inlet turbulence intensity. We demonstrate that predictions of integrated KE loss, as well as the decay trends of the aerodynamic and thermal wakes are a closer match to experimental data for the baseline algebraic Reynolds stress model than for other turbulence models in more common use for NGV predictions.

Context with other chapters

The comparison of experimental measurements and CFD predictions of NGV wake development in Chapter 6 indicated systematic undermixing in the numerical model. The causes and possibly mitigation strategies are explored in the current Chapter. The lessons learned were subsequently applied to the CFD methods in Chapter 8—a study on the impact of lean-burn combustion on NGV performance. The baseline explicit algebraic Reynolds stress model, which was identified as the most promising alternative to k–ω SST, significantly improved the predictions for the lean-burn test case. This hints at the broader applicability of current recommendations.

Publication status and co-author contributions

The chapter takes the form of a *journal paper*, which has recently been accepted for publication in the ASME Journal of Turbomachinery [7]. The DPhil candidate was responsible for conception of the project, running simulations, data analysis, and paper writing. Thomas Povey supervised all aspects of the project. A statement of authorship is included at the end of the document.

7.1 Introduction

Although recent advances in numerical algorithms and an ever-increasing availability of computing resources have facilitated one-off large eddy simulations of fully-cooled turbine stages (see e.g. Thomas et al. [197]), such simulations remain prohibitively expensive for use in design practice, meaning that engineers continue to rely on Reynolds-averaged Navier–Stokes (RANS) models to predict the performance of turbine components. RANS models rely on experimental data for calibrating closure coefficients. Calibration is often performed using measurements from flows with very low freestream turbulence, leading to unpredictable behavior in high-turbulence flows such as those encountered at the combustor–turbine interface and in the high-pressure nozzle guide vane (NGV).

For rich-burn combustor architectures, based on the limited data available from reacting gas turbine combustors (e.g. Zimmermann [73], Bicen et al. [74]) turbulence intensities between 10% and 30% have been reported at HP NGV inlet plane. Interestingly, these studies reported only a mild sensitivity of the turbulence intensity (TI) at combustor outlet to the presence of combustion as opposed to geometry. Recent literature from non-reacting low-temperature experiments [69, 75, 83] for rich-burn architectures shows average TI levels in the range 10–25%. The relative ease of instrumenting low-temperature experiments has also facilitated detailed investigations of turbulence length scales at combustor outlet. Barringer et al. [69], Cha et al. [75], and Folk et al. [83] all reported length scales similar to the combustor dilution port diameter. For typical configurations, this corresponds to integral length scales around 0.20–0.40 times the NGV axial chord length.

Turning to lean-burn combustors, Schroll et al. [55] measured turbine inlet turbulence intensities between 8–20% under reacting conditions. A number of low temperature studies have successfully used non-reacting combustor simulators to generate lean-burn representative swirl and temperature profiles (see e.g. [92, 4, 89]). In similarity to low temperature rich-burn simulators, non-reacting simulators allow for more detailed characterization of turbulence than their reacting counterparts (in which measurements are invariably limited). Peak turbulence intensities around 25% were reported by Bacci et al. [89]. For the same combustor simulator, Koupper et al. [128] measured integral length scales equal to approximately 10% of the swirler diameter. Further studies are necessary to determine the factors affecting length scales in lean-burn combustors, though intuitively we might expect the size of the turbulent structures to depend on both the swirler blade spacing and the overall size of the swirler.

For the k–ω shear stress transport (SST) model [142], the recommended *maximum* turbulent-to-molecular viscosity ratio at inlet is 10^{-2}. This value is several orders of magnitude smaller than the values typical for combustor-outlet flows (see e.g. Cha et al. [75]), who measured turbulent-to-molecular viscosity ratios around 10^4). This is one example of a high-turbulence flow which falls well outside the calibration range of most turbulence models. It is of practical interest for designers to understand how different turbulence models behave in these high turbulence environments.

To understand the behavior of various common turbulence models in a high-turbulence flow environment, we compare the standard k–ω (SKO) model [198], baseline k–ω (BSL) model [199], k–ω shear stress transport (SST) model [142], the baseline explicit algebraic Reynolds stress model (BSL-ARSM) [200, 201], and the Spalart–Allmaras (SA) model [173] in terms of their ability to accurately predict the aerodynamic and thermal field downstream of fully-cooled NGVs with high inlet turbulence. The simulation results are compared with experimental data from an annular cascade of film-cooled parts operating at engine-matched Reynolds and Mach number.

7.2 Shear stress transport model

The k–ω shear stress transport (SST) turbulence model is the de facto industry standard for most turbomachinery flows. The popularity of the SST model [142] can be attributed—in part—to its zonal treatment of boundary layer and free stream regions. The SST model uses SKO [198] near the walls (log-layer and viscous sublayer), and the standard k–ϵ (SKE) [168] model in the freestream. The zonal approach is advantageous because SKO is reasonably accurate for boundary layer flows but exhibits unrealistic sensitivity to turbulence boundary conditions (see e.g. [202]). The k–ϵ model is considered more robust in terms of its sensitivity to inlet conditions of turbulence but is less accurate for wall-bounded shear because it relies on wall functions to model the viscous sublayer. The zonal approach of k–ω SST model exploits the strengths of two constituent models in the regions in which they are most applicable. We now briefly consider the fundamentals of the underlying SKO and SKE models.

Eddy viscosity and turbulence scales

Both SKO, and SKE are eddy viscosity models: a subclass of turbulence models which use the Boussinesq approximation to determine unknown turbulent stresses. The Boussinesq approximation for the turbulent stress tensor, τ_{ij}, is given by

$$\tau_{ij} = 2\mu_{\mathrm{t}}\left(S_{ij} - \frac{1}{3}\frac{\partial U_k}{\partial x_k}\delta_{ij}\right) - \frac{2}{3}\rho k\delta_{ij} = -\overline{\rho u_i u_j} \tag{7.1}$$

where the strain rate tensor, S_{ij}, is given by

$$S_{ij} = \frac{1}{2}\left(\frac{\partial U_i}{\partial x_j} + \frac{\partial U_j}{\partial x_i}\right) \tag{7.2}$$

and where, μ_t is eddy viscosity, $\partial U_k/\partial x_k$ is the velocity divergence, ρ is volumetric mass density, k is turbulence kinetic energy (TKE; defined as $\overline{u_i u_i}/2$), and δ_{ij} is the Kronecker delta. U and u are the mean-flow and the fluctuating velocity components, respectively, using Einstein notation for indexing. By convention, τ_{ij} is equal to the *negative* Reynolds stress tensor, ($\overline{\rho u_i u_j}$), where the overbar represents Favre averaging. Equation 7.1 closes the RANS equation system by relating the turbulent stresses to the mean-flow strain rates through *turbulent eddy viscosity*, μ_t. The eddy viscosity represents momentum diffusivity through turbulence, in analogy to the dynamic viscosity which represents the momentum exchange though non-turbulent shear. In analogy to the kinematic viscosity, it is possible to define a *kinematic eddy viscosity*, ν_t, where $\nu_\mathrm{t} = \mu_\mathrm{t}/\rho$. Prandtl proposed calculating ν_t using characteristic properties of the largest turbulent eddies. Based on dimensional arguments, kinematic eddy viscosity (units of [m^2 s^{-1}]) could be regarded as proportional to the product of a characteristic turbulence velocity scale, $\mathfrak{v}$ (with units of [m s^{-1}]), and a turbulence length scale, ℓ (with units of [m]). In this abstraction, turbulence length scale might be viewed as the mean eddy diameter, and the turbulence velocity scale may be thought of as the time-average *unsteady* velocity of the fluid circulating in the eddy. Linear scaling of diffusivity with eddy size and circulation velocity makes sense because larger eddies (i.e. ℓ) will exchange mean flow momentum between two more distant points, and a greater circulation velocity (i.e. $\mathfrak{v}$) increases the time rate of transfer of momentum (i.e. diffusion). In the SKO model kinematic eddy viscosity is given by

$$\nu_\mathrm{t} = \frac{k}{\omega} \tag{7.3}$$

where k is the TKE (units of [m^2 s^{-2}]), and ω is the specific turbulence dissipation rate (units of [s^{-1}]). In continuation of the earlier dimensional arguments, k can be thought of as the square of the turbulence velocity scale, and ω can be viewed as the reciprocal of a turbulent timescale. As ever with dimensional arguments, kinematic eddy viscosity can be expressed using many combinations of variables which relate to the *energy* and *scale* of the turbulence. In the SKE model [168] kinematic eddy viscosity is expressed as

$$\nu_\mathrm{t} = \beta^* \frac{k^2}{\epsilon} \tag{7.4}$$

where β^* is a dimensionless model constant equal to 0.09, and ϵ is the turbulence dissipation rate (with units of [m^2 s^{-3}]). Equation 7.4 is based on the observations of Taylor [203], who showed (using hotwire measurements of decaying grid turbulence) that ℓ was proportional to $k^{1.5}/\epsilon$.

The SKO and SKE models can be used simultaneously by expressing the SKE model in terms of k and ω, using the identity

$$\epsilon = \beta^* k\omega \tag{7.5}$$

i.e. we convert a model of transport of k and ϵ into a model for the transport of k and ω (see full derivation in [204]). We now consider the transport equations of the combined SKO–SKE model.

SST transport equations

For both SKO and SKE models, the transport of TKE is represented by the following differential equation

$$\underset{(I)}{\frac{D(\rho k)}{Dt}} = \underset{(II)}{\mathcal{P}} - \underset{(III)}{\mathcal{E}} + \underset{(IV)}{\frac{\partial}{\partial x_j}\left(\left(\mu + \frac{\mu_\mathrm{t}}{\sigma_k}\right)\frac{\partial k}{\partial x_j}\right)} \tag{7.6}$$

where TKE production, $\mathcal{P}$ (term (*II*)), and turbulence dissipation, $\mathcal{E}$ (term (*III*)), are defined as

$$\mathcal{P} = \tau_{ij}\frac{\partial U_i}{\partial x_j} \tag{7.7}$$

$$\mathcal{E} = \rho\beta^* k\omega \tag{7.8}$$

and where $\partial U_i/\partial x_j$ is the velocity Jacobian, D/Dt is the material derivative, ρ is volumetric mass density, μ is dynamic viscosity, and σ_k is a closure coefficient. On the right-hand side of Equation 7.6, turbulence production term (*II*) represents the energy gained by turbulent eddies through interactions with the velocity gradients of the mean-flow, and dissipation term (*III*) represents the dissipation of TKE at the Kolmogorov microscale. Term (*IV*) models the combined effects of laminar viscous diffusion, pressure diffusion, and turbulent diffusion of TKE. We now consider the turbulence production term (*II*) in detail.

Expanding Equation 7.7 by using the Boussinesq approximation (Equation 7.1) for the turbulent stress, τ_{ij}, we get

$$\mathcal{P} = 2\mu_\mathrm{t} S_{ij}\frac{\partial U_i}{\partial x_j} - \frac{2}{3}\frac{\partial U_k}{\partial x_k}\left(C\mu_\mathrm{t}\frac{\partial U_k}{\partial x_k} + \rho k\right) \approx \mu_\mathrm{t} S^2 \tag{7.9}$$

where the strain invariant, S, is a coordinate-independent scalar measure of the strain rate, given by

$$S = \sqrt{2S_{ij}S_{ij}} \tag{7.10}$$

and where C is nominally equal to unity but is often treated as an empirical correction factor, which is designed to prevent excessive turbulence production through shockwaves (default value of 3; see CFX theory guide [205]). For divergence-free (i.e. incompressible) flow, it can be shown that Equation 7.9 is equal to the eddy viscosity times the square of the strain invariant, S. This simplification is convenient for discussion purposes, where the compressible definition (used in simulations) is less intuitive.

The turbulence dissipation term, $\mathcal{E}$, defined by Equation 7.8, requires an additional transport equation to determine the specific turbulence dissipation rate, ω. We recall that a physical interpretation of the specific dissipation rate is that its reciprocal is proportional to the turbulence time scale. Specific dissipation rate, ω, can be modeled using the following *empirical* transport equation

$$\underset{(I)}{\frac{D(\rho\omega)}{Dt}} = \underset{(II)}{\frac{\alpha}{\nu_t}\mathcal{P}} \underset{(III)}{- \rho\beta\omega^2} + \underset{(IV)}{\frac{\partial}{\partial x_j}\left(\left(\mu + \frac{\mu_t}{\sigma_\omega}\right)\frac{\partial\omega}{\partial x_j}\right)} + \underset{(V)}{\frac{2\rho}{\sigma_{\omega 2}\omega}\frac{\partial k}{\partial x_j}\frac{\partial\omega}{\partial x_j}} \tag{7.11}$$

where α, β, σ_ω, and $\sigma_{\omega 2}$ are closure coefficients. In analogy to the TKE equation, the production (*II*), dissipation (*III*), and diffusion terms (*IV*), appear on the right-hand side. Term (*V*) represents cross-diffusion of turbulent kinetic energy and specific dissipation rate. Cross-diffusion term (*V*) appears because of the transformation of the transport equation for ϵ (see [168]) into a transport equation for ω. The cross-diffusion term alleviates the well-known problem of the SKO model, where a small change in the freestream value of ω can give rise to a non-physical change in the solution (see e.g. Menter [142], and Wilcox [206]). Equation 7.11 is justified by dimensional considerations and empirical calibration (see discussion by Wilcox [141]), and physical interpretations of the individual terms do not necessarily exist. This contrasts with the equation for TKE transport (Equation 7.6), which can be derived directly from the exact RANS equations, even though in practice closure of most terms involves modeling assumptions.

For the SST model, the closure coefficients for SKO-regime (subscript 1), and SKE-regime (subscript 2) are summarized below:

$$\alpha_1 = 5/9 \quad \beta_1 = 0.075 \quad \sigma_{k1} = 1.176 \quad \sigma_{\omega 1} = 2$$
$$\alpha_2 = 0.44 \quad \beta_2 = 0.0828 \quad \sigma_{k2} = 1 \quad \sigma_{\omega 2} = 1.1682$$

Model/closure coefficient blending

Depending on the chosen set of closure coefficients, Equations 7.6 and 7.11 represent either the SKO or the SKE turbulence model. Using the SKO model in the boundary layer region and the SKE model in the freestream can be achieved, in practice, by linearly interpolating between the SKO closure coefficients and SKE closure coefficients using a blending function. Boundary layers are identified based on local properties of the mean flow and the turbulence. The interpolation is performed as follows

$$\phi = \phi_1 F_1 + \phi_2(1 - F_1) \tag{7.12}$$

where ϕ represents a closure coefficient (e.g. σ_k), which varies from ϕ_1 (SKO regime coefficient σ_{k1}) to ϕ_2 (SKE regime coefficient σ_{k2}) as a blending function, F_1, varies from 1 to 0.

The blending function F_1 is defined as

$$F_1 = \tanh\left(\arg_1^4\right) \tag{7.13}$$

where $\tanh$ is the hyperbolic tangent and $\arg_1$ is given by

$$\arg_1 = \min\left(\max\left(\frac{\sqrt{k}}{\beta^*\omega y}, \frac{500\mu}{\rho\omega y^2}\right), \frac{4\rho k}{CD_{k\omega}\sigma_{\omega 2} y^2}\right) \tag{7.14}$$

(*I*) (*II*) (*III*)

where y is distance to the nearest wall, and where $CD_{k\omega}$ is the cross-diffusion term from Equation 7.11 defined by

$$CD_{k\omega} = \max\left(\frac{2\rho}{\sigma_{\omega 2}\omega}\frac{\partial k}{\partial x_j}\frac{\partial \omega}{\partial x_j}, 10^{-10}\right) \tag{7.15}$$

where a lower bound of 10^{-10} is imposed to ensure $CD_{k\omega}$ remains positive. Blending function F_1 increases smoothly from 0 (SKE-regime) to 1 (SKO-regime) as $\arg_1$ varies from 0 to infinity ($F_1 > 0.99$ for $\arg_1 > 1.28$). Consider now the definition of $\arg_1$. The first sub-argument (*I*) of $\arg_1$ represents the turbulence length scale ($\ell = \sqrt{k}/\beta^*\omega$), divided by the distance to the nearest wall, y (see [142]). This term is meant to *activate* the SKO-regime (i.e. $F_1 = 1$) in the log-layer, based on the empirical observation that $\ell \approx 2.5y$ in the log-layer. The second sub-argument (*II*) of $\arg_1$ is tailored to *activate* the SKO-regime (i.e. $F_1 = 1$) in the viscous sublayer, based on the empirical observation that $1/\omega y^2$ is approximately constant in this region [142]. The third

sub-argument (*III*) of $\arg_1$ is designed to *deactivate* the blending function (i.e. $F_1 = 0$) for large positive values of $CD_{k\omega}$, which are considered indicative of free shear (i.e. SKE-regime) flow. In addition to interpolating the closure coefficients, F_1 is also used to deactivate the cross-diffusion term in Equation 7.11 near the walls, where it is not valid (for the same reasons as the SKE model). This is achieved multiplying the cross-diffusion term (V) in Equation 7.11 by $(1 - F_1)$.

Shear stress limiter

The success of the SST model can largely be accredited to the shear stress limiter (or *realizability* limiter), from which the model derives its name. The shear stress limiter improves predictions of separation in flows with moderate adverse pressure gradients. The apparent cause for the poor predictions of separation in models *without* a stress limiter is the overprediction of turbulent shear stress in the outer boundary layer [142]. The shear stress limiter—designed to prevent these overpredictions—is implemented by modifying the algebraic expression for eddy viscosity

$$\mu_\mathrm{t} = \min\left(\frac{\rho k}{\omega}, \frac{\rho a_1 k}{S F_2}\right) \tag{7.16}$$

where a_1 is the Bradshaw constant ($a_1 = 0.31$; see [207]), S is the familiar strain invariant, and F_2 is a second blending function defined as:

$$F_2 = \tanh\left(\arg_2^2\right) \tag{7.17}$$

where $\tanh$ is the hyperbolic tangent and $\arg_2$ is given by

$$\arg_2 = \max\left(\frac{2\sqrt{k}}{\beta^* \omega y}, \frac{500\mu}{\rho \omega y^2}\right) \tag{7.18}$$

where all terms have previously been defined. The first sub-argument of $\arg_2$ is equal to $2\ell/y$, and the second sub-argument of $\arg_2$ is identical to that of $\arg_1$. The first sub-argument of F_2 ensures that F_2 remains active (i.e. $F_2 = 1$) slightly further into the freestream than F_1, which ensures that the stress limiter can operate in the outer boundary layer. We now consider the operation of the stress limiter (i.e. Equation 7.16) in detail.

Outside of the boundary layer (i.e. $F_2 = 0$), the SKO model definition of eddy viscosity is used ($\mu_\mathrm{t} = \rho k/\omega$; see Equation 7.3). When $F_2 = 1$ (i.e. within the boundary layer), the limiter is active when $S > a_1\omega$. Taking the square of both sides, and multiplying by μ_t (the inequality holds because all variables are positive), it can be shown (using Equation 7.3 and the approximations that

$\mathcal{P} \approx \mu_t S^2$ and $a_1 \approx \sqrt{\beta^*}$) that the inequality is equivalent to the condition that $\mathcal{P} > \mathcal{E}$. The condition $\mathcal{P} > \mathcal{E}$ is considered indicative of an adverse pressure gradient [142]. To understand how Equation 7.16 limits the shear stress, we consider the boundary layer momentum equations, for which the primary shear stress can be approximated as $\tau_{xy} \approx \mu_t S$ (where x is the streamwise direction and y is the wall-normal direction). Substituting τ_{xy} into Equation 7.16, we see that when $F_2 = 1$, the shear stress obeys $\tau_{xy} \leq \rho a_1 k$, where a_1 is taken from the experiments of Bradshaw [207]. Accurate detection of boundary layers is essential for correct function of the limiter because the inequality is not valid in the freestream.

An interesting historical detail is that the *original* SST model [142] (often referred to as SST1994) used the magnitude of vorticity, Ω, instead of the strain rate invariant, S, for limiting shear stress in Equation 7.16. This was found to be problematic, however, because Ω amplifies numerical noise, resulting in a speckled eddy viscosity distribution (see e.g. [208]). An additional advantage of using an S-based limiter is that the inverse relation between eddy viscosity and the strain rate ensures *realizability* of the turbulent stresses. *Realizability* implies that the turbulent stresses are mathematically achievable (see Moore and Moore [209]). This imposes the constraint that each principal stress of τ_{ij} is no greater than zero (considering that the autocorrelation $-\overline{\rho u u}$ cannot be positive) and no less than $-2\rho k$ (considering that $-\overline{\rho u_i u_i} = -2\rho k$). Presumably, it is for these two reasons that the S-based limiter is more widely used in modern solvers [199]. We refer to the model using a strain-rate-based stress limiter as SST2003 (to distinguish from SST1994). As we will see in the current study, the stress limiter of the SST2003 model is too strict, and results in undermixing for engine-realistic turbulence.

Standard k–ω and baseline model

We will not formally introduce the SKO and BSL transport equations, but note that from Equations 7.6 to 7.18, the SKO model [198] can be defined by setting $F_1 = 1$ (constant) and by calculating eddy viscosity using $\mu_t = \rho k/\omega$ (i.e. by disabling the stress limiter and omitting the cross-diffusion term). Model coefficients are also modified (see [198]). Similarly, the baseline (BSL) model [142] can be defined by disabling the stress limiter, setting closure coefficient $\sigma_{k1} = 2$ (versus 1.176 for SST), but retaining the blended zonal treatment and cross-diffusion term. We perform simulations using these simplified models to investigate the effects on NGV flows of model blending and the shear stress limiter.

Production limiters

In ANSYS CFX, the SST2003, BSL, and SKO turbulence models are paired with a turbulence production limiter. The production limiter is used to impose an upper limit on the turbulence production-to-dissipation ratio

$$\mathcal{P}_{\mathrm{lim}} = \min\left(\mathcal{P}, C_{\mathrm{lim}}\mathcal{E}\right) \tag{7.19}$$

where $\mathcal{P}_{\mathrm{lim}}$ replaces $\mathcal{P}$ in Equation 7.6 and 7.11, $\mathcal{E}$ is the turbulence dissipation rate, and C_{lim} is a clipping factor for the maximum production to dissipation ratio, $(\mathcal{P}/\mathcal{E})_{\mathrm{max}}$, which holds a default value of 10 in CFX. Production limiters were introduced to mitigate the unrealistic build-up of TKE around stagnation points [210]. In the context of eddy viscosity models, the so-called stagnation point anomaly is explained by the linear nature of the Boussinesq hypothesis, by which normal strains erroneously contribute to TKE production (see explanation of Moore and Moore [209]). For NGV flows, production limiters are also relevant for the flow around the suction peak, where high strain rates otherwise result in TKE over-production (recall $\mathcal{P} \approx \mu_{\mathrm{t}} S^2$). We use a production limiter with $C_{\mathrm{lim}} = 10$, unless explicitly stated otherwise.

7.3 High turbulence flat plate test

The flat plate test is perhaps the simplest example of boundary layer flow and has been used extensively for turbulence model calibration. Good likeness to experimental data in the flat plate test can be regarded as a prerequisite for accurate predictions in more complex flows. We briefly consider the literature on flat plate tests specific to the effects of freestream turbulence.

Folk et al. [83] recently investigated boundary layer development for low and high freestream TI at the same length scale (approximately 40 mm). The study builds on earlier work of Hancock and Bradshaw [211], as well as Thole and Bogard [212], who reported elevated skin friction at high TI, but did not report/control the momentum thickness Reynolds number, Re_θ. Folk et al. [83] used a turbulence grid and a rich-burn combustor simulator, to generate turbulence intensities of approximately 2.3% and 18.7%, reporting a 20% increase in skin friction coefficient and a 22% increase in dissipation coefficient at high TI (for the same Re_θ). These effects were shown to result from deep penetration of freestream turbulence into the boundary layer.

The flat plate data of Folk et al. [83] are plotted in Figure 7.1 alongside equivalent simulations using the SST2003 turbulence model, which were performed based on the test setup description in [76]. We now review the accuracy of SST2003 for predicting the skin friction coefficient, C_{f}, and an

auxiliary boundary layer shape factor (ratio of momentum-to-energy thickness), H_{23}. The auxiliary shape factor is relevant because it can be used to estimate the dissipation coefficient, C_{d}, using the approximation $C_{\mathrm{d}} \approx C_{\mathrm{f}}/4H_{23}$ (see Folk et al. [83]). The CFD-predicted velocity profiles exhibit peaking behavior close to the leading edge of the flat plate, as well as freestream acceleration due to blockage. In the current study, the reference velocity was defined as the peak velocity of the local profile, and displacement, momentum, and energy thickness were calculated by integrating up to the point with peak velocity.

First consider the skin friction coefficient, C_{f}, which is shown in Figure 7.1a. The experimental data of Folk et al. [83] indicates a 20% increase in skin friction (average across all points) going from low TI (2.3%) to high TI (18.7%). By comparison, SST2003 CFD predicts an increase of 35% (on average over the range from $(1000 < \mathrm{Re}_\theta < 2000)$. The overall agreement between experiments and CFD is excellent, with an average overprediction of 2.8% at low TI and an average overprediction of 16.1% at high TI. A better match at low TI is expected, because turbulence models are typically calibrated using low TI data.

Now consider the auxiliary shape factor (ratio of momentum-to-energy thickness), H_{23}, which is shown in Figure 7.1b. The experiments of Folk et al. [83] indicate a 4% reduction of H_{23} for the high TI case. A similar result is given by CFD, but the shape factor is lower than corresponding experimental data by, on average, 2.7%. Once again, the agreement between experiments and CFD is excellent at low TI, and acceptable at high TI.

Folk et al. show that the dissipation coefficient can be approximated as $C_{\mathrm{d}} \approx C_{\mathrm{f}}/4H_{23}$. Experimentally-measured and CFD-predicted dissipation coefficient data (using the approximated formula) are shown in Figure 7.1c. At low TI, the CFD-predicted dissipation coefficient is—on average—accurate to within 3.1% of experimentally-measured values. Going from low to high TI, C_{d} increases by 22% in experiments, and by 46% in SST2003 CFD. At high TI, we therefore expect SST2003 to overpredict kinetic energy loss by 20% for a given Re_θ. These results are promising, because they show that SST2003 is both relatively accurate in absolute terms and predicts the correct sensitivity to freestream TI. Average dissipation coefficient data for all turbulence models considered in the current study are summarized in Appendix 7.A.

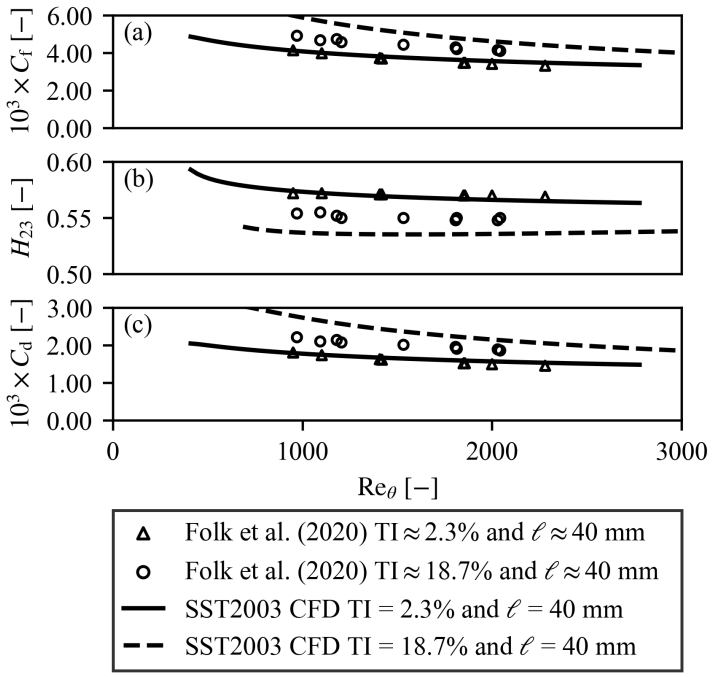


Figure 7.1: *Comparison of experimental data from Folk et al. [83] and CFD data using the SST2003 model, showing variation of: (a) skin friction coefficient, C_f; (b) auxiliary boundary layer shape factor, H_{23}; (c) dissipation coefficient, C_d, as a function of boundary layer momentum thickness,* Re_θ.

7.4 High turbulence NGV flows

Amend et al. [6] and Burdett and Povey [147] used the SST2003 model to simulate the flow of fully-cooled NGVs with turbulence of high intensity (13%) and large length scale (approximately equal to the NGV axial chord) at inlet. Both studies investigated the spreading and decay rates of the aerodynamic wake, and reported significant undermixing, when comparing SST2003 results to high-fidelity experimental validation data. Simplistically, an underprediction of spreading and decay rates indicates an underprediction of and/or incorrect distribution of eddy viscosity. Consider the contours of eddy viscosity, μ_t, from the SST2003 simulations of Amend et al. [6], which are shown in Figure 7.2 (cross-section at NGV midspan). The cascade inlet conditions were characterized using hot-wire anemometry, pressure probes, and thermocouples (for details see [6]). The integral length scale at cascade inlet was of the order of one axial chord (1.0 C_x), and the TI was approximately 13%. Most studies in which rich-burn combustor simulators have been used report integral length scales in the range 0.2 C_x to 0.4 C_x (see e.g [69, 75, 83]). In comparison to these studies we have a relatively large length scale, and this makes it particularly interesting for exploring limitations of existing turbulence models at conditions of both high turbulence and high length scale (with correspondingly lower dissipation rate with axial distance).

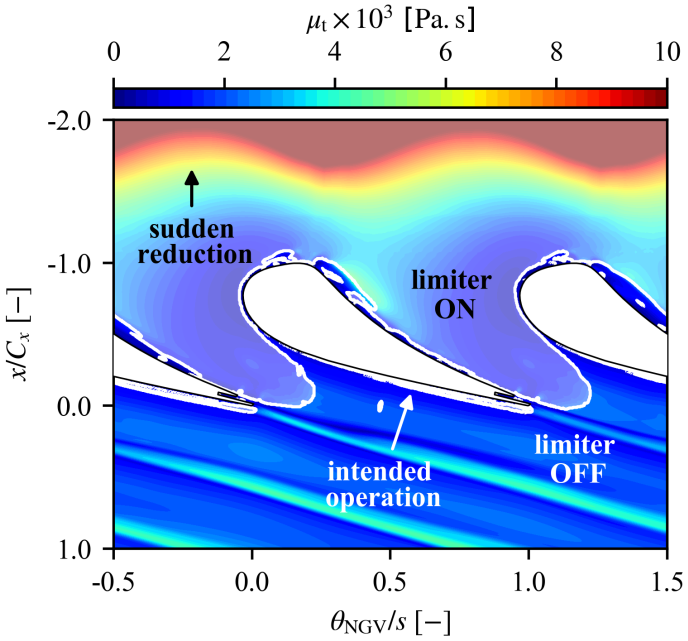


Figure 7.2: *CFD-predicted eddy viscosity, μ_t, at NGV midspan using the k–ω SST turbulence model. The shear stress limiter is active upstream of the NGVs and throughout the passage.*

The most striking feature in Figure 7.2 is a sudden reduction of eddy viscosity along a sinusoidal front, located approximately 0.8 C_x upstream of the leading edge. This reduction is not the result of a transport phenomenon, but rather is *algebraically enforced* through the shear stress limiter of the SST model (see Equation 7.16). We recall that the shear stress limiter was designed to improve predictions of separation in flows with strong adverse pressure gradients (see [142] for details). This is achieved by limiting eddy viscosity in the outer boundary layer, on the condition that $\mathcal{P} > \mathcal{E}$. The region of *intended* operation of the limiter is demonstrated on the uncovered suction side (SS). For the current case, the shear stress limiter is also *erroneously* active from far upstream of the leading edge, through the NGV passage, and extending up to the geometric throat. Erroneous activation throughout the vane passage (i.e. well beyond the outer boundary layer) is related to the combined effects of relatively large length scales in the freestream (on the order of 1.0 C_x at domain inlet) and high cross-passage strain (limiter active for $SF_2 > a_1\omega$, with S high on account of the flow field, and $F_2 = 1$ due to the large turbulence length scales in the freestream). In effect, the limiter artificially shields the near-wall region (on the vane surface) from incoming freestream turbulence, resulting in undermixing of the thermal mixing layer and aerodynamic boundary layer. The shielding phenomenon also explains why k–ω SST is sometimes reported to have a very low sensitivity to changes in the inlet turbulence. This may be desirable for external aerodynamic flows, but presents a problem in turbomachinery applications, where incoming turbulence is generally

higher, and known to affect heat transfer and kinetic energy loss.

The first blending function is also sensitive to the large freestream length scales (see $\arg_1$ in Equation 7.14), such that SKO-regime is active for approximately half of the NGV passage. As such, the intended zonal treatment (SKO in boundary layer; SKE in freestream) is not achieved. The effect is secondary to the more pressing shielding effect of the stress limiter, because its influence on results appears to be relatively small in comparison, as can be verified by modifying the first blending function.

7.5 Modified blending and stress limiter

For engine-realistic turbulence, neither the closure coefficient blending function, F_1, nor the shear stress limiter of the SST2003 model function as intended. The result is that almost the entire NGV passage is treated in the same way as the boundary layer. Both problems are related to the large turbulence length scales in the freestream. Remedial model modifications and alternatives are now considered.

Modified closure coefficient blending

The length scale-dependent term of $\arg_1$ (see Equation 7.14) can cause unreliable detection of boundary layers. This occurs because the large freestream length scales (representative of combustor outlet flow) render the log-layer indistinguishable from the freestream. The problem can be mitigated by using an alternate definition for F_1, where only the viscous sublayer is modeled using SKO (with freestream *and* log-layer modeled using SKE). Menter [142] suggests the following modified form for $\arg_1$

$$\arg_{1\mathrm{v}} = \min\left(\frac{500\mu}{\rho\omega y^2}, \frac{4\rho k}{CD_{k\omega}\sigma_{\omega 2} y^2}\right) \tag{7.20}$$

Equation 7.20 is equivalent to Equation 7.14, but with the length scale-dependent term removed. We implement this modification in CFX with a UserFortran junction box routine, which overwrites vertex values of F_1 (files and instructions available on request). Results using this modification are referred to as SSTF1V (i.e. SST with F_1 active in the viscous sublayer only). Results for this modification are presented in Appendices A and B.

Modified shear stress/realizability limiter

Now consider the *erroneous* activation of the shear stress limiter in the freestream (see Figure 7.2). Problematic behavior of the shear stress limiter has recently been reported by Wei [213], who found that stress limiter-induced undermixing could lead to premature corner separation in compressors. Wei proposed disabling the shear stress limiter entirely, reporting improved predictions using this method. In doing so, Wei effectively recovered the BSL model with slightly different closure coefficients ($\sigma_{k1} = 1.176$ instead of 2.0).

An alternative approach might involve reformulating the stress limiter to prevent erroneous activation in the freestream. This would be preferable, because completely disabling the stress limiter would likely compromise the predictive accuracy for separation. An alternative definition for the stress limiter is the *original* SST model [142], which uses the magnitude of vorticity, Ω, instead of the strain rate invariant, S, i.e.

$$\mu_{\mathrm{t}} = \min\left(\frac{\rho k}{\omega}, \frac{\rho a_1 k}{F_2 \Omega}\right) \tag{7.21}$$

Compared to Equation 7.16, Equation 7.21 reduces the artificial suppression of eddy viscosity in the freestream, because $\Omega \approx 0$ in the freestream, whereas $\Omega \approx S$ in boundary layers. In theory, the Ω-based shear stress limiter should therefore retain its *intended* operation in boundary layers, whilst eliminating the *erroneous* activation in the freestream. Where we present results using this modification we refer to them as SST1994. For consistency with the original SST model from 1994, the Ω-based limiter is paired with a production limiter clipping factor $C_{\mathrm{lim}} = 20$ (versus $C_{\mathrm{lim}} = 10$ in SST2003). Another minor difference is that the original (SST1994) model applies the production limiter to the TKE equation only, whereas CFX limits the production terms in both the TKE and specific dissipation rate equations (in accordance with SST2003). An SST1994-type limiter can be implemented in CFX by adding a source term in the ω equation, which makes up the difference between the *limited* and the *unlimited* source term. This appears to make little difference in practice, however, because production-to-dissipation ratio (as modeled) exceeds 20 only very locally (SS peak) and by a small margin.

Kalitzin et al. [214] shared the concern that the SST2003 shear stress limiter could potentially be too restrictive, noting that eddy viscosity may be reduced in regions of the flow where realizability is not necessarily violated. Kalitzin et al. suggested applying a shear stress limiter only where realizability would otherwise be violated. For compressible flow, this condition can be expressed as

$$\mu_{\mathrm{t}} \leq \frac{\rho k}{3\lambda_{\max} - \partial U_k/\partial x_k} \tag{7.22}$$

where $\lambda_{\max}$ is the largest principal strain (largest eigenvalue of the strain tensor S_{ij}), and $\partial U_k/\partial x_k$ is the familiar velocity divergence. The inequality follows from the compressible Boussinesq approximation in principal coordinates (i.e coordinates for which S_{ij} is purely diagonal). The condition is enforced using the same clipping approach as is used in Equation 7.16. We refer to this modification as SSTPSR (SST with exact principal stress realizability).

Calculating the principal strains *directly* increases computational cost. It may therefore be preferable to *estimate* the largest principal strain, $\lambda_{\max}$. Durbin [210] derived an *upper bound* for the largest eigenvalue of the strain rate tensor, $\lambda_{\max}$. For incompressible flow, realizability is guaranteed for

$$\mu_{\mathrm{t}} \leq \sqrt{\frac{1}{3}}\frac{\rho k}{S} \tag{7.23}$$

where all terms have previously been defined. Durbin used a definition for S which is a factor of $\sqrt{2}$ smaller than in the current study; the inequality has been scaled accordingly for consistency with Equation 7.10. The condition in Equation 7.23 is equivalent to the familiar SST2003 shear stress limiter (see Equation 7.16) with $a_1 = \sqrt{1/3} \approx 0.577$, provided that $F_2 = 1$ (true for large length scales). We refer to this modification as SSTDR (Durbin realizability). For boundary layers in particular, Bradshaw et al. [207] suggest that $a_1 = 0.31$ (this latter value being adopted in the SST model). This does not necessarily contradict the *inequality* of Durbin [210]. However, since the Bradshaw assumption does not hold in the freestream, we might expect that the SST2003 shear stress limiter is too strict in this region. Setting $a_1 = \sqrt{1/3}$ may partially alleviate this issue, although this can still result in condition that is *locally* too restrictive, considering that the value for $\lambda_{\max}$ is conservatively estimated as its *upper bound*. Park and Park [215] derived a *lower bound* for $\lambda_{\max}$, which is equivalent to $a_1 = \sqrt{4/3}$. This method does not reduce eddy viscosity below the realizability limit, but also does not guarantee realizability. Such a model is conceptually useful, but arguably of limited practical value. This realizability modification was not tested.

In summary, we consider the following approaches for mitigating the artificial suppression of turbulence in SST2003:

i) disabling the stress limiter completely (recovering the BSL and SKO models; tested with $C_{\mathrm{lim}} = 10$).

ii) Ω-based limiter (tested with $C_{\lim} = 20$ for consistency with the original SST1994 model [142]); we refer to this as SST1994.

iii) principal stress realizability (Equation 7.22; tested *without* a production limiter); we refer to this as SSTPSR.

iv) Durbin realizability [210] (equivalent to $a_1 = \sqrt{1/3}$; tested *without* a production limiter); we refer to this as SSTDR.

Methods (iii) and (iv) were tested *without* a production limiter because they are inherently realizable (SSTDR only where $F_2 = 1$). Considering that turbulence production scales with the difference of the principal stresses (see [209]), we expect that this approach will result in a slight over-production of turbulence, because experimental data shows that the principal stresses obey $\tau \leq -0.2\rho k$ [209] for plane-strain problems, rather than the slightly less restrictive *mathematical* condition of realizability, $\tau \leq 0$. The point is that the resulting turbulent stresses are formally *realizable*, but not necessarily *physically* achievable in practice. This is clearly a compromise but avoids sensitivity to the somewhat arbitrary production limiter clipping factor.

7.6 Additional models

The baseline algebraic Reynolds stress model, and the Spalart–Allmaras turbulence model were also tested. Both turbulence models were used in their documented forms only; for brevity we therefore introduce them only at a high level.

Explicit algebraic Reynolds stress model

Explicit algebraic Reynolds stress models (ARSMs) offer Reynolds-stress-model-like capabilities at a reduced computational cost, and with improved numerical stability (compared to full Reynolds stress models). ARSMs are classified as eddy viscosity models, but differ from SST, SKO, and BSL in that they replace the Boussinesq approximation (Equation 7.1) with a non-linear stress–strain relation as follows:

$$\tau_{ij} = -\rho k \left(a_{ij} + \frac{2}{3}\delta_{ij} \right) \tag{7.24}$$

where τ_{ij} is the turbulent stress tensor, a_{ij} is the anisotropy tensor, and δ_{ij} is the Kronecker delta. The anisotropy tensor, a_{ij}, is modeled using a polynomial of the strain rate (S_{ij}) and vorticity (Ω_{ij}) tensors (see Wallin and Johansson explicit ARSM [200]), which is derived from the exact Reynolds stress model equations by neglecting the advection and diffusion terms. The non-linear stress–strain

relation (i.e. Equation 7.24) is typically tailored to guarantee stress realizability, which eliminates the need for additional production and realizability limiters.

A modified version of the Wallin and Johansson model [200] is available in CFX, which combines a surrogate BSL model with a third-order tensor polynomial for a_{ij} [201]. We refer to this model as BSL-ARSM. Given that BSL-ARSM is inherently realizable, it is perhaps surprising that CFX defaults to a production limiter ($C_{\lim} = 10$) with this model. In the current study, the production limiter was disabled for BSL-ARSM.

Spalart–Allmaras model

The Spalart–Allmaras (SA) turbulence model [173] is an empirically-motivated transport equation for an eddy viscosity-like variable. SA is available as a partially-developed feature in ANSYS CFX. We include results from the SA model due to its historical use in turbomachinery applications. Results using the *default* wall-resolving model version are presented (as opposed to the version using wall functions, which performed poorly on the flat plate test case, and underpredicted loss for the NGV test case). Of note, SA does not model the decay of turbulent viscosity in the freestream, which is considered advantageous for external aerodynamics, but might be problematic for internal flows. For the current NGV test case this may be acceptable, however, considering that large length scales result in *naturally* low decay rates in the freestream.

7.7 Experimental data and setup

The experimental data of this study has previously been reported in Amend et al. [6], which considered the flow through an annular cascade of fully-cooled high-pressure NGVs at a Reynolds number of 7.5×10^5 (based on NGV axial chord) and a Mach number of 0.92. We briefly review the test section layout and instrumentation. For a detailed description, see [6, 121].

Test section layout

A meridional view of the test section is shown in Figure 7.3. The mainstream flow passes through a turbulence grid into a contracting inlet duct upstream of the NGVs. Both the vane airfoil and the endwalls are film-cooled. The airfoil coolant and hub-endwall coolant are supplied from a plenum at the hub. The casing endwall coolant is supplied from a separate plenum at the casing. Downstream of the NGVs, the partially mixed flow exhausts to atmospheric pressure through a parallel constant-area exit duct, which extends approximately 3 axial chords downstream of the NGV trailing edge before exhausting to a large plenum.

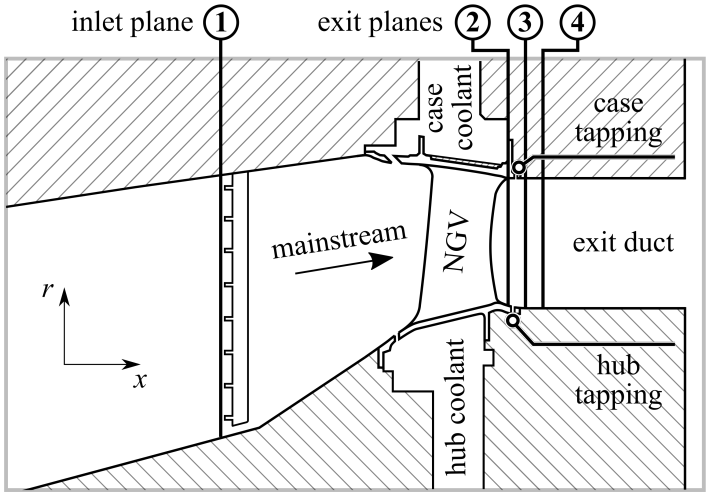


Figure 7.3: *Meridional view of the test section, showing inlet plane 1, NGVs, coolant feeds, and downstream measurements planes 2, 3, and 4.*

Instrumentation

Detailed traverse data of total pressure, total temperature, TI, and integral length scale were taken at the mainstream inlet plane (plane 1; see Figure 7.3). At plane 1, total pressure and total temperature were also monitored continuously using fixed Pitot total pressure rakes and thermocouple rakes. The mainstream mass flow rate was measured using a high-precision calibrated sonic nozzle (see high-level facility layout in [121]). Coolant stream mass flow rates were metered individually using sonic nozzles. Total pressure and total temperature in the hub and casing coolant plena were monitored. The NGV wake was characterized at three downstream measurement planes, which were located at 0.25 C_x (plane 2), 0.50 C_x (plane 3) and 0.75 C_x (plane 4) downstream of the midspan trailing edge. At each downstream plane, the flow was surveyed over two vane pitches circumferentially, and from hub to case radially. An aerodynamic five-hole probe used to measure flow angle, total pressure and Mach number, enabling the calculation of mass-flux-weighted averages. A dual-sensor thermocouple probe was used to survey the downstream thermal field.

Cascade inlet conditions

Experimentally-measured and CFD-predicted conditions of total pressure, total temperature, turbulence intensity, and length scale at plane 1 are shown as radial profiles in Figure 7.4. The experimental profiles were obtained by circumferentially averaging area traverse data from a 34-degree sector. The probes and measurement repeatability are discussed in [5]. Due to a probe size limitation, a small region near the hub could not be traversed. Similarly, the turbulence data

near the casing needed patching due to a local unsteady interaction with the probe access port. The patching method was informed by a k–ϵ CFD simulation of the upstream flow conditioning system and turbulence grid (for details see [6]).

First consider the experimentally-measured profiles in Figure 7.4. Normalized total pressure ($p_{0,\mathrm{norm}}$) was very uniform, with a variation of ±0.1% about the mean. Normalized total temperature ($T_{0,\mathrm{norm}}$) was also relatively constant across most of the span, except for the near-wall regions, where thermal boundary layers developed due to convective heat transfer from the hot flow to the test section walls. The turbulence intensity (TI) profile was reasonably flat, with an average of 13% and slightly elevated intensity in the lower half of the span. The integral length scale (defined from integral of autocorrelation; see Appendix 7.D) was on average 0.99 C_x, with a value of zero enforced at the walls of the patched profile to ensure suitability as a CFD inlet condition.

Now consider the CFD-predicted profiles at plane 1. The total pressure profile is similar in shape and magnitude; the temperature profile is flat because the walls were modeled as adiabatic; both turbulence parameters are reasonably well matched. Overall, this suggests that the patched experimentally-measured boundary conditions are appropriate for use as inlet conditions in CFD.

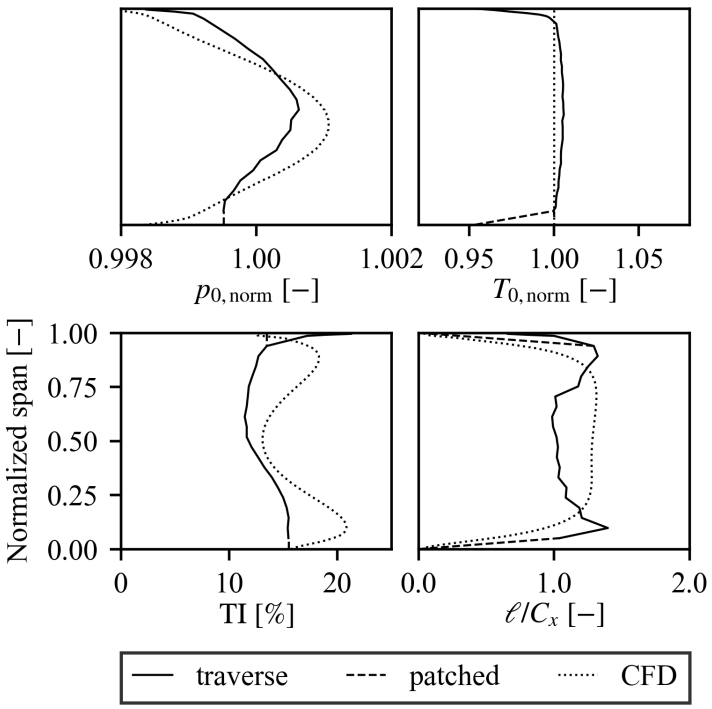


Figure 7.4: *Experimentally-measured and CFD-predicted radial profiles of normalized total pressure ($p_{0,\mathrm{norm}}$), normalized total temperature ($T_{0,\mathrm{norm}}$), turbulence intensity (*TI*), and normalized length scale (ℓ/C_x) at plane 1.*

7.8 Numerical methods

Simulations of the high-pressure NGVs were performed for eight turbulence models, using the fully-resolved vane geometry, operating at engine-matched conditions of Mach, and Reynolds numbers. We now briefly consider the computational domain, grid, model settings, and boundary conditions.

Domain and grid

The computational domain and grid are shown in Figure 7.5. The mainstream inlet is located at plane 1, and the outlet is located at the end of the exit duct (see test section layout in Figure 7.3). The film cooling holes, internal cooling passages, and trailing-edge slot were fully-resolved, with coolant introduced from inlets inside the respective plena at the hub and casing.

The 312 million-cell computational grid is hex-dominant, with refinement near walls, in proximity to small features, and inside the exit duct. A 23-cell prism layer was used for solid boundaries. A grid sensitivity study performed for the SST2003 model (see [6]). This was considered to be the most pessimistic, because the other models are more diffusive by nature. For the SST2003 simulation, average y^+ values on the pressure side, suction side, endwalls, and vane internals were 0.7, 1.3, 0.6, and 0.8, respectively.

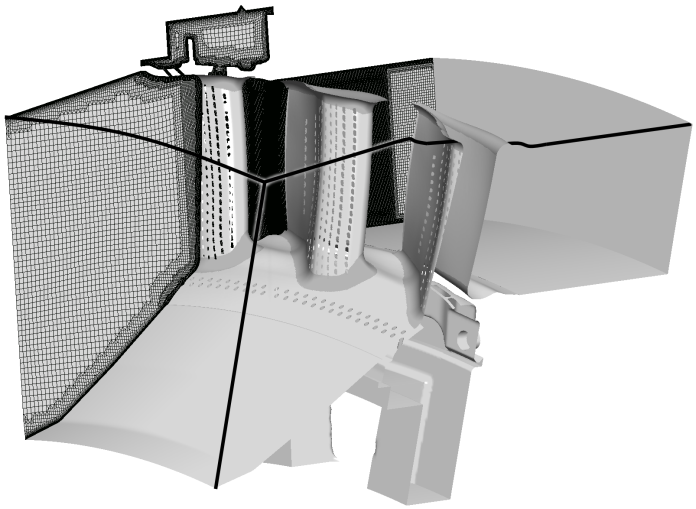


Figure 7.5: *Domain and computational grid of high-pressure NGVs with fully-resolved internals.*

Model settings and discretization

Simulations of the NGVs were performed in ANSYS CFX using the SST2003, SKO, BSL, SST1994, SSTPSR, SSTDR, BSL ARSM, and SA turbulence models. The working fluid was dry

air, which was modeled as an ideal gas with constant transport properties. The compressible energy equation (including viscous work) was used. The turbulent Prandtl number was decreased from its default value of 0.90 (calibrated for wall heat-transfer) to a value of 0.50 (calibrated for thermal mixing layers; see [174]). Advective fluxes were discretized using a blended first and second-order upwind-biased scheme, optimized to locally ensure boundedness whilst minimizing diffusiveness. Diffusion and pressure terms were evaluated using finite element shape functions. Model-specific settings for the production limiter and realizability modification/limiter are summarized in Table 7.1 below:

Table 7.1: *Summary of turbulence models, production limiter clip factor, C_{lim}, and realizability limiter formulation.*

Model	C_{lim}	Realizability limiter
SST2003	10	Equation 7.16; $a_1 = 0.31$; S-based
SKO	10	none
BSL	10	none
SST1994	20	Equation 7.21; $a_1 = 0.31$; Ω-based
SSTPSR	999	Equation 7.22
SSTDR	999	Equation 7.16; $a_1 = \sqrt{1/3}$; S-based
BSL-ARSM	999	Equation 7.24; see [200, 201]
SA	N/A	N/A

Boundary conditions

Inlet conditions of total temperature, total pressure, length scale and TI were specified as the experimentally-measured and patched profiles at plane 1 (see Figure 7.4). In ANSYS CFX, the length scale is defined as $\ell = \sqrt{k}/\beta^*\omega$ (see [205]). Good collapse of the experimentally-measured integral length scales at inlet using this definition was demonstrated in Figure 7.4 (see also the discussion about length scale definitions in Appendix 7.D). For the SA model, the experimental length scales and turbulence intensities were translated into eddy viscosity using Equation 7.3 (with k and ℓ calculated using the same method as for two-equation models). Hub and casing coolant inlets were mass flow inlets with constant total temperature, a TI of 5% and a viscosity ratio of 10. The domain outlet was a radial equilibrium condition, with an identical average pressure for all models. All remaining boundaries are walls, which were modeled as adiabatic and hydraulically smooth.

7.9 Performance metrics

In this section, metrics of aerodynamic efficiency, and wake spreading/decay rates are summarized. The efficiency of the expansion is quantified in terms of local kinetic energy (KE) loss and plane-

averaged KE loss coefficients. The local KE loss coefficient is defined by:

$$\zeta_1(r,\theta) = 1 - \frac{1 - \left(\frac{p_2(r,\theta)}{p_{02}(r,\theta)}\right)^{\chi}}{1 - \left(\frac{p_2(r,\theta)}{p_{01}}\right)^{\chi}} \tag{7.25}$$

where p_{02} and p_2 are the total and static pressure downstream of the NGVs, respectively, which vary as a function of r (radius), and θ (circumferential coordinate). p_{01} is the upstream mass-flux-averaged total pressure, and exponent χ is equal to $(\gamma - 1)/\gamma$, where γ is the ratio of specific heats (assumed constant and equal to 1.40). The local KE loss coefficient, ζ_1, represents the local KE deficit of the real flow relative to an isentropic expansion from the upstream total pressure to the local downstream static pressure.

A plane-averaged KE loss coefficient was defined following Lawaczeck [187]

$$\zeta_2 = 1 - \frac{(\dot{m}_{\mathrm{m}} T_{01} + \dot{m}_{\mathrm{c}} T_{0\mathrm{c}}) \left[1 - \left(\frac{\overline{p_2}}{\overline{p_{02}}}\right)^{\chi}\right]}{\dot{m}_{\mathrm{m}} T_{01} \left[1 - \left(\frac{\overline{p_2}}{p_{01}}\right)^{\chi}\right] + \dot{m}_{\mathrm{c}} T_{0\mathrm{c}} \left[1 - \left(\frac{\overline{p_2}}{p_{0\mathrm{c}}}\right)^{\chi}\right]} \tag{7.26}$$

where $\dot{m}_{\mathrm{m}}$ and $\dot{m}_{\mathrm{c}}$ are the mainstream and coolant mass flow rate, respectively, with corresponding mass-flux-weighted total temperatures T_{01}, and $T_{0\mathrm{c}}$. $\overline{p_{02}}$ and $\overline{p_2}$ are, respectively, the mass-flux-weighted total pressure, and the area-averaged static pressure downstream of the NGVs. For experiments, these averages are evaluated over 2 vane pitches, following the same pair of wakes in each measurement plane. Finally, $p_{0\mathrm{c}}$ is the mass-flow-weighted total pressure of the coolant feeds. The plane-averaged KE loss coefficient, ζ_2, represents the fractional KE deficit of the bulk flow, relative to mass-weighted isentropic expansions of mainstream and coolant streams to the area-averaged downstream static pressure.

The plane-averaged KE loss coefficient can be decomposed into profile-region and endwall-region KE loss coefficients. In the current study, the profile-region KE loss coefficient, ζ_{p}, is calculated using Equation 7.26, with the mass-flux-weighted total pressure, $\overline{p_{02}}$, evaluated over the central 80% of span (i.e. excluding endwall boundary layers). The endwall-region KE loss coefficient, ζ_{e}, can then be evaluated as the difference between the plane-averaged KE loss coefficient and the profile-region KE loss coefficient (i.e. $\zeta_{\mathrm{e}} = \zeta_2 - \zeta_{\mathrm{p}}$).

The thermal field is quantified in terms of the cold gas mass fraction, ψ, which is defined by:

$$\psi(r,\theta) = \frac{T_{01} - T_{02}(r,\theta)}{T_{01} - T_{0\mathrm{c}}} \tag{7.27}$$

where $T_{02}(r,\theta)$ is the downstream field of total temperature, with T_{01} and $T_{0\mathrm{c}}$ the

mass-flux-weighted total temperatures of the hot mainstream at inlet, and coolant streams at inlet, respectively. Due to spatial non-uniformity of total temperature at inlet, it is possible for ψ to be locally negative.

We also consider the aerodynamic and thermal wakes in terms of their spreading and decay rates, so as to compare to predicted mixing rates using various turbulence models for engine-realistic inlet turbulence. Amend et al. [6] studied spreading and decay rates in terms of the peak intensity and the full width at half maximum (FWHM) of ζ_1 and ψ. FWHM can be misleading for measuring spreading, however, because it does not account for wake *shape*. As an example, a wake profile with high excess kurtosis (i.e. *tailedness*) can still have low FWHM, because the distribution at levels below half the maximum do not affect the FWHM value. The degree of spreading can also be quantified in terms of the standard deviation of the wake distribution (i.e assuming the wake profile is a continuous probability density function for θ, normalized such that integrated/total probability is unity). In the current study, both the standard deviation of the wake distribution and its peak intensity were calculated based on the radially-averaged wake profiles of ζ_1 (10–90% span) and ψ (20–80% span). For annular cascades, the wake generally deforms due to radial variations in the circumferential progression rate of the wake. In a direct radial averaging approach, this can result in smearing of the peaks. For this reason, the wakes were *restacked* (peaks were circumferentially aligned), prior to averaging radially (averaging performed in the transformed coordinate system).

7.10 Results and analysis

Simulations using eight turbulence models (see Table 7.1) are compared to experimental data from fully-cooled NGVs at engine-matched conditions of Mach number, Reynolds number, and turbulence. The purpose is to compare the performance of turbulence models in terms of total KE loss and wake mixing characteristics. The aim is to help inform turbulence model selection for aerodynamic simulations in conditions of high TI and large length scale (e.g. HP NGVs).

Kinetic energy loss and cold gas mass fraction at downstream measurement plane

In this section we consider the aerodynamic and thermal wakes at the downstream measurement plane (plane 4 in Figure 7.3) 0.75 C_x downstream of the midspan trailing edge. In Figure 7.6 we compare experimental data with CFD predictions using eight different turbulence models. The downstream plane was chosen because it emphasizes turbulence model differences the most (greater development distance). The plane is close to the HP rotor leading edge plane. The local kinetic energy loss coefficient, $\zeta_1(r, \theta)$, is shown in the left column of Figure 7.6, and the cold gas mass

fraction, $\psi(r, \theta)$, is shown in the right column of Figure 7.6. Radially, the data spans from hub to casing, covering two vane pitches in the circumferential direction. The data are viewed from downstream, and in normalized cylindrical coordinates, where r_{norm} is the span-normalized radius (datumed to the hub) and θ_{norm} is the vane-pitch-normalized circumferential location. For each turbulence model, comparisons are drawn to the corresponding experimental data, and the SST2003 reference model.

We now consider each row of Figure 7.6 in turn, examining the wake shapes, peak intensity, and the width of both the aerodynamic and thermal wakes.

i) *Experimental data; row 1.* First consider the contours of KE loss (aerodynamic wake), shown on the left-hand-side. The bowed wakes (regions of total pressure deficit) can be seen at approximately $\theta_{\mathrm{norm}} = 0$ and 1. Near $r_{\mathrm{norm}} = 0$ and 1, loss increases steeply on account of the endwall boundary layers. Loss cores coalescing with the wake around 15% and 75% span correspond to secondary flows. The hub secondary flow has greater intensity on account of a lower static pressure and correspondingly higher Mach number. Now consider the contours of cold gas mass fraction (thermal wake), which are shown on the right-hand-side. As the thermal wake is dominated by (relatively spanwise uniform) coolant ejection from films on the vane surface and from the TE slot, the thermal wake shape is similar to the aerodynamic wake shape. Thermal secondary flows appear as accumulations of cold fluid (high ψ) at $\theta_{\mathrm{norm}} = 0$ and 1, around 15% and 90% span. These coalesce with the near-wall thermal deficit (increase of ψ) of the platform cooling flows (see cooling configuration in Figure 7.3).

ii) *SST2003 model; row 2.* Predictions using the SST2003 reference model give rise to aerodynamic and thermal wake *shapes* which match the experimental data reasonably well, although the CFD-predicted wakes are significantly undermixed compared to experiments (for detailed analysis and discussion see [6]). Likewise, features of the aerodynamic and thermal *endwall flow* are adequately captured but appear undermixed compared to experimental data. Undermixing is related to the shear stress limiter (see Equation 7.16), which is active throughout the vane passage (see Figure 7.2) and reduces eddy viscosity significantly below the realizability limit. This inhibits turbulence production and stresses (via eddy viscosity), consequently reducing mixing of the aerodynamic boundary layer and thermal mixing layer with the freestream.

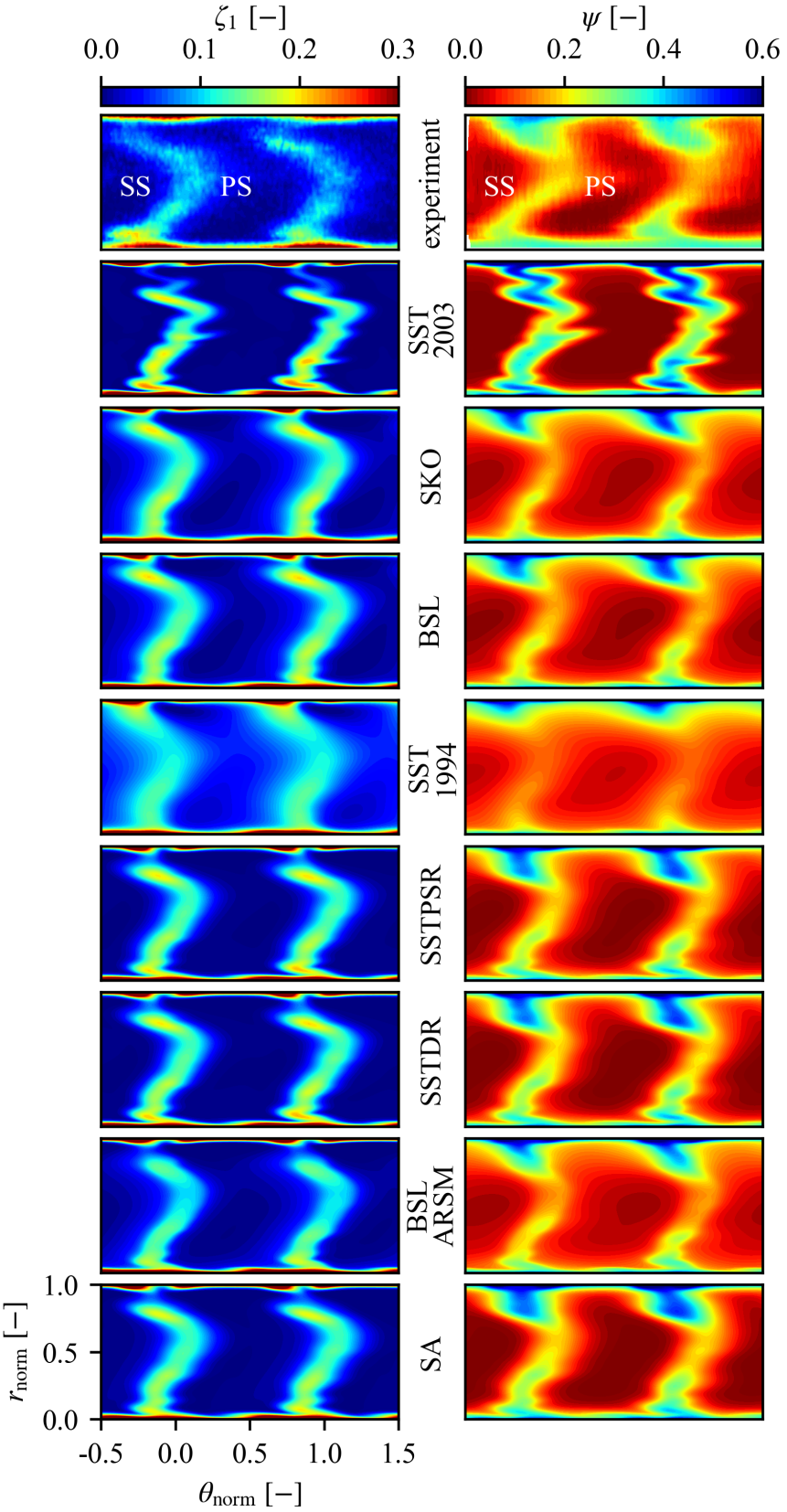


Figure 7.6: *Comparison of experimental measurements and CFD predictions using eight turbulence models at measurement plane 4 (0.75 C_x): (left column) local kinetic energy loss coefficient, ζ_1; (right column) cold gas mass fraction, ψ.*

iii) *SKO and BSL models; rows 3 and 4*. These models are mathematically very similar to each other; the only distinction is that the k–ω cross-diffusion term is omitted in SKO, and that closure coefficients are not blended in the SKO model. For this reason, and because predictions are almost identical, we treat the results together. We recall that SKO and BSL differ from SST2003 in that they do not incorporate a shear stress/realizability limiter. The effect is twofold because—without a realizability limiter—the incoming eddy viscosity is fully advected (i.e. not suppressed algebraically), which has the knock-on effect of amplifying TKE production around the SS peak ($\mathcal{P} \approx \mu_\mathrm{t} S^2$). The additional TKE enhances diffusion of the airfoil boundary layers, which leads to aerodynamic wakes that are broader and more radially uniform than using the SST2003 model. Peak KE loss in the profile-region (central 80% of span) is not significantly reduced, however, because the greater turbulence also increases KE dissipation at the wall (see flat plate data). In terms of the aerodynamic wake shape, the casing secondary flow loss cores in SKO and BSL predictions migrate closer to the casing, which leads to reduced likeness with experiments. The near-endwall KE loss distributions are very similar to that of SST2003, and experiments. Now consider the predicted thermal wake for the SKO and BSL models. The thermal wake is significantly more mixed-out than for the SST2003 model, with lower peak ψ in the profile region of the wake (central 80% of span). Secondary flows marked by cold gas (roll-up of the platform cooling flow) are also more mixed-out than the SST2003 model, such that their shape is a better match with experimental data. In between the wakes, the predicted penetration depth of endwall coolant into the freestream is significantly greater than the SST2003 prediction and slightly greater than experiments (i.e. overmixed).

iv) *SST1994 model; row 5*. This model uses a vorticity-based shear stress limiter (see Equation 7.21) which is only active in boundary layers. In other words, the model is not realizable in the freestream, which leads to over-production of TKE and excessive spreading of both aerodynamic and thermal wakes, compared to experiments. The increase in spreading (when compared to SKO and BSL) can be explained by the relaxed production limiter clip factor of 20 (used for consistency with [142]) versus the default value, $C_\mathrm{lim} = 10$ (used for SST2003, SKO, and BSL). In combination with a non-realizable stress–strain relation, $C_\mathrm{lim} = 20$ allows for greater freestream production of TKE around the SS peak than any other model. The additional TKE increases eddy viscosity and KE loss. Predictions from the SST1994 model feature a speckled eddy viscosity distribution around the SS peak (not shown), which occurs

due to numerical error in the strain rate tensor and a feedback loop with the realizability limiter (see also [208]).

v) *SSTPSR and SSTDR models; rows 6 and 7.* These models are based on the same transport equations as the SST model but use modified definitions for the realizability/stress limiter. SSTPSR enforces *exact* stress realizability (see Equation 7.22) by calculating principal strains directly, and SSTDR *estimates* principal strains using incompressible arguments (see Equation 7.23). Both models were tested *without* a TKE production limiter ($C_{\lim} = 999$). This corresponds to the condition of maximum TKE production, given the requirement that principal Reynolds stresses cannot be negative. This contrasts with the SST2003 model, which is also realizable, but enforces a much stricter limit on TKE production and turbulent stresses. The SSTPSR and SSTDR models are discussed collectively because they are conceptually alike (exact stress realizability), and because their aerodynamic and thermal wake profiles at 0.75 C_x are very similar. Compared to the SST2003 predictions, the predicted aerodynamic and thermal wakes were slightly broader, with enhanced radial mixing. Peak intensity of KE loss was very similar to the SST2003 model. The predicted thermal wake shapes and secondary flows marked by cold gas (platform cooling roll-up) were considerably more mixed-out than using the SST2003 model, but slightly less mixed than in experiments. Overall the results for SSTPSR and SSTDR were similar; users may prefer to use SSTDR because of the relative ease of implementation and reduced computational cost.

vi) *BSL-ARSM model; row 8.* In this model the Boussinesq approximation is replaced with a non-linear stress–strain relation (i.e. Equation 7.24) with inbuilt realizability. For this reason, BSL-ARSM can be used without a TKE production limiter (i.e., $C_{\lim} = 999$). The predictions using the BSL-ARSM model show significantly wider and less intense wakes than the SST2003 model. Overall, the BSL-ARSM model appears to give the best match with experiments among the models tested. The thermal field matches experiments well both in terms of profile-region coolant spreading and the shape of secondary flows marked by cold gas, but is slightly overmixed near the endwalls.

vii) *Spalart–Allmaras (SA) model; row 9.* This model differs from the other models in that it is based on a single transport equation for an eddy viscosity-like variable (instead of separate transport equations for k and ω). The SA model predicts an aerodynamic wake that is similar to that from the SSTPSR and SSTDR models, both in terms of shape and peak intensity. The

corresponding thermal wake is slightly less mixed-out than for the SSTPSR and SSTDR models, especially in terms of the endwall cooling flow. Overall, SA may be an attractive choice for aerodynamic calculations because its predictions are similar to the SSTDR/SSTPSR models but the model is easier to recalibrate than its two equation counterparts. Notably, by nature of the construction of the Boussinesq approximation (see Equation 7.1) *without* the TKE term, the SA model *always* produces non-realizable stresses. Nevertheless, diffusivity does not *explode* (like in SST1994, for example) because the positive feedback loop through the TKE production term is not present. Despite non-physical Reynolds stresses, turbulent momentum diffusion is adequately captured because the effect depends on *spatial gradients* of the stresses, not their absolute values. Non-realizable stresses *may* affect diffusion of the thermal field, however, because the turbulent viscous work term in the RANS energy equation depends on the *absolute* values of the turbulent stresses. This might also explain why the thermal field of the SA model appears slightly less mixed than for the SSTPSR and SSTDR models, despite having a very similar aerodynamic field.

Plane-averaged, profile-region, and endwall-region loss

High freestream TI has been shown to increase the KE loss in both the flat plate environment [83, 211, 212] and NGV [83, 82, 216]. We therefore consider the impact of turbulence model on integrated KE loss. The trends of plane-averaged KE loss coefficient, ζ_2, profile-region KE loss coefficient (central 80% span), ζ_p, and endwall-region KE loss coefficient (top and bottom 10% span), ζ_e, are shown in Figure 7.7a to Figure 7.7c, respectively, as a function of normalized axial distance, x/C_x. CFD data were interrogated at axial intervals of approximately 0.4 mm. Experimental data are shown for planes 2, 3, and 4 (0.25, 0.50, and 0.75 C_x, respectively); the same pair of wakes was considered at each plane (i.e. the same region of flow). Experimental bias uncertainty for ζ was approximately ±0.0016 (absolute; 95% confidence interval). The bias uncertainty was calculated from manufacturer-quoted instrument accuracy for combined linearity, hysteresis, and repeatability error.

First, consider the trends of plane-averaged KE loss coefficient (ζ_2) in Figure 7.7a. The CFD-predicted trends are relatively similar to each other in terms of *shape* but are offset in absolute value of the coefficient. We consider the CFD predictions in ascending order of ζ_2. Plane-averaged KE loss was lowest for the SST2003 model, with an 11.9% underprediction relative to experiments (on average across planes 2, 3, and 4). Losses were very similar between SSTDR (1.4% lower than experiment), BSL-ARSM (1.2% lower than experiments), SSTPSR

(1.5% greater than experiment), and SA (3.3% greater than experiment). The predictions of these four models are within the estimated experimental bias uncertainty range at all 3 planes. The remaining three models (BSL; SKO; SST1994) significantly overpredict plane-averaged KE loss: by 21.1% for the BSL model, by 23.3% for the SKO model, and by 56.1% for the SST1994 model. This result is consistent with the expectation that turbulence models with less restrictive turbulence production terms (realizability limiter and production clip factor) will predict greater KE losses. Indeed, only the non-realizable models (BSL, SKO, and SST1994,) *overpredicted* the experimentally-measured plane-averaged KE loss. Conversely, in the presence of large length scales, SST2003 enforces the most restrictive condition of realizability in the freestream and was the only model to *underpredict* plane-averaged KE loss. The agreement of the realizable models (SSTDR, SSTPSR, and BSL-ARSM) with the experimental data is—of course—a good outcome, but the performance would be expected to worsen if surface roughness effects were modelled. The effect was investigated by performing an SST2003 simulation, using a sandgrain roughness of 2.5 $\times$ 10^{-4} $\times$ C_x for all wetted NGV surfaces (based on representative profilometry data of a similar new vane; see Michaud et al. [137]). The roughened walls gave rise to a 15.0% increase in plane-averaged KE loss, compared to the SST2003 simulation with smooth walls. Another effect which is known to affect KE loss is the state of the boundary layer (turbulent vs. laminar). The turbulence models assume fully turbulent boundary layers by design (high dissipation coefficient) across the entire vane surface. In the real flow—although the leading edge showerhead cooling flows are expected to cause immediate transition—there is likely local relaminarization on the SS [217], which has an associated dissipation coefficient lower than that for an equivalent turbulent flow (see dissipation coefficient correlations [145]). If this relaminarization could be accurately modelled in CFD, we would expect this to reduce the predicted profile-region KE loss. That is, the effect of adding this in the modeling would act in a contrary direction to the effect of adding surface roughness.

Now consider the trends of profile-region KE loss coefficient, ζ_{p}. These are shown in Figure 7.7b. The general trend of both the experimental measurements and CFD-predicted data for profile-region KE loss coefficient is a gently asymptotic form which remains approximately constant for $x/C_x > 0.50$. Asymptotic behavior indicates that secondary kinetic energy has fully mixed out (see also discussion in [6] and [147]), meaning that the approximately constant plateau value can be viewed as the mixed-out profile-region KE loss. As with the plane-averaged KE loss coefficient data (Figure 7.7a) the CFD trends for all eight turbulence models are similar in *shape* to each other

but offset in absolute value of the coefficient.

Consider now the CFD predictions of profile-region KE loss in ascending order of profile-region KE loss coefficient: SST2003 predicts a trend of ζ_{p} that is (average of planes 2–4) 11.8% lower than experimentally-measured value; SSTPSR, BSL-ARSM, and SSTDR have average overpredictions of 1.5%, 1.7%, and 1.7%, respectively; SA has greater profile-region loss, with an average overprediction of 8.4%; for the non-realizable two-equation models, overpredictions of ζ_{p} were 29.4% (BSL), 31.4% (SKO), and 73.0% (SST1994). Once again, the models with *exact* realizability matched experimental data best, with significant overpredictions for the non-realizable models, and a slight underprediction using SST2003. In superposition with surface roughness effects, we expect profile-region loss to increase for all models. This could well worsen the good agreement between experimental data and the SSTDR, SSTPSR, and BSL ARSM models. Indeed, the profile-region loss coefficient increased by 15.1% in the SST2003 simulation including surface roughness, which corresponds to a 1.6% overprediction, compared to experiments. Similarly, we might expect a slight reduction of the CFD-predicted profile KE loss, if SS boundary layer relaminarization had been modeled (boundary layers are currently modeled as fully turbulent).

Finally, consider the trends of endwall-region KE loss coefficient, ζ_{e}. These are shown in Figure 7.7c (note scaled y-axis). All CFD-predicted trends of ζ_{e} essentially overlay. Considering that $\zeta_2 = \zeta_{\mathrm{p}} + \zeta_{\mathrm{e}}$, this indicates that the variations of plane-averaged (i.e total) KE loss are primarily driven by an increase of profile-region KE loss. This suggests that models can be tuned to match profile loss in isolation. A possible explanation for the low sensitivity of endwall-region KE loss to the turbulence model is that the CFD inlet boundary condition (experimentally-measured at plane 1; see Figure 7.3) has much lower eddy viscosity near the endwalls, than in the freestream. Recalling that TKE production is proportional to eddy viscosity, this reduces the influence of the production limiter and/or realizability modification in this region. Endwall-region KE loss predictions from all models fall inside the experimental bias uncertainty range at planes 3 and 4, with a mis-match at plane 2 ($0.25C_x$). We note that some aspects of the experimental measurement uncertainty are hard to quantify, particularly in relation to measuring very thin boundary layers (exacerbated at plane 2) with a probe of finite tip diameter.

For completeness, we note the presence of small variations in the BSL ARSM trends of profile-region and plane-averaged KE loss. These occur due to non-monotonic decrease of mass-flux-averaged total pressure. This effect was investigated using a simplified test case. The behavior

was insensitive to grid coarsening, time-step refinement, and floating-point precision, but appeared to be amplified/damped depending on the inlet turbulence. This suggests that the phenomenon is model-related. The BSL-ARSM model is a fairly recent development, and this may be the result of some model-instability at extreme boundary conditions of turbulence.

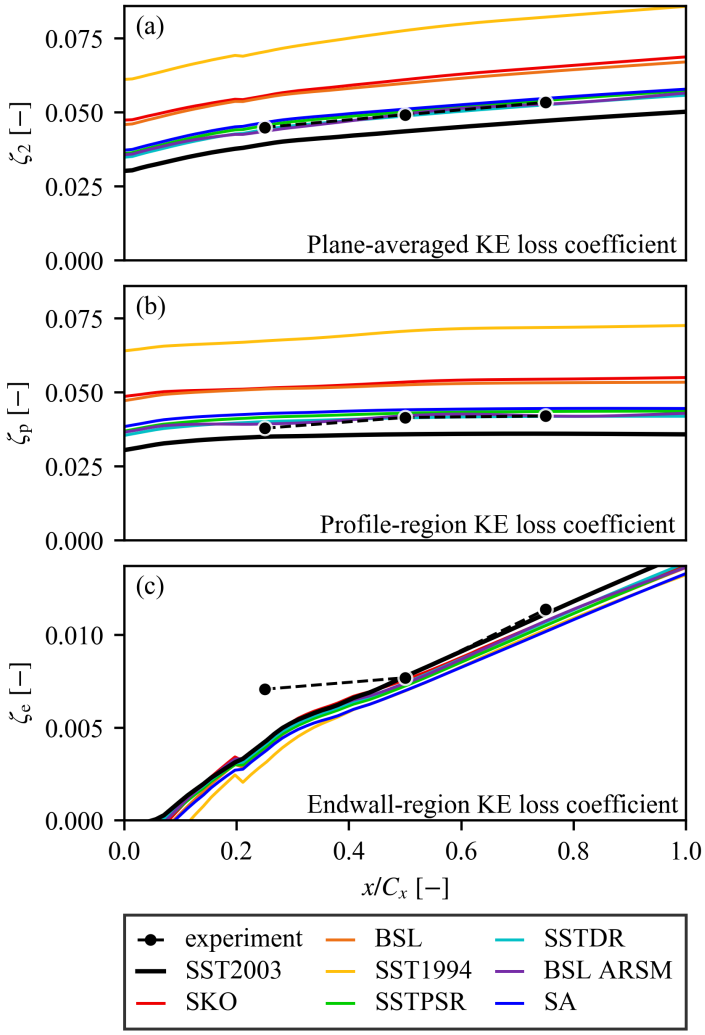


Figure 7.7: *Comparison of experimental measurements and CFD predictions using eight turbulence models, showing axial evolution of: (a) plane-averaged kinetic energy loss coefficient, ζ_2; (b) profile-region kinetic energy loss coefficient (10–90% span), ζ_p; (c) endwall-region kinetic energy loss coefficient (0–10% and 90–100% span), ζ_e.*

Aerodynamic and thermal wake shapes

Undermixing of NGV wakes is a frequently-observed phenomenon affecting CFD predictions using *steady* RANS models. Lower-than-experimental spreading-rate and peak-decay-rate occur because trailing edge *unsteady* vortex shedding and the associated mixing cannot be captured by *steady* RANS. The studies of Burdett and Povey [147], as well as Kopriva et al. [179] demonstrated that

using *unsteady* RANS increases the CFD-predicted spreading/decay rates slightly, when compared to steady RANS, resulting in marginally better collapse with experimental data.

An additional mechanism which affects the wake width downstream of the NGVs is SS boundary layer growth. Using a linear turbine cascade, Folk et al. [83] investigated the effects of high inlet TI, reporting a 37% increase of kinetic energy loss, and a 28% increase of wake width (compared to low TI inlet conditions). Blade-surface boundary layer measurements using hotwire probes showed that the increase in kinetic energy loss and wake width for high TI conditions were primarily driven by enhanced mixing between the freestream and the SS boundary layer. The boundary layer diffusion effect is separate from (but possibly interacting with) the unsteady trailing edge effects but does not appear to be inherently unsteady in itself. It should be possible to predict the non-coupled component of this effect with *steady* RANS.

Before examining the spreading and decay rates of the aerodynamic and thermal wakes, we analyze the *shapes* of the wakes. Radially-averaged profiles of the *restacked* aerodynamic and thermal wakes at 0.75 C_x (plane 4; see Figure 7.3) are shown in Figure 7.8. The restacked aerodynamic and thermal wakes were averaged over span ranges of 10–90%, and 20–80% respectively. The averaging window for the thermal wake was slightly narrower than for the aerodynamic wake to reduce the influence of endwall coolant penetration, which was sensitive to the choice of turbulence model (see Figure 7.6). Experimental data are marked using circles. The bias uncertainty in ζ_1 was estimated to be ±0.0016 (absolute; 95% confidence interval). The bias uncertainty in ψ was estimated to be ±0.04 (absolute; 95% confidence interval; propagated from K-type thermocouple bias uncertainty [195]). CFD data are shown for the eight turbulence models in Table 7.1.

First consider the circumferential aerodynamic wake profiles (restacked and radially-averaged) of local KE loss coefficient, ζ_1, shown in Figure 7.8a. The experimentally-measured wake profile is approximately symmetric, with peak value $\zeta_1 = 0.103$. All CFD-predicted wake profiles have slight asymmetry with greater weight towards the SS, and with significantly greater peak loss than the experiment (between 20.0% and 49.0% greater). CFD predictions using the SST2003, SKO, BSL, SSTPSR, SSTDR, and SA models all have similar peak loss, which is between 40.7% and 49.0% higher than the experimentally-measured value. This suggests that the realizability modification differences between these models do not have a strong influence on peak loss. SST1994 and BSL-ARSM have closer peak loss to the experimental value, with respective over-predictions of 23.5% and 20.0%. The turbulence models differentiate themselves from each other mostly in terms of

their KE loss distribution on the SS of the wake (see also contours of Figure 7.6). This is consistent with Folk et al. [83], who found that freestream turbulence primarily affects the SS boundary layer, and the corresponding SS of the wake. The pressure side (PS) wake profile was less affected by the choice of turbulence model (except for the SST1994 model). Over-spreading for the SST1994 model (on both PS and SS) is related to the relaxed TKE production limiter clip factor ($C_{\mathrm{lim}} = 20$), and the lack of a freestream realizability limiter, which give rise to excessive spreading rates and KE losses.

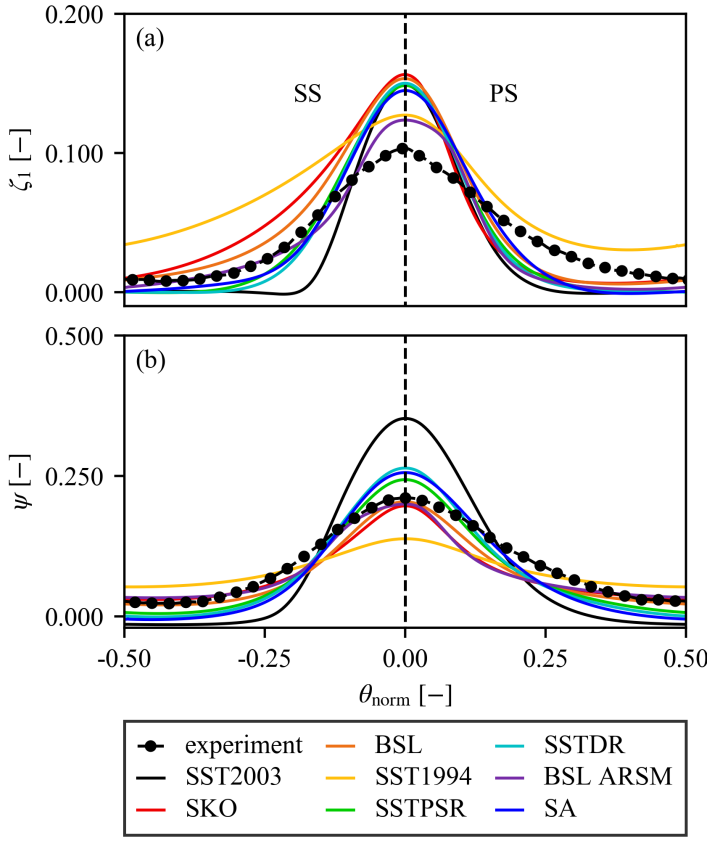


Figure 7.8: *Comparison of experimental measurements and CFD predictions using eight turbulence models, showing radially-averaged profiles of: (a) local KE loss coefficient, ζ_1 (aerodynamic wake; 10–90% span); (b) cold gas mass fraction, ψ (thermal wake; 20–80% span) at 0.75 C_x (plane 4). Wakes were restacked (peaks circumferentially aligned) and centered about $\theta_{\mathrm{norm}} = 0$ prior to radial averaging.*

Now consider the circumferential profiles of the restacked and radially-averaged thermal wake, which are shown in terms of the cold gas mass fraction, ψ, in Figure 7.8b. The experimentally-measured thermal wake is broadly symmetric about the peak value of cold gas mass fraction (0.211) and similar in shape to the corresponding aerodynamic wake. The CFD-predicted thermal wakes are also generally symmetric, but the wake widths are sensitive to

the turbulence model. The thermal wake peak intensity was greatest for SST2003 (0.352 cold gas mass fraction; +66.6% compared to experiments). The remaining models, by descending order of peak cold gas mass fraction, were SSTDR (0.264; +24.9%), SA (0.256; +21.1%), SSTPSR (0.243; +15.1%), BSL (0.204; −3.4%), BSL-ARSM (0.200; −5.4%), SKO (0.197; −6.9%), and SST1994 (0.138; −34.6%). Perhaps surprisingly, the model ordering by peak cold gas mass fraction does not correlate one-to-one with the ordering by peak KE loss. The reason is that cold gas mass fraction is a conserved quantity, such that greater diffusivity (i.e. eddy viscosity) will always lead to additional spreading *and* decay. For the aerodynamic wake, greater model diffusivity increases wake width, but is also accompanied by a rise in the profile-region KE loss coefficient (due to additional turbulent shear stress near the walls). As such, peak KE loss coefficient values do not necessarily decrease when the wake width increases. This implies that the thermal field is easier to optimize, because the cost function is simpler.

Aerodynamic wake spreading and decay

We now consider the spreading and decay trends of the aerodynamic wake for experiments and eight turbulence models. Spreading and decay rates merit attention because the dynamic loading of the HP rotor blade depends on the intensity of the NGV wake. Aerodynamic wake width and intensity are studied using radially-averaged profiles (10–90% span) of the restacked wake. A wide span range was chosen to reduce bias from local gaps or hotspots in the wake, and to improve precision uncertainty of the experimental data. We consider the axial range 0.0 C_x and 1.0 C_x. We quantify wake width in terms of the pitch-normalized standard deviation of the wake distribution, σ/s, and we quantify wake intensity in terms of the peak value of (radially-averaged) local KE loss, $\zeta_{1,\max}$. The pitch-normalized standard deviation σ/s has been multiplied by $\sqrt{12}$ (the standard deviation of a uniform distribution over the interval 0 to 1 in pitch is $1/\sqrt{12}$) such that the "width parameter" is unity for uniformly distributed KE loss.

First consider the trends of pitch-normalized and rescaled aerodynamic wake width (i.e. standard deviation of the wake distribution), σ/s, which are shown in Figure 7.9a. The experimental trend is for an approximately linear increase in wake width with axial distance. The CFD trends are broadly similar, but with periodic inflections, owing to varying wake whirl angle, which affects the wake width when evaluated on an axial plane (see discussion in [6]). We now consider the CFD models in ascending order of average wake width.

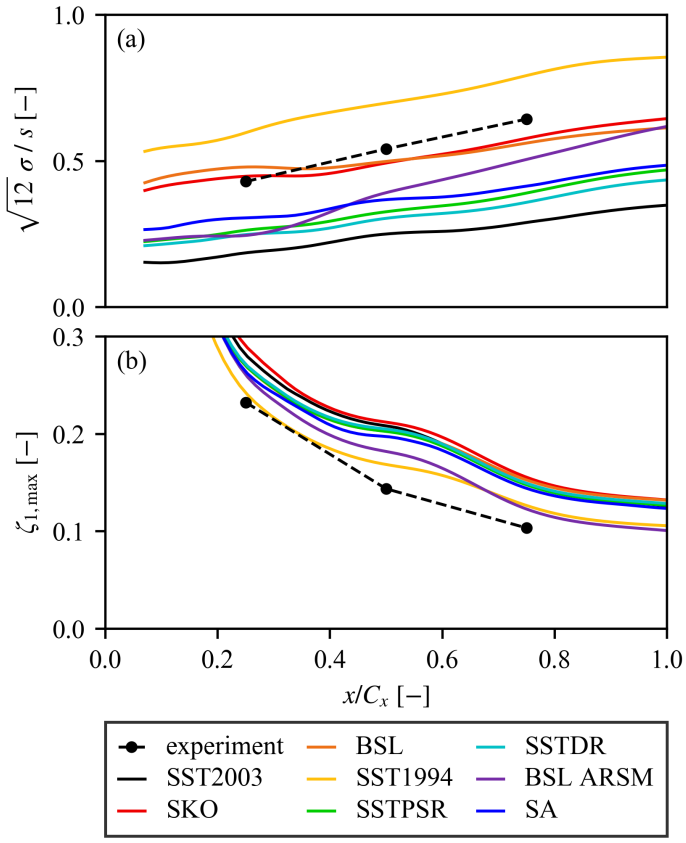


Figure 7.9: *Comparison of experimental measurements and CFD predictions using eight turbulence models, showing the axial evolution of: (a) pitch-normalized and rescaled standard deviation of the aerodynamic wake distribution, σ/s; (b) peak local KE loss coefficient, $\zeta_{1,\max}$. Wake peaks were circumferentially aligned (i.e restacked) prior to radial averaging (10–90% span).*

SST2003 predicted the narrowest wake with a width 55.0% lower than experiments (average across planes 2, 3, and 4). SSTDR, SSTPSR, and SA closed the gap with experiments slightly, with respective underpredictions of 42.1%, 37.5%, and 32.2%. Wake width for BSL-ARSM was on average 30.7% lower than for experiments. SKO and BSL had respective underpredictions of 5.0% and 4.0%, and were the best match with experiments. As illustrated by the circumferential profiles of Figure 7.8, the increase in wake width (compared to SST2003) is biased towards the SS, with relatively little change in the PS wake. The point is that the good agreement of both SKO and BSL model predictions with experimental data occurs due to excessive spreading of the SS boundary layer, which compensates for the underprediction of PS wake spreading. The SS spreading is precipitated by an overprediction of TKE production in the vane passage (both models are non-realizable). For both models, the excessive width of the SS-wake is accompanied by an approximately 30% overprediction of profile-region KE loss. SST1994 was the only model to

overpredict aerodynamic wake width (+30.3%). Excessive spreading occurs because the model is non-realizable (i.e. susceptible to turbulence overproduction) and has a relaxed clip factor ($C_{\mathrm{lim}} = 20$). This was accompanied by a 73.0% overprediction of profile-region KE loss. The takeaway is that—for high TI NGV flows—turbulence model choice can significantly affect predictions of aerodynamic wake width through the degree of boundary layer spreading on the SS of the airfoil. SS boundary layer spreading correlates with increased profile-region KE loss, such that models that more accurately predict wake width generally overpredict loss.

Let us now consider the *growth rate* of the aerodynamic wake, which we define as the increase in width between 0.25 C_x and 0.75 C_x. Except for SST1994 and BSL-ARSM, CFD-predicted wake growth rates are fairly similar to each other and fall in the range between 38–61% of the experimentally-measured growth rate. Lower-than-experimental growth rates in CFD may partly be explained by the absence of unsteady vortex shedding effects, which were not modeled. It is therefore especially surprising that the SST1994 and BSL-ARSM models predicted growth rates that were in relatively close agreement with experiments. We consider the cause of this behavior now. For SST1994, the wake growth rate was 91.5% of the experimentally-measured values. Compared to the other *linear* eddy viscosity models, the spreading rate in SST1994 is amplified by the abnormally high TKE in the *freestream*, which originates from the region of TKE over-production around the SS-peak. The point is that while this may *imitate* unsteady effects, the greater spreading rate is an artifact of excessive production of TKE in the vane passage. We recall that this also led to a 73.0% overprediction of the profile-region KE loss coefficient. For BSL-ARSM, the wake growth rate was 121% of experimentally-measured values. Higher spreading rates in BSL-ARSM are potentially helpful because they improve the collapse with the experimental data *without* compromising the model accuracy in terms of its integral KE loss predictions. The mechanism for accelerated wake spreading in BSL-ARSM is not currently understood, but is likely related to how the constitutive relation for turbulent stress (i.e. Equation 7.24) responds to free shear.

Now consider the axial evolution of peak aerodynamic wake intensity, $\zeta_{1,\mathrm{max}}$, which is shown in Figure 7.9b. The experimental trend is quasi-exponential decay. The CFD-predicted trends are similar in shape, but with higher peak wake intensities. Periodic inflections in the CFD trends appear due to the varying streamwise pressure gradient, which increases/decreases KE loss production rates (through mixing) as the wake passes through the NGV downstream potential field (see discussion in [6]). As already discussed in the context of Figure 7.8, peak aerodynamic wake

intensity was over-predicted by all turbulence models, with most models falling in the range +30.0% to +41.0% (average across planes 2–4). The SST1994 and BSL-ARSM models are the exception, with respective wake depth overpredictions of only 14.7% and 19.2% (average across planes 2, 3, and 4). Slightly greater peak wake intensity *decay rates* in SST1994 and BSL-ARSM occur for the same reasons as the elevated *growth rates*.

In summary we conclude that the generic eddy viscosity models are unlikely to yield accurate predictions of both NGV integral KE loss *and* aerodynamic wake development *simultaneously* because the free shear response of the model drives both the production of TKE in the vane passage and the mixing of the wake. Therefore, any closure coefficient adjustments designed to increase free shear diffusivity in the wake (to *imitate* unsteady phenomena) are likely to also lead to an overproduction of TKE around the SS-peak, ultimately resulting in an overprediction of integral KE loss and increased spreading of the SS boundary layer. A solution might be separate zonal treatment of the wake region and the vane passage region, as has been explored by Pacciani et al. [218] and Marioni et al. [219]. In this type of approach, wake mixing can be tuned independently from KE dissipation and SS boundary layer spreading. The disadvantage is that such models lack generality, because they require *a priori* knowledge of the flow.

Thermal wake spreading and decay

We now consider the spreading and decay trends of the thermal wake for experimental measurements and predictions from eight turbulence models. Thermal wake width and intensity are presented in terms of cold gas mass fraction, ψ. Wake width and peak intensity are calculated from radially-averaged profiles of the restacked wake (20–80% span). Compared to the analysis of the *aerodynamic* wake, the radial averaging window was reduced to 20–80% to mitigate the influence of endwall coolant spreading into the 10–90% span range for *some* turbulence models (see Figure 7.6). We consider the axial range 0.0 C_x and 1.0 C_x. Wake width was quantified using the pitch-normalized standard deviation of the thermal wake distribution (scaled by $\sqrt{12}$), and wake depth is defined as the peak cold gas mass fraction, $\psi_{\max}$.

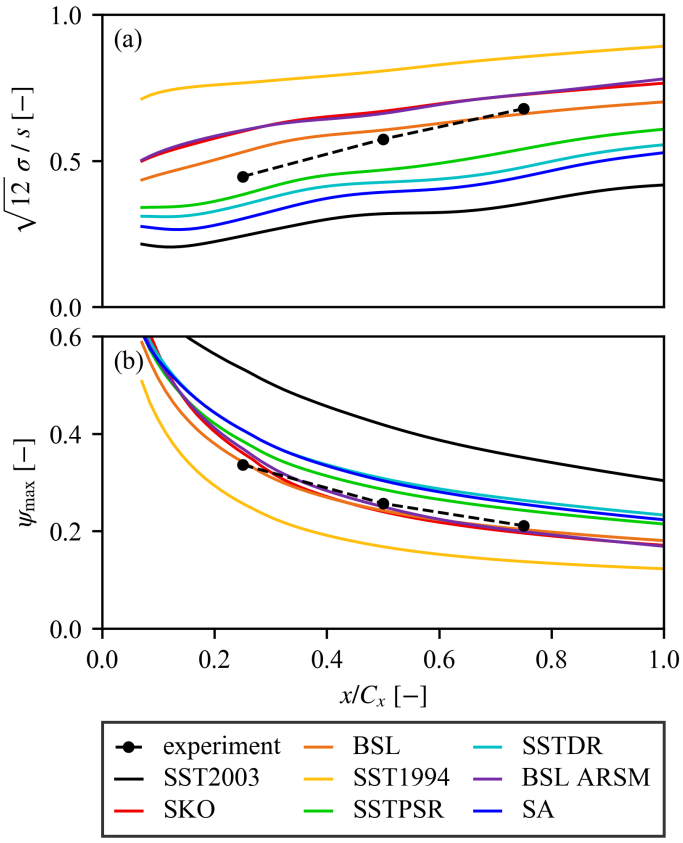


Figure 7.10: *Comparison of experimental measurements and CFD predictions using eight turbulence models, showing the axial evolution of: (a) pitch-normalized and rescaled standard deviation of the thermal wake distribution, σ/s; (b) peak cold gas mass fraction, $\psi_{\max}$. Wake peaks were circumferentially aligned (i.e restacked) prior to radial averaging (20–80% span).*

First consider the trends of pitch-normalized and rescaled thermal wake width, σ/s, which are shown in Figure 7.10a as a function of the normalized axial distance, x/C_x (datumed to trailing edge). In similarity to the *aerodynamic* wake, the experimental *thermal* wake width increases approximately linearly with axial distance. CFD trends of the thermal wake width are approximately correlated with corresponding CFD predictions of aerodynamic wake width. This is expected, because the turbulent enthalpy flux is modeled using eddy diffusivity (turbulent Prandtl number of 0.50), such that the diffusivities of enthalpy and momentum are proportional. Accordingly, SST2003 predicted by far the narrowest thermal wake, with an average width 45.9% less than the experimental measurements (average across planes 2, 3, and 4). Thermal wake width was also underpredicted by the SA (−32.3%), SSTDR (−25.6%), and SSTPSR (−17.5%) models. The gradual increase in average thermal wake width from model-to-model is related to relaxation of the stress limiting conditions and TKE production limiters, which gives rise to elevated

freestream turbulence. The BSL, BSL-ARSM, SKO, and SST1994 models overpredicted the thermal wake width by +7.2%, +19.3%, +19.4%, and +46.1%, respectively. Notably, the proportion of models overpredicting *thermal* wake width (four out of eight models) was greater than the number overpredicting *aerodynamic* wake width (one out of eight models). The reason is that the thermal mixing layer (i.e. film coolant on the airfoil) is generally thicker than the attendant aerodynamic boundary layer, such that coolant is more exposed to the freestream turbulence and also more sensitive to its modelling. This may also explain why the CFD-predicted thermal wakes are broadly symmetric, whereas the corresponding aerodynamic wakes are weighted towards the SS.

Now consider the axial trends of peak cold gas mass fraction, $\psi_{\max}$, which are shown in Figure 7.10b. Because cold gas mass fraction is a conserved quantity, we expect the trends of peak thermal wake intensity to decay with the inverse of wake width, such that *width times intensity* is approximately constant. Indeed, both the experimentally-measured and CFD-predicted trends of $\psi_{\max}$ are related approximately inversely to the normalized axial distance. Overpredictions of $\psi_{\max}$ (compared to experiments; average across planes 2, 3, and 4) occurred for the SST2003 (+62.5%), SSTDR (+21.9%), SA (+20.0%), and SSTPSR (+13.5%) models. The ordering is slightly different to that of the thermal wake *width*, due to the compounding effect of the wake *shape* (i.e. width times intensity is only *approximately* constant). Although it is a useful representation, this points to a limitation of quantifying wake width using a single scalar metric. Next, consider the BSL-ARSM, SKO, and BSL models, which predicted thermal wake intensity exceptionally well, with respective differences from experiments of only +0.5%, −2.2%, and −2.5%. Unfortunately, this good agreement is likely the result of compensating error, whereby the absence of unsteady vortex shedding effects (not modeled) is offset by excessive turbulence model diffusivity in the vane passage. This can be verified by inspecting the thickness of the endwall coolant layers for these models (see Figure 7.6), which over-penetrate the freestream when compared to experimental measurements. If we take the—probably reasonable—assumption that unsteady effects are negligible for the real (i.e. experimental) endwall flow, this indicates that thermal field diffusivity for otherwise steady turbulent phenomena is overpredicted. In applications where the accurate prediction of endwall coolant spreading is a priority, the SSTPSR and SSTDR models may offer a better compromise (see Figure 7.6).

7.11 Conclusion

The performance of eight eddy viscosity turbulence models was investigated for a high-pressure NGV flow with engine-realistic turbulence (large length scale, high intensity). The models considered were SST2003 [199], SKO [198] (k–ω without cross-diffusion), BSL [142], SST1994 [142], SSTPSR (SST with exact principal stress realizability; see Kalitizin et al. [214]), SSTDR (SST with Durbin realizability condition [210]), BSL-ARSM [201], and Spalart–Allmaras [173]. The purpose was to evaluate model accuracy for predicting KE losses, boundary layer spreading, and wake mixing in applications with high levels of freestream turbulence. Each model was benchmarked against the experimental flat plate data of Folk et al. [83], and the fully-cooled NGV flow of Amend et al. [6].

For the flat plate test, CFD predictions were compared to experimentally-measured dissipation coefficient data for inlet conditions of low TI (2.3%) and high TI (18.7%). To emulate turbulence conditions representative of a rich-burn combustor, Folk et al. [83] performed their flat plate experiments with exceptionally large freestream length scales (roughly 40 times the momentum thickness). For low TI, all turbulence models except SKO predicted average dissipation coefficients within 10% of the experimentally-measured value. Good agreement between CFD and experiments at low TI may have been expected on the basis that turbulence models are typically calibrated at low TI conditions, but we note that freestream length scales were considerably larger than most turbulence model calibration data. At high TI, all models correctly predicted an increase of the dissipation coefficient (compared to low TI), but systematically overpredicted the absolute values, when compared to experiments (maximum error of +34.2%; see Appendix 7.A). We conclude that turbulence models tend to overpredict skin friction losses for high TI wall-bounded flows.

For the fully-cooled NGV test case, CFD-predicted trends of KE loss, and aerodynamic/thermal wake mixing were compared to experimental measurements for inlet conditions of large length scale, high intensity turbulence ($\ell \approx C_x$; TI $\approx$ 13%). Simulations using the *de facto* industry standard SST2003 model revealed that SST blending functions effectively malfunction for large freestream length scales due to the explicit appearance of the length scale in the blending function arguments. This resulted in the vane passage being effectively treated as a boundary layer both in terms of closure coefficient blending and stress limiter activation (see Figure 7.11 and Figure 7.2). This highlights the potential pitfalls of automatic zonal treatments. Remedial turbulence model modifications and alternatives were explored.

The first SST blending function (responsible for closure coefficient blending) was modified to activate in the viscous sublayer only. This led to better-behaved zonal treatment (see Figure 7.11) but did not affect KE loss or wake development significantly. Considering the low sensitivity of results, the modification was not carried forward into the subsequent adaptations of the shear stress limiter, which we consider now.

Erroneous activation of the SST2003 shear stress limiter throughout the vane passage (see Figure 7.2) is conceptually similar to the intended operation of a *realizability limiter*. While stress realizability (i.e. the condition that turbulent stresses are mathematically achievable) can generally be regarded as a favorable model attribute, the stress limiting condition imposed by SST2003 is almost twice as restrictive as the classical realizability limit of Durbin [210], and therefore not necessarily valid in the freestream. Artificial reduction of turbulence in the freestream is especially problematic at high TI conditions, because flat plate data shows that freestream turbulence has a significant effect on predictions of KE dissipation [83]. Turbulence-driven diffusion of the aerodynamic boundary layer, and thermal mixing layer *on the vane surface* is also expected to play a significant role in the eventual width of the corresponding wakes. To investigate the role of freestream turbulence, results from turbulence models with various types of stress/realizability limiters (including SST2003) were compared against experimental measurements of KE loss and aerodynamic/thermal wake development. Other common eddy viscosity models, such as SA, BSL, SKO, and BSL-ARSM were also benchmarked. For completeness, we note that the experimental validation data includes the additional effect of unsteady trailing-edge vortex shedding, which also enhances aerodynamic and thermal field diffusivity, but which is not captured by *steady* RANS simulations. If modeled using *unsteady* RANS, we would expect for these effects to increase aerodynamic/thermal wake width slightly whilst reducing peak intensity proportionately, *without* affecting integral KE loss (see Burdett and Povey [147]).

Integrated loss was studied in terms of the plane-averaged KE loss coefficient, which was decomposed into contributions from the endwall (0–10% and 90–100% span) and profile regions (central 80% span). Endwall-region KE loss was relatively insensitive to the turbulence model, which led us to study integrated loss by proxy of the profile-region KE loss coefficient alone. Model-to-model variations of profile-region KE loss were as high as 196%. The CFD-predicted profile loss correlated inversely with the restrictiveness of the production and/or realizability limiter. The reason is that the models largely differentiate themselves from each other in terms of the TKE produced around the SS peak, which drives subsequent SS boundary layer losses.

Accordingly, SST2003 predicted the lowest KE loss, with an average deficit of 11.8%, when compared to experiments. Profile-region KE loss predictions from the realizable SSTDR, SSTPSR, and BSL-ARSM models were within 2% of the experimentally-measured values. We should not place too much emphasis on the good absolute accuracy, considering that the effects of surface roughness (which increases loss) and potential boundary layer relaminarization (which would reduce loss) were not modeled. Non-realizable two-equation models (SKO, BSL, and SST1994) should be avoided at high TI conditions, because they significantly overpredict profile-region KE loss (29–73%) on account of TKE *overproduction* around the SS peak. Their results also exhibit dependence on the arbitrary production limiter threshold, which is used as a safeguard against uncontrolled TKE production.

Aerodynamic wake development was studied in terms of the radially-averaged profiles (10–90% span) of the local KE loss coefficient. All turbulence models overpredicted aerodynamic *wake depth* (i.e. peak KE loss) by between 15 to 41%, compared to experiments, presumably due to the absence of unsteady vortex shedding effects in the steady RANS simulations. Predictions of aerodynamic *wake width* varied between 45% and 130% of the experimentally-measured average (across planes 2, 3, and 4; see Figure 7.3). Model-to-model differences in aerodynamic *wake width* were largely dominated by the degree of SS boundary layer diffusion, which was driven by levels of TKE production around the SS-peak. When benchmarking CFD predictions against experimental data taken *downstream of the vanes*, this mechanism of boundary layer spreading is easily conflated with unsteady vortex shedding effects, which were not modeled. Steady RANS simulations using the SKO and BSL models, for example, predicted similar aerodynamic wake width as experiments (underpredictions of 5%, and 4%, respectively). In these cases, the SS spreading effect compensated for the absent unsteady effect, but came at the expense of an overprediction of KE loss (approximately 30%), and greater wake asymmetry than for experimental data (see Figure 7.8). Of course, it would be desirable—in principle—if eddy viscosity models could accurately mimic unsteady effects (considering the lower computational cost). The current results emphasize, however, that SS spreading and wake growth rates downstream of the TE are inherently linked, because they both depend on the free shear response of the model. It is therefore not possible to independently enhance wake spreading rates, because the necessary model modifications would also trigger additional TKE production around the SS-peak, resulting in excessive KE dissipation and diffusivity throughout the vane passage. Simultaneous predictive accuracy for KE loss, SS boundary layer diffusion, and wake spreading

would likely require the separate zonal treatment of the wake and the vane passage (see e.g. [218, 219]).

Thermal field development was investigated using radially-averaged profiles (20–80% span) of the cold gas mass fraction. Because cold gas mass fraction is a conserved quantity, thermal wake width and peak intensity were approximately inversely related (both as a function of axial distance and from model-to-model). This is in contrast to the aerodynamic wake (i.e. KE loss), for which the models with widened wakes also experienced a rise of integrated loss, causing peak KE loss decay trends to remain largely unchanged. Because turbulent enthalpy fluxes were modeled using eddy diffusivity (turbulent Prandtl number of 0.50), we expect thermal field mixing to scale with aerodynamic diffusivity. Indeed, the thermal field of the SST2003 simulation was the most undermixed, with a deficit in wake width of 45.9% and an excess in peak intensity of 62.5%, compared to experiments (average across planes 2, 3, and 4). Predictions of peak cold gas mass fraction from the SA, SSTDR, and SSTPSR models closed the gap with experiments by approximately 70% of the initial difference. SKO, BSL, and BSL-ARSM achieved the best absolute agreement with experiments, although over-penetration of endwall coolant into the freestream (when compared to experiments) suggests that this only occurs because excessive diffusivity in the vane passage compensates for the fact that unsteady vortex shedding effects were not modelled. Where endwall coolant mixing is a priority, the SSTPSR or SSTDR models might be a good choice. Finally, we note that the turbulent Prandtl number of 0.5, used in the current simulations, is not suitable for wall heat transfer problems. Here it may be helpful to blend the turbulent Prandtl number (0.5 in the freestream; 0.9 near the wall) using the *modified* first blending function (see Appendix 7.B).

Turbulence model sensitivity to a change of inlet TI was investigated in terms of CFD-predicted profile-region KE loss coefficient and aerodynamic wake width (see Appendix 7.C). As expected, all models predicted an increase of profile-region KE loss and aerodynamic wake width for inlet TI increasing from 1.3% to 13% (constant length scale; $\ell \approx C_x$). Surprisingly, the profile-region KE loss coefficient and wake width rose by only 2.7% and 2.1% (respectively) using SST2003: a result which might be regarded as non-physical (too low) when compared to representative experimental studies. The realizable models achieved a better match with the reported sensitivity in the literature. Notably, for all *linear* eddy viscosity models, the increase of wake width (for TI increasing from 1.3% to 13%) was approximately proportional to the corresponding increase of profile KE loss. This reiterates the strong correlation between SS spreading and profile KE loss for this type of

turbulence model.

An unresolved ambiguity in modeling large length scale turbulence is the translation of experimentally measured *integral* length scales into *turbulence length scales* (to estimate turbulence dissipation rate). Especially at high TI, the chosen definition has a significant impact on predictions of SS spreading and KE loss. Considering that the *turbulence length scale* is largely a modelling concept, the proportionality constant between turbulence length scale and integral length scale might be viewed as an optimization parameter. Surprisingly, the values of the proportionality constant found in the literature vary by an order of magnitude, depending on the CFD package. We recommend explicitly reporting the method used to estimate turbulence dissipation rate from experimental measurements.

Nomenclature

Roman

a_1	Bradshaw constant	[–]
a_{ij}	Reynolds stress anisotropy	[–]
$\mathrm{arg}_{1/2}$	Blending function 1/2 argument	[–]
C	Compressible production coefficient	[–]
C_d	Dissipation coefficient	[–]
C_f	Skin friction coefficient	[–]
C_lim	Production limiter clip factor	[–]
$\mathcal{E}$	Turbulence dissipation rate	[kg m^{-1} s^{-3}]
$F_{1/2}$	Blending function 1/2 of SST model	[–]
H_{23}	Momentum-to-energy thickness ratio	[–]
k	Turbulence kinetic energy	[m^2 s^{-2}]
ℓ	Turbulence/integral length scale	[m]
$\dot{m}$	Mass flow rate	[kg s^{-1}]
p	Pressure (total or static)	[Pa]
$\mathcal{P}$	Shear production of turbulence	[kg m^{-1} s^{-3}]
Re_θ	Momentum thickness Reynolds number	[–]
r	Radius	[m]
s	Angular vane pitch	[°]
S	Strain rate invariant	[s^{-1}]
S_{ij}	Strain rate tensor	[s^{-1}]
T	Temperature (static or total)	[K]
u	Fluctuating flow velocity component	[m s^{-1}]
U	Mean-flow velocity component	[m s^{-1}]
$\mathfrak{v}$	Turbulence velocity scale	[m s^{-1}]
x	Cartesian coordinate	[m]
y	Wall distance	[m]

Greek

α	Closure coefficient for production of ω	[–]
β	Closure coefficient for dissipation of ω	[–]
β^*	Closure coefficient for dissipation of k	[–]
γ	Ratio of specific heats	[–]
δ_{ij}	Kronecker delta	[–]
ϵ	Turbulence dissipation rate	[m^2 s^{-3}]
ζ_1	Local KE loss coefficient	[–]
ζ_2	Plane-averaged KE loss coefficient	[–]
ζ_p	Profile-region KE loss coefficient	[–]
ζ_e	Endwall-region KE loss coefficient	[–]
θ	Circumferential coordinate	[°]
λ	Strain rate tensor eigenvalue	[s^{-1}]
μ	Dynamic viscosity	[Pa s]
μ_t	Eddy (turbulent) viscosity	[Pa s]
ν_t	Kinematic eddy viscosity	[m^2 s^{-1}]
ρ	Volumetric mass density	[kg m^{-3}]
σ	Standard deviation of circumferential wake profile when treated as a probability density function	[°]
σ_k	Eddy diffusivity of k	[–]
σ_ω	Eddy diffusivity of ω	[–]
χ	Isentropic expression	[–]
ω	Specific turbulence dissipation rate	[s^{-1}]
ψ	Cold gas mass fraction	[–]
Ω	Vorticity magnitude	[s^{-1}]
Ω_{ij}	Vorticity tensor	[s^{-1}]

Subscripts

0	Stagnation property
1	Model coefficient for k–ω regime flow
2	Model coefficient for k–ϵ regime flow
c	Coolant stream property
ijk	Einstein notation indices
m	Mainstream property
norm	Normalized quantity

Appendix 7.A Flat plate test data

RANS simulations of a flat plate were completed for conditions of low and high freestream TI at inlet. The purpose was to evaluate the accuracy of common turbulence models in a high-turbulence environment by comparing them with experimental validation data. The experimental data and test section geometry are from Folk et al. [83, 76]. The simulations were completed on a nominally two-dimensional CFD grid, which was extruded by a single cell in the spanwise direction of the flat plate. The inlet was located 120 mm upstream of the elliptical leading edge (6:1 aspect ratio) of the flat plate, and was specified as a constant total gauge pressure of 340 Pa, a turbulence length scale of 40 mm ($\ell = \sqrt{k}/\beta^*\omega$), and a total temperature of 293.15 K. The low and high turbulence

cases correspond to inlet TI levels of 2.3% and 18.7%, respectively. The outlet condition was an absolute static pressure of 1.0 atm (ambient pressure). Model-specific production and realizability limiter settings are summarized in Table 7.1. Dissipation coefficient data for low and high TI inlet conditions are summarized in Table 7.2.

At low TI, all models except SKO predict the dissipation coefficient accurately to within 10% of the experimental data of Folk et al. [83]. The significant overprediction of C_{d} in SKO (+18.1%) presumably arises due to the well-known sensitivity of SKO to freestream values of ω, which are unusually low in the current simulations (see discussion in [202]).

At high TI, the dissipation coefficient was systematically overpredicted, with a maximum error of +34.2% (for SST1994). The model-to-model variation was also somewhat greater at high TI, which presumably occurs because the models differentiate themselves from each other in how they handle extreme levels of turbulent stress (realizability and production limiters). For the flat plate test case, SA was the most accurate model.

Table 7.2: *Flat plate test average dissipation coefficient, C_{d}. CFD data were resampled at experimental values of Re_θ.*

	Low turbulence $10^3 \times C_{\mathrm{d}}$ (vs. exp)	High turbulence $10^3 \times C_{\mathrm{d}}$ (vs. exp)
Experiments (exp.) Folk et al. [83]	1.601	2.024
SST2003	1.651 (+3.1%)	2.416 (+19.4%)
SSTF1V	1.726 (+7.8%)	2.614 (+29.2%)
SKO	1.891 (+18.1%)	2.609 (+28.9%)
BSL	1.735 (+8.4%)	2.620 (+29.4%)
SST1994	1.699 (+6.1%)	2.716 (+34.2%)
SSTPSR	1.743 (+8.9%)	2.552 (+26.1%)
SSTDR	1.736 (+8.4%)	2.521 (+24.6%)
BSL-ARSM	1.715 (+7.1%)	2.691 (+33.0%)
SA	1.734 (+8.3%)	2.051 (+1.3%)
SKE ($C_{\mathrm{lim}} = 10$)	1.697 (+6.0%)	2.631 (+30.0%)

Appendix 7.B Modified blending function

For the NGV test case, the first blending function (see Equation 7.13) does not function as intended, because the first sub argument of the closure coefficient blending function (see Equation 7.14) is sensitive to the large freestream turbulence length scales. As a result, the intended zonal treatment is not achieved. We consider a modified definition of the first blending function, $F_{1\mathrm{v}}$, which is calculated using the function argument, $\mathrm{arg}_{1\mathrm{v}}$, defined in Equation 7.20 and activates SKO-regime in the viscous sublayer only. We now compare results using the *default* blending

function (SST2003) and *modified* blending function (SSTF1V) in terms of their regional treatment (SKO vs SKE), as well as their KE loss, and wake mixing character. Both simulations correspond to the high inlet turbulence condition (TI $\approx$ 13%; $\ell \approx 1.0\ C_x$). Consider now the blade-to-blade midspan section of the NGVs, shown in Figure 7.11. Inside the contoured regions, the closure coefficients are closer to SKO-regime than to SKE-regime (i.e. F_1 or $F_{1v} > 0.50$), and outside the contoured regions the closure coefficients are closer to SKE-regime (i.e. F_1 or $F_{1v} \leq 0.5$). The edge of the contoured regions can therefore be viewed as the location where the turbulence model is switched. We now review the zonal treatment in SST2003 and SSTF1V.

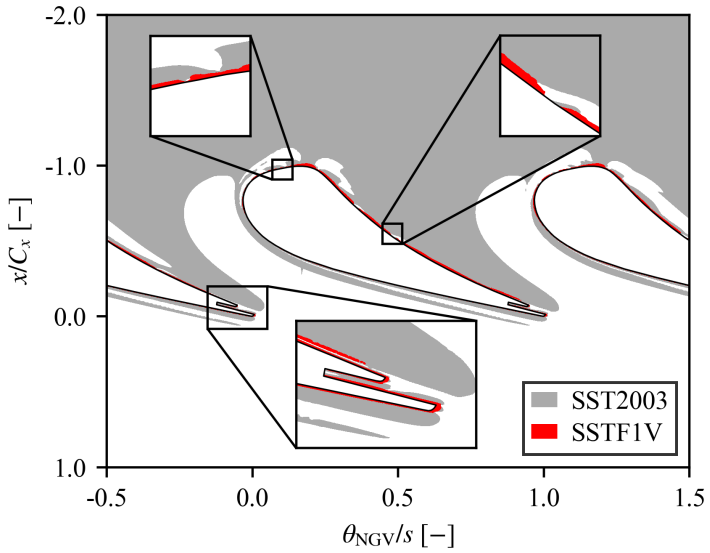


Figure 7.11: *Comparison of the first blending function at midspan for the SST2003 (default zonal treatment) and SSTF1V (SKO regime in viscous sublayer only) models. The highlighted regions indicate where F_1 and F_{1v} are greater than 0.50.*

For the SST2003 model, the region upstream of the NGVs, and the PS-half of the vane passage use SKO, whereas the SS-half of the vane passage and the wake use SKE. The gaps in the SKO-regime zone near the leading edge and on the PS are explained by the film cooling holes (internals obscured). For the modified blending function (SSTF1V model), only the near-wall regions use SKO-regime (see detail view of trailing edge, leading edge and PS). Overall, the behavior of the SSTF1V model appears more predictable and well-behaved in the presence of film cooling and large length scales. We briefly consider the effect of the differing coefficient blending on predictions of KE loss and wake mixing.

The plane-averaged KE loss coefficient increased by 1.8% for SSTF1V, when compared to SST2003 (average across planes 2, 3, and 4). The increase was primarily driven by the profile-region KE loss coefficient, which increased by 2.1%, while the endwall-region KE loss coefficient

only rose by 0.2%. Changes in wake width/depth were +1.8%/−0.7% for the restacked aerodynamic wake, and +1.2%/−1.0% for the restacked thermal wake. We conclude that KE loss and wake spreading/decay predictions are not significantly affected by the different zonal treatment.

Appendix 7.C Inlet turbulence intensity

Turbulence model sensitivity to inlet TI was investigated by performing additional simulations of the NGVs for an inlet TI of 1.3% (reduced from TI ≈ 13%; length scale unchanged). For the sake of brevity, we consider the TI sensitivity of *profile-region* KE loss coefficient, and *aerodynamic* wake width only. Endwall losses were not significantly affected, and *thermal* wake width was approximately proportional to the *aerodynamic* wake width.

Turbulence model predictions of profile-region KE loss coefficient, ζ_{p}, and the pitch-normalized and rescaled aerodynamic wake width, σ/s, are shown in Figure 7.12 for inlet conditions of low (TI ≈ 1.3%) and high (TI ≈ 13%) turbulence. The values are shown for an axial plane located 0.75 C_x downstream of the midspan trailing edge (plane 4; see Figure 7.3). The results at this station were representative of the overall trend. The vertical dashed lines correspond to the loss/width predicted by the SST2003 model at low TI.

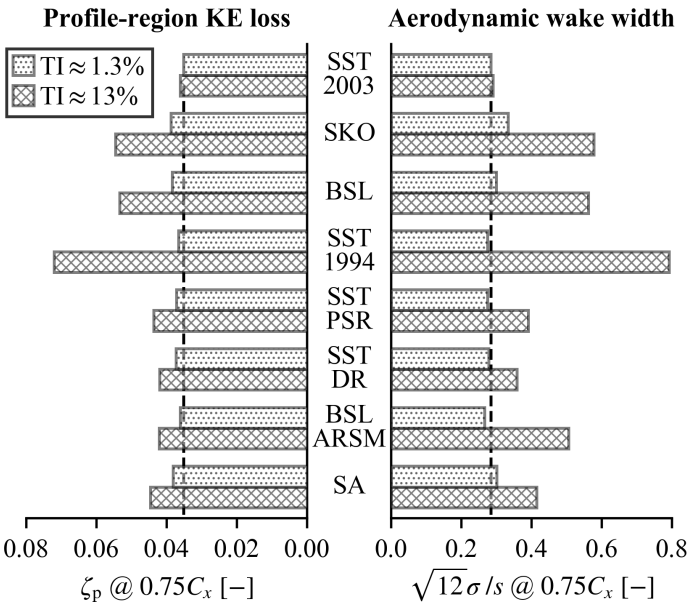


Figure 7.12: *Comparison of CFD-predicted values of profile-region KE loss coefficient, and rescaled and pitch-normalized aerodynamic wake width, at 0.75 C_x (plane 4) for conditions of low (TI ≈ 1.3%) and high (TI ≈ 13%) inlet turbulence.*

First consider the profile-region KE loss coefficient, ζ_{p}, which is shown on the left side of Figure 7.12. Regrettably, no experimental validation data was taken at the low TI inlet condition. Consulting experimental studies concerning the effect of inlet TI on the profile loss of turbine cascades, we expect an increase of profile loss at high turbulence conditions. Ames and Plesniak [82] measured an 8.4% rise in profile loss (for inlet conditions changing from a TI of 1.1% with $\ell \approx 0.84C_x$ to a TI of 12.0% with $\ell \approx 0.43C_x$), and Folk et al. [83] reported a 37% increase of profile loss (for TI increasing from approximately 1.5% to 10%; constant length scale, $\ell \approx 0.18C_x$). Surprisingly, the SST2003 model predicted only a 2.7% increase of the profile-region KE loss coefficient for the current NGV test case (for TI increasing from 1.3% to 13%; $\ell \approx C_x$). The outcome was unexpected, because flat plate tests using the SST2003 model (see Figure 7.1) showed a 46% increase of the dissipation coefficient between the low and high TI condition, which corresponded to a slight overprediction, when compared to the experimental flat plate data of Folk et al. [83]. This reiterates the dominant role of stress limiting conditions in the predictions of NGV loss. For the realizable models, the increase of profile-region KE loss at high TI was 12.5% (SSTDR), 16.8% (BSL ARSM), and 17.3% (SSTPSR), which is somewhat better-aligned with the existing literature. SA predicted a similar increase of 17.1%, while BSL, SKO, and SST1994 saw profile-region KE loss rise by 38.7%, 40.7%, and 96.9%, respectively. The conclusion is that all turbulence models correctly predict increasing KE loss with increasingly TI, but with increasing variation in absolute value between models as TI increases (9.6% of the model average at low TI; 73.9% of the model average at high TI).

Now consider the pitch-normalized and rescaled aerodynamic wake width, σ/s, which is shown on the right side of Figure 7.12. At high TI, Ames and Plesniak [82] reported an 11.3% increase of wake width, while Folk et al. [83] found that wake width was increased by approximately 28%. In the framework of an eddy viscosity model, this can be explained by recalling that kinematic eddy viscosity (i.e. diffusivity of momentum) scales linearly with TI for a constant length scale. For the current test case, SST2003 had the lowest sensitivity to inlet TI, with wake width increasing by only 2.1%. For the other models, wake width increased by between 29% and 189%. The increases were approximately proportional with the corresponding change of the profile-region KE loss coefficient (for TI increasing from 1.3% to 13%). This is in line with our earlier observation that wake width and profile-region KE loss are inherently linked for linear eddy viscosity models, since both are driven by the TKE production around the SS peak. Indeed, the only *non-linear* eddy viscosity model (i.e. BSL ARSM) is the exception to this rule, with a disproportionate increase of wake

width, compared to the rise of KE loss. The underlying mechanism is not currently understood but is likely related to spatially-varying degrees of *coherence* between the turbulent stress and mean flow strain tensors, which allows for independent modulation of TKE production (see discussion by Moore and Moore [209]).

Appendix 7.D Length scale definition

CFD simulations of the unwrapped and defeatured NGV airfoil at midspan (two-dimensional; uncooled) revealed a strong positive correlation between the inlet turbulence length scale (for constant TI) and the predicted profile KE loss coefficient and wake width. This emphasizes the importance of characterizing both the energy and scale of the incoming turbulence. There is currently no established common practice for translating experimentally-measured *integral* length scales into modeled *turbulence* length scales (and vice versa). This is relevant because length scales are typically used to estimate the turbulence dissipation rate when setting RANS inlet boundary conditions. While the expression of Taylor [203]

$$\ell = Ak^{1.5}/\epsilon \tag{7.28}$$

holds on dimensional grounds, the appropriate value of the proportionality constant A remains debated. Cha et al. [75], Folk [76], and Amend et al. [6] used $A = 1$, when comparing RANS-predicted turbulence length scales to experimentally-measured integral length scales. $A = 1$ is also used by the ANSYS CFX solver [205]. The outcomes from the studies using $A = 1$ are inconclusive, however, with Amend et al. [6], Folk [76], and Cha et al. [75] reporting that CFD-predicted length scales were 15%, 108%, and approximately 200% greater, respectively, than experimentally-measured integral length scales. It is interesting to note that the study of Cha et al. [75] would have achieved a good collapse had the proportionality constant of Moore and Moore [209] been used (they estimated $A = 0.32$ based on hotwire measurements of integral length scale, and k, with ϵ estimated from turbulence spectra). The ANSYS Fluent solver uses $A \approx 0.164$, while Wilcox [141] suggests that a value $A = 0.09$ is most appropriate. The point is that whilst the chosen value of the proportionality constant A can have a strong influence on CFD predictions of KE loss and wake width, values in common use vary by an order of magnitude.

Additional uncertainty arises due to variation in the definition of the experimentally-measured integral length scale. In the current study, the integral length scale was calculated as the product of the local velocity magnitude and an average integral time scale. The average integral time scale was

defined as the arithmetic mean of the components in x, r, and θ, each of which was calculated from the integral of the normalized autocorrelation function of the corresponding velocity component from zero time-shift to the first zero crossing. To build understanding in this field, and where back-to-back comparisons are desired, we emphasize the importance of reporting both the method for calculating experimentally-measured *integral* length scales, and the proportionality constant used to calculate ϵ from k and ℓ.

8 | Impact of lean-burn combustor flow on NGV performance

In this Chapter we investigate the impact of lean-burn-representative swirl and temperature distortion on the aerothermal performance of fully-cooled high-pressure nozzle guide vanes (NGV) from a modern aero-engine. Experiments were carried out in the Engine Component AeroThermal (ECAT) facility at the University of Oxford. This is a fully-annular warm-flow engine-parts facility, designed to operate at engine-representative conditions of Reynolds and Mach number. Inlet profiles of swirl, turbulence, and non-dimensional total temperature were generated using a non-reacting combustor simulator. The NGV outlet flow was experimentally characterized at three downstream planes in experiments with and without lean-burn-representative inlet conditions. Area-survey measurements included distributions of whirl angle, kinetic energy (KE) loss, and non-dimensional total temperature. Experimental data is compared to CFD simulations. Fully-featured NGV geometry (including film cooling holes and internal passages) was used, to account for internal cooling flow redistribution resulting from altered external loading. We show that lean-burn inlet conditions result in significant surface flow redistribution, relatively high levels of residual swirl in the downstream flow, and a small increase of integrated KE loss.

Context with other chapters

The current Chapter examines the effect of lean-burn combustor outflow on NGV aerothermal performance. The methods and analysis are built on insights gained throughout the preceding chapters. For example, the combustor simulator used in the current study is described in Chapter 3. Detailed mean-flow and turbulence measurements at vane inlet are presented in Chapter 4. Similarly in Chapter 6, NGV performance was studied for uniform inlet conditions, which corresponds to the reference condition of the current study. The experimental data under uniform inflow was also used to benchmark CFD methods in Chapter 7. A strong sensitivity of mixing behavior and aerodynamic loss to the chosen turbulence model was uncovered. The current study uses the baseline k–ω algebraic Reynolds stress model, which was identified as the best compromise for the uniform test case.

Publication status and co-author contributions

The chapter takes the form of a *journal paper*, which is currently under review at the ASME Journal of Turbomachinery. The DPhil candidate was responsible for carrying out aerodynamic experiments, running simulations, analyzing results, and ultimately writing the paper. Nafiz Chowdhury collected the thermal field data, and supported facility operation throughout aerodynamic experiments. Thomas Povey was responsible for the conception of the project, supervised data analysis, and helped shape the discussion. A statement of authorship is included at the end of the document.

8.1 Introduction

Nitrogen oxide (NO_x) emissions have been linked to increased mortality from respiratory conditions and have been identified as a potential forcing agent for global climate change [24]. Lean-burn combustion architectures promise to reduce aero-engine NOx emissions by reducing peak combustion temperature. As demonstrated by both prototype [50] and in-service systems [44], this is achieved by increasing the proportion of engine core-flow that passes through the fuel-injector. The intended result is lower peak temperature, but with the consequence of greater residual swirl. In addition to combustion-related challenges (flashback, altitude relight, instability; see [3]) there are considerations relating to the performance of the high-pressure turbine. This has been extensively studied using computational fluid dynamics (CFD) and in a number of experiments using non-reacting combustor simulators.

The literature on lean-burn combustor–turbine interaction highlights the high-pressure stage performance sensitivity to: circumferential alignment of fuel injectors relative to the nozzle guide vanes (NGV); the swirl sense (co-rotating or counter-rotating w.r.t. the NGV flow); the injector-NGV count ratio; and the resulting temperature profile shape. Here we refer to co-rotating flow as that in which the direction of the angular momentum vector of the swirler vortices is the same as that of the NGV outlet flow, and where in counter-rotating flow they are opposed. Thus, in co-rotating flow, the vortex could—loosely—be considered to augment the turning at the casing (also off-loading the vane) and lessen the turning at the hub (also increasing loading of the vane). In counter-rotating flow the effects at case and hub are reversed. As a natural development of trying to understand interactions, the question of optimum circumferential clocking of the fuel injectors (and associated vortices) *relative* to the NGV arises. Both *passage-clocked* and *leading-edge-clocked* (LE-clocked) vortex alignment has been studied, often in experiments or simulations with an NGV-to-injector counts of two. Integer NGV-to-injector count has the advantage of being efficient for CFD, and suitable for experiments in which *stage* performance is to be studied (capacity; efficiency; inter-stage pressure ratio; etc.)

Some of the first investigators of lean-burn combustor–turbine interactions examined the effect of inlet swirl alone; that is, without temperature distortion. Qureshi et al. [124, 58] and Beard et al. [96] experimentally tested LE-clocked configurations with co-rotating swirl, making comparisons to a baseline case with uniform inflow. They found that with the introduction of lean-burn swirl there was 1.2% decrease in turbine stage efficiency, a 2.0% reduction in stage capacity, and increased NGV and rotor heat-transfer. The reduced stage efficiency and capacity were attributed to additional

losses arising from off-design incidence operation of the NGV. Qureshi et al. [124] suggested that enhanced rotor heat transfer might be related to the greater inlet turbulence intensity. In the NGV, combustor-swirl significantly altered the surface streamline pattern. One consequence was amplified secondary flow intensity at the hub, which was attributed to increased loading, caused by positive incidence in this region. The altered secondary flow structure affected NGV endwall heat transfer, with circumferentially-averaged Nusselt number increasing by up to 26% at the hub, and decreasing as much as 7% at the casing [58].

Efforts in finding an optimum combination of swirl clocking and direction were pioneered by Khanal et al. [106], who reported that passage-clocking of a combined co-rotating swirl-core with hot-streak was preferable to LE-clocking in terms of the combined heat load of NGV and rotor. This marked what might be called the *second wave* of lean-burn-interaction studies, and the authors argued that swirl and temperature distortion effects must be studied together because the individual effects superposed poorly. Griffini et al. [112] studied the effects of swirl (counter-rotating only) and hot streak clocking on the overall cooling effectiveness of NGV using conjugate CFD, and found that a passage-clocked-swirl configuration had reduced average metal temperature and reduced peak metal temperature when compared to a LE-clocked configuration. This was largely in line with [106]. Li et al. [116] performed a computational study in which both heat load and stage efficiency were considered, and concluded that LE-clocking with counter-rotating swirl was an optimum arrangement for their stage design. It is apparent that the development of the flow field within the high-pressure stage is sensitive to both the turbine geometry and the shape of the upstream swirl and temperature profiles. This highlights the importance of validating design tools with high quality experimental data.

Effects of lean-burn on the thermal performance of *film-cooled* NGV were examined by Griffini et al. [112], Bacci et al. [113], and Werschnik et al. [100]. For LE-clocked-swirl the greatest influence was around the showerhead of the vortex-aligned vane, where a low-pressure region at the vortex center had the effect of increasing coolant flow at the location where it impinged on the vane. This had the effect of improving film coverage locally, at the expense of greater coolant flow [113]. The swirl-induced change in airfoil loading caused greater mass efflux from film-cooling holes in regions with reduced external pressure [112]. Externally, the coolant films migrated according to the streamline pattern set-up by the swirling flow. As the vanes had been designed for uniform flow, this generally resulted in less uniform coolant coverage, especially on the pressure-side. Platform cooling performance also deteriorated: when lean-burn flow was introduced the mean

Nusselt number increased, and the mean film cooling effectiveness decreased [100]. Importantly, these studies emphasize that coolant migration effects can only be accurately predicted by models which consider both the internal and external geometry.

As understanding of turbomachinery has advanced, there has been increasing interest in turbulence and unsteady phenomena. For example, Folk et al. [83] demonstrated a strong sensitivity of NGV loss to the inlet turbulence intensity. Likewise, elevated turbulence is known to enhance heat transfer, and accelerate film coolant decay [100], both of which have detrimental effects on thermal performance. Although the effects of turbulence are now reasonably well documented under experimental conditions, uncertainty surrounding real-world turbine performance persists because measuring combustor turbulence under *reacting conditions* is extremely difficult, and therefore combustor turbulence characteristics are poorly characterized. Schroll et al. [55] overcame this difficulty using particle image velocimetry, measuring turbulence intensities between 8–20% at the outlet of a single-sector reacting lean-burn combustor. In the related numerical study of Adoua and Page [63] the authors argued that turbulence intensity was *reduced* under reacting conditions, primarily because of volume-dilation-induced axial acceleration. Scarcity of data means there is still uncertainty about the nature of turbulence in many real-engines environments. Notwithstanding this limitation, high quality experimental data from non-reacting combustor simulators is important for numerical model *validation*.

A recent example of CFD model validation is the study of Thomas et al. [197], which compared experimental data from a fully-cooled turbine stage with combustor simulator (the FACTOR consortium project) to a large eddy simulation of the same. The simulation results were *qualitatively* similar to experiments, but with significant discrepancies in terms of the thermal field downstream of the NGVs. The authors attributed this to the modeling method for film cooling holes, which used patch inlets. This demonstrates the importance of resolving internal cooling passages. Scale resolving simulations of this kind show great promise in improving predictions of large-scale unsteadiness and free shear mixing, but currently remain too resource-intensive for design work, which continues to rely heavily on Reynolds-averaged Navier–Stokes (RANS) methods. In this vein, Adams et al. [104] compared experimental data from a combustor simulator and cooled 1.5-stage turbine (the Oxford Turbine Research Facility) with unsteady RANS (URANS). Downstream of the rotor, URANS solutions were undermixed, showing greater persistence of the radial temperature distortion than measured experimentally. Importantly, the study demonstrates that changes in NGV aerodynamics are primarily impacted by combustor

swirl, whereas changes in rotor aerodynamics are primarily driven by temperature distortion.

In this study we present high-fidelity experimental data of fully-cooled NGVs subject to inlet swirl and temperature distortion. Cascade inlet conditions of total pressure, flow angles, temperature distortion, and turbulence were characterized using an upstream traverse system. We present detailed surveys of the aerodynamic and thermal fields downstream of the NGV at three axial planes, allowing us to analyze the development of residual swirl, kinetic energy loss, and hot streak migration. Comparisons are made to corresponding measurements with uniform inflow. We compare this data to CFD simulations using fully-resolved NGV geometry. The unusually high-fidelity data allow detailed investigation of the impact of lean-burn flows on the first-stage nozzle aerothermal performance, and benchmarking of the CFD method.

8.2 Experimental methods

Experiments were conducted in the Engine Component AeroThermal (ECAT) facility at the University of Oxford (see Kirollos et al. [121]). The ECAT facility is a fully-annular NGV test facility used to test in-service and prototype engine hardware at engine-matched conditions of Reynolds number, Mach number, and coolant-to-mainstream mass flow ratio. The facility can operate in warm-flow (used for these tests) or hot-flow [169] mode, and for the experiments we report was configured *with* and *without* a lean-burn simulator [4]. The simulator reproduced target conditions of swirl, temperature distortion, and turbulence.

Test section overview

Meridional views of the ECAT facility working section, configured for both *uniform* and *lean-burn* testing, are shown in Figure 8.1. For the uniform test case (top of Figure 8.1), the upstream flow passes through a turbulence grid into a contracting inlet duct, which has a similar design to the annulus line of the engine. The NGVs are supplied with coolant from plena at the hub and casing. The NGV exit flow exhausts to ambient conditions through a parallel annular exit duct, which extends approximately three axial chords downstream of the NGV trailing edge (TE).

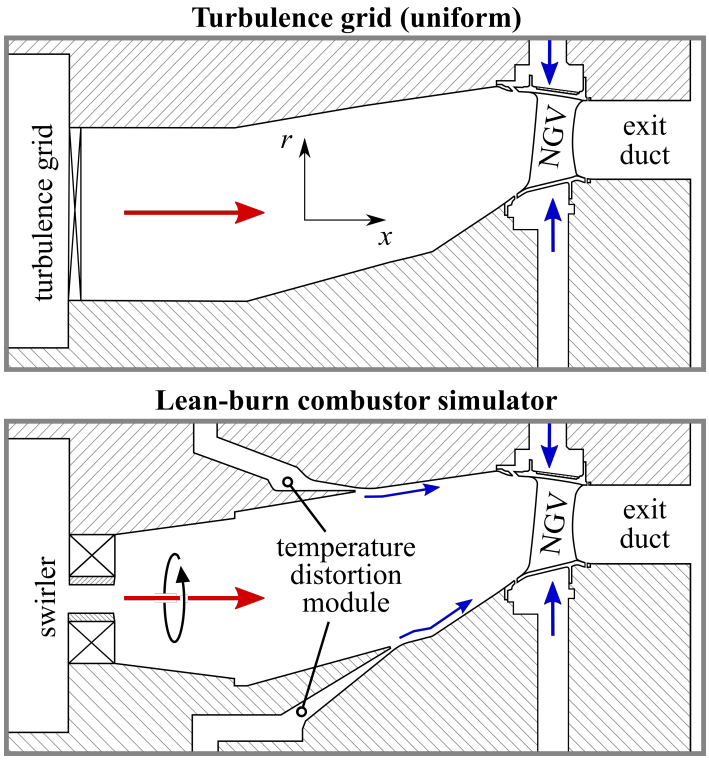


Figure 8.1: *Meridional view of the ECAT facility working section in the uniform configuration (with turbulence grid) and lean-burn configuration (with combustor simulator).*

Lean-burn-representative inlet conditions are generated using a non-reacting combustor simulator (see Amend et al. [4]). This is illustrated in the bottom half of Figure 8.1. The 20 counter-clockwise (CCW) oriented (when viewed from upstream) swirlers have the same sense of rotation as the NGV (co-rotating). The nominal swirl number (intensity) of the flow was estimated to be 0.26 using correlations based on the geometric design. This number was later confirmed using CFD simulations. The vane count was 40, giving a count ratio of 2:1 with the swirler. The *swirler* centerline is geometrically clocked onto the leading-edges of alternating vanes. Vanes are manufactured in pairs, and (inheriting language from the design process) we refer to the swirler-aligned vane as the trailing vane (TV) and the other mis-aligned vane as the leading vane (LV). Leading and trailing vanes are aerodynamically identical, but have slightly different cooling systems. Combustor temperature distortion is simulated by injecting cold air into the swirling hot stream from annular slots at the hub and casing walls.

The ECAT facility combustor simulator [4] is closely related to the combustor simulator recently used by Adams et al. [104, 62] to investigate the effect of lean-burn on the performance of a 1.5-stage turbine. Both simulators were developed in parallel from the prototype of Hall and Povey [92]. We draw comparisons with the results of Adams et al. [104] to add depth to the analysis.

Instrumentation and measurements

A schematic of the working section in the lean-burn configuration is shown in Figure 8.2, with the key measurement planes marked. Cascade inlet conditions of total pressure and total temperature at plane 1 were monitored using spanwise rakes, totaling 32 Pitot and 32 thermocouple probes split across 8 circumferential locations. Additionally, detailed area surveys of total pressure, total temperature, flow angles, and turbulence were acquired at plane 1 using a case-mounted upstream traverse system [5]. Slightly further downstream, at plane 1b, Amend et al. [4] characterized the combustor simulator flow (but not the turbulence grid) at low back pressure (i.e. without NGV installed). This data is used in the analysis of thermal field development. Stagnation pressure and temperature were measured in the temperature distortion module plena, and the vane coolant plena.

Downstream static pressure was measured along the circumference of two vane pairs, which were instrumented with 16 tappings on each of the platform overhangs at the hub and casing. Exit planes 2, 3, and 4 were located 0.25, 0.50, and 0.75 C_x axially downstream of the midspan TE, respectively. The aerodynamic and thermal field at planes 2, 3, and 4 was surveyed over the full span radially, and across two vane pitches circumferentially using an aerodynamic five-hole probe (reporting flow angle, Mach number, and total pressure), Pitot probe (near wall region only), and dual-sensor thermocouple probe. To eliminate bias from hardware variations, the uniform and lean-burn test cases considered the same physical parts, and followed the same wakes when moving between planes (i.e. the traverse was clocked to follow the flow). Details of probe design, traverse resolution, and measurement uncertainty are summarized by Amend et al. [6].

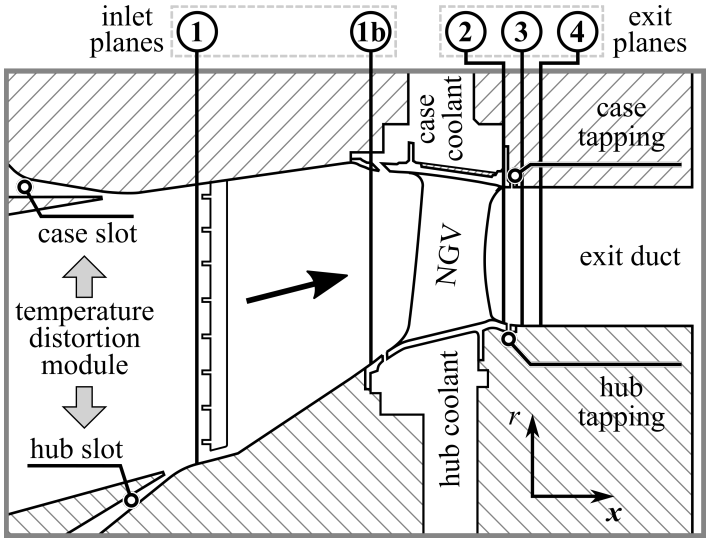


Figure 8.2: *Schematic of the working section in the lean-burn configuration, showing the temperature distortion module slots, NGV, coolant feeds, and exit duct.*

Experimental operating conditions

Cascade operating conditions for the uniform and lean-burn experiments are summarized in Table 8.1. The thermal field measurements were performed with a mainstream-to-coolant temperature ratio of approximately 1.2, whereas the aerodynamic field was surveyed without temperature distortion. Reynolds number, Mach number, and coolant-to-mainstream mass flow ratio were well-matched between the uniform and lean-burn test cases.

Table 8.1: *Operating conditions for uniform and lean-burn experiments.*

	Uniform	**Lean-burn**
Swirl number, S [–]	0.0	0.26
Vane Reynolds number, Re [–]	7.7×10^5	7.6×10^5
Vane Mach number, M_2 [–]	0.91–0.93	0.91–0.93
Vane coolant-to-mainstream mass flow ratio, $\dot{m}_\mathrm{c}/\dot{m}_1$ [–]	0.14	0.13
Mainstream total temperature, T_{01} [K]	325–355	320–350
Combustor coolant total temperature, $T_{0\mathrm{b}}$ [K]	N/A	290–300
Vane coolant total temperature, $T_{0\mathrm{c}}$ [K]	284–292	290–300
Plane 1 total pressure uniformity [–]	±0.1%	±1.1%
Plane 1 turbulence intensity, TI [–]	13%	15%

8.3 Performance metrics

This section summarizes the performance metrics used for the inlet flow survey (plane 1), and in the analysis of the aerodynamic and thermal fields downstream of the NGV (planes 2, 3, and 4).

Flow angle definitions

Absolute whirl angle, α, and absolute pitch angle, β, are given by

$$\alpha = \arctan \frac{V_\theta}{V_x} \qquad\qquad \beta = \arctan \frac{V_r}{V_x} \tag{8.1}$$

where V_x, V_r, and V_θ are the axial, radial, and circumferential velocity components (respectively) in a cylindrical coordinate frame defined by the machine axis. V_θ and α are positive in the NGV turning direction (left-handed coordinate system). The same definitions are used for the upstream and downstream analyses.

Upstream normalized total pressure

An *upstream* normalized total pressure, $p_{01,\mathrm{norm}}(r,\theta)$ is defined as

$$p_{01,\mathrm{norm}}(r,\theta) = \frac{p_{01}(r,\theta)}{p_{01,\mathrm{rake}}} \tag{8.2}$$

where $p_{01}(r,\theta)$ is the total pressure at plane 1 measured using the case-mounted traverse (as a

function of radius r, and circumferential position θ; 0.75 second sampling period), and $p_{01,\mathrm{rake}}$ is the ensemble average of the 32 stationary Pitot pressures at the same axial plane over the same time period. Normalization allows us to differentiate between spatial non-uniformities, and temporal variations of the inlet flow (these are low-frequency and very small in magnitude). We use $p_{01,\mathrm{norm}}$ to estimate the instantaneous mass-flux-weighted total pressure at plane 1 from the instantaneous total pressure reported by the rake.

Upstream non-dimensional total temperature

Next, we define a non-dimensional upstream total temperature, Θ_1, by

$$\Theta_1(r,\theta) = \frac{T_{01}(r,\theta) - T_{0\mathrm{b}}}{T_{01,\mathrm{rake}} - T_{0\mathrm{b}}} \tag{8.3}$$

where $T_{01}(r,\theta)$ is the filtered instantaneous total temperature measured at plane 1 (continually moving traverse; see [5]), $T_{0\mathrm{b}}$ is the mass-flow-weighted total temperature in the cold-stream plena of the combustor simulator temperature distortion module, and $T_{01,\mathrm{rake}}$ is the instantaneous ensemble average of the filtered rake total temperatures at plane 1 (hot stream). Only the thermocouples in the core-flow (and not the coolant layer) of the plane 1 rake measurement are included in the average value $T_{01,\mathrm{rake}}$. Values of Θ_1 range between 0 and 1 (higher values correspond to higher temperature). We use Θ_1 to infer the temperature distribution at plane 1 in real-time, using the total temperatures measured by the rake and inside the temperature distortion module plena. Noting that there is no cold-flow for the uniform test case, we set $T_{0\mathrm{b}}$ = 293.15 K (i.e. the ambient temperature during testing).

Upstream turbulence intensity and integral length scale

Turbulence intensity, TI, and integral length scale, ℓ, are defined by

$$\mathrm{TI} = \sqrt{2k/3}/V \tag{8.4}$$

$$\ell = \tau V \tag{8.5}$$

where k is turbulence kinetic energy, V is absolute velocity, and τ is the integral timescale (average of three components). Turbulence kinetic energy, velocity, and timescales were measured using a pair of split-fiber (hotwire) probes (see [5] for details of setup). The components of the integral time scale (in x, r, and θ) were defined as the integral of the normalized autocorrelation function of the corresponding velocity component from zero time shift to the first zero crossing.

Kinetic energy loss coefficients

The aerodynamic efficiency of the NGV was quantified using a number of kinetic energy (KE) loss coefficients. We adopt the definitions used during a prior analysis of the uniform test case [6], which made use of a *local* KE loss coefficient (ζ_1); a *circumferentially-averaged* KE loss coefficient (ζ_3); a *plane-averaged* KE loss coefficient (ζ_4); and a *mixed-out* KE loss coefficient (ζ_5). *Local* and *circumferentially-averaged* KE loss coefficients correspond to the definitions of Burdett and Povey [147]; the *plane-averaged* KE loss coefficient was defined following Lawaczeck [187]; and *mixed-out* conditions were calculated according to the Dzung method [188, 189]. For brevity, we do not rehearse the definitions here.

Non-dimensional downstream/surface total temperature

Total temperatures on wetted surfaces and in the flow downstream of the NGV were transformed into a non-dimensional total temperature, Θ_2, according to

$$\Theta_2(x, r, \theta) = \frac{T_{02}(x, r, \theta) - T_{0\mathrm{c}}}{T_{01,\mathrm{rake}} - T_{0\mathrm{c}}} \tag{8.6}$$

where $T_{02}(x, r, \theta)$ is the local total temperature, $T_{0\mathrm{c}}$ is the mass-flow-weighted total temperature in the vane coolant plena, and $T_{01,\mathrm{rake}}$ is the arithmetic mean of rake thermocouples at plane 1 (*excluding* thermocouples immersed in the coolant layer). Θ_2 ranges between 0 and 1; higher values indicate higher temperature. The definitions of Θ_1 and Θ_2 are equivalent when $T_{0\mathrm{b}} = T_{0\mathrm{c}}$. When presenting adiabatic wall temperatures, we use the symbol Θ_{w} for clarity but follow the same definition as that in Equation 8.6.

8.4 Combustor simulator outlet profiles

An upstream traverse system [5] was used to survey the inlet flow at plane 1 (see Figure 8.2) over a 34.4-degree circumferential sector, and across the full span radially. The mean-flow and the turbulence at inlet were fully characterized using a combination of total pressure, thermocouple, and split-fiber (hotwire) probes. The intention was to use this data as reference conditions for experimental measurements downstream of the NGV, and as inlet boundary conditions for complementary CFD simulations. Due to a probe size limitation, a small region at the hub could not be traversed. The approach taken to estimate values of missing data is explained later in this section. Amend et al. [6] previously presented the inlet profiles for the *uniform* inlet condition (plane 1). For brevity, we only present the lean-burn simulator profiles in this paper.

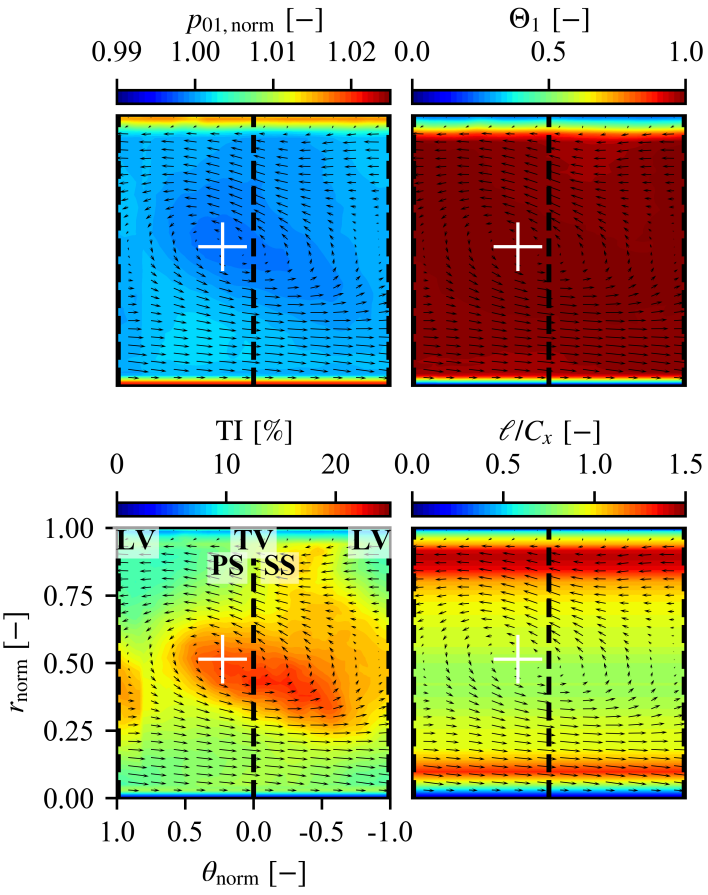


Figure 8.3: *Distributions of normalized total pressure ($p_{01,\mathrm{norm}}$), non-dimensional total temperature (Θ_1), turbulence intensity (TI), and normalized integral length scale (ℓ/C_x) at plane 1 for a single periodic swirler sector (18 degrees). Data are viewed from upstream. The vectors indicate the in-plane flow direction and magnitude for an equivalent horizontal duct.*

Experimentally-measured combustor simulator outlet profiles (plane 1) of normalized total pressure ($p_{01,\mathrm{norm}}$), non-dimensional total temperature (Θ_1), turbulence intensity (TI), and normalized integral length scale (ℓ/C_x) are shown in Figure 8.3. The distributions were obtained by mapping the surveyed 34.4-degree sector onto a single swirler sector (18 degrees). Regions of duplicate data were averaged, with slight smoothing across circumferential boundaries to ensure periodicity (required for suitability as a CFD boundary condition). The x-axis (θ_{norm}) is the vane-pitch-normalized circumferential coordinate, where $\theta_{\mathrm{norm}} = 0$ is the swirler centerline, which is clocked onto the leading edges of alternating NGVs (recall that the NGVs have a 2:1 count ratio with the swirlers). The axially-projected locations of NGV LE are indicated by the vertical dashed lines. Of note, the x-axis is inverted (i.e. descending towards the right) because the $+\theta$ direction was defined as the turning direction of the NGV, which is CCW (left) when viewed from upstream. The y-axis (r_{norm}) is the normalized span fraction. The superimposed vector field

represents the in-plane flow direction and magnitude for an equivalent horizontal duct. The inclination of the duct (around 15 degrees) is accounted for by plotting the *deviatory* radial vector component (see transformation method of Bacci et al. [107]).

First consider the in-plane flow field in upstream plane 1, shown by the vector field superimposed on all subplots of Figure 8.3. The swirl direction is CCW when viewed from upstream. Maximum and minimum whirl angles at plane 1 were approximately +30 degrees and −38 degrees respectively. By plane 1b (0.5 axial chords upstream of vane LE) these were shown to be attenuated to +20 degrees and −22 degrees (see five-hole probe measurements of Amend et al. [4]). The attenuation arises because of the axial acceleration due to the converging duct. The center of circulation—indicated by a white cross—is located approximately 2 degrees to the left of the geometric center of the swirler ($\theta_{\mathrm{norm}} = 0$). This type of circumferential vortex core migration has previously been reported by Bacci et al. [107] and Schmid et al. [98]. The mechanism is that as individual vortices mix-out through inter-vortex free shear, conservation of angular momentum causes bulk-turning of the flow (see discussion in [4]). In the study of Bacci et al. [107], the vortex was slightly PS-biased, leading to NGV flows more typical of passage-clocked swirl. For the current study, the center of circulation is also slightly PS-biased, but the migration effect had minimal impact, because the whirl angle is relatively circumferentially-uniform at a particular radial height, and therefore affects the flow in alternating vane passages similarly regardless of clocking (i.e. the swirl is less localized; see distributions from Amend et al. [4]). This is consistent with recent observations from the similar combustor simulator of Adams et al. [104] (also derived from the prototype of Hall and Povey [92]), for which NGV inlet profiles were likened to a *circumferentially-shearing* flow.

Now consider the distribution of normalized total pressure ($p_{01,\mathrm{norm}}$; see Equation 8.2), which is shown in the top left subplot of Figure 8.3. Between 4 and 91% span, normalized total pressure is approximately uniform. Here the maximum variation is ±0.2% of the rake average, with a local minimum of 0.998 at the vortex center. Towards the casing the normalized total pressure increases steeply, reaching a maximum of 1.017 near the wall. Normalized total pressures higher than unity are associated with coolant ejection from the annular temperature profile generator slots, and is a consequence of the particular design decisions taken (matched total pressure is also possible). Mild excess near-wall total pressure may be a characteristic of lean-burn combustor designs in which there is significant combustor liner coolant. Indeed, a similar near-wall total pressure excess of approximately 1.0% was observed in the lean-burn combustor outlet profiles used by Shapar

and Caloni [56] in a turbine optimization study. These originated from a high-fidelity simulation of a lean-burn combustor prototype. It was not possible to perform measurements in the 0–3% span region (near hub flow) and this region was *patched* with data from CFD simulations of the combustor simulator. The maximum normalized total pressure in the patched data was 1.020. This is slightly higher than the maximum value at the casing (1.017), but this is explained by the fact that the exit of the hub coolant feed is closer to plane 1 than the exit of the casing coolant feed slot. Thus the hub coolant flow is less mixed out at the measurement plane.

It is worth noting that the pressure surpluses in the hub and case coolant flows mix out fairly rapidly downstream of the injection slots, with the non-uniformity approximately halving by plane 1b (non-uniformity of ±0.4%; see measurements in [4]).

Now consider the distribution of the non-dimensional total temperature (Θ_1; see Equation 8.3), which is shown in the top right subplot of Figure 8.3. The profile is broadly radial in nature (i.e. low circumferential distortion), with approximately uniform temperature ($\Theta_1 \approx 1$) over the wide region between 6% and 89% span. Near the casing, the temperature decreases steeply due to coolant injected from the temperature distortion module (emulating the effect of combustor liner cooling). The patched region at the hub (0–3% span) was linearly interpolated between the last measured point (3% span) and an assumed value of $\Theta_1 = 0$ at the wall. The assumed value is justified on the basis that this point is just downstream of the hub slot exit, and therefore should be fully covered by unmixed hub coolant flow. This total temperature profile mixes rapidly between plane 1 and plane 1b, leading to a more rounded radial distribution at the NGV inlet (see measurements in [4]).

Now consider the distribution of the turbulence intensity (TI; see Equation 8.4), which is shown in the lower left subplot of Figure 8.3. The average turbulence intensity is approximately 15%, but with a large region of elevated intensity approximately downstream of the swirler geometric center. Here the peak value of turbulence intensity was 22%. In the hub and case coolant jets, the turbulence intensity reduces: values of TI = 10% were measured near the casing wall; values of 8% were estimated at the hub wall based on a CFD-predicted profile linearly scaled to match the last measured value in the near hub flow (at 5% span).

Finally, consider the profiles of normalized integral length scale (ℓ/C_x; see Equation 8.5), shown in the lower right subplot of Figure 8.3. Experimentally-measured length scales had relatively high precision uncertainty because the sampling period had to be optimized for the relatively short (approximately 60 s) facility run duration. As CFD simulations of the combustor simulator showed that ℓ varied primarily as a function of the radius, the measured distribution was

circumferentially-averaged. Though a relatively crude approach, this ensures that the profile is suitable for use as a CFD inlet condition. In the resulting profile, the circumferentially-averaged length scale was approximately constant between 20% and 75% span (average of 0.88 C_x), with slightly higher values in the free-shear layers between the hub and case cooling flows and the main-flow. These elevated values might be related to unsteadiness of the shear layer. Near the casing, ℓ/C_x decreased on approach to the wall, with the lowest measured value being 0.34. This is consistent with the commonly-observed linear variation of length scale in the near-wall region (see e.g. Wilcox [141]). In principle, we would expect $\ell/C_x = 0$ at the wall. The non-zero value in current measurements is likely explained by an interaction with the probe access port at the casing, resulting in a disturbed cavity flow (instead of a boundary layer flow). For compatibility with the numerical model, $\ell/C_x = 0$ was enforced at both the hub and casing walls, interpolating linearly with the last measured values of $\ell/C_x = 0.80$ and 0.58 at 5% and 98% span, respectively.

8.5 Numerical methods

Simulations of the fully-featured NGV were performed for uniform and lean-burn-representative inlet conditions. The purpose of these simulations was twofold: insight into the effects of inlet swirl and inlet temperature distortion on the flow in regions which were difficult to measure; assessment of the accuracy of CFD methods for lean-burn-representative inlet conditions. In this section we describe the domain, boundary conditions, and model settings.

Computational domain and grid

The mesh used in the current study has previously been described by Amend et al. [6], and is therefore summarized only briefly. The mainstream inlet is located at plane 1 (see Figure 8.2), and the outlet is located approximately three axial chords downstream of the vane TE at the outlet of the vane exit duct. The internals of the vanes are fully-resolved, with coolant introduced from inlets inside the hub and casing plena. Resolving the vane internals ensures that coupling effects arising from the impact of the altered external loading (due to inlet swirl) on the internal flow redistribution is correctly accounted for. The mesh contains roughly 312 million cells, approximately half of which were internal. A second mesh *excluding airfoil film cooling* (no internals; same refinement level; 151 million cells) is used to investigate the effect of inlet swirl on the surface streamlines, which would otherwise be interrupted by the presence of cooling holes.

Boundary conditions

We now consider the domain boundary conditions for the uniform and the lean-burn-representative test cases. In each case, the aim was to replicate the respective experimental boundary conditions.

For the *uniform test case*, the inlet boundary conditions at plane 1 were specified as the experimentally-measured radial profiles of total pressure, total temperature, turbulence intensity, and turbulence length scale. For further detail see [6]. The average turbulence intensity at plane 1 was 13%, and the turbulence length scale was on the order of one axial chord ($\ell/C_x \approx 1$). The flow direction was in the meridional plane, with a pitch angle distribution bounded by the hade angles at the hub and casing walls.

For the *lean-burn test case*, the inlet profiles of total pressure, total temperature, flow angles, turbulence intensity, and turbulence length scale were specified as the pre-conditioned (periodic; missing data patched) experimentally-measured area maps at plane 1 (see Figure 8.3). The inlet values of turbulence dissipation rate, ϵ, were estimated using the CFX definition of the turbulence length scale ($\epsilon = k^{1.5}/\ell$; see CFX solver theory guide), where the turbulence length scale, ℓ, was assumed to be equal to the integral length scale (see discussion on the choice of scaling constant [7]). A comparison between CFD-predicted turbulence dissipation rates at plane 1 with those estimated from experimentally-measured integral length scales suggests that this is a good approximation for the present combustor simulator flow.

For both uniform and lean-burn test cases, coolant plena inlets were specified with boundary conditions of constant mass-flow rate and total temperature (average across experimental dataset), and with a turbulence intensity of 5% and a viscosity ratio of 10. The domain outlet had a radial equilibrium condition specified. Periodic interfaces were conformal (one-to-one node mapping). All wetted surfaces were modeled as hydraulically smooth. For simulations using the mesh that *excluded airfoil film cooling*, boundary conditions were the same as for the cooled simulations.

Model and solver settings

Simulations were performed using ANSYS CFX (version 22.1). The working fluid was dry air, which was treated as an ideal gas with constant transport properties. The mean-flow energy equation included the viscous-work term, and turbulent fluxes were modeled with eddy diffusivity using a turbulent Prandtl number of 0.50 (optimized for free shear mixing of coolant; see [174]). Turbulence was modeled using the baseline explicit algebraic Reynold Stress Model (BSL-ARSM; see [201]), with the turbulence production limiter disabled. These settings were shown to offer a

good compromise between predictions of integral loss, and aerodynamic wake mixing for the uniform test case, but were found to result in slight overmixing of the thermal field. Choice of turbulence model for this problem is discussed by Amend and Povey [7]. The mean-flow and turbulence equation systems were discretized with a second-order upwind-biased numerical scheme.

8.6 NGV loading and streamline pattern

The effects of inlet swirl on the NGV surface static pressure distribution and surface streamline pattern were investigated using CFD. This allows analysis of the cooling system response, which is affected both in terms of internal flow redistribution due to altered external pressure, and in terms of the external migration of film coolant on the vane surface. The NGV static pressure distribution is also relevant from an external-aerodynamic standpoint because changes in loading and flow pattern alter the KE loss distributions and secondary flow intensity.

NGV loading distribution

The *change* in normalized static pressure ($\Delta p_2/p_{01}$) due to swirl is shown in Figure 8.4. Normalized static pressure is defined as the surface static pressure (p_2) normalized by the mass-flux-weighted total pressure at plane 1 (p_{01}). The distributions are shown for the PS and SS of both the TV and LV. Looked at in terms of *changes* in static pressure on the PS and SS, local loading is reduced when the pressure on the PS decreases *relative* to that on the SS (i.e. when $\Delta p_{2,\mathrm{PS}} < \Delta p_{2,\mathrm{SS}}$).

We first note that the changes on the TV and LV are extremely similar to each other. We recall that the yaw angle of the incoming flow is relatively uniform circumferentially, resulting in comparable incidence onto both vanes. This behavior has been seen in other studies with these *circumferentially-shearing* swirl profiles at inlet [104, 56]. For lean burn combustors with flow patterns of this type, design integration with the NGV may be simpler (same airfoil for TV and LV).

The sense of swirl in this study was co-rotating, such that it caused negative incidence in the (approximately) upper half of the span range (reduced loading) and positive incidence in the lower half of the span range (increased loading). Accordingly (see Figure 8.4), in the upper half of the span range we see an increase in SS pressure and a decrease in PS pressure (reduced loading); the effect is reversed in the lower half of the span range. The changes are fairly uniform with chord along the PS of the vane (slight changes in the entire vane exit flow field), but concentrated towards the LE on the SS of the vane (change in SS peak only). Therefore, the LE region is much more affected than the TE region in terms of loading, with limited changes beyond 40% axial chord.

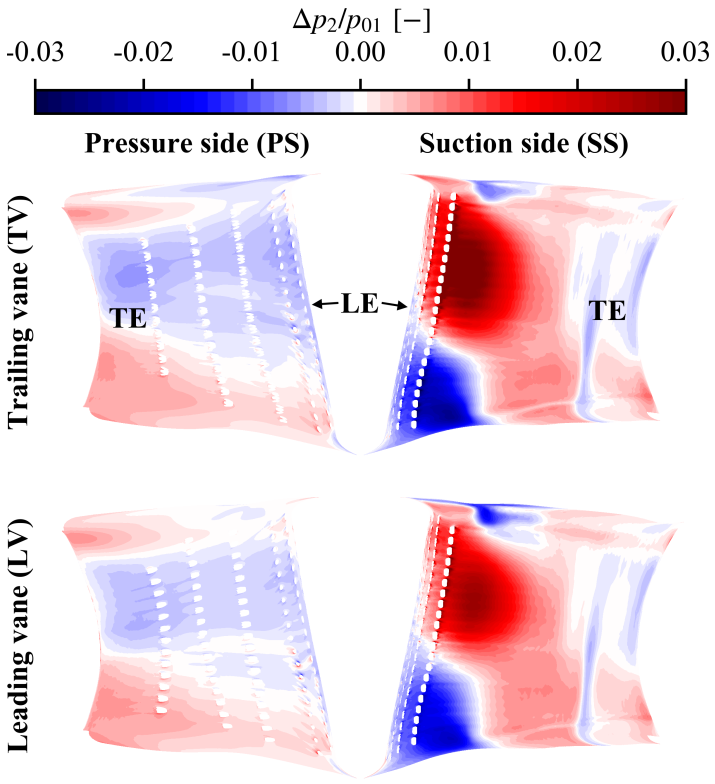


Figure 8.4: *CFD-predicted change of normalized static-to-upstream-total pressure ratio ($\Delta p_2/p_{01}$) on the vane surface with the introduction of inlet swirl (relative to uniform inlet condition).*

Surface streamlines

CFD-predicted surface streamlines for uniform and lean-burn-representative (swirling) inlet conditions are shown in Figure 8.5. The surface streamlines are based on simulations of the vanes *excluding* film cooling. Although film cooling locally enhances momentum flux and could—in principle—alter the streamline pattern, similar uncooled simulations have been shown to be a good predictor of surface streamline pattern (see Adams et al. [104]). An advantage of uncooled simulations is that that surface flow is uninterrupted and therefore easier to interpret *visually*.

First consider the surface streamlines for the uniform test case, which are shown on the left side of Figure 8.5. The streamline pattern is effectively identical for both vanes. On both the PS and SS, surface streamlines between 15% and 80% span are approximately parallel to each other, with mild upwash near the stagnation line (combined effect of haded inlet duct and a backwards-swept LE). From mid-chord onwards on both the PS and SS there is mild downwash over most of the surface, caused by low momentum fluid migrating radially-inwards in the radial pressure gradient set up by the mainstream flow. The effect is less pronounced on the SS than the PS because the ratio of local momentum to radial static pressure gradient is lower. Near the hub and casing endwalls, the streamlines are disturbed by low-intensity secondary flows.

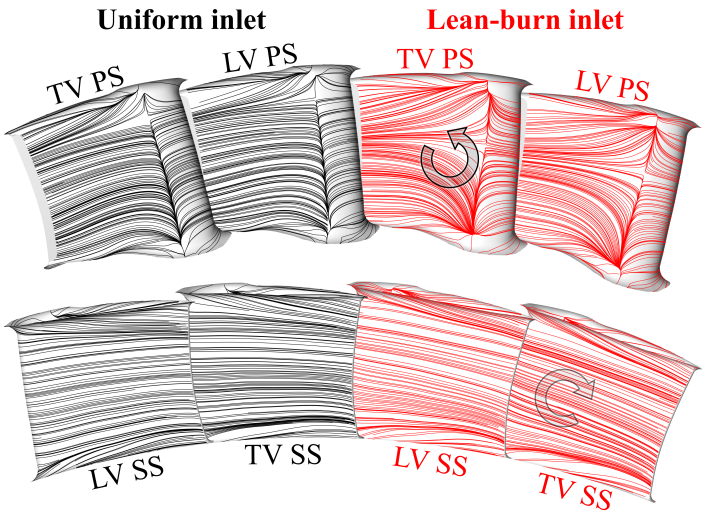


Figure 8.5: *CFD-predicted surface streamlines for uniform inlet (left) and lean-burn-representative inlet conditions (right). The direction and clocking of the incoming swirl is marked.*

Now consider the surface streamline pattern for case with lean-burn-representative (swirling) inlet flow, shown on the right side of Figure 8.5. The streamline pattern is relatively similar for both vanes. This is a result of the incoming flow pattern, which is relatively circumferentially-uniform at a particular radial height. The introduction of swirling flow causes significant upwash on the lower span sections of the PS, and significant downwash on the upper span sections. This causes the streamlines to coalesce towards the midspan: coolant concentration in this region is therefore expected. The SS is much less affected by the introduction of inlet swirl, but the very mild downwash we see in the uniform case is slightly enhanced by inlet swirl. This is consistent with the fact that the dominant pressure disturbance associated with inlet swirl is one that enhances the radially-inwards pressure field on the early SS (see Figure 8.4). The introduction of inlet swirl seems also to slightly suppress the casing secondary flow, which remains confined closer to the endwall under swirling inlet conditions.

Finally, consider the leading-edge stagnation lines for the uniform and lean-burn-representative test cases. For uniform inflow, the stagnation line is almost straight, aligning with the SS crown and—more significantly—the film cooling hole pattern. With the introduction of swirl, the stagnation line migrates towards the PS in the lower half of the span, and towards the SS in the upper half of the span, creating a mild sinusoidal shape. This causes some LE film trajectories to move from one side of the vane to the other (from PS to SS and vice versa). This has implications for the cooling budget of the two surfaces, but also makes the affected holes susceptible to separation because their lay-orientation (with respect to the local surface) opposes the external

flow direction. Clearly the vane aerodynamics and cooling system would need to be designed for a specific lean burn inlet condition, considering both swirl and temperature distortion.

8.7 Effect on cooling system

Inlet swirl significantly alters both the vane surface pressure distribution and surface streamline pattern, leading to changes in individual film mass flow rates (internal redistribution) and external coolant migration. We study these effects in this section.

Description of internal cooling configuration

The PS and SS of the vane airfoil each feature five rows of film cooling holes. The TE is cooled by a letterbox-style slot with PS-ejection (i.e. with SS overhang), extending along the full span. The hub and casing endwalls are cooled by two staggered rows of film cooling holes. Vane airfoil coolant (PS, SS, and TE slot) and hub endwall coolant is supplied from a shared plenum at the hub. The casing endwall coolant is fed from a separate plenum. Both plena are shown schematically in Figure 8.2.

Internal flow redistribution

We now consider the redistribution of the internal cooling flows by looking at the impact of lean-burn swirl on the row-wise and span-wise cooling mass flow rates.

Consider first the effect of swirl on row-wise coolant redistribution. Row-wise normalized mass flow rates ($\dot{m}/\dot{m}_c$) for uniform and lean-burn-representative inlet conditions are shown in Figure 8.6, considering the TV and the LV separately.

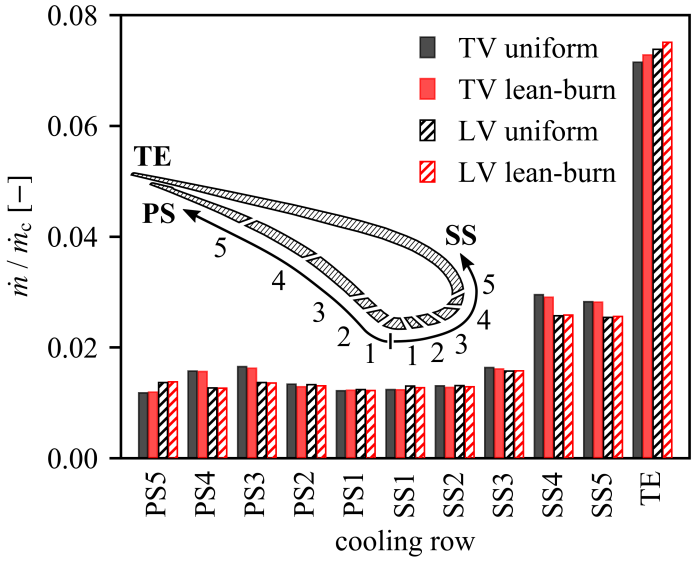


Figure 8.6: *Normalized row-wise mass flow rates for the trailing vane (TV) and leading vane (LV), under uniform and lean-burn-representative inlet conditions.*

We see from Figure 8.6 that *row-wise* redistribution of coolant with the introduction of lean-burn swirl is relatively subtle. The normalized mass flow through the TE slot increases by 1.9% for the TV and by 1.7% for the LV under lean-burn conditions. The increase in TE slot mass fraction is caused by an increase in the total-to-static pressure ratio at the TE slot exit, caused by a reduction in the base pressure. For the vane surface cooling rows (excluding TE slots), the maximum percentage increase in mass flow was for PS row 5 of the TV (+1.1%), and the maximum decrease was for PS row 2 of the TV (−3.4%). The reason for the limited sensitivity of row-wise mass flows is that the change in external static pressure is approximately anti-symmetric about the midspan (see Figure 8.4). A reduction in the mass flow at one end of the cooling row is therefore compensated for by a proportionate rise in mass flow at the other end. We explore this effect further now.

Mass flow rates of individual film cooling holes are now investigated to consider *span-wise* redistribution effects. Intuitively, we expect that mass flows will depend primarily on the static pressure at the exit of the film cooling hole. In Figure 8.7, for each cooling hole we plot the *actual ratio* of coolant mass flow rates for lean-burn and uniform conditions, $\dot{m}_2/\dot{m}_1$ (where $\dot{m}_1$ is the uniform coolant hole mass flow rate, and $\dot{m}_2$ lean-burn mass flow rate) against an *estimated ratio* based on isentropic mass flow function and area-averaged static pressure across the film cooling hole exit (and mass-flux-weighted total temperature and pressure entering the hub coolant plenum). Presented in this way, the spread on the y-axis shows the actual distribution of mass flow ratio changes with swirl, and the goodness of correlation (with a linear trend of slope unity) shows the degree to which the change is purely explained by external static pressure changes. Scatter points are colored to distinguish PS, SS, and TE (each TE slot is treated as a single hole).

Looking first at the changes in actual mass flow rate ratios, we see that the introduction of swirl causes changes of +19.1% and −14.2% for individual SS holes, and +8.9% and −11.4% for PS holes. The mass flow of the TE slots increased by 1.7% and 1.9%. The change for SS holes is significantly greater than for PS holes, in line with the greater change in static pressure on the SS than on the PS (see Figure 8.4).

Now consider the comparison of the actual and estimated mass flow rate ratios. There is reasonably good agreement with a linear trend of slope unity, showing that to first order the mass flow rate changes can be explained by changes in external static pressure. With reference to the static pressure *change* distributions in Figure 8.4, this implies that the PS experiences internal coolant redistribution from hub (increased static pressure) to casing (decreased static pressure), while the opposite is true for the SS. Deviations from the linear trend are explained by the fact that

internal duct pressure losses, and cross flow effects on both the inlet and outlet of the hole are not captured by the low-order model.

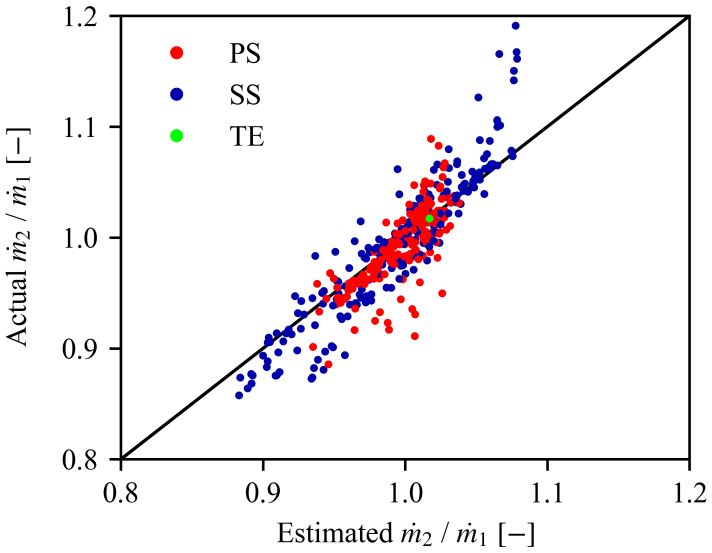


Figure 8.7: *Actual mass flow rate ratios (swirl-to-uniform) for individual holes compared to estimated mass flow rate ratios.*

Adiabatic wall temperature

We now consider the effect of lean-burn swirl and inlet temperature distortion (see Figure 8.3) on CFD-predicted adiabatic wall temperatures of the vane airfoil. The three primary mechanisms are: a change in the inlet external driving temperature (see discussion of Qureshi et al. [220]); a swirl-induced change in surface streamline pattern which causes change in coolant flow migration and temperature field migration (see discussion of Khanal et al. [106]); a change in freestream turbulence which affects both the lateral spreading and streamwise decay rates of coolant films (see discussion of Schmidt and Bogard [221]). To separate the effect of local coolant concentration and local driving temperature (which are easily conflated) we perform additional uniform and lean-burn-swirl simulations with *constant total temperature* at inlet specifically with the purpose of investigating the effects of swirl and turbulence on a like-for-like basis with the uniform test case. Separation of effects in this way is justified by the Munk and Prim [103] principle, according to which the streamline pattern remains unchanged for a changing inlet temperature profile.

Airfoil surface distributions of normalized adiabatic wall temperature, Θ_w (see Equation 8.6) from simulations with constant inlet total temperature but with uniform and lean-burn-representative inlet conditions for swirl and turbulence are shown in Figure 8.8. Corresponding surface-averaged values are reported in Table 8.2. Here we are interested in

qualitative comparison of overall trends and note that absolute values are unlikely to be highly accurate due to the choice of turbulent Prandtl number, which was optimized for free shear thermal mixing, in favor of wall heat transfer.

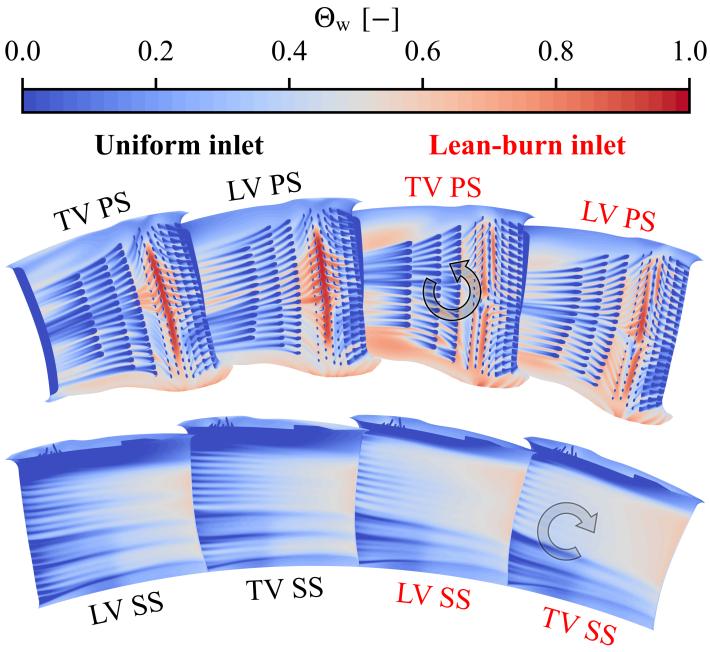


Figure 8.8: *CFD-predicted normalized adiabatic wall temperature (Θ_w) under uniform (left) and lean-burn-representative (right) inlet conditions for swirl and turbulence but with constant inlet total temperature.*

First, consider the CFD-predicted distributions of Θ_w under uniform flow conditions. In the upstream view (top row), both airfoils exhibit an elongated hotspot along the stagnation line. For reasons relating to the combustor hot-streak clocking in the real engine, the TV and LV feature different film cooling designs. This leads to slightly different adiabatic wall temperature distributions, even under uniform inlet conditions. Notably, the TV PS is on average slightly colder (Θ_w = 0.335) than the LV PS (Θ_w = 0.363; see Table 8.2), indicating better film coverage. The LV PS Θ_w distribution is also slightly less radially uniform, with a colder region between approximately 10–40% span. On the SS (bottom row) the TV and LV have more similar Θ_w distributions, the predominant feature being increasing adiabatic wall temperature towards the TE as the films mix out with the freestream (lower film effectiveness). Near the casing (80–100% span) there is a notably cold region of secondary flow with entrained endwall coolant.

Now consider the impact of lean-burn-representative inlet conditions for swirl and turbulence. Looking first at the upstream view (top row) of the PS and early SS, the most striking difference compared to the uniform flow case is the reduced intensity of the stagnation line hotspot. With reference to the surface streamline pattern in Figure 8.5, this is explained by coolant migration,

which is locally redirected towards the spanwise (as opposed to the chordwise) direction, thus improving the coverage uniformity in the LE region. This effect is likely reinforced by the elevated turbulence intensity, which promotes lateral spreading of films (see Schmidt and Bogard [221]). Despite a reduced *maximum* adiabatic wall temperature, the *area-average* adiabatic wall temperature on the PS increases significantly (from 0.349 on-average across both vanes to 0.404; see Table 8.2). This appears to be associated with poor film coverage and possibly the accelerated decay of films under high turbulence conditions [221]. Poor film coverage is especially apparent on the mid-to-late TV PS, where the upper half of the film-cooled region is significantly colder than the lower half. This is caused by two effects. Firstly, by variation of cooling hole mass flow rates on account of swirl-induced changes in static pressure (see Figure 8.4), which results in a net internal redistribution of coolant from hub to casing on the PS. Secondly, by changes in the external streamline pattern, which causes the flow to concentrate around 60% span. Because the streamline pattern redistributes coolant away from the near-wall regions, the adiabatic wall temperature on the aft PS near both the hub and casing increases. We recall that here we are concerned with the effect of swirl and turbulence only, and that for an engine-realistic inlet temperature distribution the radial adiabatic wall temperature variation would be less severe.

Finally, consider the downstream view (bottom row) of the adiabatic wall temperature distribution on the mid-to-late SS. The area-averaged adiabatic wall temperature increased with lean-burn conditions (from 0.239 to 0.290 on-average across both vanes; see Table 8.2); i.e. there is lower film performance with lean-burn conditions. We recall that the internal flow redistribution effect on the SS is such that the lower half of the span is slightly colder than the upper half. This effect is evident in Figure 8.8. Swirl-induced secondary flows cause downwash in the lower half of the span, and seem to confine the casing secondary flow closer to the wall.

Table 8.2: *Area-averaged normalized adiabatic wall temperature (Θ_w) under uniform and lean-burn-representative inlet conditions for swirl and turbulence but with constant inlet total temperature.*

	Uniform	**Lean-burn**
TV PS	0.335	0.400
TV SS	0.241	0.295
LV PS	0.363	0.408
LV SS	0.237	0.284
PS average	0.349	0.404
SS average	0.239	0.290

8.8 Effect on downstream flow

In this section, we consider the effect of inlet swirl and temperature distortion on experimentally-measured and CFD-predicted distributions of vane exit whirl angle (α), local KE loss (ζ_1), and non-dimensional total temperature (Θ_2) at three downstream planes. We also characterize integral KE loss using plane-averaged and mixed-out KE loss coefficients. Experimental measurements are compared with CFD predictions using the BSL-ARSM turbulence model.

Whirl angle and residual combustor swirl

Experimentally-measured and CFD-predicted whirl angle (α) distributions for the uniform and lean-burn-representative test cases are shown in Figure 8.9. Data are viewed from downstream, and cover two vane pitches, equivalent to one swirler pitch. We consider the effect of inlet swirl on the flowfield at downstream planes 2, 3, and 4 (located at 0.25 C_x, 0.50 C_x, and 0.75 C_x downstream of the midspan TE, respectively; see Figure 8.2). As we move between planes, the analysis regions move to track the same wakes in both the experimental and CFD results (method uses the mass-flux-weighted whirl angle). Thus, the abscissa, θ_{norm}, represents the vane-pitch-normalized circumferential location in the wake-following coordinate frame. The ordinate, r_{norm}, is the normalized span datumed to the radius at the hub. The wakes of the TV and LV are centered around $\theta_{\mathrm{norm}} = 0$, and 1, respectively. Whirl angles are presented in terms of the deviation from the midspan TE metal angle (α_{TE}), where a positive value ($\alpha - \alpha_{\mathrm{TE}} > 0$) corresponds to over-turning. A contour of the normalized local KE loss coefficient corresponding to $\zeta_1/\zeta_{\mathrm{ref}} = 0.5$ is superimposed to outline the aerodynamic wakes. Here, the *reference* KE loss coefficient, ζ_{ref}, is defined as the experimentally-measured mixed-out KE loss coefficient at plane 4 for the uniform test case (i.e. a single value for all normalizations). For the test case with inlet swirl, the wakes of NGV aligned with the swirler/vortex are marked with a circular arrow indicating the direction of swirl.

The flow field for the uniform test case was previously analyzed in detail using experimental measurements (first column), and CFD simulations (second column) [6]. We briefly review the key observations, starting with the experimentally-measured whirl angle distribution at plane 2 (first row and column). For uniform inlet conditions, the radial variation of whirl angle generally follows the spanwise metal angle distribution of the NGV, which has slightly higher turning in the upper half of the span. Circumferential non-uniformities are associated with the potential field of the TE, which *locally* reduces the whirl angle of the downstream flow in regions circumferentially

aligned with the *axially-projected* location of the TE. For a discussion of this effect see [6]. Outlines of the aerodynamic wakes at plane 2 are slightly bowed towards higher θ_{norm} at midspan, approximately following the shape of the compound-leaned TE as viewed on an axial cross-section. At downstream planes 3 and 4 (see rows two and three) the radial variation in whirl angle is similar to plane 2, but there is a reduction in circumferential non-uniformities due to decreasing potential field intensity and turbulent mixing of the flow. Aerodynamic wakes become increasingly distorted at planes 3 and 4, due to radial variations in the progression rate of the wake (i.e. angular versus axial displacement; $d\theta/dx \approx \tan(\alpha)/r$. CFD predictions of whirl angle (second column) are in generally good agreement with the experimentally-measured distributions.

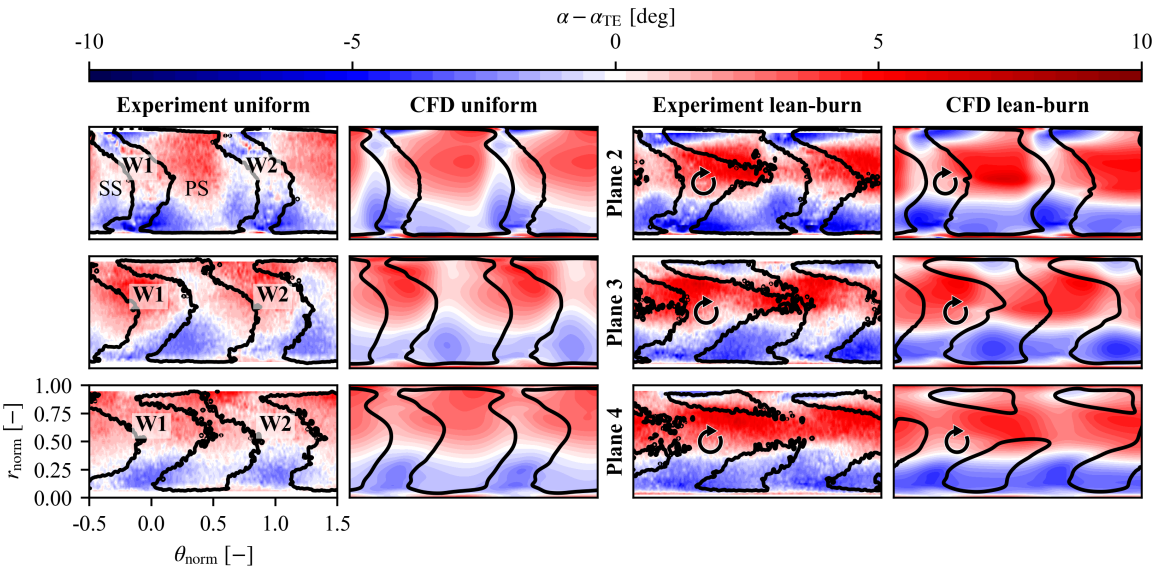


Figure 8.9: *Experimentally-measured and CFD-predicted whirl angle (α) distributions at planes 2, 3, and 4, for both uniform and lean-burn-representative inlet conditions. A contour of normalized local KE loss coefficient corresponding to $\zeta_1/\zeta_{\mathrm{ref}} = 0.5$ is superimposed. Data are viewed from downstream. The circular arrows indicate the wakes associated with NGVs aligned with the swirler centerline.*

Now consider the experimentally-measured distributions of whirl angle under lean-burn-representative inlet conditions (third column of Figure 8.9). Visually, the whirl angle distributions appear periodic according to the vane pitch and not the swirler pitch; this is expected because the potential field is dominated by the vane, with only a secondary influence of inlet swirl. The area map at plane 2 (first row) broadly resembles that of the uniform test case, but with superimposed distortion from upstream swirl. In accordance with the direction of upstream swirl (see circular arrow), whirl angle increases between 35% and 80% span and is reduced below 35%. Above 80% span, wedge-shaped regions of underturned fluid appear towards the casing. Here, the change in whirl angle *opposes* the anticipated distortion based on the upstream direction of swirl.

The underturning is caused by a radial band of elevated total pressure (combined influence of inlet pressure profile and casing endwall cooling), which renders the affected streamlines less responsive to the static pressure field set up by the bulk flow. The effect is of the same mechanism as, but opposite in sign to, the commonly observed overturning of endwall boundary layer fluid (which has a deficit of total pressure). Similar trends were observed by Adams et al. [104], who also had elevated near-endwall upstream total pressure and associated underturning. In our test case we also have *mildly* elevated total pressure near the hub, and expect associated underturning: there is no obviously-distinguishable effect in the data, but the expected location is in a larger region of underturned flow due to upstream swirl. At downstream planes 3 and 4, the flow field becomes increasingly uniform in the circumferential direction, while the radial distribution remains largely unaffected. The CFD (see fourth column) and experimental data are in very good agreement at all axial planes.

Consider now the locations of the aerodynamic wakes under lean-burn-representative inlet conditions. With inlet swirl, the wakes experience significantly greater circumferential stretching between planes 2 and 4 than for the uniform test case. Amplified wake stretching is explained by the effect of whirl angle distortion on wake progression rates ($d\theta/dx \approx \tan(\alpha)/r$): the combination of raised whirl angles around the midspan (35–80% span), and reduced whirl angles near the walls (0–35% and 80–100% span) gives rise to a lead–lag effect, whereby the overturned flow near the midspan migrates towards higher θ_{norm} at a faster rate than the underturned near-wall flow. Similarly, the plane-to-plane *streamwise distance*, s, is also extremely sensitive to whirl angle distortion, increasing with the *secant* of the whirl angle; i.e. $ds/dx \approx \sec(\alpha)$. For a representative exit angle of 75 degrees, this corresponds to a 7% increase of streamwise distance for every degree increase in turning (locally linear assumption). We discuss the influence of streamwise development distance on perceived mixing rates in a later section on aerodynamic losses.

Now consider the experimentally-measured and CFD-predicted radial profiles of the circumferentially mass-flux-weighted absolute whirl angle, α, which are shown in Figure 8.10 for the uniform and the lean-burn-representative test cases. We consider the profiles at plane 4 (0.75 C_x; see Figure 8.2), which corresponds to the approximate location of the high-pressure rotor LE.

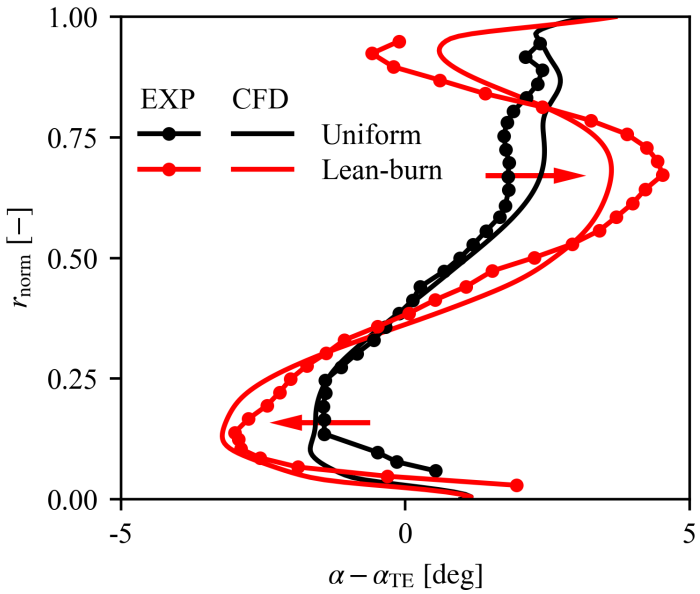


Figure 8.10: *Experimentally-measured and CFD-predicted radial distributions of circumferentially mass-flux-averaged absolute whirl angle (α) at plane 4 (0.75 C_x), for uniform and lean-burn-representative inlet conditions.*

Under uniform inlet conditions, the experimentally-measured trend is approximately linear from hub to casing (y-axis), which reflects the radial variation of the metal angle (lower turning at the hub). Slightly negative deviation angles at midspan (i.e. flow angles *exceeding* the midspan metal angle α_{TE}) are explained by an expansion of the passage area between the true TE and the measurement plane (flared endwalls).

Under lean-burn-representative inlet conditions the experimentally-measured radial distribution of whirl angle deviates from the uniform trend according to the direction of the upstream swirl (see arrows). In the previously-identified region of overturning (35–80% span), the maximum increase of whirl angle was 2.7 degrees relative to uniform inlet conditions, while the maximum reduction in the 0–35% span range was 2.3 degrees. In the region of total-pressure-driven underturning towards the casing (80–100% span), the maximum reduction was 2.6 degrees.

CFD predictions for both test cases match the experimental measurements reasonably well. The CFD-to-experiment RMS/maximum errors were 0.5/1.8 and 0.7/2.5 degrees for uniform and swirling inlet conditions, respectively. For the lean-burn-representative test case, CFD underpredicts peak whirl angle by 0.9 degrees, and exhibits lower sensitivity to the pressure-driven underturning effect towards the casing (80–100% span) than was measured experimentally.

Plane-averaged whirl angles (mass-flux-weighted) were only slightly affected by inlet swirl: experimentally-measured plane-averaged deviation angles were +0.59 degrees for the uniform test case and +0.27 degrees with inlet swirl; CFD-predicted plane-averaged deviation angles were +0.63

for the uniform test case and +0.40 degrees with inlet swirl. That is, experiments and CFD both show a small, but systematic decrease of the plane-averaged whirl angle of around 0.2 degrees under swirling inlet conditions (within uncertainty limits in the case of experiments).

Kinetic energy loss coefficient

Experimentally-measured and CFD-predicted distributions of the normalized local KE loss coefficient ($\zeta_1/\zeta_{\mathrm{ref}}$) for the uniform and lean-burn-representative test cases are shown in Figure 8.11. The local KE loss coefficient quantifies the fractional KE deficit of the flow, relative to and normalized by an ideal expansion from the mass-flux-weighted total pressure at plane 1 to the local downstream static pressure. We recall that the normalizing reference KE loss coefficient (ζ_{ref}) is defined as the experimentally-measured mixed-out KE loss coefficient at plane 4 for the uniform test case. The effect of lean-burn inlet conditions on aerodynamic wake development is studied using area maps at downstream planes 2, 3, and 4. A wake-tracking method is used (previously described).

Before investigating the effect of lean-burn on local KE loss, we briefly review the key features of the aerodynamic wakes under uniform inlet conditions, starting with the experimentally-measured distribution at plane 2 (0.25 C_x; first row and column of Figure 8.11). The data are viewed from downstream. The wakes of the TV (marked W1), and LV (W2) are centered about $\theta_{\mathrm{norm}} = 0$, and 1 (respectively) in the wake-tracking reference frame. Both wakes are gently bowed so that at midspan they are at higher θ_{norm}, following the compound-leaned shape of the TE on an axial cross-section. The region between 10% and 90% span is dominated by profile loss, which is relatively uniform in the spanwise direction. Secondary flow loss cores located around 12% and 79% span cause a slight broadening of the wake, accompanied by local maxima of KE loss. The steep rise of the local KE loss coefficient near the walls is driven by the endwall boundary layers. As expected, the aerodynamic wakes gradually mix out at downstream planes 3 and 4 (second and third row of first column), leading to progressive broadening of the wake, and an attendant decrease in peak KE loss. Simultaneously, the endwall boundary layers at the hub and casing grow in thickness. The CFD simulation of the uniform test case (second column) captures the KE loss distribution in the profile-region reasonably well, but underpredicts radial spreading of endwall boundary layers slightly.

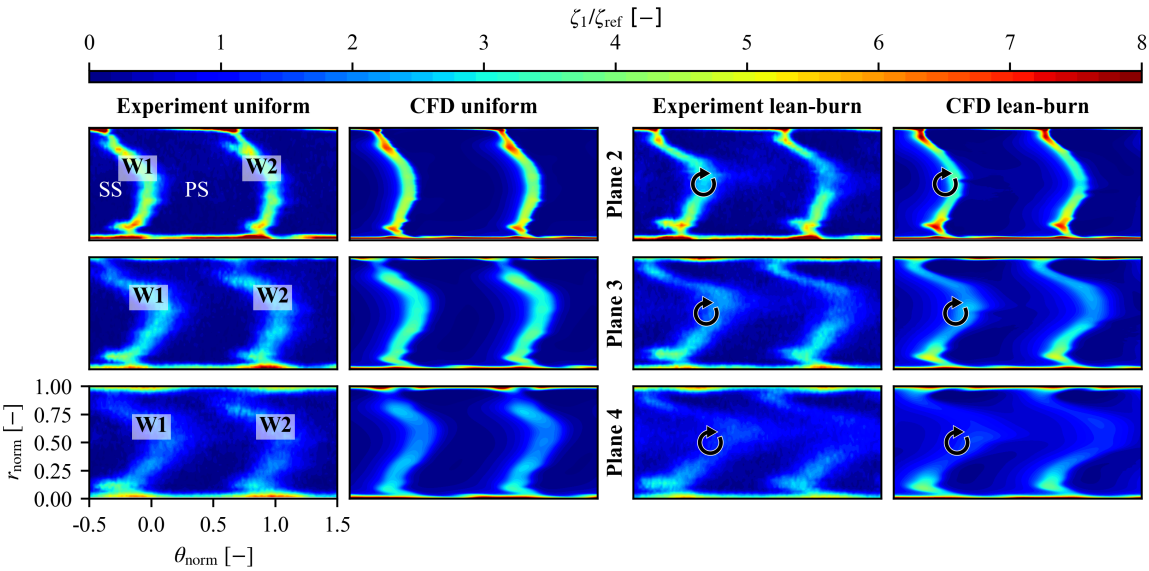


Figure 8.11: *Normalized local kinetic energy loss coefficient (ζ_1/ζ_{ref}) distributions at planes 2, 3, and 4, for experiments and CFD, for both uniform and lean-burn-representative inlet conditions. Data are viewed from downstream. The circular arrows indicate the wakes of NGVs aligned with the swirler centerline.*

Let us now examine the experimentally-measured distributions of normalized local KE loss coefficient under lean-burn-representative inlet conditions, which are shown in the third column of Figure 8.11. Aerodynamic wakes W1 and W2 appear to respond similarly to lean-burn inlet conditions, and we therefore analyze the wakes together, but for completeness mark the swirler-clocked vane wake with circular arrows. We begin by examining the aerodynamic wakes at plane 2 (0.25 C_x; first row and third column). The wakes are more circumferentially stretched than for uniform inlet conditions, an effect that is explained by the difference in wake progression rates (i.e. whirl angles) between the TE and plane 2. Around the midspan, the wakes are broader and have lower peak KE loss than was the case for uniform inlet conditions. This behavior is likely driven by the elevated midspan turbulence intensity at inlet (TI $\approx$ 13% for uniform flow; TI $\approx$ 20% for lean-burn inlet) which promotes diffusion.

Secondary flow structures respond according to the local change in aerodynamic loading due to inlet swirl. At the hub, incidence and loading increase, which causes the hub secondary flow to grow in size. Conversely, swirl-induced off-loading of the casing causes the corresponding loss cores to shrink. The casing secondary flow also migrates radially outwards from around 79% span under uniform inlet conditions to approximately 90% span with inlet swirl. This is in accord with the change in SS surface streamline pattern (Figure 8.5). Curiously, despite an increase in near-wall *upstream* total pressure with lean-burn inlet conditions, the endwall distribution of KE loss downstream of the vanes remains effectively unchanged. The low sensitivity is explained by the

high *absolute* KE loss in the endwall boundary layers, which is large in comparison to the change in upstream total pressure.

Consider now the development of the experimentally-measured aerodynamic wakes at downstream plane 3 (0.50 C_x; second row) and plane 4 (0.75 C_x; third row). Strikingly, the plane-to-plane mixing rate is significantly greater than for uniform inlet conditions, especially around the midspan. One might assume that this is attributed solely to the elevated upstream turbulence intensity (lean-burn profile peaking around at midspan). Noting however the strong correlation between wake width/depth and *streamwise distance* (as opposed to *axial distance*; see Burdett and Povey [147]), we believe that the enhanced mixing is reinforced by whirl angle distortion (i.e. residual swirl) via its effect on streamwise distance ($ds/dx \approx \sec(\alpha)$). With reference to the whirl angle distribution at plane 4 (see Figure 8.10), whirl angle between 35% and 80% span is increased by 1.6 degrees on average (2.7 degrees maximum) relative to uniform conditions, which corresponds to plane-to-plane increases of the *streamwise distance* around 12% (average) and 24% (maximum). Under the assumption that the wake grows approximately linearly with *streamwise distance* (see discussion in [6, 147]), this would account for proportionally wider wakes (the rest being attributed to increased turbulence).

Finally, consider the CFD-predicted distributions of normalized local KE loss coefficient, which are shown in the fourth column of Figure 8.11. CFD captures the wake shape, secondary flow footprint, and profile-region mixing rates very well. The relatively high accuracy of these predictions of wake mixing is perhaps surprising, considering that unsteady vortex shedding was not modeled (steady RANS simulations). The good agreement with experimental data is because the BSL-ARSM model is observed to have higher SS diffusion and free-shear mixing (for certain inlet conditions) than other models (see discussion in [7]), for example the more popular shear stress transport model. This may be an argument for using the BSL-ARSM model in certain cases.

Consider now the experimentally-measured and CFD-predicted *radial profiles* of normalized circumferentially-averaged KE loss ($\zeta_3/\zeta_{\text{ref}}$) at plane 4, which are shown in Figure 8.12. The circumferentially-averaged KE loss coefficient quantifies the mass-flux-weighted KE deficit in a radial band, relative to and normalized by the KE of an ideal expansion from the mass-flux-weighted total pressure at plane 1 to the circumferentially-averaged downstream static pressure of the radial band in question.

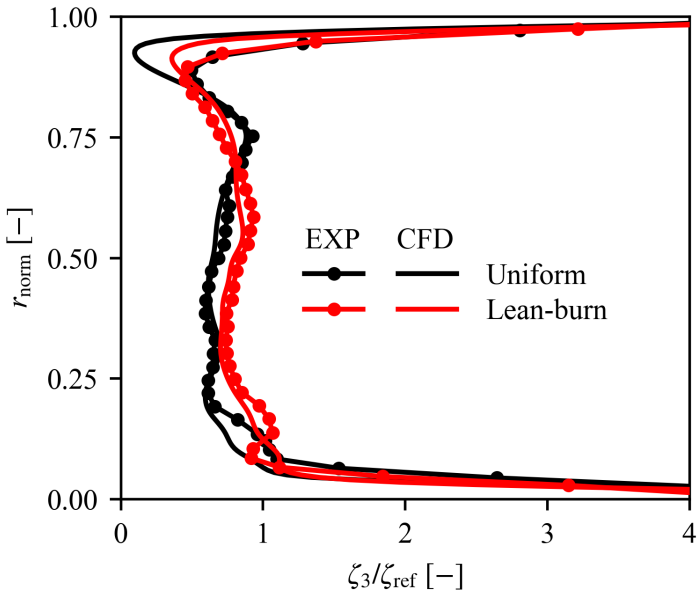


Figure 8.12: *Experimentally-measured and CFD-predicted radial distributions of normalized circumferentially-averaged KE loss coefficient (ζ_3/ζ_{ref}) at plane 4 (0.75 C_x), for uniform and lean-burn-representative inlet conditions.*

First, consider the experimentally-measured circumferentially-averaged KE loss coefficient under uniform inlet conditions. The radial distribution is relatively uniform between 20% and 65% span. The casing secondary flows manifests as a local maximum of KE loss around 75% span. Approaching the casing wall, KE loss reaches a minimum at 89% span, before steeply rising in the endwall boundary layer (95–100% span). The minimum appears to be associated with high total pressure casing platform coolant advected from upstream of the NGV, with the effect possibly being enhanced by radially-inward migration of the high-loss secondary flow core (away from the location of this minimum in loss). The hub secondary flow (in the range 10–15% span)—relatively mixed-out at plane 4—merges with the hub endwall boundary layer and is manifest as a weak peak in the profile in this span range.

Now consider the experimentally-measured circumferentially-averaged KE loss coefficient under simulated lean-burn inlet conditions. Relative to the uniform test case, KE loss increases between 15% and 70% span, whilst reducing below 15%, and above 70% span. This trend loosely corresponds to the total pressure non-uniformity at vane inlet. Indeed, noting that ζ_3 is defined relative to an ideal expansion from the *average* total pressure upstream of the vanes—given the same *absolute* total pressure loss as for the uniform test case—we would expect the circumferentially-averaged KE loss coefficient to decrease near the walls (elevated upstream p_0) and to increase around the midspan (lower-than average upstream p_0). In line with the analysis of

Figure 8.11, we see that the hub secondary flow is amplified with lean-burn inlet conditions, and the casing secondary flow is suppressed. This was explained by changes in span-wise loading distribution. The global minimum in loss at 89% span becomes deeper with lean burn inlet conditions, likely enhanced (in our definition of loss) due to slightly higher local upstream total pressure. Similarly, a local minimum develops around 10% span, likely caused by the hub peak in upstream total pressure. Endwall boundary layers were not significantly affected by lean-burn, except for a very subtle thinning at the hub.

Finally, consider the CFD predictions of circumferentially-averaged KE loss coefficient. In both cases, CFD predictions are in excellent agreement with experimental measurements in the region between 20% and 85% span. The CFD-predicted secondary flows at the hub appear somewhat over-mixed, and the depth of the minimum in loss at 89% span is overpredicted. Endwall boundary layers are also somewhat thinner than in experiments (i.e. undermixed). We conclude that BSL-ARSM predicts KE loss in the profile region very well, but is less accurate in high-gradient regions of secondary or endwall flow.

Axial development of integral kinetic energy loss

We conclude our analysis of NGV aerodynamic performance by investigating the effect of lean-burn inlet conditions on the integrated KE loss. Specifically, we examine the axial trends of the plane-averaged KE loss coefficient (ζ_4; definition of Lawaczeck [187]), and the mixed-out KE loss coefficient (ζ_5; Dzung mixing model [188, 189]). This data is shown in Figure 8.13. A profile–endwall decomposition of KE loss was not performed, considering possible ambiguity in mapping of upstream and downstream total pressures. Experimental data is reported at downstream planes 2, 3, and 4, and CFD trends were generated by sampling results at axial intervals of 0.014 C_x. All data were normalized by the reference KE loss coefficient, ζ_{ref}. Summary results are reported in Table 8.3.

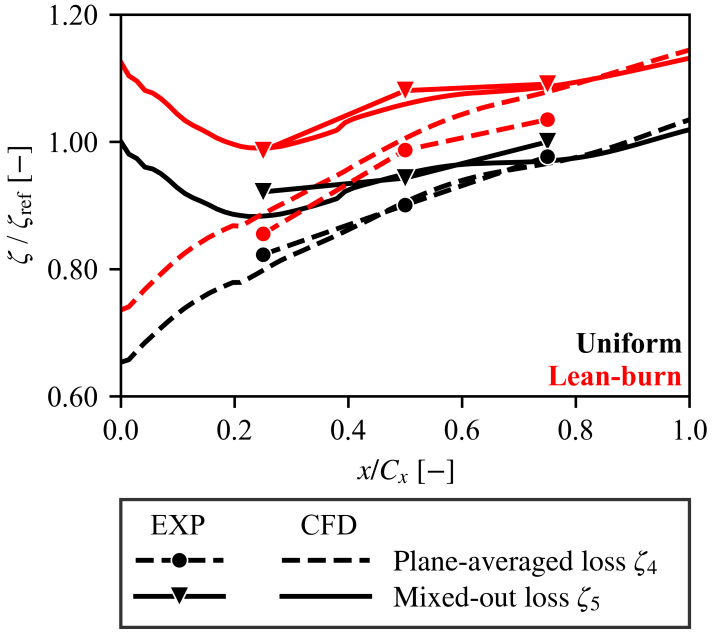


Figure 8.13: *Experimentally-measured and CFD-predicted axial development of normalized plane-averaged KE loss coefficient (ζ_4), and Dzung mixed-out KE loss coefficient (ζ_5) for uniform and simulated lean-burn inlet conditions.*

First, consider the experimentally-measured axial development of integral KE loss under uniform inlet conditions. The normalized *plane-averaged* KE loss coefficient is shown using circular markers and increases approximately linearly with axial distance. The plane-to-plane increase is caused by endwall boundary layer growth, and wake mixing losses. Consider also, the *mixed-out* KE loss coefficient, which is a measure of the KE loss associated with a flow that is hypothetically-mixed to a prescribed equilibrium state according to one-dimensional conservation laws. This offers a more rational comparison between two flows of differing states of local mixing. We see (as expected) that the mixed-out KE loss coefficient (triangular markers) is consistently greater than the corresponding plane-averaged KE loss for the uniform test case. With increasing axial distance, the plane-averaged trend approaches the mixed-out trend quasi-asymptotically indicating *realization* of mixing losses and reduction of flow secondary kinetic energy.

Now consider the experimentally-measured trends of plane-averaged and mixed-out KE loss coefficient under simulated lean-burn conditions. The trends are similar in shape to those for uniform flow, but with both the plane-averaged and mixed-out KE loss coefficients vertically offset from the trends of the uniform test case. Plane-averaged and mixed-out KE loss increased by 6.5% and 10.3%, respectively, on average across planes 2–4 (see summary in Table 8.3). The additional loss might be attributed to off-design flow incidence and greater turbulence intensity.

Now consider the CFD-predicted trends for the uniform and the lean-burn test cases. The CFD trends are in very good agreement with the experimental data, with plane-averaged and mixed-out KE loss increasing by 11.4% and 11.9%, respectively, under simulated lean-burn conditions. The CFD predictions were in good absolute agreement with experimental data, with average differences for plane-averaged KE loss of −1.2% and +3.3% for the uniform and the lean-burn test case, respectively.

Table 8.3: *Comparison of experimentally-measured and CFD-predicted normalized plane-averaged/mixed-out loss coefficients.*

	Plane 2	**Plane 3**	**Plane 4**
Uniform experiment	0.823/0.921	0.901/0.943	0.977/1.000
Lean-burn experiment	0.855/0.986	0.987/1.081	1.035/1.091
Uniform CFD	0.798/0.883	0.905/0.949	0.966/0.970
Lean-burn CFD	0.887/0.990	1.006/1.059	1.079/1.087
Hybrid case 1 CFD	0.873/0.975	0.985/1.038	1.059/1.067
Hybrid case 2 CFD	0.819/0.903	0.935/0.976	0.994/0.995

Separating mean-flow and turbulence effects

It is unclear from the simulations presented what proportion of the increase in overall KE loss is attributable to turbulence effects or mean flow effects (swirl, and total pressure non-uniformity). Two additional simulations were performed in an attempt to decouple these effects.

The additional simulations used hybrid boundary conditions, with the turbulence conditions at inlet swapped between the uniform and lean-burn test cases. Hybrid case 1 used the combustor simulator swirl, pressure, and temperature profiles, but with turbulence representative of the uniform inlet condition. Hybrid case 2 used uniform flow, but with turbulence representative of the lean-burn condition. The results are reported in Table 8.3, and show that between 74% and 82% of the additional losses are caused by mean-flow effects (swirl and total pressure distortion), with only 18% to 26% being related to turbulence. Critically, approximately 23% (or $0.026 \times \zeta_{\mathrm{ref}}$) of the additional losses occur *upstream of the vanes* due to the mixing-out of the non-uniform inlet profile. If these were accounted for as combustion losses (noting that the secondary kinetic energy that ultimately manifest as loss is associated with the combustor), the rise of the *experimentally-measured* plane-averaged and mixed-out KE loss coefficients due to lean burn falls to 3.6% and 7.8%, respectively.

The conclusion is that losses *attributable to interaction of the swirl and pressure profiles with the NGV* (as opposed to with the combustion profile mixing out) are relatively minor; an outcome supported by the results of Adams et al. [104]. This, of course, is for an NGV that was optimized for

uniform inlet flow. It is likely that there would be no (or very little) decrease in NGV performance for a vane optimized for lean-burn inlet conditions (see e.g. [56]).

Downstream thermal field

The effect of combined inlet swirl and temperature distortion on the downstream thermal field is now examined. The thermal field affects rotor-relative incidence angles, the thermal loading of the rotor, and unsteady temperature segregation effects. Experimentally-measured and CFD-predicted distributions of the normalized downstream total temperature (Θ_2) for the uniform and lean-burn-representative test cases are presented in Figure 8.14.

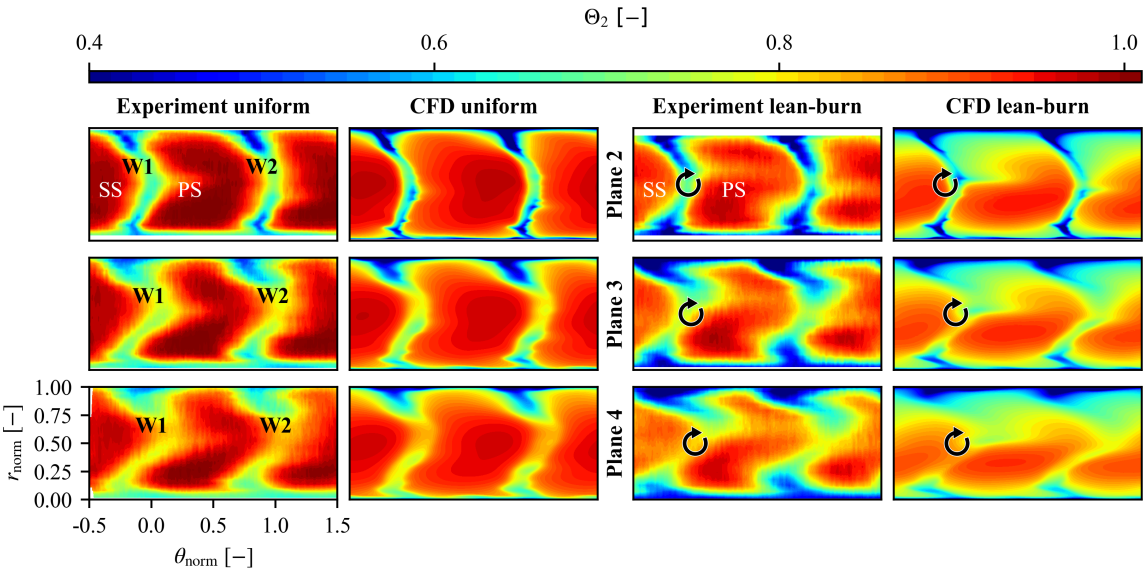


Figure 8.14: *Experimentally-measured and CFD-predicted downstream normalized total temperature (Θ_2) distributions at planes 2, 3, and 4, for both uniform and lean-burn-representative inlet conditions. Data are viewed from downstream. The circular arrows indicate the wakes of NGVs aligned with the swirler centerline.*

First consider the experimentally-measured distributions of Θ_2 for the uniform test case, shown in the first column of Figure 8.14. At plane 2 (first row), airfoil and TE slot coolant has developed into a *thermal wake* which follows the approximate shape of the corresponding aerodynamic wake. Cold layers at the hub and case endwalls correspond to platform coolant advected from upstream of the airfoils. Endwall coolant is rolled-up by secondary flows, which causes an accumulation of cold fluid around the junctions of the wakes with the wall. There are slight differences between the two wakes, related to differences in the cooling design (discussed previously): for example, W1 has slightly greater depth around the midspan, when compared to W2. By the same mechanisms as for the aerodynamic field, the thermal wakes distort and mix-out as they progress from plane 2 to planes 3, and 4. We also see radial spreading of the endwall coolant.

CFD simulations for uniform test case are shown in the second column. These are generally in excellent agreement with the experimental data (reproducing the W1–W2 variations reasonably well) but with a tendency to be overmixed, as evidenced by the wider thermal wakes, and the overpenetration of endwall coolant into the hot freestream.

Now consider the experimentally-measured distributions of Θ_2 with lean-burn-representative inlet conditions of swirl and inlet temperature distortion, shown in the third column of Figure 8.14. As discussed previously, we anticipate that the thermal field will be affected by internal and external coolant redistribution, enhanced mixing due to turbulence, and migration of the inlet temperature profile. At plane 2, the wakes have lower depth at midspan, but gradually broaden and increase in depth towards the endwalls. This combination is suggestive of superimposed *radial gradients* of total temperature, which are most likely the radially mixed-out inlet temperature profile. Freestream regions midway between wakes are noticeably colder across the full range of span. This is likely caused by partially mixed out combustor coolant transported into the freestream by the swirl pattern.

Consider now the experimentally-measured distributions of Θ_2 at planes 3 and 4 for lean-burn inlet conditions. The plane-to-plane circumferential migration and distortion pattern is determined by the mean flow and was similar to that of the aerodynamic wakes with lean-burn inlet conditions. Apparently colder endwalls at planes 3 and 4 is an artefact of the plane 2 data not being traversed so close to the wall. Another interesting difference is that W1 is more washed out around 40% span than W2, whereas the opposite was true with uniform inflow. This appears to be due to external migration of coolant, noting that W1 is narrower and shallower than W2 even at plane 2. The result is perhaps surprising, because the external surface streamline pattern was similar for both vanes (see Figure 8.5), but the effect on the downstream profile is clearly seen in both experimental and CFD results (considered now).

CFD simulations with simulated lean-burn are shown in the fourth column of Figure 8.14. They are generally in good agreement with the experimental data, but with a tendency to be overmixed. In the CFX solver, turbulent fluxes of the BSL-ARSM equations are modeled using the standard eddy viscosity instead of the effective eddy viscosity (see CFX solver theory guide). It remains unclear, however, whether this simplification extends to the turbulent enthalpy flux of the energy equation. Since the standard eddy viscosity is generally greater than the effective eddy viscosity, this could explain why the thermal wake was overmixed while the aerodynamic wake was not.

Thermal field development is now examined by considering the radial profiles of circumferentially mass-flux-weighted normalized total temperature. These are shown in Figure

8.15. Profiles are shown for uniform and lean-burn conditions at plane 4 alongside the corresponding inlet profiles at plane 1, and—for the lean-burn test case only—a profile taken at plane 1b (0.50 C_x upstream of LE; see Figure 8.2; from the study of Amend et al. [4]).

A direct comparison of inlet and outlet profiles requires equivalence of Θ_1 and Θ_2 definitions, which is satisfied when $T_{0b} = T_{0c}$ (i.e. when combustor and vane coolant temperatures are equal). For the purpose of discussion, this is assumed to hold true for the lean-burn case, noting however that in practice the cold stream temperatures can differ by up to 2 K. For the uniform test case, T_{0b} is undefined, and a normalization is performed assuming T_{0b} is equal to 293.15 K (approximate ambient conditions). Although this is a crude method, it helps illustrate the relative magnitude of the thermal deficits due to convective heat losses (uniform case) and explicit temperature distortion (lean-burn case).

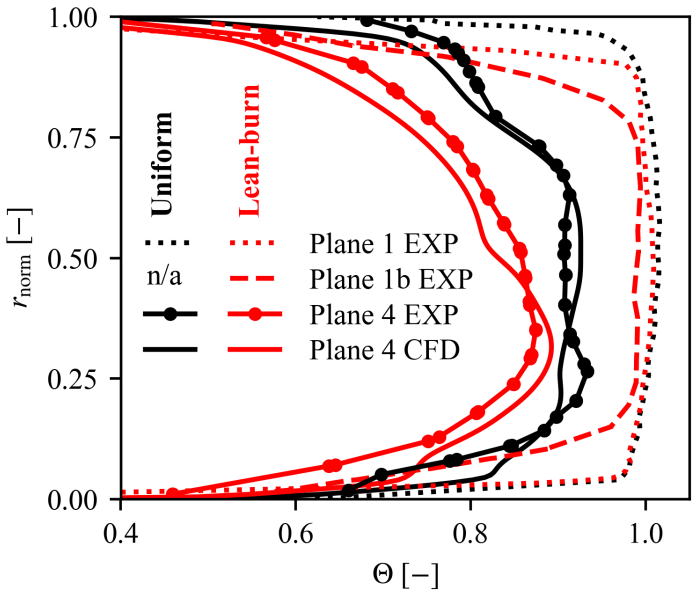


Figure 8.15: *Experimentally-measured and CFD-predicted radial distributions of circumferentially mass-flux-weighted normalized total temperature (Θ) at plane 1, plane 1b, and plane 4 for uniform and simulated lean-burn conditions.*

First consider the thermal field development under uniform inlet conditions. At inlet plane 1, the experimentally-measured total temperature (also used as a CFD inlet condition) is approximately constant between 5% and 95% span, with thermal boundary layers developing near the walls on account of heat losses to the test section walls. At downstream plane 4, experimentally-measured normalized total temperature is approximately constant between 20% and 65% span, but with a reduced value of $\Theta \approx 0.91$ (cf. $\Theta \approx 1.00$ at inlet). As previously discussed, this region is dominated by coolant ejected onto the vane surfaces and from TE slots. The cold regions approaching the endwalls (0–20%; 65–100% span) are caused by platform coolant. There is

evidence of radial spreading caused by diffusion and coolant wash-up local to secondary flows (see area maps in Figure 8.14). The integrated enthalpy deficit and spanwise penetration depth of the temperature deficit is greater at the casing, because the casing platform coolant mass flow is greater than that at the hub. CFD captures the spanwise temperature distribution reasonably well, but with small differences in high-gradient near-wall regions (differences in mixing rate).

Now consider the radial profiles of normalized total temperature under lean-burn inlet conditions. In the experimentally-measured inlet temperature profiles significant radial mixing occurs upstream of the NGV between plane 1 (dotted line) and plane 1b (dashed line). This leads to radial spreading of the hub and case coolant layers. This is accompanied by an increase in the near-wall temperature (expected based on energy-conservation argument). The *temperature deficit* between the profiles and a hypothetical line of $\Theta = 1$ increases, however, especially at the hub. Although on first inspection this seems to not satisfy energy conservation, the explanation is a simultaneous *reduction* of the near-wall mass-flux (coolant jets mixing-out *kinematically*). Because plane 1b has significantly greater mass flux uniformity than plane 1, downstream profiles are more easily compared to plane 1b.

Finally, consider the experimentally-measured plane 4 profile of Θ with lean-burn inlet conditions (circular markers). Compared to the uniform test case, normalized total temperature is globally lower, particularly in proximity to the endwalls. This is consistent with expectation based on superimposed inlet temperature distortion. A significant reduction of Θ between 25% and 70% span (i.e. where $\Theta \approx 1.00$ at plane 1b) indicates that the inlet temperature profile continues to mix radially throughout the vane passage. This effect is conflated with the coolant redistribution effect discussed earlier.

Separating effects on downstream thermal field due to inlet temperature profile migration and coolant migration

We attempt to decouple effects (on the downstream thermal field) associated with inlet temperature profile migration and swirl-induced coolant migration using additional uniform and lean-burn simulations with *constant inlet total temperature* (at plane 1) but otherwise nominal boundary conditions and coolant flows.

Here, we treat the non-dimensional total temperature field, Θ_2, as a hot gas ($\Theta_2 = 1$) with superposed effects due to two cold streams ($\Theta_2 = 0$). The cold streams represent the combustor coolant flow and vane coolant flow. We define their mass fractions as λ_b, and λ_c, respectively. In flows dominated by advection and mixing (as opposed to molecular conduction), it can be shown

that $\Theta_2 = 1 - \lambda_b - \lambda_c$. For *constant inlet total temperature* (hot stream only), λ_b is everywhere zero, meaning that thermal field non-uniformities arise from vane coolant migration/mixing alone (i.e. $\Theta_c = 1 - \lambda_c$). The value of λ_b can then be obtained by substitution i.e. $\lambda_b = \Theta_c - \Theta_2$. This approach is justified by the Munk and Prim [103] principle, according to which the streamline pattern is unaffected by a change in inlet temperature profile alone. The values of λ_c and λ_b are presented in Figure 8.16, where they are cast as equivalent non-dimensional total temperatures, $\Theta = 1 - \lambda$.

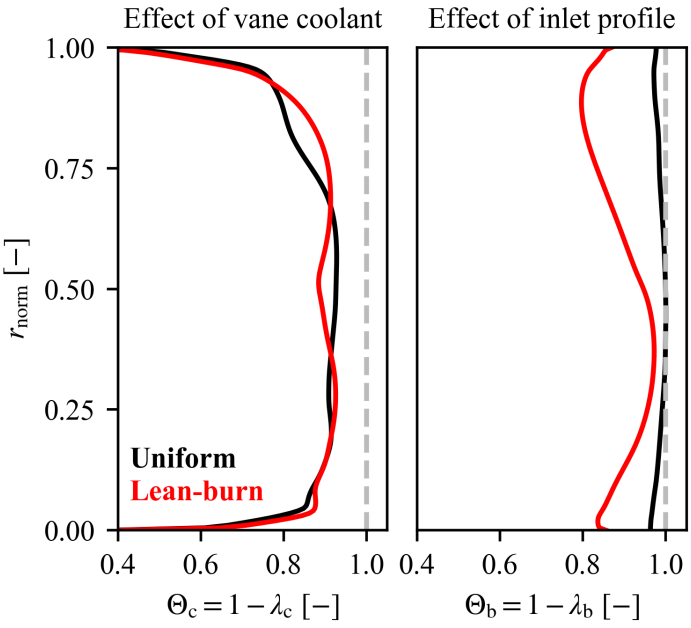


Figure 8.16: *CFD-predicted radial distributions of circumferentially mass-flux-averaged normalized total temperature at plane 4 arising from: vane coolant migration alone (Θ_c; left); inlet temperature profile migration alone (Θ_b; right).*

First consider the radial profiles of Θ_c obtained directly from the additional uniform and lean-burn CFD cases with *constant total temperature* at inlet, which are shown in the left subplot of Figure 8.16. We study these together to analyze swirl-induced coolant migration. With lean-burn, coolant migration leads to colder flow (higher coolant concentration) in the 35–65% span range, and warmer flow in the 20–35% and 65–95% span ranges (lower coolant concentration). These effects are associated with streamline convergence and divergence in the area profile.

Using the Munk and Prim superposition principle, we isolate the effect of combustor coolant (λ_b) by subtracting the temperature field under *nominal conditions* from that of the case with *constant inlet total temperature*: $\lambda_b = \Theta_c - \Theta_2$. The corresponding non-dimensional thermal field ($\Theta_b = 1 - \lambda_b$) is that which would hypothetically arise from *inlet temperature profile migration* alone, but accounting for *aerodynamic* interactions with the vane coolant flow.

Plane 4 radial distributions of Θ_b are shown in right subplot of Figure 8.16. For the uniform test case, the influence of the inlet profile is very subtle, with Θ_b decreasing slightly (by no more than 3.7%) towards the endwalls and reaching minima of 0.963 and 0.971 at 1% and 96% span, respectively. The effect occurs due to radial mixing of the upstream thermal boundary layers (see Figure 8.15). For lean-burn, the effect is more pronounced, with Θ_b decreasing at every spanwise location, compared to the uniform test case. This indicates that the influence of combustor coolant is felt across the entire span. As expected, the general distribution is for decreasing Θ_b in the near-wall regions. The slight increase in Θ_b in the very-near-wall region might be explained by the *aerodynamic* mass-displacement effect of platform cooling flow, which reduces interaction of near-wall inlet flow with the very-near-wall region (some interaction occurs through mixing). Θ_b reaches minima of 0.836 and 0.797 at 2% and 89% span, respectively.

We conclude that changes in the downstream thermal field are primarily driven by mixing-out of the inlet temperature profile, with only a secondary influence of coolant redistribution.

8.9 Conclusions

The effect of lean-burn combustor outlet flow on the aerothermal field development downstream of fully-cooled NGVs was investigated. Experiments were performed using real engine hardware. CFD simulations used fully-featured NGV geometry.

In some combustor–turbine interaction studies, there is significant sensitivity to vortex clocking, leading to adjacent passages having significantly different flow patterns. This is a characteristic of well-defined vortex formations of relatively small scale. In the current study, based on a lean-burn engine architecture, we found that the swirl pattern had primarily radial variation (individual vortices relatively mixed out) in swirl, and observed that both passages responded similarly (swirler-to-vane ratio of 1:2). This behavior has been seen in other studies (e.g. [104, 56]).

The effects of lean-burn inlet conditions on airfoil loading, coolant migration, and adiabatic film effectiveness were studied using CFD. Results were as follows:

i) The swirl-induced change of incidence caused normalized static pressure on both airfoils to rise on the lower PS and the upper SS. The upper PS, and lower SS experienced a reduction in pressure. This corresponds to increased loading in the lower half of the span, and decreased loading in the upper half.

ii) Individual cooling hole mass flow rates changed by as much as +19.1% and −14.2% with one standard deviation being ±5.4%.

iii) Row-wise coolant mass flow rates changed relatively little because the redistribution effect between holes was approximately antisymmetric about the midspan.

iv) Compared to uniform inflow, the surface streamline pattern exhibited significantly greater radial flow component in the LE region, had significantly converging flow (to around the 60% span region) on the PS, and mildly downwashing flow on the SS. This improved film-coverage around the stagnation line, reducing the peak adiabatic wall temperature around the LE. In the aft region of the vane, changes in individual film cooling mass flow rates and changes in surface coolant migration combined to give rise to significant spanwise variations in film coverage. Overall there was significant degradation of cooling performance with lean burn inlet conditions, partly due to poor film coverage (consequence of the vane being optimized for uniform inlet conditions), and possibly exacerbated by elevated freestream turbulence, which is known to increase the streamwise decay rates of cooling films.

The effects of lean-burn inlet conditions on downstream distributions of whirl angle, KE loss, and non-dimensional total temperature were studied experimentally and computationally. Results were as follows:

i) Experimentally-measured downstream whirl angle distributions were distorted in the direction of upstream swirl at a particular radial location. In general, this leads to higher whirl angle in the upper half of the span and lower whirl angle in lower half. A small radial band of underturned fluid near the casing opposed the expected trend due to swirl, and was linked to a local excess in the upstream total pressure (consistent with results of Adams et al. [104]). In the radial profiles, peak whirl angle increased by 2.7 degrees, and the minimum decreased by 2.6 degrees.

ii) Experimentally-measured distributions of KE loss showed significant circumferential stretching of the wakes due to the introduction of inlet swirl. The wakes also mixed-out more rapidly, due to the greater freestream turbulence and—in areas of overturning due to swirl—due to an increase in the plane-to-plane streamwise distance. Changes in aerodynamic loading amplified the hub secondary flow of both airfoils. Casing secondary flows were suppressed. Integral KE loss was quantified using plane-averaged and mixed-out KE loss coefficients, which were on average 3.6% and 7.8% greater with simulated lean-burn, after adjusting for differences in mixing losses that occur *upstream of the vanes*. If the loss that

occurs in the inlet field is not accounted for, the increase in loss with lean-burn increases to 6.5% and 10.3%, respectively.

iii) The analysis of the experimentally-measured thermal field revealed significant mixing of the inlet temperature profile, both upstream of the vanes, and throughout the vane passage. The thermal field also showed evidence of vane coolant redistribution, but this effect was small in comparison to the influence of the inlet temperature profile.

In terms of the performance of the CFD method we observe the following:

i) The BSL-ARSM turbulence model predicted downstream distributions of residual swirl, and KE loss very well. Despite using a steady turbulence modeling approach, aerodynamic wake mixing rates were surprisingly well matched to experiments. This is an artifact of the BSL-ARSM model, whereby wake decay is accelerated for large length scales and high turbulence intensity (see [7]). This happens for non-physical reasons, meaning it is unlikely to work *reliably* for a wide range of inlet boundary conditions.

ii) Predictions of the thermal field were qualitatively in good agreement with the experimental data but showed signs of overmixing. This contrasts with significant undermixing that is typical of simulations using the more common k–ω shear stress transport model. It seems that accurate prediction of the thermal field remains a significant challenge. From a practical standpoint, this might be addressed by carefully tuning the turbulent Prandtl number.

This study represents a comprehensive analysis of the impact of lean burn combustor flow on NGV performance, gives insight into the robustness of typical engine parts to inlet profile changes, and highlights areas for redesign to optimize for lean-burn profiles.

Nomenclature

Roman

C_x	Axial chord length	[m]
k	Turbulence kinetic energy	[m^2 s^{-2}]
ℓ	Turbulence/integral length scale	[m]
$\dot{m}$	Mass flow rate	[kg s^{-1}]
M	Mach number	[–]
p	Pressure	[Pa]
r	Radius	[m]
Re	Reynolds number	[–]
s	Streamwise distance	[m]
S	Swirl number	[–]
T	Temperature	[K]
V	Velocity magnitude	[m s^{-1}]
V_x	Axial velocity	[m s^{-1}]
V_r	Radial velocity	[m s^{-1}]
V_θ	Circumferential velocity	[m s^{-1}]
x	Axial coordinate	[m]

Greek

α	Absolute whirl angle	[°]
β	Absolute pitch angle	[°]
ϵ	Turbulence dissipation rate	[m^2 s^{-3}]
ζ_1	Local KE loss coefficient	[–]
ζ_3	Circumferentially-averaged KE loss coefficient	[–]
ζ_4	Plane-averaged KE loss coefficient	[–]
ζ_5	Mixed-out KE loss coefficient (Dzung method)	[–]
θ	Circumferential coordinate	[°]
Θ	Non-dimensional total temperature	[–]
λ	Cold gas mass fraction	[–]
τ	Integral time scale	[s]

Subscripts

0	Stagnation property
1	Upstream of NGV (plane 1)
2	Downstream of NGV (plane 2–4)
b	Related to the temperature distortion module
c	Related to the NGV coolant plenum
norm	Normalized by reference quantity
rake	Quantity as measured by upstream rake (plane 1)
w	Value at the (adiabatic) wall

9 | Conclusion

The conclusion is divided into three sections, summarizing important outcomes relating to: facility and equipment design (Chapters 3, 4, and 5); the effect of lean-burn on NGV aerothermal performance (Chapter 8); numerical modeling observations and recommendations for the types of flows studied in this work (Chapters 3, 6, 7, and 8).

9.1 Facility and equipment design

- Well-behaved combustor simulator exit flow was confirmed by traversing the NGV inlet datum plane from downstream *with the NGV removed*. This marks the successful commissioning of this module in the Engine Component AeroThermal (ECAT) facility.

- Because combustor simulator experiments were performed *with the NGV removed*, simulations were carried out to evaluate the influence of the NGV potential field. The potential field increased incidence onto the NGV, whereas the distributions of total pressure loss coefficient and non-dimensional total temperature were largely unaffected.

- At the NGV inlet plane, the combustor simulator vortex was circumferentially displaced from the swirler axis by approximately 3–4°. This emphasizes that geometric alignment with the swirler does not necessarily translate into aerodynamic alignment with the associated vortex. A possible mechanism for the circumferential migration effect was proposed.

- A dedicated upstream traverse system was designed, built, and commissioned to enable the measurement of inlet flow conditions *with vanes installed*. The new system proved itself a compact yet versatile drop-in solution, significantly expanding future testing capability.

- A detailed survey of the upstream flow was performed using the new traverse system. A key aspect of this endeavor was the experimental characterization of combustor simulator turbulence, which had not been considered as part of the initial commissioning tests.

- Upstream traverse measurements with a turbulence grid installed in place of the combustor simulator revealed significant flow non-uniformity at the NGV inlet plane. Using full-annulus simulations, this was traced to an unforeseen installation effect in the facility settling plenum.

- To mitigate this effect, the ECAT facility flow conditioning system was redesigned in collaboration with Matthew Stokes. Future modifications to the gas path should be evaluated using simulations spanning the *full annulus and axial extent* of the facility working section.

9.2 Impact of lean-burn on NGV performance

- The impact of lean-burn on NGV performance was studied for a leading-edge-clocked swirler configuration (2:1 NGV-to-swirler count) with co-rotating swirl (increased hub incidence). Because the combustor simulator vortex was relatively mixed-out, there was no obvious sensitivity of the NGV flow to the circumferential alignment relative to the swirler.

- The radial distribution of whirl angle downstream of the NGV was qualitatively similar to that under uniform inflow, but with superposed distortion according to the upstream direction of swirl. The maximum changes were +2.7°/−2.6°. A secondary underturning effect near the endwalls was associated with a local excess of total pressure in the upstream profile.

- Swirl-induced incidence amplified NGV secondary flow intensity at the hub, and reduced secondary flow intensity at the casing.

- The plane-averaged kinetic energy loss coefficient downstream of the NGV increased by 6.5%, compared to the uniform inflow baseline. Using simulations, it was estimated that inlet swirl and non-uniform total pressure were responsible for approximately three quarters of the increase, with the remaining quarter related to elevated freestream turbulence intensity.

- A significant proportion of the excess loss developed *upstream* of the NGV from mixing-out of the incoming combustor simulator flow. When this was accounted for as combustion loss, then the increase in loss due to lean burn decreased from +6.5% to +3.6%. Therefore, loss directly associated with the interaction between the swirl profile and the NGV flow was low.

- Lean-burn primarily affected the downstream thermal field through the direct transport and mixing of the inlet temperature profile, with a secondary influence from streamline convergence/divergence on the NGV pressure side, which caused film coolant to concentrate towards the midspan and dilute near the endwalls.

- Swirl-induced changes in vane loading caused the mass flow of individual film cooling holes to change by up to 19% in simulations. Because the effect was approximately anti-symmetric about the midspan, row-to-row and vane-to-vane coolant redistribution was minimal.

- Simulations predicted a decrease in area-averaged film effectiveness from 0.71 to 0.65. This was ascribed to poor film coverage on account of the altered surface streamline pattern, and was possibly exacerbated by elevated freestream turbulence, which accelerates film decay.

9.3 Numerical modeling observations and recommendations

- For the combustor simulator, the standard k–ϵ and k–ω shear stress transport (SST) models outperformed the Speziale-Sarkar-Gatski Reynolds stress model. Their seemingly superior accuracy is likely linked to the low swirl number of the flow (see Escue and Cui [144]).

- For an NGV flow with uniform inlet conditions, the k–ω SST model predicted a radial distribution of downstream whirl angle that fell within 1.6° of the experimentally-measured profile. Plane-averaged kinetic energy loss coefficient was under-predicted by 12% on average. Thermal field predictions were qualitatively in good agreement with measurements.

- Modeling film cooling holes using point sources should be avoided, because it couples momentum flux to the mesh resolution, and therefore tends to generate spurious losses. Short of fully resolving the internal cooling geometry, patch sources in the shape of the film cooling holes offer a good compromise between accuracy, and computational cost.

- Using the k–ω SST model, NGV aerodynamic and thermal wake width were underpredicted by 38% and 34% respectively, with corresponding overpredictions in wake depth of 45% and 53%. Undermixing appears to be a common problem in flows where unsteady vortex shedding occurs in reality, but is not modeled in simulations.

- For large freestream turbulence length scales, the shear stress limiter and zonal treatment of the k–ω SST model were shown to malfunction, resulting in excessively strict stress-limiting conditions in the freestream. It was argued that this could further contribute to undermixing.

- Various alternative limiter formulations were tested with regard to their effect on mixing and loss. As expected, the degree of mixing and integral loss increased as the limiter was relaxed.

- For large turbulence time scales in particular, the perfect coherence between the stress and strain tensors that is assumed by linear eddy viscosity models becomes physically unrealistic. This renders them susceptible to turbulence overproduction around the suction side crown.

- From the practical standpoint of tuning these models to match experiments more closely, this suggests a compromise needs to be struck between allowing sufficient stress (driving mixing and loss) and preventing run-away turbulence production. Even so, given the non-physical nature of the underlying Boussinesq hypothesis, any such model calibration would likely only be applicable to a specific family of NGV designs. It is inferred that NGV flows could stand to benefit from modeling freestream turbulence using scale-resolving methods.

References

[1] Ritchie, H., 2020. Climate change and flying: what share of global CO2 emissions come from aviation? Our World in Data, https://ourworldindata.org/co2-emissions-from-aviation [online resource].

[2] Grewe, V., Rao, A.G., Grönstedt, T., Xisto, C., Linke, F., Melkert, J., Middel, J., Ohlenforst, B., Blakey, S., Christie, S., Matthes, S., Dahlmann, K., 2021. Evaluating the climate impact of aviation emission scenarios towards the Paris agreement including COVID-19 effects. Nature Communications, Jun 2021, 12, doi:10.1038/s41467-021-24091-y.

[3] Liu, Y., Sun, X., Sethi, V., Nalianda, D., Li, Y.G., Wang, L., 2017. Review of modern low emissions combustion technologies for aero gas turbine engines. Progress in Aerospace Sciences, Oct 2017, 94, doi:10.1016/j.paerosci.2017.08.001.

[4] Amend, J., Lubbock, R., Ornano, F., Povey, T., 2023. Lean-burn combustor simulator for an engine-component test facility: an experimental and computational study. ASME J. Turbomach., Jun 2023, 145(6), doi:10.1115/1.4056387.

[5] Amend, J.E., Povey, T., 2022. Ultra-compact traverse system for transonic annular cascade. GPPS Chania22, Sep 12–14, 2022, Chania, Greece, paper no. GPPS-TC-2022-0017, doi:10.33737/gpps22-tc-17.

[6] Amend, J., Ornano, F., Chowdhury, N., Lubbock, R., Povey, T., 2024. Aerodynamic and thermal field development of cooled transonic HP NGV. ASME J. Turbomach., Feb 2024, 146(2), doi:10.1115/1.4063879.

[7] Amend, J., Povey, T., 2024. Comparison of eddy viscosity models for high turbulence NGV flows. Manuscript accepted for publication in the ASME J. Turbomach., paper no. TURBO-23-1103.

[8] International Air Transport Association, 2023. Fuel fact sheet.

[9] Zheng, X.S., Rutherford, D., 2020. Fuel burn of new commercial jet aircraft: 1960 to 2019. White paper of the International Council on Clean Transportation.

[10] International Civil Aviation Organization, 2022. Report on the feasibility of a long-term aspirational goal (LTAG) for international civil aviation CO_2 emission reductions.

[11] International Air Transport Association, 2021. Resolution on the industry's commitment to reach net zero carbon emissions by 2050.

[12] International Air Transport Association, 2023. Fact Sheet: EU and US policy approaches to advance SAF production.

[13] Schumann, U., 1997. The impact of nitrogen oxides emissions from aircraft upon the atmosphere at flight altitudes 8–15 km—results from the AERONOX project. Atmospheric Environment, Jun 1997, 31(12), doi:10.1016/S1352-2310(96)00326-3.

[14] Cumpsty, N. A., 1997. Jet Propulsion: A Simple Guide to the Aerodynamic and Thermodynamic Design and Performance of Jet Engines. Cambridge University Press, Cambridge, United Kingdom.

[15] Li, X., Sun, B., You, H., Wang, L., 2015. Evolution of Rolls-Royce air-cooled turbine blades and feature analysis. Procedia Engineering, 99, doi:10.1016/j.proeng.2014.12.689.

[16] Horlock, J.H., 2001. The basic thermodynamics of turbine cooling. ASME J. Turbomach., Jul 2001, 123(3), doi:10.1115/1.1370156.

[17] Wilcock, R.C., Young, J.B., Horlock, J.H., 2005. The effect of turbine blade cooling on the cycle efficiency of gas turbine power cycles. ASME J. Eng. Gas Turbines Power, Jan 2005, 127(1), doi:10.1115/1.1805549.

[18] Masiol, M., Harrison, R.M., 2014. Aircraft engine exhaust emissions and other airport-related contributions to ambient air pollution: a review. Atmospheric Environment, Oct 2014, 95, doi:10.1016/j.atmosenv.2014.05.070.

[19] Barrett, S.R.H., Britter, R.E., Waitz, I.A., 2010. Global mortality attributable to aircraft cruise emisisons. Environ. Sci. Tech., Oct 2010, 44(19), doi:10.1021/es101325r.

[20] Anenberg, S.C., Horowitz, L.W., Tong, D.Q., West, J.J., 2010. An estimate of the global burden of anthropogenic ozone and fine particulate matter on premature human mortality using atmospheric modeling. Environmental Health Perspectives, Sep 2010, 118(9), doi:10.1289/ehp.0901220.

[21] Kapadia, Z.Z., Spracklen, D.V., Arnold, S.R., Borman, D.J., Mann, G.W., Pringle, K.J., Monks, S.A., Reddington, C.L., Benduhn, F., Rap, A., Scott, C.E., Butt, E.W., Yoshioka, M., 2016. Impacts of aviation fuel sulfur content on climate and human health. Atmospheric Chemistry and Physics, 16(16), doi:10.5194/acp-16-10521-2016.

[22] Zhang, C., Stevenson, D., 2022. Characteristic changes of ozone and its precursors in London during COVID-19 lockdown and the ozone surge reason analysis. Atmospheric Environment, Mar 2022, 273, doi:10.1016/j.atmosenv.2022.118980.

[23] Bendtsen, K.M., Bengtsen, E., Saber, A.T., Vogel, U., 2021. A review of health effects associated with exposure to jet engine emissions in and around airports. Environmental Health, 20, doi:10.1186/s12940-020-00690-y.

[24] Lee, D.S., Fahey, D.W., Forster, P.M., Newton, P.J., Wit, R.C.N., Lim, L.L., Owen, B., Sausen, R., 2009. Aviation and global climate change in the 21st century. Atmospheric Environment, Jul 2009, 43(22–23), doi:10.1016/j.atmosenv.2009.04.024.

[25] Grewe, V., Matthes, S., Dahlmann, K., 2019. The contribution of NO_x emissions to climate change: are we ignoring methodological flaws? Envion. Res. Lett., Dec 2019, 14(12), doi:10.1088/1748-9326/ab5dd7.

[26] Terrenoire, E., Hauglustaine, D.A., Cohen, Y., Cozic, A., Valorso, R., Lefevre, F., Matthes, S., 2022. Impact of present and future aircraft NO_x and aerosol emissions on atmospheric composition and associated direct radiative forcing of climate. Atmos. Chem. Phys., 22(18), doi:10.5194/acp-22-11987-2022.

[27] Prather, M., Sausen, R., Grossmann, A.S., Haywood, J.M., Rind, D., Subbaraya, B.H., 1999. Potential climate change from aviation. Aviation and the Global Atmosphere. A Special Report of IPCC Working Groups I and III. Cambridge University Press, Cambridge, UK, pp. 185–215.

[28] Zhang, H., Shen, Z., Wei, X., Zhang, M., Li, Z., 2012. Comparison of optical properties of nitrate and sulfate aerosol and the direct radiative forcing due to nitrate in China. Atmospheric Research, 113, doi:10.1016/j.atmosres.2012.04.020.

[29] Hauglustaine, D.A., Balkanski, Y., Schulz, M., 2014. A global model simulation of present and future nitrate aerosols and their direct radiative forcing of climate . Atmospheric Chemistry and Physics, Oct 2014, 14(20), doi:10.5194/acp-14-11031-2014.

[30] Kärcher, B., 2018. Formation and radiative forcing of contrail cirrus. Nature Communications, May 2018, 9, doi:10.1038/s41467-018-04068-0.

[31] ICAO, 2023. Annex 16 - Environmental Protection - Volume II - Aircraft Engine Emissions, 5th edition.

[32] Miller, M., Brook, P., Eyers, C., 2009. Reduction of sulphur limits in aviation fuel standards (SULPHUR). EASA research project EASA.2008/C1.

[33] Lee, D.S., Allen, M.R., Cumpsty, N., Owen, B., Shine, K.P., Skowron, A., 2023. Uncertainties in mitigating aviation non-CO_2 emissions for climate and air quality using hydrocarbon fuels. Environ. Sci. Atmos., 2023, 3, doi:10.1039/D3EA00091E.

[34] Faber, J., Kiraly, J., Lee, D., Owen, B., O'Leary, A., 2022. Potential for reducing non-CO_2 emissions through clean jet fuel. CE Delft, report no. 22.210410.022.

[35] Wulff, A., Hourmouziadis, J., 1997. Technology review of aeroengine pollutant emissions. Aerospace Science and Technology, Dec 1997, 1(8), pp. 557–572, doi:10.1016/S1270-9638(97)90004-3.

[36] Lefebvre, A.H., Ballal, D.R., 2010. Gas turbine combustion: alternative fuels and emissions, third edition. CRC Press, ISBN:9781420086041.

[37] Saboohi, Z., Ommi, F., Fakhrtabatabaei, B., 2016. Development of an augmented conceptual design tool for aircraft gas turbine combustors. Int. Jnl. of Multiphysics, Mar 2016, 10(1), doi:10.21152/1750-9548.10.1.53.

[38] Diehl, L.A., Biaglow, J.A., 1974. Measurement of gaseous emissions from a turbofan engine at simulated altitude conditions. NASA Technical Memorandum X-3046, Lewis Research Center, Cleveland, Ohio, USA.

[39] Bulzan, D., Anderson, B., Wey, C., Howard, R., Winstead, E., Beyersdorf, A., Corporan, E., DeWitt, M.J., Klingshirn, C., Herndon, S., Miake-Lye, R., Timko, M., Wood, E., Tacina, K.M., Liscinsky, D., Hagen, D., Lobo, P., Whitefield, P., 2010. Gaseous and particulate emissions results of the NASA alternative aviation fuel experiment. ASME Turbo Expo, Jun 14–18, 2010, Glasgow, United Kingdom, paper no. GT2010-23524, doi:10.1115/GT2010-23524.

[40] Lefebvre, A.H., 1995. The role of fuel preparation in low emissions combustion. ASME Turbo Expo, Jun 5–8, 1995, Houston, Texas, USA, paper no. 95-GT-465, doi:10.1115/95-GT-465.

[41] Andrews, G.E., 2013. Ultra-low nitrogen oxides (NO_x) emissions combustion in gas turbine systems *in* Modern Gas Turbine Systems. Woodhead Publishing Limited, pp. 715–790, doi:10.1533/9780857096067.3.715.

[42] Miller, C.J., Prashanth, P., Allroggen, F., Grobler, C., Sabnis, J.S., Speth, R.L., Barrett, S.R.H., 2022. An environmental cost basis for regulating aviation NO_x emissions. Environ. Res. Commun., 4(5), doi:10.1088/2515-7620/ac6938.

[43] Bahr, D.W., 1982. HC and CO emissions abatement via selective fuel injection. ASME Turbo Expo, Apr 18–22, 1982, London, United Kingdom, paper no. 82-GT-178, doi:10.1115/82-GT-178.

[44] Foust, M.J., Thomsen, D., Stickles, R., Cooper, C., Dodds, W., 2012. Development of the GE Aviation low emissions TAPS combustor for next generation aircraft engines. 50th AIAA Aerospace Sciences Meeting, Jan 9–12, 2012, Nashville, Tennessee, USA, paper no. AIAA 2012-0936, doi:10.2514/6.2012-936.

[45] Gleason, C.C., Bahr, D.W., 1979. Experimental clean combustor program (ECCP). NASA Report no. CR-135384.

[46] Stickles, R., Barrett, J., 2013. TAPS II technology final report. Report prepared by General Electric for the Federal Aviation Administration, report no. DOT/FAA/AEE/2014-03.

[47] Mosier, S.A., Pierce, R.M., 1980. Advanced combustion systems for stationary gas turbine engines: volume I. Review and preliminary evaluation. Report prepared for the United States Environmental Protection Agency, report no. EPA-600/7-80-017a.

[48] McKinney, R.G., Sepulveda, D., Sowa, W., Cheung, A.K., 2007. The Pratt & Whitney TALON X low emissions combustor: revolutionary results with evolutionary technology. 45th AIAA Aerospace Sciences Meeting, Jan 8–11, 2007, Reno, Nevada, USA, paper no. AIAA 2007-386, doi:10.2514/6.2007-386.

[49] Haselbach, F., Parker, R., 2012. Hot end technology for advanced, low emission large civil aircraft engines. 28th International Congress of the Aeronautical Sciences, Sep 23–28, 2012, Brisbane, Australia.

[50] Lazik, W., Doerr, T., Bake, S., Bank, R., Rackwitz, L., 2008. Development of lean-burn low-NOx combustion technology at Rolls-Royce Deutschland. ASME Turbo Expo, Jun 9–13, 2008, Berlin, Germany, paper no. GT2008-51115, doi:10.1115/GT2008-51115.

[51] McGuirk, J.J., 2014. The aerodynamic challenges of aeroengine gas-turbine combustion systems. The Aeronautical Journal, Jun 2014, 118(1204), doi:10.1017/S0001924000009386.

[52] ICAO, 2023. Aircraft engine emissions databank, version 29B.

[53] Gupta, A.K., Lilley, D.G., Syred, N., 1984. Swirl flows. Gordon & Breach Science Publications, ISBN:9780996100427.

[54] Lucca-Negro, O., O'Doherty, T., 2001. Vortex breakdown: a review. Progress in Energy and Combustion Science, 2001, 27(4), doi:10.1016/S0360-1285(00)00022-8.

[55] Schroll, M., Doll, U., Stockhausen, G., Meier, U., Willert, C., Hassa, C., Bagchi, I., 2017. Flow field characterization at the outlet of a lean burn single-sector combustor by laser-optical methods. ASME J. Eng. Gas Turbines Power, Jan 2017, 139(1), doi:10.1115/1.4034040.

[56] Shahpar, S., Caloni, S., 2013. Aerodynamic optimization of high-pressure turbines for lean-burn combustion system. ASME J. Eng. Gas Turbines Power, May 2013, 135(5), doi:10.1115/1.4007977.

[57] Qureshi, I., Povey, T., 2011. A combustor-representative swirl simulator for a transonic turbine research facility. Journal of Aerospace Engineering, Jul 2011, 225(7), doi:10.1177/0954410011400817.

[58] Qureshi, I., Smith, A.D., Povey, T., 2013. HP vane aerodynamics and heat transfer in the presence of aggressive inlet swirl. ASME J. Turbomach., Mar 2013, 135(2), doi:10.1115/1.4006610.

[59] Koupper, C., Caciolli, G., Gicquel, L., Duchaine, F., Bonneau, G., Tarchi, L., Facchini, B., 2014. Development of an engine representative combustor simulator dedicated to hot streak generation. ASME J. Turbomach., Nov 2014, 136(11), doi:10.1115/1.4028175.

[60] Chevrier, M., Bertrand, H., 2017. Full Aero-thermal Combustor-Turbine interactiOn Research (FACTOR) - final publishable summary report.

[61] Beard, P.F., Adams, M.G., Nagawakar, J.R., Stokes, M.R., Wallin, F., Cardwell, D.N., Povey, T., Chana, K.S., 2019. The LEMCOTEC 1 1/2 stage film-cooled HP turbine: design, integration and testing in the Oxford Turbine Research Facility. Proceedings of the 13th European Conference on Turbomachinery Fluid Dynamics & Thermodynamics, Apr 8–12, 2019, Lausanne, Switzerland, paper no. ETC2019-216, doi:10.29008/ETC2019-216.

[62] Adams, M.G., Povey, T., Hall, B.F., Cardwell, D.N., Chana, K.S., Beard, P.F., 2020. Commissioning of a combined hot-streak and swirl profile generator in a transonic turbine test facility. Journal Eng. Gas Turbines Power, Mar 2020, 142(3), doi:10.1115/1.4044224.

[63] Adoua, R., Page, G.J., 2017. Effect of combustion on turbulence in a gas turbine combustion chamber. ASME Turbo Expo, Jun 26–30, 2017, Charlotte, North Carolina, USA, paper no. GT2017-64694, doi:10.1115/GT2017-64694.

[64] Cha, C.M., Hong, S., Ireland, P.T., Denman, P., Savarianandam, V., 2012. Experimental and numerical investigation of combustor–turbine interaction using an isothermal non-reacting tracer. ASME J. Eng. Gas Turbines Power, Aug 2012, 134(8), doi:10.1115/1.4005815.

[65] Doll, U., Stockhausen, G., Heinze, J., Meier, U., Hassa, C., Bagchi, I., 2017. Temperature measurements at the outlet of a lean burn single-sector combustor by laser optical methods. ASME J. Eng. Gas Turbines Power, Feb 2017, 139(2), doi:10.1115/1.4034355.

[66] Jianchen, W., Zhichao, W., Xin, H., Meng, H., Cunxi, L., Wenjie, T., 2023. The effects of fuel distribution on exit temperature distributio nin a centrally staged combustor. Physics of Fluids, Jun 2023, 35(6), doi:10.1063/5.0149820.

[67] Insinna, M., Salvadori, S., Martelli, F., 2014. Simulation of combustor/NGV interaction using coupled RANS solvers: validation and application to ta realistic test case. ASME Turbo Expo, Jun 16–20, 2014, Düsseldorf, Germany, paper no. GT2014-25433, doi:10.1115/GT2014-25433.

[68] Mazzei, L., Puggelli, S., Bertini, D., Andreini, A., Facchini, B., Vitale, I., Santoriello, A., 2019. Numerical and experimental investigation on an effusion-cooled lean burn aeronautical combustor: aerothermal field and emissions. ASME J. Eng. Gas Turbines Power, Apr 2019, 141(4), doi:10.1115/1.4041676.

[69] Barringer, M.D., Thole, K.A., Polanka, M.D., 2007. Experimental evaluation of an inlet profile generator for high-pressure turbine tests. ASME J. Turbomach., Apr 2007, 129(2), doi:10.1115/1.2436897.

[70] Huang, Y., Yang, V., 2005. Effect of swirl on combustion dynamics in a lean-premixed swirl-stabilized combustor. Proceedings of the Combustion Institute, Jan 2005, 30(2), doi:10.1016/j.proci.2004.08.237.

[71] Shi, L., Wu, P., Huang, H., Wang, C., Tan, X., Shen, Y., Song, J., 2023. Impact of swirling flow on the overall cooling effectiveness and TBCs insulation characteristics of turbine vane. Coatings, 13(11), doi:10.3390/coatings13111863.

[72] Greifenstein, M., Heinze, J., Willert, C., Voigt, L., Zedda, M., Richter, C., Dreizler, A., 2020. Time-resolved temperature profile measurements in the exhaust of a single sector gas turbine combustor at realistic operating conditions. Experiments in Fluids, 61, doi:10.1007/s00348-020-03011-8.

[73] Zimmermann, D.R., 1979. Laser anemometer measurements at the exit of a T63-C20 combustor. NASA Report no. CR-159623.

[74] Bicen, A.F., Tse, D., Whitelaw, J.H., 1988. Flow and combustion characteristics of an annular combustor. Combustion and Flame, May 1988, 72(2), doi:10.1016/0010-2180(88)90117-4.

[75] Cha, C.M., Ireland, P.T., Denman, P.A., 2012. Turbulence levels are high at the combustor–turbine interface. ASME Turbo Expo, Jun 11–15, 2012, Copenhagen, Denmark, paper no. GT2012-69130, doi:10.1115/GT2012-69130.

[76] Folk, M.B., 2019. The impact of combustor turbulence on loss mechanisms in the high pressure turbine. PhD thesis, Cambridge University, Cambridge, United Kingdom.

[77] Hassa, C., Voigt, L., Schroll, M., Heinze, J., Willert, C., Bagchi, I., 2018. Optische Messung von Geschwindigkeit und Temperatur am Austritt einer Magerbrennkammer unter realistischen Betriebsbedingunen. Deutscher Luft- und Raumfahrtkongress, Sep 4–6, 2018, Friedrichshafen, Germany, doi:10.25967/480105.

[78] Anacleto, P.M., Fernandes, E.C., Heitor, M.V., Shtork, S.I., 2003. Swirl flow structure and flame characteristics in a model lean premixed combustor. Combust. Sci. and Tech. 175(8), doi:10.1080/00102200390218859.

[79] Terhaar, S., Oberleithner, K., Paschereit, C.O., 2015. Key parameters governing the precessing vortex core in reacting flows: an experimental and analytical study. Proceedings of the Combustion Institute, 2015, 35(3), doi:10.1016/j.proci.2014.07.035.

[80] Oberleithner, K., Terhaar, S., Rukes, L., Paschereit, C.O., 2013. Why non-uniform density suppresses the precessing vortex core. J. Eng. Gas Turbines Power, Dec 2013, 135(12), doi:10.1115/1.4025130.

[81] Povey, T., Qureshi, I., 2009. Developments in hot-streak simulators for turbine testing. ASME J. Turbomach., Jul 2009, 131(3), doi:10.1115/1.2987240.

[82] Ames, F.E., Plesniak, M.W., 1997. The influence of large-scale high-intensity turbulence on vane aerodynamic losses, wake growth, and the exit turbulence parameters. ASME J. Turbomach., Apr 1997, 119(2), doi:10.1115/1.2841100.

[83] Folk, M., Miller, R.J., Coull, J.D., 2020. The impact of combustor turbulence on turbine loss mechanisms. ASME J. Turbomach., Sep 2020, 142(9), doi:10.1115/1.4047615.

[84] Giller, L., Schiffer, H.P., 2012. Interactions between the combustor swirl and the high pressure stator of a turbine. ASME Turbo Expo, Jun 11–15, 2012, Copenhagen, Denmark, paper no. GT2012-69157, doi:10.1115/GT2012-69157.

[85] Krichbaum, A., Werschnik, H., Wilhelm, M., Schiffer, H.P., Lehmann, K., 2015. A large scale turbine test rig for the investigation of high pressure turbine aerodynamics and heat transfer with variable inflow conditions. ASME Turbo Expo, Jun 15–19, 2015, Montreal, Canada, paper no. GT2015-43261, doi:10.1115/GT2015-43261.

[86] Luque, S., Kanjirakkad, V., Aslanidou, I., Lubbock, R., Rosic, B., Uchida, S., 2015. A new experimental facility to investigate combustor–turbine interactions in gas turbines with multiple can combustors. ASME J. Eng. Gas Turbines Power, May 2015, 137(5), doi:10.1115/1.4028714.

[87] Hong, Y., Yanmin, Q., Jing, R., Hongde, J., 2013. Effect of inlet swirl on the model leading edge of turbine vane. ASME Turbo Expo, Jun 3–7, 2013, San Antonio, Texas, USA, paper no. GT2013-94471, doi:10.1115/GT2013-94471.

[88] Bacci, T., Caciolli, G., Facchini, B., Tarchi, L., Koupper, C., Champion, J.-L, 2015. Flowfield and temperature profiles measurements on a combustor simulator dedicated to hot streaks generation. ASME Turbo Expo, Jun 15–19, 2015, Montreal, Quebec, Canada, paper no. GT2015-42217, doi:10.1115/GT2015-42217.

[89] Bacci, T., Facchini, B., Picchi, A., Tarchi, L., Koupper, C., Champion, J.-L., 2015. Turbulence field measurements at the exit of a combustor simulator dedicated to hot streaks generation. ASME Turbo Expo, Jun 15–19, 2015, Montreal, Quebec, Canada, paper no. GT2015-42218, doi:10.1115/GT2015-42218.

[90] Krumme, A., Tegeler, M., Gattermann, S., 2019. Design, integration and operation of a rotating combustor-turbine-interaction test rig within the scope of EC FP7 project FACTOR. 13th European Conference on Turbomachinery Fluid Dynamics & Thermodynamics, Apr 8–12, 2019, Lausanne, Switzerland, paper no. ETC2019-035, doi:10.29008/etc2019-035.

[91] Wolf, T., Lehmann, K., Willer, L., Pahs, A., Rößling, M., Dorn, L., 2017. Interturb: high-pressure turbine rig for the investigation of combustor-turbine interaction. ASME Turbo Expo, June 26–30, 2017, Charlotte, North Carolina, USA, paper no. GT2017-64153, doi:10.1115/GT201764153.

[92] Hall, B.F., Povey, T., 2015. Experimental study of a non-reacting low NOx combustor simulator for scaled turbine experiments. ASME Turbo Expo, Jun 15–19, 2015, Montreal, Quebec, Canada, paper no. GT2015-43530, doi:10.1115/GT2015-43530.

[93] Notaristefano, A., Gaetani, P., 2020. Design and commissioning of a combustor simulator combining swirl and entropy wave generation. Int. J. Turbomach. Propuls. Power, 5(4), doi:10.3390/ijtpp5040027.

[94] Soares, C., 2015. Gas turbines - a handbook of air, land, and sea applications, 2nd edition. Butterworth-Heinemann, Kidlington, UK, ISBN:9780124104617.

[95] Vagnoli, S., Verstraete, T., 2015. Numerical study of the combustor–turbine interaction using coupled unsteady solvers. 22nd International Symposium on Air Breathing Engines, Oct 25–30, 2015, Phoenix, Arizona, USA, paper no. ISABE2015-20179.

[96] Beard, P.F., Smith, A.D., Povey, T., 2014. Effect of combustor swirl on transonic high pressure turbine efficiency. ASME J. Turbomach., Jan 2014, 136(1), doi:10.1115/1.4024841.

[97] Johansson, M., Povey, T., Chana, K., Abrahamsson, H., 2017. Effect of low-NOx, combustor swirl clocking on intermediate turbine duct vane aerodynamics with an upstream high pressure turbine stage—an experimental and computational study. ASME J. Turbomach., Jan 2017, 139(1), doi:10.1115/1.4034311.

[98] Schmid, G., Krichbaum, A., Werschnik, H., Schiffer, H.P., 2014. The impact of realistic combustor swirl in a 1 1/2 stage axial turbine. ASME Turbo Expo, Jun 16–20, Düsseldorf, Germany, paper no. GT2014-26716, doi:10.1115/GT2014-26716.

[99] Werschnik, H., Schneider, M., Herrmann, J., Ivanov, D., Schiffer, H.P., Lyko, C., 2017. The influence of combustor swirl on pressure losses and the propagation of coolant flows at the large scale turbine rig (LSTR): experimental and numerical investigation. Int. J. Turbomach. Propuls. Power, Aug 2017, 2(3), doi:10.3390/ijtpp2030012.

[100] Werschnik, H., Hilgert, J., Wilhelm, M., Bruschewski, M., Schiffer, H.P., 2017. Influence of combustor swirl on endwall heat transfer and adiabatic effectiveness at the large scale turbine rig. ASME J. Turbomach., Aug 2017, 139(8), doi:10.1115/1.4035832.

[101] Sen, B., Schmidt, L., Bogard, D.G., 1996. Film cooling with compound angle holes: heat transfer. ASME J. Turbomach., Oct 1996, 118(4), doi:10.1115/1.2840937.

[102] Wilhelm, M., Schmidt, M., Goertz, F., Schiffer, H.P., Lyko, C., 2017. Influence of combustor swirl on turbulence at the large scale turbine rig. 23rd International Symposium on Air Breathing Engines, Sep 3–8, 2017, Manchester, UK, paper no. ISABE-2017-21393.

[103] Munk, M., Prim, R., 1947. On the multiplicity of steady gas flows having the same streamline pattern. National Academy of Sciences of the USA, May 1947, 33(5), doi:10.1073/pnas.33.5.137.

[104] Adams, M.G., Beard, P.F., Stokes, M.R., Wallin, F., Chana, K.S., Povey, T., 2021. Effect of a combined hot streak and swirl profile on cooled 1.5-stage turbine aerodynamics: an experimental and computational study. ASME J. Turbomach., Feb 2021, 143(2), doi:10.1115/1.4049103.

[105] Kerrebrock, J. L., Mikolajczak, A. A., 1970. Intra-stator transport of rotor wakes and its effects on compressor performance. ASME J. Engineering for Power, Oct 1970, 92(4), doi:10.1115/1.3445365.

[106] Khanal, B., He, L., Northall, J., Adami, P., 2013. Analysis of radial migration of hot-streak in swirling flow through high-pressure turbine stage. ASME J. Turbomach., Jul 2013, 135(4), doi:10.1115/1.4007505.

[107] Bacci, T., Lenzi, T., Picchi, A., Mazzei, L., Facchini, B., 2019. Flow field and hot streak migration through high pressure cooled vanes with representative lean burn combustor outflow. ASME J. Eng. Gas Turbines Power, Apr 2019, 141(4), doi:10.1115/1.4040714.

[108] Krumme, A., Buske, C., Bachner, J.R., Dähnert, J., Tegeler, M., Ferraro, F., Gövert, S., Kocian, F., di Mare, F., Pahs, A., 2019. Investigation of combustor-turbine-interaction in a rotating cooled transonic high-pressure turbine test rig: part 1 — experimental results. ASME Turbo Expo, Jun 17–21, 2019, Phoenix, Arizona, USA, paper no. GT2019-90733, doi:10.1115/GT2019-90733.

[109] Gövert, S., Ferraro, F., Krumme, A., Buske, C., Tegeler, M., Kocian, F., di Mare, F., 2019. Investigation of combustor-turbine-interaction in a rotating cooled transonic high-pressure turbine test rig: part 2 — numerical modelling and simulation. ASME Turbo Expo, Jun 17–21, 2019, Phoenix, Arizona, USA, paper no. GT2019-90736, doi:10.1115/GT2019-90736.

[110] Flaszynski, P., Piotrowicz, M., Bacci, T., 2021, Clocking and potential effects in combustor–turbine stator interactions. Aerospace, 2021, 8(10), doi:10.3390/aerospace8100285.

[111] Mansouri, Z., Jefferson-Loveday, R., 2022. Heat transfer characteristics of a high-pressure turbine under combined distorted hot-streak and residual swirl: an unsteady computational study. Int. J. Heat Mass Transfer, Oct 2022, 195, doi:10.1016/j.ijheatmasstransfer.2022.123143.

[112] Griffini, D., Insinna, M., Salvadori, S., Martelli, F., 2016. Clocking effects of inlet nonuniformities in a fully cooled high-pressure vane: a conjugate heat transfer analysis. ASME J. Turbomach., Feb 2016, 138(2), doi:10.1115/1.4031864.

[113] Bacci, T., Becchi, R., Picchi, A., Facchini, B., 2019. Adiabatic effectiveness on high-pressure turbine nozzle guide vanes under realistic swirling conditions. ASME J. Turbomach., Jan 2019, 141(1), doi:10.1115/1.4041559.

[114] Rahim, A., He, L., Romero, E., 2014. Rotor blade heat transfer characteristics for high pressure turbine stage under inlet temperature and velocity traverses. ASME Turbo Expo, Jun 16–20, Düsseldorf, Germany, paper no. GT2014-26832, doi:10.1115/GT2014-26832.

[115] Jeon, J., Son, C., Kim, J., 2021. Influence of swirl clocking on the performance of turbine stage with three-dimensional nozzle guide vane. Energies, 14(17), doi:10.3390/en14175503.

[116] Li, Y., Su, X., Yuan, X., 2019. The effect of mismatching between combustor and HP vanes on the aerodynamics and heat load in a 1-1/2 stages turbine. Aerospace Science and Technology, Mar 2019, 86, doi:10.1016/j.ast.2018.12.023.

[117] Pyliouras, S., Schiffer, H.P., Janke, E., Willer, L., 2012. Effects of non-uniform combustor exit flow on turbine aerodynamics. ASME Turbo Expo, Jun 11–15, 2012, Copenhagen, Denmark, paper no. GT2012-69327, doi:10.1115/GT2012-69327.

[118] Wang, Z., Wang, D., Wang. Z., Feng, Z., 2018. Heat transfer analyses of film-cooled HP turbine vane considering effects of swirl and hot streak. Applied Thermal Engineering, Sep 2018, 142, doi:10.1016/j.applthermaleng.2018.07.044.

[119] Shang, T., Epstein, A.H., 1997. Analysis of hot streak effects on turbine rotor heat load. ASME J. Turbomach., Jul 1997, 119(3), doi:10.1115/1.2841156.

[120] Lubbock, R.J., Oldfield, M.L.G., 2018. Turbulent velocity and pressure fluctuations in gas turbine combustor exit flows. J. Power Energy, Jun 2018, 232(4), doi:10.1177/0957650917732885.

[121] Kirollos, B., Lubbock, R., Beard, P.F., Goenaga, F., Rawlinson, A., Janke, E., Povey, T., 2017. ECAT: an engine component aerothermal facility at the University of Oxford. ASME Turbo Expo, Jun 26–30, 2017, Charlotte, North Carolina, USA, paper no. GT2017-64736, doi:10.1115/GT2017-64736.

[122] Barringer, M., Thole, K.A., Polanka, M.D., 2004. Developing a combustor simulator for investigating high pressure turbine aerodynamics and heat transfer. ASME Turbo Expo, Jun 14–17, 2004, Vienna, Austria, paper no. GT2004-53613, doi:10.1115/GT2004-53613.

[123] Cresci, I., Ireland, P.T., Bacic, M., Tibbott, I., Rawlinson, A., 2015. Realistic velocity and turbulence intensity profiles at the combustor-turbine interaction (CTI) plane in a nozzle guide vane test facility. 11th European Conference on Turbomachinery Fluid Dynamics & Thermodynamics, Mar 23–27, 2015, Madrid, Spain, paper no. ETC2015-255.

[124] Qureshi, I., Beretta, A., Chana, K.S., Povey, T., 2012. Effect of aggressive inlet swirl on heat transfer and aerodynamics in an unshrouded transonic HP turbine. ASME J. Turbomach., Nov 2012, 134(6), doi:10.1115/1.4004876.

[125] Duchaine, F., Dombard, J., Gicquel, L., Koupper, C., 2017. Integrated large eddy simulation of combustor and turbine. ASME Turbo Expo, Jun 26–30, 2017, Charlotte, North Carolina, USA, paper no. GT2017-63473, doi:10.1115/GT2017-63473.

[126] Rehder, H.J., Pahs, A., Bittner, M., Kocian, F., 2017. Next generation turbine testing at DLR. ASME Turbo Expo, Jun 26–30, 2017, Charlotte, North Carolina, USA, paper no. GT2017-64409, doi:10.1115/GT2017-64409.

[127] Hall, B.F., Chana, K.S., Povey, T., 2014. Design of a non-reacting combustor simulator with swirl and temperature distortion with experimental validation. J. Eng. Gas Turbines Power, Aug 2014, vol. 136(8), doi:10.1115/1.4026809.

[128] Koupper, C., Gicquel, L., Duchaine, F., Bacci, T., Facchini, B., Picchi, A., Tarchi, L., Bonneau, G., 2016. Experimental and numerical calculation of turbulent timescales at the exit of an engine representative combustor simulator. ASME J. Eng. Gas Turbines Power, Feb 2016, 138(2), doi:10.1115/1.4031262.

[129] Koupper, C., Bonneau, G., Gicquel, L., Duchaine, F., 2016. Large eddy simulations of the combustor turbine interface: study of the potential and clocking effects. ASME Turbo Expo, Jun 13–17, 2016, Seoul, South Korea, paper no. GT2016-56443, doi:10.1115/GT2016-56443.

[130] Bacci, T., Picchi, A., Lenzi, T., Facchini, B., 2019. Turbulence intensity measurements across a NGV cooled cascade with representative lean burn combustor outflow. 13th European Conference on Turbomachinery Fluid Dynamics & Thermodynamics, Apr 8–12, 2019, Lausanne, Switzerland, paper no. ETC2019-100, doi:10.29008/ETC2019-100.

[131] Messenger, A., Povey, T., 2020. Calibrated low-order transient thermal and flow models for robust test facility design. Journal of the Global Power and Propulsion Society, 2020, 4, doi:10.33737/jgpps/122270.

[132] Povey, T., Qureshi, I., 2008. A hot-streak (combustor) simulator suited to aerodynamic performance measurements. Journal of Aerospace Engineering, Jun 2008, 222(6), doi:10.1243/09544100JAERO363.

[133] Chaluvadi, V.S.P., Kalfas, A.I., Banieghbal, M.R., Hodson, H.P., Denton, J.D., 2001. Blade-row interaction in a high-pressure turbine. J. Propulsion Power, Aug 2001, 17(4), doi:10.2514/2.5821.

[134] Kilik, E., 1976. The influence of swirler design parameters on the aerodynamics of downstream recirculation region. PhD thesis, Cranfield University, Cranfield, United Kingdom.

[135] Chigier, N.A., Beer, J.M., 1964. Velocity and static-pressure distributions in swirling air jets issuing from annular and divergent nozzles. ASME J. Fluids Eng., Dec 1964, 86(4), doi:10.1115/1.3655954.

[136] Burdett, D., Povey, T., 2022. Experimental and numerical analysis of loss characteristics of cooled transonic nozzle guide vanes. ASME J. Turbomach., May 2022, 144(5), doi:10.1115/1.4053019.

[137] Michaud, M., Jackson, D., Goenaga, F., Povey, T., 2023. Experimental study of impact of in-service deterioration on aerodynamic performance of high-pressure nozzle guide vanes. ASME J. Turbomach., Jun 2023, 145(6), doi:10.1115/1.4056774.

[138] Burdett, D., Lubbock, R.J., Povey, T., 2018. An impulse response technique to improve the effective frequency response of pressure probes. 24th Symposium on Measuring Techniques in Turbomachinery, Aug 30–31, 2018, Prague, Czech Republic, paper no. MTT2418B23.

[139] Paniagua, G., Dénos, R., Oropesa, M., 2002. Thermocouple probes for accurate temperature measurements in short duration facilities. ASME Turbo Expo, Jun 3–6, 2002, Amsterdam, The Netherlands, paper no. GT2002-30043, doi:10.1115/GT2002-30043.

[140] Carslaw, H.S., Jaeger, J.C., 1959. Conduction of heat in solids (2nd edition). Oxford University Press, London, United Kingdom.

[141] Wilcox, D.C., 2006. Turbulence Modeling for CFD (3rd edition). DCW Industries, 5354 Palm Drive, La Cañada, California 91011, USA, ISBN:9781928729082.

[142] Menter, F.R., 1994. Two-equation eddy-viscosity turbulence models for engineering applications. AIAA Journal, Aug 1994, 32(8), doi:10.2514/3.12149.

[143] Speziale, C.G., Sarkar, S., Gatski, T.B., 1991. Modelling the pressure-strain correlation of turbulence: an invariant dynamical systems approach. Journal of Fluid Dynamics, Jun 1991, 227, doi:10.1017/S0022112091000101.

[144] Escue, A., Cui, J., 2010. Comparison of turbulence models in simulating swirling pipe flows. Applied Mathematical Modelling, Oct 2010, 34(10), doi:10.1016/j.apm.2009.12.018.

[145] Denton, J.D., 1993. Loss mechanisms in turbomachines. ASME Turbo Expo, May 24–27, 1993, Cincinnati, Ohio, USA, paper no. 93-GT-435, doi:10.1115/93 GT 435.

[146] Michaud, M., Chowdhury, N., Povey, T., 2023. Experimental study of impact of in-service deterioration on thermal performance of high-pressure nozzle guide vanes. ASME J. Turbomach., Feb 2023, 145(2), doi:10.1115/1.4055864.

[147] Burdett, D., Povey, T., 2022. Experimental and numerical analysis of loss characteristics of cooled transonic nozzle guide vanes. ASME J. Turbomach., May 2022, 144(5), doi:10.1115/1.4053019.

[148] Atkins, N.R., Ainsworth, R.W., Harvey, N.W., 2007. Aerodynamic performance measurement in a fully scaled transient turbine test facility. ASME Turbo Expo, May 14–17, 2007, Montreal, Canada, paper no. GT2007-27142, doi:10.1115/GT2007-27142.

[149] Cernat, B.C., Lavagnoli, S., 2021. Experimental investigation of tip design effects on the unsteady aerodynamics and heat transfer of a high speed turbine. ASME J. Turbomach., accepted manuscript, doi:10.1115/1.4050443.

[150] Dahlqvist, J., Fridh, J., Fransson, T., 2014. Test turbine instrumentation for cavity purge investigations. The XXII Symposium on Measuring Techniques in Turbomachinery, Sep 4-5, 2014, Lyon, France.

[151] Wolf, T., Janke, E., Benton, R., Kost, F., Haselbach, F., Gegg, S., 2011. Design and test of a highly loaded single-stage high pressure turbine. ASME Turbo Expo, June 6–10, 2011, Vancouver, British Columbia, Canada, paper no. GT2011-45342, doi:10.1115/GT2011-45342.

[152] Cuadrado, D.G., Aye-Addo, P.A.N., Andreoli, V., Bhatnagar, L., Lozano, F., Fisher, J., Paniagua, G., Saavedra, J., Inman, D., Meyer, T., Bloxham, M., Clemens, E., Stults, B., White, T., Wallace, A., Johnson, D., 2019. Purdue small turbine aerothermal rotating rig (STARR). AIAA Propulsion and Energy Forum, Aug 19-22, 2019, Indianapolis, Indiana, USA, doi:10.2514/6.2019-4004.

[153] Bhatnagar, L., Paniagua, G., Cuadrado, D.G., Aye-Addo, P.A.N., Castillo Sauca, A., Lozano, F., Bloxham, M., 2022. Uncertainty in high-pressure stator performance measurement in an annular cascade at engine-representative Reynolds and Mach. ASME J. Eng. Gas Turbines Power, Feb 2022, 144(2), doi:10.1115/1.4052385.

[154] Bohn, D., Funke, H., Gier, J., 1999. Numerical and experimental investigations on the flow in a 4-stage turbine with special focus on the development of a radial temperature streak. ASME Turbo Expo, Jun 7–10, 1999, Indianapolis, Indiana, USA, paper no. 99-GT-027, doi:10.1115/99-GT-027.

[155] Anthony, R.J., Clark, J.P., 2013. A review of the AFRL turbine research facility. ASME Turbo Expo 2013, Jun 3–7, 2013, San Antonio, Texas, USA, paper no. GT2013-94741, doi:10.1115/GT2013-94741.

[156] Sieverding, C.H., Arts, T., 1992. The VKI compression tube annular cascade facility CT3. ASME Turbo Expo 1992, June 1–4, 1992, Cologne, Germany, paper no. 92-GT-336, doi:10.1115/92-GT-336.

[157] Jonsson, I., Chernoray, V., Rojo, B., 2018. Surface roughness impact on secondary flow and losses in a turbine exhaust casing. ASME Turbo Expo, Jun 11–15, 2018, Oslo, Norway, paper no. GT2018-75541, doi:10.1115/GT2018-75541.

[158] Jonsson, I., 2021. Experimental study of internal jet engine structures, PhD thesis, Department of Mechanics and Maritime Sciences, Chalmers University of Technology, Göteborg, Sweden, Ny serie nr 2021:5049.

[159] Martinez-Botas, R.F., Main, A.J., Lock, G.D., Jones, T.V., 1993. A cold heat transfer tunnel for gas turbine research on an annular cascade. ASME Turbo Expo, May 24–27, 1993, Cincinnati, Ohio, paper no. 93-GT-248, doi:10.1115/93-GT-248.

[160] Mashburn, D.N., Stevens, R.H., Woodall, H.C., 1977. Traverse probe system. USA patent no. US4016768A.

[161] Singh, B.B.M., Joshy, J., Rao, P.S., 2021. Probe-based circumferential traversing system. USA patent no. US11187560B2, publication no. WO2021067083A1.

[162] Wittig, J.M., 1976. Probe mechanism for three dimensional investigation of conditions in a fluid flow. USA patent no. US3977249.

[163] Lepicovsky, J., 2003. Application of a split-fiber probe to velocity measurement in the NASA research compressor. ASME/JSME 4th Joint Fluids Summer Engineering Conference, Jul 6–10, 2003, Honolulu, Hawaii, USA, paper no. FEDSM2003-45607, doi:10.1115/fedsm2003-45607.

[164] King, L.V., 1914. On the convection of heat from small cylinders in a stream of fluid: determination of the convection constants of small platinum wires with applications to hot-wire anemometry. Philosophical Transactions of the Royal Society of London, Series A, 214, doi:10.1098/rsta.1914.0023.

[165] Bearman, P.W., 1969. Corrections for the effect of ambient temperature drift on hot-wire measurements in incompressible flow. National Physical Laboratory Aerodynamics Division, Teddington, England, NTIS Issue Number 197105.

[166] Jørgensen, F., 2005. How to measure turbulence with hot-wire anemometers: a practical guide. Published by Dantec Dynamics, P.O. Box 121, Tonsbakken 16-18, DK-2740 Skovlunde, Denmark, publication no. 9040U6154.

[167] Sciacchitano, A., Wieneke, B., 2016. PIV uncertainty propagation. Meas. Sci. Technol., Jun 2016, 27(8), doi:10.1088/0957-0233/27/8/084006.

[168] Launder, B.E., Spalding, D.B., 1974. The numerical computation of turbulent flows. Computer Methods in Applied Mechanics and Engineering, Mar 1974, 3(2), doi:10.1016/0045-7825(74)90029-2.

[169] Messenger, A., Cartlidge, J., Chowdhury, N., Goenaga, F., Povey, T., 2023. ECAT+: a second-generation high-temperature aerothermal facility at the University of Oxford. ASME Turbo Expo, Jun 26–30, 2023, Boston, Massachusetts, USA, paper no. TURBO-23-102935.

[170] Ainley, D.G., Mathieson, G.C.R., 1951. A method of performance estimation for axial-flow turbines. Aeronautical research council technical report no. R & M 2974. Her Majesty's Stationery Office, London, United Kingdom.

[171] Dunham, J., Came, P.M., 1970. Improvements to the Ainley-Mathieson method of turbine performance prediction. ASME J. Eng. Power, Jul 1970, 92(3), doi:10.1115/1.3445349.

[172] Benner, M.W., Sjolander, S.A., Moustapha, S.H., 2006. An empirical prediction method for secondary losses in turbines—part II: a new secondary loss correlation. ASME J. Turbomach., Apr 2006, 128(2), doi:10.1115/1.2162594.

[173] Spalart, P.R., Allmaras, S.R., 1992. A one-equation turbulence model for aerodynamic flows. 30th Aerospace Sciences Meeting and Exhibit, January 6–9, 1992, Reno, Nevada, USA, doi:10.2514/6.1992-439.

[174] Chambers, A.J., Antonia, R.A., Fulachier, L., 1985. Turbulent Prandtl number and spectral characteristics of a turbulent mixing layer. International Journal of Heat and Mass Transfer, Aug 1985, 28(8), doi:10.1016/0017-9310(85)90248-0.

[175] Georgiadis, N.J., Yoder, D.A., 2013. Recalibration of the shear stress transport model to improve calculation of shock separated flows. 51st AIAA Aerospace Sciences Meeting including the New Horizons Forum and Aerospace Exposition, Jan 7–10, 2013, Grapevine, Texas, USA, paper no. AIAA 2013-0685, doi:10.2514/6.2013-685.

[176] Costa Rocha, P.A., Barbosa Rocha, H.H., Moura Carneiro, F.O., Vieira da Silva, M.E., Valente Bueno, A., 2014. k–ω SST (shear stress transport) turbulence model calibration: a case study on small scale horizontal axis wind turbine. Energy, Feb 2014, 65, doi:10.1016/j.energy.2013.11.050.

[177] Yasa, T., Paniagua, G., Fridh, J., Vogt, D., 2010. Performance of a nozzle guide vane in subsonic and transonic regimes tested in an annular sector. ASME Turbo Expo, Jun 14–18, 2010, Glasgow, United Kingdom, paper no. GT2010-22901, doi:10.1115/GT2010-22901.

[178] Sieverding, C.H., Manna, M., 2020. A review on turbine trailing edge flow. International Journal of Turbomachinery Propulsion and Power, Jun 2020, 5(2), doi:10.3390/ijtpp5020010.

[179] Kopriva, J.E., Laskowski, G.M., Reza, M., Sheikhi, H., 2013. Assessment of high pressure cooled and uncooled turbine blade wakes via RANS and URANS at engine scale conditions. ASME Turbo Expo, Jun 3–7, 2013, San Antonio, Texas, USA, paper no. GT2013-94285, doi:10.1115/GT2013-94285.

[180] Kapteijn, C., Amecke, J., Michelassi, V., 1996. Aerodynamic performance of a transonic turbine guide vane with trailing edge coolant ejection: part I—experimental approach. ASME J. Turbomach., Jul 1996, 118(3), doi:10.1115/1.2836698.

[181] Leonard, T., Gicquel, L.Y.M., Gourdain, N., Duchaine, F., 2015. Steady/unsteady Reynolds-averaged Navier–Stokes and large eddy simulations of a turbine blade at high subsonic outlet Mach number. ASME J. Turbomach., Apr 2015, 137(4), doi:10.1115/1.4028493.

[182] Fadai-Ghotbi, A., Manceau, R., Borée, J., 2008. Revisiting URANS computations of the backward-facing step flow using second moment closures. Influence of the numerics. Flow, Turbulence and Combustion, Oct 2008, 81(3), doi:10.1007/s10494-008-9140-8.

[183] Spalart, P.R., 2009. Reflections on RANS modelling. 3rd Symposium on Hybrid RANS-LES Methods, Jun 10–12, 2009, Gdansk, Poland, doi:10.1007/978-3-642-14168-3_2.

[184] Vinnemeier, F., Simon, L., Koschel, W., 1990. Korrektur des Kopfgeometrieeinflusses einer Fünfloch-Drucksonde auf die Meßergebnisse / Correction method for the head geometry influence of a five-hole pressure probe on the measurement results. Technisches Messen, Dec 1990, 57(JG), doi:10.1524/teme.1990.57.jg.296.

[185] Glawe, G.E., Holanda, R., Krause,L.N., 1978. Recovery and radiation corrections and time constants of several sizes of shielded an unshielded thermocouple probes for measuring gas temperature. NASA technical paper no. 1099. Lewis Research Center, Cleveland, Ohio, USA.

[186] Nix, A.C., Smith, A.C., Diller, T.E., Ng,W.F., Thole K.A., 2002. High intensity, large length-scale freestream turbulence generation in a transonic turbine cascade. ASME Turbo Expo, Jun 3–6, 2002, Amsterdam, The Netherlands, paper no. GT2002-30523, doi:10.1115/GT2002-30523.

[187] Lawaczeck, O., 1977. The influence of jets of cooling air exhausted from the trailing edges of a supercritical turbine cascade on the aerodynamic data. 50th meeting of the AGARD propulsion and energetics panel, Sep 19–23, 1977, Ankara, Turkey, AGARD CP229 paper no. 30.

[188] Dzung, L.S., 1971. Konsistente Mittelwerte in der Theorie der Turbomaschinen für kompressible Medien. BBC Mitteilungen, 58, pp. 485–492.

[189] Pianko, M., Wazelt, F., 1983. Propulsion and energetics panel working group 14 on suitable averaging techniques in non-uniform internal flows. AGARD advisory report no. 182, NATO Advisory Group for Aerospace Research and Development, Neuilly-sur-Seine, France.

[190] Burdett, D., Povey, T., 2022. Analysis of averaging methods for nonuniform total pressure fields. ASME J. Turbomach., May 2022, 144(5), doi:10.1115/1.4053020.

[191] Burdett, D., Povey, T., 2023. Impact of trailing edge overhang length on the loss characteristics of fully cooled transonic nozzle guide vanes. ASME J. Turobmach., May 2023, 145(5), doi:10.1115/1.4056056.

[192] Coull, J.D., 2017. Endwall loss in turbine cascades. ASME J. Turbomach., Aug 2017, 139(8), doi:10.1115/1.4035663.

[193] Erickson, E.L., Ames, F.E., Bons, J.P., 2010. Effects of a realistically rough surface on vane aerodynamic losses including the influence of turbulence condition and Reynolds number. ASME Turbo Expo, Jun 14–18, 2010, Glasgow, United Kingdom, paper no. GT2010-22173, doi:10.1115/GT2010-22173.

[194] Thomas, F.O., Liu, X., 2004. An experimental investigation of symmetric and asymmetric turbulent wake development in pressure gradient. Physics of Fluids, May 2004, 16(5), doi:10.1063/1.1687410.

[195] Nakos, J.T., 2004. Uncertainty analysis of thermocouple measurements used in normal and abnormal thermal environment experiments at Sandia's radiant heat facility and Lurance canyon burn site. Sandia National Laboratories report no. SAND2004 1023, Sandia National Laboratories, Albuquerque, New Mexico, USA.

[196] Roy, C.J., 2003. Grid convergence error analysis for mixed-order numerical schemes. AIAA Journal, Apr 2003, 41(4), doi:10.2514/2.2013.

[197] Thomas, M., Dombard, J., Duchaine, F., Gicquel, L., Koupper, C., 2019. Large eddy simulation of combustor and complete single-stage high-pressure turbine of the FACTOR test rig. ASME Turbo Expo, Jun 17–21, 2019, Phoenix, Arizona, USA, paper no. GT2019-91206, doi:10.1115/GT2019-91206.

[198] Wilcox, D.C., 1988, Reassessment of the scale-determining equation for advanced turbulence models. AIAA Journal, Nov 1988, 26(11), doi:10.2514/3.10041.

[199] Menter, F.R., Kuntz, M., Langtry, R., 2003. Ten years of industrial experience with the SST turbulence model. 4th International Symposium on Turbulence, Heat and Mass Transfer, Oct 12–17, 2003, Antalya, Turkey, pp. 625–632.

[200] Wallin, S., Johansson, A.V., 2000. An explicit algebraic Reynolds stress models for incompressible and compressible turbulent flows. Journal of Fluid Mechanics, Jan 2000, 403, doi:10.1017/S0022112099007004.

[201] Menter, F.R., Garbaruk, A.V., Egorov, Y., 2012. Explicit algebraic Reynolds stress model for anisotropic wall-bounded flows. Progress in Flight Physics, 3, doi:10.1051/eucass/201203089.

[202] Menter, F.R., 1992. Influence of freestream values on k-omega turbulence model predictions. AIAA Journal, Jun 1992, 30(6), doi:10.2514/3.11115.

[203] Taylor, G.I., 1935, Statistical theory of turbulence. Proceedings of the Royal Society of London. Series A, Mathematical and Physical Sciences, 151(873), jstor.org/stable/96557.

[204] Bredberg, J., 2001. On two-equation eddy-viscosity models. Internal Report 01/8, Department of Thermo and Fluid Dynamics, Chalmers University of Technology, Göteborg, Sweden.

[205] ANSYS Inc. 2022. ANSYS CFX solver theory guide. Canonsburg, Pennsylvania, USA.

[206] Wilcox, D.C., 2008, Formulation of the k-omega turbulence model revisited. AIAA Journal, Nov 2008, 46(11), doi:10.2514/1.36541.

[207] Bradshaw, P., Ferriss, D.H., Atwell, N.P., 1967. Calculation of boundary-layer development using the turbulent energy equation. Journal of Fluid Mechanics, May 1967, 28(3), doi:10.1017/S0022112067002319.

[208] Spalart, P.R., Rumsey, C.L., 2007. Effective inflow conditions for turbulence models in aerodynamic calculations. AIAA Journal, October 2007, 45(10), doi:10.2514/1.29373.

[209] Moore, J.G., Moore, J., 1999. Realizability in two-equation turbulence models. 30th AIAA Fluid Dynamics Conference, Jun 28–July 1, 1999, Norfolk, Virginia, USA, paper no. AIAA-99-3779, doi:10.2514/6.1999-3779.

[210] Durbin, P.A., 1996. On the k-3 stagnation point anomaly. International Journal of Heat and Fluid Flow, Feb 1996, 17, doi:10.1016/0142-727X(95)00073-Y.

[211] Hancock, P.E., Bradshaw, P., 1983. The effect of free-stream turbulence on turbulence boundary layers. ASME J. Fluids Eng., Sep 1983, 105(3), doi:10.1115/1.3240989.

[212] Thole, K.A., Bogard, D.G., 1996. High freestream turbulence effects on turbulent boundary layers. ASME J. Fluids Eng., Jun 1996, 118(2), doi:10.1115/1.2817374.

[213] Wei, S., 2021. Turbulence modelling for complex flows in turbomachinery. PhD thesis, Cambridge University, Cambridge, United Kingdom.

[214] Kalitzin, G., Medic, G., Xia, G., 2016. Improvement to SST turbulence model for free shear layers, turbulent separation, and stagnation point anomaly. 54th AIAA Aerospace Sciences Meeting, Jan 4–8, 2016, San Diego, California, USA, doi:10.2514/6.2016-1601.

[215] Park, C.H., Park. S.O., 2005. On the limiters of two-equation turbulence models. International Journal of Computational Fluid Dynamics, Jan 2005, 19(1), doi:10.1080/10618560412331286292.

[216] Chowdhury, N., Dey, P.K., Ames, F.E., 2011. The influence of inlet contraction on vane aerodynamic losses and secondary flows with variable turbulence and Reynolds number. ASME Turbo Expo, Jun 6–10, 2011, Vancouver, Canada, paper no. GT2011-45737, doi:10.1115/GT2011-45737.

[217] Mayle, R.E., 1991. The role of laminar-turbulent transition in gas turbine engines. ASME Turbo Expo, Jun 3–6, 1991, Orlando, Florida, USA, paper no. 91-GT-261, doi:10.1115/91-GT-261.

[218] Pacciani, R., Marconcini, M., Bertini, F., Rosa Taddei, S., Spano, E., Zhao, Y., Akolekar, H.D., Sandberg, R.D., Arnone, A., 2021. Assessment of machine-learned turbulence models trained for improved wake-mixing in low-pressure turbine flows. Energies, Dec 2021, 14(24), doi:10.3390/en14248327.

[219] Marioni, Y.F., Adami, P., Vazquez-Diaz, R., Cassinelli, A., Sherwin, S., Montomoli, F., 2022. Development of machine-learnt turbulence closures for wake mixing predictions in low-pressure turbines. ASME Turbo Expo, Jun 13–17, 2022, Rotterdam, The Netherlands, paper no. GT2022-82531, doi:10.1115/GT2022-82531.

[220] Qureshi, I., Beretta, A., Povey, T., 2011. Effect of simulated combustor temperature nonuniformity on HP vane and endwall heat transfer: an experimental and computational investigation. ASME J. Eng. Gas Turbines Power, Mar 2011, 133(3), doi:10.1115/1.4002039.

[221] Schmidt, D.L., Bogard, D.G., 1996. Effects of free-stream turbulence and surface roughness on film cooling. ASME Turbo Expo, Jun 10–13, 1996, Birmingham, United Kingdom, paper no. 96-GT-462, doi:10.1115/96-GT-462.

Statement of Authorship for joint/multi-authored papers for PGR thesis

To appear at the end of each thesis chapter submitted as an article/paper

The statement shall describe the candidate's and co-authors' independent research contributions in the thesis publications. For each publication there should exist a complete statement that is to be filled out and signed by the candidate and supervisor **(only required where there isn't already a statement of contribution within the paper itself).**

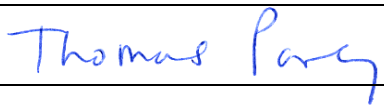
Title of Paper	Lean-burn combustor simulator for an engine-component test facility: an experimental and computational study
Publication Status	☒ Published ☐ Accepted for Publication ☐ Submitted for Publication ☐ Unpublished and unsubmitted work written in a manuscript style
Publication Details	Amend, J., Lubbock, R., Ornano, F., Povey, T., 2023. "Lean-burn combustor simulator for an engine-component test facility: an experimental and computational study." ASME J. Turbomach., Jun 2023, 145(6), doi:10.1115/1.4056387.

Student Confirmation

Student Name:	Jonas Amend		
Contribution to the Paper	Jonas Amend: completed detailed domain, mesh, and turbulence model sensitivity study; developed processing routines for simulation data; analyzed experimental and simulation data; created all figures; wrote manuscript; wrote rebuttal Roderick Lubbock: designed, and assembled the combustor simulator; collected experimental data; developed processing routines for experimental data Francesco Ornano: performed preliminary simulations of the combustor simulator; provided advice for later simulations Thomas Povey: supervised all aspects of the work		
Signature 		Date	December 21, 2023

Supervisor Confirmation

By signing the Statement of Authorship, you are certifying that the candidate made a substantial contribution to the publication, and that the description described above is accurate.

Supervisor name and title: Prof. Thomas Povey		
Supervisor comments The description Jonas gives looks accurate.		
Signature 	Date	January 9, 2024

This completed form should be included in the thesis, at the end of the relevant chapter.

Statement of Authorship for joint/multi-authored papers for PGR thesis

To appear at the end of each thesis chapter submitted as an article/paper

The statement shall describe the candidate's and co-authors' independent research contributions in the thesis publications. For each publication there should exist a complete statement that is to be filled out and signed by the candidate and supervisor **(only required where there isn't already a statement of contribution within the paper itself).**

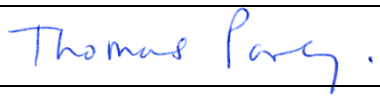
Title of Paper	Ultra-compact traverse system for transonic annular cascade
Publication Status	☒ Published ☐ Accepted for Publication ☐ Submitted for Publication ☐ Unpublished and unsubmitted work written in a manuscript style
Publication Details	Amend, J., Povey, T., 2022. "Ultra-compact traverse system for transonic annular cascade." GPPS Chania22, Sep 12–14, 2022, Chania, Greece, paper no. GPPS-TC-2022-0017, doi:10.33737/gpps22-tc-17.

Student Confirmation

Student Name:	Jonas Amend		
Contribution to the Paper	Jonas Amend: designed traverse system, probes, and control electronics; programmed traverse control system; calibrated split-fiber probes, performed experimental measurements, programmed data processing routines; wrote manuscript; wrote rebuttal; presented paper at the GPPS Chania22 Conference Thomas Povey: supervised all aspects of the work including (but not limited to) advising on design decisions, planning the experimental test campaign, manuscript writing, and delivery at the conference		
Signature 		Date	December 21, 2023

Supervisor Confirmation

By signing the Statement of Authorship, you are certifying that the candidate made a substantial contribution to the publication, and that the description described above is accurate.

Supervisor name and title: Prof. Thomas Povey		
Supervisor comments The description Jonas gives looks accurate.		
Signature 	Date	January 9, 2024

This completed form should be included in the thesis, at the end of the relevant chapter.

Statement of Authorship for joint/multi-authored papers for PGR thesis

To appear at the end of each thesis chapter submitted as an article/paper

The statement shall describe the candidate's and co-authors' independent research contributions in the thesis publications. For each publication there should exist a complete statement that is to be filled out and signed by the candidate and supervisor **(only required where there isn't already a statement of contribution within the paper itself).**

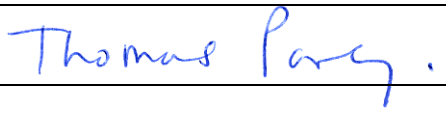
Title of Paper	Aerodynamic and thermal field development of cooled transonic HP NGV
Publication Status	☒ Published ☐ Accepted for Publication ☐ Submitted for Publication ☐ Unpublished and unsubmitted work written in a manuscript style
Publication Details	Amend, J., Lubbock, R., Ornano, F., Chowdhury, N., Povey, T., 2024. "Aerodynamic and thermal field development of cooled transonic HP NGV." ASME J. Turbomach., Feb 2024, 146(2), doi:10.1115/1.4063879.

Student Confirmation

Student Name:	Jonas Amend		
Contribution to the Paper	Jonas Amend: collected NGV aerodynamic field data; performed all simulations including mesh sensitivity study; wrote routines for processing of experimental data and simulations; analyzed experimental data and simulations; created all figures; wrote manuscript; wrote rebuttal Roderick Lubbock: collected thermal field data; developed pre-processing routines for raw pressure and temperature signals Francesco Ornano: performed preliminary simulations of the NGV; mentored Jonas Amend in meshing, and setting up NGV simulations Nafiz Chowdhury: collected NGV thermal field data; supported test facility operations throughout collection of NGV aerodynamic field data Thomas Povey: supervised all aspects of the work		
Signature 		Date	December 21, 2023

Supervisor Confirmation

By signing the Statement of Authorship, you are certifying that the candidate made a substantial contribution to the publication, and that the description described above is accurate.

Supervisor name and title: Prof. Thomas Povey		
Supervisor comments The description Jonas gives looks accurate.		
Signature 	Date	January 9, 2024

This completed form should be included in the thesis, at the end of the relevant chapter.

Statement of Authorship for joint/multi-authored papers for PGR thesis

To appear at the end of each thesis chapter submitted as an article/paper

The statement shall describe the candidate's and co-authors' independent research contributions in the thesis publications. For each publication there should exist a complete statement that is to be filled out and signed by the candidate and supervisor **(only required where there isn't already a statement of contribution within the paper itself).**

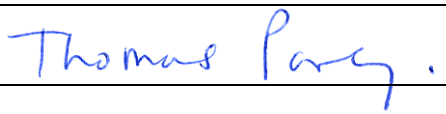
Title of Paper	Comparison of eddy viscosity models for high turbulence NGV flows
Publication Status	☐ Published ☒ Accepted for Publication ☐ Submitted for Publication ☐ Unpublished and unsubmitted work written in a manuscript style
Publication Details	Amend, J., Povey, T., 2024. "Comparison of eddy viscosity models for high turbulence NGV flows." Manuscript accepted for publication in the ASME J. Turbomach., paper no. TURBO-23-1103.

Student Confirmation

Student Name:	Jonas Amend		
Contribution to the Paper	Jonas Amend: performed simulations; performed analysis; wrote manuscript; wrote rebuttal Thomas Povey: supervised all aspects of the work		
Signature 		Date	December 21, 2023

Supervisor Confirmation

By signing the Statement of Authorship, you are certifying that the candidate made a substantial contribution to the publication, and that the description described above is accurate.

Supervisor name and title: Prof. Thomas Povey		
Supervisor comments The description Jonas gives looks accurate.		
Signature 	Date	January 9, 2024

This completed form should be included in the thesis, at the end of the relevant chapter.

Statement of Authorship for joint/multi-authored papers for PGR thesis

To appear at the end of each thesis chapter submitted as an article/paper

The statement shall describe the candidate's and co-authors' independent research contributions in the thesis publications. For each publication there should exist a complete statement that is to be filled out and signed by the candidate and supervisor **(only required where there isn't already a statement of contribution within the paper itself).**

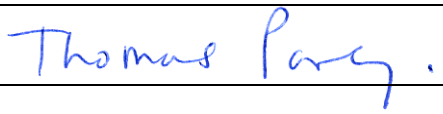
Title of Paper	Impact of lean-burn combustor flow on NGV performance
Publication Status	☐ Published ☐ Accepted for Publication ☒ Submitted for Publication ☐ Unpublished and unsubmitted work written in a manuscript style
Publication Details	Amend, J., Chowdhury, N., Povey, T., [under review]. "Impact of lean-burn combustor flow on NGV performance." Currently under review at the ASME J. Turbomach., paper no. TURBO-23-1329.

Student Confirmation

Student Name:	Jonas Amend		
Contribution to the Paper	Jonas Amend: collected NGV aerodynamic field data; performed all simulations; wrote routines for processing of experimental data and simulations; analyzed experimental data and simulations; created all figures; wrote manuscript Nafiz Chowdhury: collected NGV thermal field data; supported test facility operations throughout collection of NGV aerodynamic field data Thomas Povey: supervised all aspects of the work		
Signature 		Date	December 21, 2023

Supervisor Confirmation

By signing the Statement of Authorship, you are certifying that the candidate made a substantial contribution to the publication, and that the description described above is accurate.

Supervisor name and title: Prof. Thomas Povey		
Supervisor comments The description Jonas gives looks accurate.		
Signature 	Date	January 9, 2024

This completed form should be included in the thesis, at the end of the relevant chapter.

MPLS DIVISION GRADUATE SCHOOL
Science and Technology for Tomorrow

Mathematical, Physical and Life Sciences Divisional Office
9 Parks Road, Oxford OX1 3PD

UNIVERSITY OF OXFORD

Mr Jonas Elias Amend
Christ Church College
Oxford

20 December 2022

Student No: 1234368

Dear Mr Amend,

Permission to Submit an Integrated Thesis

I am pleased to inform you that you have been granted permission to submit an integrated thesis in Engineering Science.

An integrated thesis may either be a hybrid of conventional chapters and high-quality scientific papers, or be fully paper-based. Regardless of the format, the content of the thesis should reflect the amount, originality and level of work expected for a conventional thesis. It should not be assumed that the act of publication (in whatever form) means the work is of suitable academic quality and content for inclusion in a thesis, and students should discuss all papers in detail with their supervisor before including. The collection of papers must include a separate introduction, a full literature review, discussion and a conclusion, so that the integrated thesis can be read as a single, coherent document.

Yours sincerely,

Robyn Mitchell

Robyn Mitchell
Graduate Studies Assistant

cc Supervisor: Professor T Povey, Department of Engineering Science
Tutor for Graduates, Christ Church College
Research Degree Examinations Office

Telephone: +44 (0)1865 282579 Email: graduate.studies@mpls.ox.ac.uk Web: www.mpls.ox.ac.uk